
VORTEX DYNAMICS IN TWO-DIMENSIONAL BOSE–EINSTEIN CONDENSATES

Andrew J. Groszek

Submitted in total fulfilment of the requirements of
the degree of Doctor of Philosophy

Academic advisors:

Dr. Tapio Simula

Prof. David Paganin

Prof. Kristian Helmerson



MONASH University

School of Physics & Astronomy, Monash University

March, 2018

© Andrew J. Groszek, 2018

Abstract

Superfluids such as dilute gas Bose–Einstein condensates (BECs) can support topological excitations including quantised vortices. These vortices are in many ways similar to those found in classical fluids and may be viewed as the elementary building blocks of turbulence in superfluids, coined quantum turbulence (QT). By elucidating the relationship between classical and quantum fluid dynamics, progress towards uncovering the universal properties underlying the poorly understood phenomenon of hydrodynamic turbulence may be achieved. In this thesis, we focus our attention on the dynamical behaviour of two-dimensional (2D) BECs, in which the quantised vortices are reduced to point-like objects. This regime is not only simpler in many ways than its three-dimensional counterpart, but is also understood to give rise to unique dynamical features such as large scale Onsager vortex clusters in 2D turbulence.

To understand the fundamental properties of vortex motion in 2D, we consider the simplest case of a single vortex in a BEC. We derive a general and exact equation of motion for a vortex in a 2D BEC, and demonstrate its accuracy for one- and two-vortex configurations using Gross–Pitaevskii simulations. In doing so, we are able to resolve a number of inconsistencies in past literature. We then proceed with an analysis of two-vortex motion, which we model using a simplified point-vortex description. We identify an untraversable boundary in the phase space of possible initial conditions, corresponding to a topological change in the vortex trajectories.

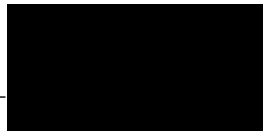
We then move to a detailed examination of 2D QT, in which we focus specifically on understanding and characterising the formation of Onsager vortex clusters. We first investigate the effects of geometry on the dynamical formation of Onsager vortices in decaying turbulence, and determine that harmonic traps prevalent in experiments considerably decrease the visibility of these large scale flows when compared to uniform, steep-walled configurations. We then use Monte Carlo simulations to probe the highest energy limit, where we identify the condensation of Onsager vortices, in analogy with a BEC. With our definition, we are able to draw a distinction between vortex clustering and condensation, and we determine that the latter does not take place in our dynamical simulations. Finally, we introduce a technique to measure the vortex temperature—an observable that can be used to quantitatively describe the emergence of vortex clusters in 2D turbulence. Applying our methodology to simulations of decaying turbulence, we confirm that the visual inspection of vortex clustering is accompanied by an increase in the temperature of the vortices.

Declaration

This thesis contains no material which has been accepted for the award of any other degree or diploma at any university or equivalent institution and that, to the best of my knowledge and belief, this thesis contains no material previously published or written by another person, except where due reference is made in the text of the thesis.

Andrew Groszek

Name



12/3/18

Date

Acknowledgements

A vast number of people have contributed to this project, many of whom may not have even realised it. Without their input and encouragement, I never would have made it far enough to be writing this document.

First and foremost, I would like to thank my primary supervisor, Tapio, for his ongoing support over the past three and a half years. Not only has he always been willing to make time for me, but his seemingly endless positivity and sheer passion for science have served as an inspiration since I first started working with him. I'm very grateful as well to my two secondary supervisors, David and Kris, who have been consistently able to contribute profound insight towards my project when I needed it most. I would also like to thank the many collaborators I have had the pleasure of working with throughout my PhD: Matt, Anderson, Pekko, Rahil, Tom, Shaun and Bhavraj. I am grateful in particular to Matt for inviting me to visit him up in Brisbane in 2017, and to the UQ cold atoms group for making me feel so welcome during my short stay. I am also indebted to the cold atoms group at Monash, most of whom have assisted me in some way or another over the years, and whose friendship I have greatly appreciated.

Throughout my PhD, I have had the enormous privilege of attending many conferences and schools, both overseas and interstate. These experiences have been a definite highlight of my time as a researcher, and I am sincerely grateful to everyone I've met on these trips for making them so enjoyable, and for the many fascinating discussions (scientific or otherwise) that resulted. Thanks as well must go to the KOALA 2016 organising committee. Hosting a conference proved to be one of the most challenging experiences of my entire PhD, but it was without a doubt the most rewarding.

I would also like to acknowledge the ever-evolving postgraduate community in the School of Physics & Astronomy at Monash. My PhD experience would not have been the same if I didn't have such wonderful people to share it with. Thanks as well for putting up with me as the postgrad representative for the past year, and I apologise for filling everyone's inboxes with spam telling them to come and be sociable, despite probably having better things to do with their time. I would also like to thank the other two postgrad reps I suffered through the last year or so alongside—Vaishali and Hayley. I had a surprisingly fun time, and I'm impressed at how well we managed to unite the recently merged schools of physics and astronomy. And of course, no Monash physics graduate's acknowledgements section would be complete without a mention of Jean. She is practically a second

mother to all of us, and we would be helpless without her.

Finally, I would like to express my gratitude to all my non-physicist friends who have accompanied me on this journey. I have learned that maintaining contact with the outside world is essential for preventing the gradual descent into madness that accompanies academic life. Special mentions go to Erika, Kaustav, Eve, Josh, Angus, Ashley, Von, Mischel, Andrew and Tom. And last, but certainly not least, I must thank my family—Mum, Dad, Em, Nick, Chris and Jess—for their unconditional love and support, despite having no idea what exactly it is that I've been doing for the last three and a half years. When you read this, you'll finally know.

CONTENTS

1	Introduction	1
1.1	Bose–Einstein condensates: An overview	2
1.2	Vortices in Bose–Einstein condensates	5
1.3	Thesis scope and motivations	8
1.4	Thesis overview	9
1.5	List of publications	11
2	Theoretical background	13
2.1	Bose–Einstein condensation	13
2.2	Superfluidity	15
2.3	Mean-field theory	16
2.3.1	The Gross–Pitaevskii equation	16
2.3.2	The two-dimensional Gross–Pitaevskii equation	18
2.3.3	Energy and chemical potential	18
2.3.4	The Thomas–Fermi approximation	19
2.3.5	The healing length	21
2.3.6	Excitations	22
2.4	Quantised vortices	23
2.4.1	Properties of the superfluid flow	23
2.4.2	Vortex energetics	25
2.5	Quantum hydrodynamics	26
2.5.1	Hydrodynamic Gross–Pitaevskii equation	26
2.5.2	The Helmholtz decomposition	27
2.5.3	Vortex dynamics	28
3	Turbulence	33
3.1	Classical turbulence	33
3.1.1	Overview	33
3.1.2	Statistical properties of classical turbulence	35
3.1.3	Classical turbulence in two dimensions	38
3.2	The point-vortex approximation	41
3.2.1	Vortices as point-particles	41

3.2.2	Statistical mechanics of point-vortices	44
3.3	Quantum turbulence	46
3.3.1	Overview	46
3.3.2	Quantum–classical analogues	47
3.3.3	Quantum turbulence in two dimensions	50
4	Numerical techniques	53
4.1	Non-dimensionalisation	53
4.2	Numerical integration of the Gross–Pitaevskii equation	54
4.2.1	Discretisation	54
4.2.2	Split-step Fourier method	56
4.2.3	Initial state generation	60
4.3	Numerical integration of point-vortex equations	61
4.4	Implementation	62
4.4.1	Gross–Pitaevskii equation integrator	62
4.4.2	Point-vortex model integrator	62
4.5	Vortex detection and classification	63
4.5.1	Detection of vortices	63
4.5.2	Classification of vortex configurations	63
5	Vortex dynamics in nonuniform Bose–Einstein condensates	69
5.1	Motivation	69
5.2	The vortex velocity in an inhomogeneous superfluid	71
5.3	Numerical study of the velocity of a single vortex	73
5.3.1	The motion of a single vortex in an axisymmetric trap	73
5.3.2	Numerical methods	74
5.3.3	Results	75
5.4	Comparison with results in the literature	82
5.4.1	The two standard approaches	82
5.4.2	Potential sources of confusion	84
5.4.3	Image vortices	85
5.4.4	Further comparisons	86
5.5	Generalising the point-vortex model	86
5.5.1	Requirements of a point-vortex model	87
5.5.2	The point-vortex model	87
5.5.3	Testing the model	90
5.6	Summary	92

6	Dynamics of two same-sign point-vortices	95
6.1	Motivation	95
6.2	Point-vortex model	96
6.3	Results	98
6.3.1	Position-space representation	99
6.3.2	Velocity-space representation	103
6.4	Summary	108
7	Onsager vortex formation in decaying quantum turbulence	111
7.1	Motivation	111
7.2	Model	113
7.2.1	System parameters	113
7.2.2	Numerical techniques	113
7.3	Results	114
7.3.1	Macroscopic dynamical behaviour	114
7.3.2	Statistical mechanics interpretation	115
7.3.3	Vortex annihilation is a many-vortex process	120
7.3.4	Rate equation for evaporative heating of vortices	123
7.3.5	Interaction between vortices and boundaries	125
7.3.6	Onsager vortex formation as a function of trap steepness	126
7.4	Summary	127
8	Vortex condensation	129
8.1	Motivation	129
8.2	Vortex–particle duality	130
8.3	Ideal vortex gas approximation	131
8.4	Interacting vortex gas approximation	132
8.5	Fraction of condensed vortices	135
8.6	Two-species Monte Carlo results	135
8.7	One-species Monte Carlo results	138
8.8	Evaporative heating of vortices	141
8.9	Summary	142
9	Vortex thermometry for turbulent two-dimensional fluids	145
9.1	Motivation	145
9.2	Monte Carlo thermometry	146

9.3	Thermometry of decaying two-dimensional turbulence	148
9.3.1	System parameters	148
9.3.2	Emergence of vortex equilibria	148
9.3.3	Dependence on initial condition	150
9.3.4	Evaporative heating of the vortex gas	152
9.4	Summary	153
10	Conclusions and outlook	155
10.1	Summary	155
10.2	Outlook	156
	References	159

1

INTRODUCTION

This thesis presents a computational and theoretical study of vortex dynamics and quantum turbulence in two-dimensional superfluid Bose–Einstein condensates (BECs). Broadly speaking, the interest in these topics is twofold. On the one hand, superfluid systems are intrinsically interesting in their own right, and present a fascinating intersection between quantum mechanics and fluid dynamics. But on the other, there is also hope that superfluids may hold the key to making progress towards solving the formidable challenge of hydrodynamic turbulence, which to this day is still poorly understood. It is becoming apparent that there are deep connections between quantum and classical fluids, and it is anticipated that uncovering these connections may advance our understanding of the universal properties of turbulence.

However, the field of superfluid turbulence research is still in its infancy, and we are only just beginning to grasp the problem ahead of us. To date, only a small number of experiments have been devoted to studying quantum turbulence in BECs, although that is anticipated to change in the near future. Meanwhile, theoretical efforts have been intensifying, and much progress has been made over the past decade towards elucidating the underlying properties of this intriguing dynamical system. One aspect of quantum turbulence that is already understood to play a large role in determining the fluid behaviour is its dimensionality—a feature that is shared by turbulence in classical fluids. As such, turbulence in two dimensions is not only a conceptual and computational simplification of the problem, but also presents a dynamical regime in which new and interesting physics not available in three dimensions arises.

Before delving into the details of quantised vortices and turbulence, however, it is useful to take a step back and consider this project within the broader context of Bose–Einstein condensate research. This is a field that is constantly evolving, and which encompasses a diverse range of physics. To demonstrate this, we provide a brief overview of the topics of interest in the field—both past and present—in

Sec. 1.1 below. Given the sheer amount of work that has been done, it is difficult to adequately describe all of it. As such, the purpose of the review presented here is more to give the reader a ‘flavour’ of BEC research, and in doing so motivate the widespread interest in these systems. Since the main focus of the thesis is the study of quantised vortices, we proceed by introducing this topic in Sec. 1.2, where we provide a brief background of past and contemporary research directions. We then conclude this introductory chapter with three sections devoted to outlining the contents of the thesis. A broad statement of the goals and scope of our work is presented in Sec. 1.3, followed by a specific overview of all subsequent chapters in Sec. 1.4. Finally, the list of publications that have resulted from this work is presented in Sec. 1.5.

1.1 Bose–Einstein condensates: An overview

At the time of writing this thesis, over two decades have passed since the first realisation of Bose–Einstein condensation¹ in dilute ultracold atomic gases [1–3]. During this time, the study of these systems has become not only ubiquitous, but broadly varied in scope [4]. The widespread interest in Bose–Einstein condensates stems largely from the fact that these systems provide a rare manifestation of quantum mechanics at macroscopic length scales. In addition, they are highly controllable in experimental settings, and can be manipulated in a plethora of ways using optical and magnetic fields. Bose–Einstein condensates are also exceptionally well-suited to a theoretical treatment, because the weak interactions between the atoms in the dilute gas allow for the application of a straightforward and remarkably accurate mean-field approach [5–7]. For these reasons, dilute gas BECs present an ideal physical system in which to explore the rich and diverse properties of quantum mechanics [8–10].

There are now dozens of research laboratories around the world regularly producing ultracold atomic BECs. Typically, these systems consist of $\sim 10^3$ – 10^6 constituent particles, and are on the order of $\sim 100\ \mu\text{m}$ in size. They are created by cooling a dilute gas of atoms (such as alkalis ^{87}Rb , ^{23}Na or ^{41}K) past a certain critical temperature—generally between 0.1 – $1\ \mu\text{K}$ —at which point the condensate spontaneously forms. The cooling process usually takes place in two stages. Firstly, *laser cooling* [11–13] is applied to lower the temperature of the gas to $\sim 100\ \mu\text{K}$, allowing the atoms to be held in place using magnetic and/or optical fields. Once

1. A formal definition of Bose–Einstein condensation is left for Sec. 2.1; for now, it suffices to consider a BEC as a collection of particles acting in unison as a single quantum state.

this has been achieved, *evaporative cooling* [14] is used to eject the most energetic particles from the gas, leaving those which remain significantly colder, on average. This second stage of cooling causes $\sim 90\%$ of the trapped atoms to be lost, but reduces the temperature to $\sim 10\text{--}100\text{ nK}$, which is cold enough for most of the atoms to enter the condensed state. At these temperatures, the diluteness of the gas is essential², as it prevents the atoms from forming a solid.

In the years since their initial experimental realisation, atomic BECs have accumulated interest across a wide variety of fields, and have found numerous applications. They have been utilised as *quantum simulators* [15–18] to study comparatively complicated condensed matter systems such as high temperature superconductors, since the strong interactions in those systems prohibit the study of their fundamental properties. They have also been applied to the field of *quantum metrology* [19–21], where tools such as quantum entanglement and spin squeezing are employed to obtain precision measurements beyond the classical limit. Bose–Einstein condensates are also candidates to become *quantum computers* [22–24], as the atoms can take on the role of quantum bits and be used to form the logic gates fundamental to computation.

One of the features of BECs that makes them so versatile is their highly configurable geometry, which can be tuned in experimental settings via an adjustment of the applied magnetic and optical fields that form the *trapping potential* for the atoms. The most commonly used configuration is a *harmonic trap*, which in a three-dimensional (3D) setup forces the atomic cloud to take on an approximately spherical profile with a radially decreasing density. One-dimensional (1D) and two-dimensional (2D) geometries are also readily achievable via an adjustment of the applied field strengths in each direction [25]. By changing the dimensionality of the BEC, new regimes of physical behaviour can be explored. For example, 2D systems exhibit a Berezinskii–Kosterlitz–Thouless transition [26–28], in which vortex–antivortex pairs spontaneously unbind above a certain critical temperature [29,30]. Likewise, in 1D, phase fluctuations [31] and atomic interactions [32] are understood to play a larger role than in other dimensionalities.

New physics also emerges when the atoms are confined in an *optical lattice* configuration. A one-, two- or three-dimensional grid of individual trapping sites can be created using an interference pattern produced by counter-propagating laser beams in each direction. The degree of control is so high that individual atoms can be trapped in each lattice site, and their tunneling and interaction

2. Typical BECs are $\sim 10^4$ times less dense than air at room temperature and atmospheric pressure.

properties can be observed and modified [33]. In this setup, cold atoms constitute a particularly interesting analogue with condensed matter systems, due to the crystalline nature of the lattice. This connection has been directly established via the observation of a superfluid–Mott insulator transition in optical lattices [34,35].

As a result of years of experimental advances, control over the trapping geometry is now at an unprecedented level. Arbitrary potentials can be created using a variety of methods, such as ‘painting’ time-averaged optical fields using a rapidly moving laser [36] or programming static potentials directly onto digital-micromirror devices [37]. Recently, experiments have also begun to move towards uniform traps with hard walls [38–42]. As we will see in later chapters, this geometry is particularly relevant for studying vortex motion and quantum turbulence in two dimensions.

In this thesis, we will be interested predominantly in the dynamical properties that emerge when a Bose–Einstein condensate is perturbed from equilibrium. Significant research in the early days of BEC went into creating and measuring the elementary *excitations* of the condensate, which take the form of *sound waves*, and in a trap can give rise to collective oscillations of the entire cloud [43–48]. BECs are also capable of exhibiting *nonlinear* dynamics, including topological features such as *solitons* and *quantised vortices*. A soliton or solitary wave is a one-dimensional localised density extremum that travels at constant velocity without dispersing. These excitations have been studied extensively [49], and can be created in condensates with both repulsive [50–52] and attractive [53,54] atomic interactions. The interest in these phenomena can be attributed, in part, to their occurrence in a range of disparate physical systems, such as nonlinear optical fields [55] and shallow liquids [56]. In BECs, many fascinating dynamical processes involving solitons have been observed, such as their interaction [57] and collision [58] dynamics, and their decay into vortex rings via the snake instability [59]. Since quantised vortices are the main topic of interest in our work, they will be treated in detail in Sec. 1.2 below.

Although we will only consider the ‘simplest’ case of a *scalar* dilute gas BEC in the work presented here, it is worth noting that many more exotic varieties of condensates are now possible. Simultaneously trapping multiple hyperfine states of a single bosonic species of atom gives rise to a *spinor* condensate [60,61], which can be used to study uniquely magnetic phenomena such as *spin mixing* [62] and *spin–orbit coupling* [63,64]. These systems were first realised in 1998 [65], and have since become the subject of their own field of research [66]. Another

example is the *dipolar* BEC, in which the atoms exhibit a strong electric or magnetic dipole moment, giving rise to long range dipole–dipole interactions (in addition to the usual contact interactions relevant to dilute gases). Dipolar condensates have recently been created [67, 68], and already much interesting physics has been seen to result from their interactions, such as the existence of strictly *d*-wave properties [69], and the formation of stable quantum droplets [70, 71]. It is also possible for ultracold fermionic gases to condense via the creation of bosonic molecules [72], and these systems are now the centre of their own mature field of research [73]. Finally, we note that Bose–Einstein condensation can be extended beyond dilute gases altogether: *exciton–polariton* [74, 75], *magnon* [76] and *photon* [77] condensates have now been experimentally realised, which all possess the distinctive feature of being attainable at room temperatures.

1.2 Vortices in Bose–Einstein condensates

Dilute gas Bose–Einstein condensates are, in general, *superfluid* in nature. Consequently, the possible flow patterns are severely restricted, as we will discuss in Chapter 2. Unlike in a classical fluid, vorticity cannot be continuously distributed throughout a superfluid, and as a result any circulation is ‘stored’ in points of vanishing density, known as quantised vortices. In this thesis, we restrict our focus to the case of single component BECs, where the quantised vortices are, loosely speaking, analogous to vortices in classical fluids: they are line-like objects about which there is rotational fluid flow. However, they are also distinct from classical vortices in a number of fundamental ways:

- (i) The circulation around a quantised vortex must take on a discrete value (as we will see in Chapter 2). Classical vortices, by contrast, have no such restrictions on their velocity field and can thus have any value of circulation.
- (ii) Quantised vortices are localised in space and have a well-defined core structure, whereas classical vortices are poorly defined and can exist in a variety of forms.
- (iii) Quantised vortices are *topologically protected*, meaning that they cannot be locally removed from the system—they must either leave the fluid via the boundary, or undergo an *annihilation* event (see Sec. 2.5.3). Classical vortices, on the other hand, can dissipate via viscous action, thereby transferring all of their energy into the surrounding fluid.

The analogy between classical and quantum fluid flows will be revisited and expanded upon in the context of turbulence in Chapter 3.

Quantised vortices were first conceptualised by Onsager [78] and Feynman [79] over 60 years ago in the context of superfluid helium. Shortly thereafter, their existence was confirmed experimentally by Vinen³ [82]. Throughout the half century since, quantised vortices have been studied extensively in liquid helium [83], and have also been identified in a vast number of other physical contexts [84], such as superconductors [85], nonlinear optical fields [86–88], and free-electron waves [89–91].

In the early days of atomic BEC, it was uncertain whether these systems should exhibit superfluidity, and thus whether they could support quantised vortices at all (see, e.g. Ref. [92]). However, in 1999, the possibility of these states was confirmed experimentally by Matthews *et al.* [93]—an achievement that marked the beginning of a new era in BEC research [see Fig. 1.1(a)]. In the nearly two decades since, experiments and theoretical works investigating the properties of vortices have proliferated [94, 95]. There now exist a multitude of experimental techniques with which vortices can be created, such as topological phase imprinting [93, 96], rotating [97, 98] or oscillating [99–101] the external potential, or stirring the cloud with a repulsive laser [102–104]. Vortices can also form spontaneously via the Kibble–Zurek mechanism [105, 106] during a quench past the BEC phase transition [107], or when three or more condensate fragments are interfered with one another [108].

Broadly speaking, early research on vortices in BECs focused on two problems: the motion of a single vortex, and the formation of large *vortex lattices*. In a harmonically trapped BEC, a solitary vortex was observed to orbit around the trap centre [110]—behaviour well predicted by theory [111, 112]. The tilting [113, 114] and bending [115] of a vortex were also studied, and evidence was found for the excitation of *Kelvin waves* along the filament of the defect [116] (see Sec. 2.5.3.2). When the condensate was rapidly rotated, large numbers of vortices were observed to form [97], and these were observed to arrange themselves into a triangular *Abrikosov* lattice structure [117] to minimise their energy [see Fig. 1.1(b)]. Lattices as large as ~ 100 vortices were created [118, 119], and their

3. The direct observation of quantised vortex lines in superfluid helium proved elusive, however, due to their $\sim 10^{-10}$ m core size. Two-dimensional images of vortices were obtained by Yarmchuk *et al.* [80] in the late 1970s, although it was not until the mid-2000s that full three-dimensional visualisation was first reported by Bewley *et al.* [81]. In both cases, the vortices were imaged using micron-sized particles that tracked the vortex cores.

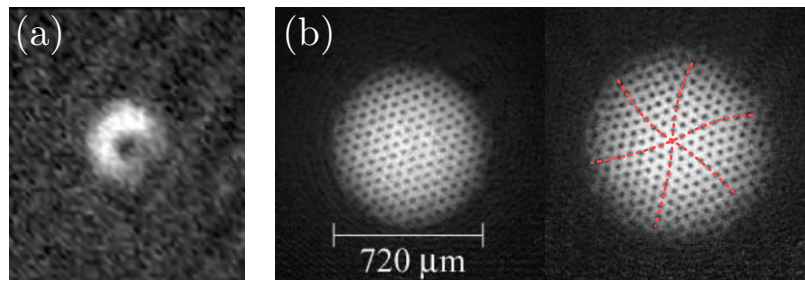


Figure 1.1: Experimental images of vortices in Bose–Einstein condensates, adapted from Refs. [93, 109]. The greyscale in each figure corresponds to the line density of atoms integrated over the z -direction (perpendicular to the page), and the vortices are visible as dark spots. (a) The first observation of a vortex in a BEC by Matthews *et al.* [93]. (b) Two images of a vortex lattice from Ref. [109] (note that the distance scale only applies to this frame). In the right hand figure, a sinusoidal Tkachenko wave is visible across the lattice, highlighted with red dashed lines.

excitations, known as *Tkachenko oscillations* [120, 121], were probed by perturbing the condensate [122, 123]. Under certain regimes of forcing, it was shown that an initially hexagonal lattice could be deformed into a square structure [124]. Rapidly rotating condensates promised particularly interesting physical consequences due to a prediction that the lattice would melt and give rise to *quantum Hall*-like behaviour at extremely high rotation frequencies [125, 126]. Due to experimental limitations, however, this prediction has never been realised in the laboratory.

More recently, focus has shifted towards investigating the dynamics of small numbers of vortices. Experimental observations of vortex–antivortex dipoles [102, 127–129] and clusters of two, three and four vortices [128, 130–132] have taken place. Such measurements have only been made possible in recent years by advances in deterministically creating [133], manipulating [134] and imaging [127, 135] vortices in BECs. These experiments have been complemented by numerous theoretical and computational studies examining both dynamics [136–140] and stationary states [141–144] of vortex dipoles and small clusters. These few-vortex configurations are of interest, in part, because of the potential insight they can provide into the onset of chaos and turbulence.

Currently, the most pertinent topic of research involving vortices in BECs is *quantum turbulence* [145–150]—a highly nonequilibrium dynamical state that corresponds to the chaotic motion of large numbers of vortex filaments, and features a strong interplay between vortices and sound waves. Quantum turbulence has

received significant attention both experimentally [101, 103, 151–155] and theoretically [156–171] in recent years, and it is becoming clear that superfluids may help us to shed light on the fundamental properties of hydrodynamic turbulence, which remains poorly understood in contemporary physics. In analogy with classical fluids, dimensionality has a significant effect on the turbulent behaviour, and our focus on two dimensions leads to interesting properties such as *Onsager vortex clusters* and *negative absolute temperature* states [78]. We will discuss quantum turbulence, and introduce these concepts in detail, in Chapter 3.

1.3 Thesis scope and motivations

In this thesis, we investigate the dynamics of quantised vortices in trapped two-dimensional Bose–Einstein condensates. Broadly speaking, we focus on two disparate dynamical scenarios. Firstly, we study the motion of one- and two-vortex configurations. In this regime, the dynamics are *regular* and the vortices follow deterministic, periodic trajectories through the atomic cloud. As such, we place emphasis here on precisely describing their orbital motion. By contrast, adding more vortices to the system gives rise to *chaos* and turbulence—a subject that constitutes the second major focus of our work. Due to the complexity of the dynamics in this regime, we must resort to statistical measures, which ignore the fine details of the system and instead capture only its coarse-grained behaviour.

We make use of two distinct approaches to carry out our investigations. The first of these is the *Gross–Pitaevskii equation*—the most widely used formalism for modelling Bose–Einstein condensates. This model accurately describes the vortices and their interactions with the embedding superfluid, and therefore contains the essential physics of interest to us. We also employ a simplified *point-vortex model* in which the vortices are approximated as particles with zero spatial extent. In this approach, the vortex dynamics are described with a set of coupled ordinary differential equations, which include inter-vortex interactions and relevant boundary conditions. This method, however, ignores the background superfluid, and hence many fine details of the dynamics are lost. To ensure it is adequate in the scenario being studied, we must therefore benchmark it against the Gross–Pitaevskii equation.

We apply these models in two ways. The first is to predict dynamics: in each approach, we input an initial vortex configuration and calculate the resulting motion as a function of time. However, when the dynamics are turbulent, it is also useful to characterise the behaviour of large vortex configurations using

equilibrium *Monte Carlo* simulations. In this case, there are no dynamics—rather, we set the approximate energy of the system, and determine the most probable configuration of the vortices under that constraint.

The primary motivations of the research presented in this thesis can be summarised as follows:

- (i) In the few-vortex regime, we aim to describe exactly the motion of vortices in a two-dimensional Bose–Einstein condensate.
- (ii) In the many-vortex regime, our main goal is to characterise the dynamical formation of large scale vortex clusters in two-dimensional quantum turbulence. We wish to understand why it occurs, what properties of the system it depends on, and how to quantify it. Where possible, we would also like to identify features that are universal in 2D quantum turbulence, irrespective of system properties such as geometry.
- (iii) We aim, in part, to guide future experiments in the study of 2D quantum turbulence. To facilitate this goal, we choose to simulate systems which are either currently realisable in the laboratory, or will be in the near future.

1.4 Thesis overview

This thesis comprises ten chapters, the remaining nine of which are structured as follows. Chapter 2 explains the essential theory relevant to the study of Bose–Einstein condensates. The mean-field Gross–Pitaevskii equation is derived, and a number of important results of this formalism are outlined. The existence of quantised vortices is motivated from the theory, and many basic properties of these topological defects are described in detail.

Chapter 3 presents a brief review of some key properties of turbulence in classical fluids. We highlight in particular the differences between two- and three-dimensional hydrodynamic turbulence, with a focus on the statistical behaviour in each case. We then introduce the concept of quantum turbulence, and emphasise the similarities and differences between turbulent behaviour in classical fluids and superfluids. We also introduce the point-vortex model in the context of 2D turbulence, and emphasise its aptitude for describing quantised vortices in superfluids.

In Chapter 4, we specify the details of our numerical simulations—the discrete representation of a continuous field, the algorithms used for performing numerical

integration, and our specific implementation of them. We also describe how vortices are detected and classified in our simulations, a step which is essential for studying their dynamics and statistical behaviour.

Chapter 5 presents a study of the dynamics of one and two quantised vortices in a trapped BEC. We derive an exact equation of motion for a vortex in a generally nonuniform two-dimensional condensate, and show numerically that it describes the motion of a single vortex in a trapped system more accurately than any other approach that has been suggested in the literature. We then use our equation of motion to derive a set of point-vortex equations for vortices in harmonically trapped BECs, and show that our new model improves over those that have been used in previous works.

Continuing the theme of few-vortex dynamics, we explore the motion of two same-sign point-vortices in a harmonic trap in Chapter 6. We discover that a previously identified bifurcation in their dynamics is associated with an impenetrable boundary in the phase space of possible initial conditions for the two vortices. On each side of this boundary, we find that the vortex trajectories are topologically distinct.

In Chapter 7, we begin our investigation of quantum turbulence in 2D trapped Bose–Einstein condensates. We focus here on the effects of trapping geometry with regards to the emergence of large scale Onsager vortex clusters, and find that the standard harmonic traps used in experiments reduce the visibility of these large scale clusters when compared with hard-walled uniform traps. We also examine the microscopic processes underpinning the dynamics, and find that vortex–antivortex annihilation is usually a three- or four-vortex event, a feature that is reflected in the vortex number decay behaviour.

In Chapter 8, we use Monte Carlo simulations to identify a *condensation* process that takes place for extremely high energy vortex configurations. We introduce a new observable—the vortex condensate fraction—to quantify this condensation process, which is in analogy with Bose–Einstein condensation of massive particles. Using this observable, we are able to unambiguously distinguish between vortex clustering and vortex condensation, which has not previously been achieved. We also show that, unlike clustering, condensation does not take place in our dynamical Gross–Pitaevskii simulations.

Chapter 9 introduces a new method of characterising turbulence in two-dimensional fluids. For decades, Onsager’s *vortex temperature* parameter has been discussed in the context of 2D turbulence, although it has never been mea-

sured directly. Here, we suggest a new methodology for doing so, which requires only the knowledge of the locations and signs of all vortices in the fluid. Using our measurement technique, we are able to quantitatively demonstrate that vortex *evaporative heating* is driving the system towards negative temperature states.

Finally, we summarise our results in Chapter 10, and provide a brief discussion on future directions for this research.

1.5 List of publications

The results from a number of published and submitted papers are presented in this work. The list of these is included below. Where I am not the first author of the work, I outline my specific contributions.

- Chapter 5—Ref. [172]: A. J. Groszek, D. M. Paganin, K. Helmerson, and T. P. Simula, ‘*Motion of vortices in inhomogeneous Bose–Einstein condensates*’, *Physical Review A* **97**, 023617 (2018).
- Chapter 6—Ref. [140]: A. V. Murray, A. J. Groszek, P. Kuopanportti, and T. Simula, ‘*Hamiltonian dynamics of two same-sign point vortices*’, *Physical Review A* **93**, 033649 (2016). For this work, I contributed to the analysis of the data, the discussion of results, and the preparation of the manuscript.
- Chapter 7—Ref. [169]: A. J. Groszek, T. P. Simula, D. M. Paganin, and K. Helmerson, ‘*Onsager vortex formation in Bose–Einstein condensates in two-dimensional power-law traps*’, *Physical Review A* **93**, 043614 (2016).
- Chapter 8—Ref. [173]: R. Valani, A. J. Groszek, and T. P. Simula, ‘*Condensation of Onsager vortices*’, arXiv:1612.02930. For this work, I contributed to the simulations, the analysis of the data, the discussion of results, and the preparation of the manuscript.
- Chapter 9—Ref. [170]: A. J. Groszek, M. J. Davis, D. M. Paganin, K. Helmerson, and T. P. Simula, ‘*Vortex thermometry for turbulent two-dimensional fluids*’, *Physical Review Letters* **120**, 034504 (2018).

2

THEORETICAL BACKGROUND

This chapter outlines the theory underpinning both Bose–Einstein condensation and superfluidity. We first define these two concepts in depth, before deriving the mean-field Gross–Pitaevskii model which is used throughout this thesis to simulate condensate dynamics. Following a brief discussion on some important consequences of this theory, we rigorously introduce the concept of a quantised vortex. Finally, we draw an analogy with classical fluids, and describe a number of well-known dynamical processes involving quantised vortex lines.

2.1 Bose–Einstein condensation

All known elementary particles fall into one of two categories, depending on their intrinsic angular momentum. Particles with integer spin are known as *bosons*, while those with half-odd-integer spin are said to be *fermions*. Quantum mechanically, these two species of particles behave very differently. When two identical bosons are interchanged, their wavefunction ψ is unchanged (up to a phase factor of $2n\pi$, with $n \in \mathbb{Z}$):

$$\psi(\mathbf{r}_1, \mathbf{r}_2) = \psi(\mathbf{r}_2, \mathbf{r}_1). \quad (2.1)$$

As a result, they obey Bose–Einstein statistics, and are able to occupy the same quantum mechanical state (i.e. $\mathbf{r}_1 = \mathbf{r}_2$ is allowed). By contrast, the wavefunction of two fermions is antisymmetric under their exchange:

$$\psi(\mathbf{r}_1, \mathbf{r}_2) = -\psi(\mathbf{r}_2, \mathbf{r}_1), \quad (2.2)$$

and hence the overall phase is changed by $(2n+1)\pi$. Because of this, two fermions cannot occupy the same state, since $\psi(\mathbf{r}, \mathbf{r}) = -\psi(\mathbf{r}, \mathbf{r})$ is only true for a vanishing wavefunction. This property is known as Pauli exclusion, and more generally, fermions are said to obey Fermi–Dirac statistics [174].

The possibility of *Bose–Einstein condensation* comes as a direct consequence of

these quantum statistics. Einstein realised this in 1924–1925 [175, 176], shortly after Bose suggested applying the machinery of statistical mechanics to a gas of quantised particles of light [177]. Einstein found that particles obeying Bose’s statistical framework are, by necessity, indistinguishable from one another, and hence that there is no upper limit on the number of particles occupying a single quantum state. As a result, he predicted that there exists a critical temperature below which the particles form a ‘condensed substance’, as they begin to preferentially occupy the lowest energy state. In modern terms, this degenerate quantum state is known as a Bose–Einstein condensate—a state of matter in which the constituent particles ‘synchronise’ with one another to form a single macroscopic quantum object.

An alternative framework for describing the transition to BEC is in terms the *thermal de Broglie wavelength* of the bosons. This quantity corresponds to the characteristic extent of each bosonic wavepacket—as the de Broglie wavelength grows, the wave nature of the particles becomes more apparent. The thermal de Broglie wavelength is defined

$$\lambda_{\text{dB}} = \frac{h}{\sqrt{2\pi mk_B T}}, \quad (2.3)$$

where h is Planck’s constant, k_B is Boltzmann’s constant, m is the mass of the atoms, and T is the temperature. In this picture, the critical temperature T_c corresponds to the point at which λ_{dB} becomes greater than the mean interatomic spacing $n^{1/d}$, where d is the spatial dimensionality and n is the atomic density (with units appropriate for d). Hence,

$$T_c \sim \frac{h^2 n^{2/d}}{2\pi m k_B}. \quad (2.4)$$

At this temperature, the wavefunctions of the particles in the gas begin to overlap, and thus their behaviour becomes correlated over large length scales.

One important feature of Bose–Einstein condensation is that the growth of the condensate is a continuous function of temperature. For $T > T_c$, the *condensate fraction* (the percentage of atoms that are condensed) is zero. Between $T = T_c$ and $T = 0$, the condensate fraction rises continuously to unity. In general, the expression for the condensate fraction in an ideal gas (i.e. no interactions) is [10]:

$$\frac{N_0}{N} = 1 - \left(\frac{T}{T_c} \right)^\alpha, \quad (2.5)$$

where N_0 is the number of atoms in the condensed state, N is the total number

of atoms in the system, and α is a dimensionless parameter which depends on physical properties such as dimensionality and geometry. For example, $\alpha = 3/2$ for particles in a three-dimensional box. The effects of interactions also introduce corrections to this expression [178]. In a dilute gas, any atoms in thermally excited states are generally referred to as the *thermal cloud*, and their interaction with the condensate atoms can have important implications for the behaviour of the BEC. In experiments, it is common to reach condensate fractions beyond ~ 0.9 [179].

2.2 Superfluidity

For over a decade following Einstein's prediction of Bose–Einstein condensation, it was thought that this phenomenon could only occur in ideal, non-interacting gases, and hence that it had no implications for physically realistic systems [180]. It was not until 1938 that this idea was challenged, when London [181] first suggested a link between BEC and the then recently discovered [182, 183] phenomenon of *superfluidity* in ^4He . In the years following, a theoretical framework emerged in which the connection between BEC and superfluidity became rigorously established [184–188].

We now understand superfluidity to arise fundamentally from the interactions between Bose–Einstein condensed particles, which allows them to acquire a macroscopically agreed upon phase. This gives rise to a variety of phenomena, such as [146]:

- (i) Frictionless flow below a certain critical velocity v_c , determined by the *Landau criterion* [185]:

$$v_c = \min\left(\frac{\varepsilon(p)}{p}\right). \quad (2.6)$$

Here, $\varepsilon(p)$ is the dispersion relation, relating the energy ε of an excitation to its momentum p . For flow rates above this velocity, it becomes energetically favourable for the fluid to generate excitations, leading to dissipation.

- (ii) Two-fluid behaviour, whereby the *superfluid* component (corresponding to the condensed atoms) and the *normal* component (corresponding to the excitations) appear to behave semi-independently. In the limit $T \rightarrow 0$, the superfluid fraction approaches unity, while for $T > T_c$, it vanishes¹.

1. This two-fluid behaviour was recently demonstrated rather strikingly in an experimental examination of *thermal counterflow*, where the two components of the fluid move in opposite directions in response to a temperature gradient [189].

- (iii) Rotation which is restricted to quantised vortex lines. This property will be described in detail in Sec. 2.4.

However, the link between BEC and superfluidity is a subtle one. Although a macroscopically occupied state is necessary for superfluidity to manifest, the opposite is not true². A simple example is the case of a BEC of non-interacting particles, for which the dispersion relation takes the form of a free particle, $\varepsilon(p) = p^2/2m$. As a result, the critical velocity in Eq. (2.6) vanishes, and dissipationless flow is forbidden. Hence, a superfluid can never form in such a system. It is also incorrect to equate the superfluid fraction with the condensate fraction—in superfluid helium, these can differ significantly. For example, as $T \rightarrow 0$, the superfluid fraction approaches 1 (as mentioned above), while the condensate fraction is thought to only reach ~ 0.1 , due to a phenomenon known as quantum depletion, which arises from the interactions [188].

2.3 Mean-field theory

2.3.1 The Gross–Pitaevskii equation

The standard theoretical approach used to predict the properties of a dilute gas Bose–Einstein condensate at zero temperature is known as the *Gross–Pitaevskii equation* [190, 191]. In this description, the many-body quantum field operator corresponding to the gas of bosons is replaced with a classical field, under the assumption that the number of condensed particles is large. Here we present a brief derivation of the model.

We begin with the second quantised Hamiltonian for an interacting Bose gas:

$$\hat{H} = \int \hat{\Psi}^\dagger(\mathbf{r}, t) \left(-\frac{\hbar^2}{2m} \nabla^2 + V_{\text{trap}}(\mathbf{r}, t) \right) \hat{\Psi}(\mathbf{r}, t) d\mathbf{r} + \frac{1}{2} \iint \hat{\Psi}^\dagger(\mathbf{r}, t) \hat{\Psi}^\dagger(\mathbf{r}', t) V_{\text{int}}(\mathbf{r} - \mathbf{r}') \hat{\Psi}(\mathbf{r}', t) \hat{\Psi}(\mathbf{r}, t) d\mathbf{r} d\mathbf{r}'. \quad (2.7)$$

In this expression, $\hat{\Psi}(\mathbf{r}, t)$ is the quantum field operator describing the gas of bosons, $\hat{\Psi}^\dagger(\mathbf{r}, t)$ is its Hermitian conjugate, $V_{\text{trap}}(\mathbf{r}, t)$ corresponds to an externally applied trapping potential, $V_{\text{int}}(\mathbf{r} - \mathbf{r}')$ is the interaction potential, $\hbar = h/2\pi$ is the reduced Planck’s constant, and ∇^2 is the Laplacian operator. In the first integral, the Laplacian term corresponds to the kinetic energy of the bosons. In

2. Actually, ‘quasi-long-range’ order (and therefore superfluidity) is possible without BEC in 2D systems below the Berezinskii–Kosterlitz–Thouless transition. However, given the lack of true long-range order, the whole system cannot be considered to be a single BEC.

general, the interactions may be strong (as is the case for liquid helium), making the second term difficult to deal with. However, for a dilute gas BEC, we can proceed by assuming that the interaction is short-ranged, and that the potential can be reasonably approximated as a contact interaction. Therefore, we make the approximation

$$V_{\text{int}}(\mathbf{r} - \mathbf{r}') \approx g \delta(\mathbf{r} - \mathbf{r}'), \quad (2.8)$$

where the interaction parameter g is defined:

$$g = \frac{4\pi\hbar^2 a_s}{m}. \quad (2.9)$$

Here, a_s is the s -wave scattering length, a physical constant describing the length scale at which the contact interactions become relevant. In general, it is possible for the scattering length to be negative, a scenario in which the interatomic interactions are attractive³. Throughout this thesis, however, we will only be interested in the case of repulsive interactions, where $a_s > 0$.

Substituting Eq. (2.8) into the Hamiltonian, we can integrate out the Dirac delta, $\delta(\mathbf{r} - \mathbf{r}')$ in the second term of Eq. (2.7), resulting in

$$\begin{aligned} \hat{H} = & \int \hat{\Psi}^\dagger(\mathbf{r}, t) \left(-\frac{\hbar^2}{2m} \nabla^2 + V_{\text{trap}}(\mathbf{r}, t) \right) \hat{\Psi}(\mathbf{r}) \, d\mathbf{r} \\ & + \frac{g}{2} \int \hat{\Psi}^\dagger(\mathbf{r}, t) \hat{\Psi}^\dagger(\mathbf{r}, t) \hat{\Psi}(\mathbf{r}, t) \hat{\Psi}(\mathbf{r}, t) \, d\mathbf{r}. \end{aligned} \quad (2.10)$$

If we assume that the condensate mode is highly occupied, we can express the total field operator as:

$$\hat{\Psi}(\mathbf{r}, t) = \psi(\mathbf{r}, t) + \delta\hat{\Psi}(\mathbf{r}, t) \quad (2.11)$$

where the classical field $\psi(\mathbf{r}, t) \equiv \langle \hat{\Psi}(\mathbf{r}, t) \rangle$ describes the condensate, while the additional field operator $\delta\hat{\Psi}(\mathbf{r}, t)$ accounts for the fluctuations resulting from excited atoms (by definition, $\langle \delta\hat{\Psi}(\mathbf{r}, t) \rangle = 0$). This decomposition is possible because, when the condensate mode is highly occupied, the corresponding creation and annihilation operators commute to good approximation, meaning that the field behaves classically [7, 186].

To determine how the field $\hat{\Psi}(\mathbf{r}, t)$ evolves in time, we can use the Heisenberg

3. In this case, the atomic cloud becomes unstable and collapses when the atom number exceeds a certain critical value, as has been observed experimentally [192].

equation of motion:

$$i\hbar \frac{\partial}{\partial t} \hat{\Psi}(\mathbf{r}, t) = [\hat{\Psi}(\mathbf{r}, t), \hat{H}], \quad (2.12)$$

where the square brackets here denote commutation. If we then apply the decomposition Eq. (2.11), and assume that there are no atoms in thermally excited states (i.e. $T = 0$), then we can ignore the $\delta\hat{\Psi}(\mathbf{r}, t)$ term entirely. Doing so, Eq. (2.12) simplifies to the Gross–Pitaevskii equation (GPE):

$$i\hbar \frac{\partial}{\partial t} \psi(\mathbf{r}, t) = \left[-\frac{\hbar^2}{2m} \nabla^2 + V_{\text{trap}}(\mathbf{r}, t) + g |\psi(\mathbf{r}, t)|^2 \right] \psi(\mathbf{r}, t). \quad (2.13)$$

By convention, ψ is normalised to the number of atoms N in the condensate⁴, i.e. $\int |\psi(\mathbf{r}, t)|^2 d\mathbf{r} = N$, meaning that the particle density of the gas is now given by $n(\mathbf{r}, t) = |\psi(\mathbf{r}, t)|^2$. Evidently, the GPE takes the form of a nonlinear Schrödinger equation, where the nonlinearity arises from the atomic interactions. By convention, the field ψ is usually referred to as the macroscopic *wavefunction* or the *order parameter* of the condensate.

2.3.2 The two-dimensional Gross–Pitaevskii equation

Since our focus for the majority of this thesis will be restricted to two-dimensional systems, we must make a slight adjustment to Eq. (2.13) by making the replacement $g \rightarrow g_{2D}$. The effective two-dimensional interaction parameter g_{2D} is obtained by integrating the three-dimensional parameter over the z -coordinate: $g_{2D} = g \int |\psi_z(z)|^4 dz$, where we have decomposed the field such that $\psi(x, y, z) = \psi_{2D}(x, y)\psi_z(z)$. If the fluid density is uniform in the z -direction and has a spatial extent of l_z , then $g_{2D} = g/l_z$. Beyond this chapter, when we refer to $\psi(\mathbf{r}, t)$ and g , we will actually mean $\psi_{2D}(x, y, t)$ and g_{2D} ; however, for brevity we will drop the subscripts. We also take the convention $\int n(\mathbf{r}, t) d\mathbf{r} = 1$, and hence $g_{2D} \rightarrow g_{2D}N$.

2.3.3 Energy and chemical potential

The energy functional corresponding to the GPE, Eq. (2.13), is given by:

$$E[\psi(\mathbf{r}, t)] = \int \left[\frac{\hbar^2}{2m} |\nabla\psi(\mathbf{r}, t)|^2 + V_{\text{trap}}(\mathbf{r}, t) |\psi(\mathbf{r}, t)|^2 + \frac{g}{2} |\psi(\mathbf{r}, t)|^4 \right] d\mathbf{r}. \quad (2.14)$$

4. Note that now $N = N_0$, since $T = 0$, and we are assuming that the effects of quantum depletion are negligible [8].

Under evolution of Eq. (2.13), this quantity is conserved. It is often useful to consider the separate contributions to this equation, which we define as

$$E_K(t) = \int \frac{\hbar^2}{2m} |\nabla\psi(\mathbf{r}, t)|^2 d\mathbf{r} \quad (2.15a)$$

$$E_P(t) = \int V_{\text{trap}}(\mathbf{r}, t) |\psi(\mathbf{r}, t)|^2 d\mathbf{r} \quad (2.15b)$$

$$E_I(t) = \int \frac{g}{2} |\psi(\mathbf{r}, t)|^4 d\mathbf{r}, \quad (2.15c)$$

the kinetic, potential, and interaction energies, respectively.

Another quantity of relevance is the *chemical potential* μ , defined $\mu \equiv \partial E / \partial N$ (the amount of energy which would be created by adding a single particle to the system). If ψ is stationary [i.e. $\psi(\mathbf{r}, t) = \psi(\mathbf{r}) \exp(-i\mu t / \hbar)$], then Eq. (2.13) reduces to:

$$\mu\psi(\mathbf{r}) = \left[-\frac{\hbar^2}{2m} \nabla^2 + V_{\text{trap}}(\mathbf{r}) + g|\psi(\mathbf{r})|^2 \right] \psi(\mathbf{r}), \quad (2.16)$$

the stationary GPE, with ‘eigenvalue’ μ^5 . Comparing Eqs. (2.16) and (2.14), it can be seen that the chemical potential of a stationary solution can be expressed as an identity:

$$\mu = \frac{1}{N} (E_K + E_P + 2E_I). \quad (2.17)$$

It is also worth noting that, in a uniform system, the kinetic and potential terms in Eq. (2.16) vanish, leaving $\mu = gn$ for a stationary solution. Even for a nonuniform system, it is often worth considering the ‘local’ chemical potential $\mu(\mathbf{r}) = gn(\mathbf{r})$, which may vary as a function of space.

2.3.4 The Thomas–Fermi approximation

We can also use the GPE to approximate the shape of the ground state condensate within a trapping potential when the number of particles is very large. As N is increased, the condensate begins to extend spatially due to the repulsive interactions, and eventually the spatial variation of the wavefunction decreases enough for the kinetic energy term in the GPE to become negligible compared to the potential and interaction terms. This limit is known as the *Thomas–Fermi*

5. Strictly speaking, this is not a true eigenvalue equation, since the ‘eigenstate’ $\psi(\mathbf{r})$ appears in the nonlinear term.

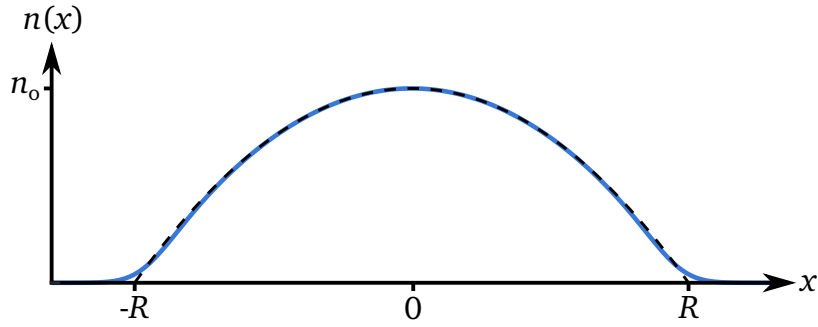


Figure 2.1: A one-dimensional slice through the ground state density profile for a harmonically trapped two-dimensional Bose–Einstein condensate, with $g_{2D} \approx 500 \hbar^2/m$. The blue line shows the numerically obtained ground state using the Gross–Pitaevskii equation, while the black dashed line shows the Thomas–Fermi approximation, Eq. (2.21).

approximation⁶. Using Eq. (2.16), this leaves

$$\mu = V_{\text{trap}}(\mathbf{r}) + gn(\mathbf{r}), \quad (2.18)$$

which can be rearranged to give a prediction for the density profile

$$n(\mathbf{r}) = \frac{1}{g} (\mu - V_{\text{trap}}(\mathbf{r})) \Theta(\mu - V_{\text{trap}}(\mathbf{r})), \quad (2.19)$$

where $\Theta(x)$ is the Heaviside step function. In this approximation, the density is zero whenever $V_{\text{trap}}(\mathbf{r}) \geq \mu$.

The most commonly used configuration is a harmonic trap, for which the potential takes the form

$$V_{\text{trap}}(\mathbf{r}) = \frac{1}{2}m(\omega_x^2 x^2 + \omega_y^2 y^2 + \omega_z^2 z^2), \quad (2.20)$$

where ω_i is the *trapping frequency* for the dimension $i \in \{x, y, z\}$, which determines the extent of the cloud in that direction (a higher frequency corresponds to a stronger confinement). For an isotropic trap, $\omega_i = \omega$, and Eq. (2.19) reduces to

$$\begin{aligned} n(r) &= \frac{1}{g} \left(\mu - \frac{1}{2}m\omega^2 r^2 \right), \quad r \leq R, \\ &= n_0 \left(1 - \frac{r^2}{R^2} \right), \quad r \leq R, \end{aligned} \quad (2.21)$$

6. Note that this approximation requires $a_s > 0$.

where $n_o \equiv \mu/g$, and $\mu = m\omega^2 R^2/2$, since $n(R) = 0$ by definition. The length scale R is commonly referred to as the Thomas–Fermi radius. A comparison between the approximation, Eq. (2.21) and the numerically calculated ground state density in a harmonically trapped BEC is shown in Fig. 2.1. There is a minor discrepancy between the two near $x = \pm R$, which becomes more pronounced as N is decreased.

2.3.5 The healing length

In addition to the characteristic size R of the atomic cloud and the scattering length a_s , there is another intrinsic length scale of fundamental relevance to BEC physics. This scale, known as the *healing length* ξ , is the distance over which the condensate returns to its background value if forced to zero (for example, at a sharp boundary, or at the core of a vortex—see Sec. 2.4.2). The healing length can be determined by equating the kinetic and interaction energies:

$$\frac{\hbar^2}{2m\xi^2} = gn, \quad (2.22)$$

resulting in

$$\xi = \frac{\hbar}{\sqrt{2mgn}}. \quad (2.23)$$

If the density varies over this length scale, the total energy generated by the perturbation is minimised, since there are energy costs associated with creating both density (interaction energy) and density gradients (kinetic energy). In an experimental setup, the ratio of relevant length scales is typically on the order of

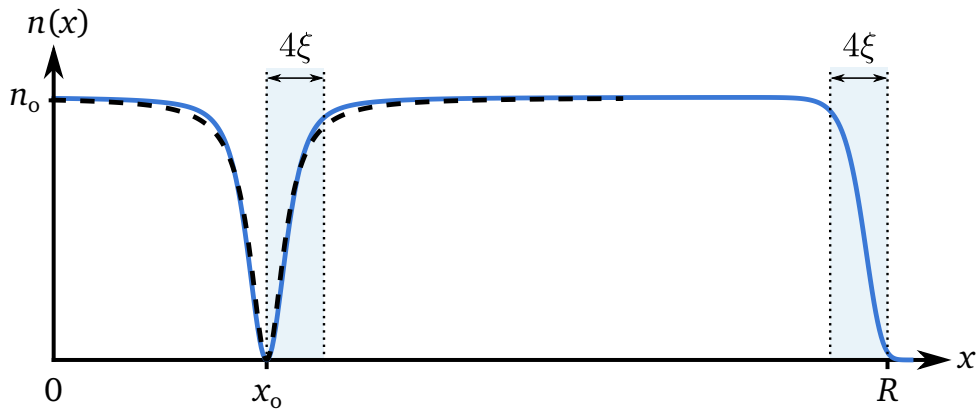


Figure 2.2: A one-dimensional slice through the condensate density for a system with a vortex located at x_o . The black dashed line shows the analytical approximation of the core shape, Eq. (2.41). For $x > R$, there is a sharply rising external potential, forcing the condensate density to zero.

$R/\xi \sim 10\text{--}100$. Figure 2.2 depicts a one-dimensional slice through a condensate that contains a vortex at x_0 , and has a strong external potential for $x > R$. Both density variations occur over the order of a few healing lengths.

2.3.6 Excitations

As well as topological excitations such as vortices and solitons, BECs give rise to *quasiparticle*⁷ excitations, whose energy is given in a uniform system by the Bogoliubov excitation spectrum [186]:

$$\varepsilon(p) = \left[\frac{p^2}{2m} \left(\frac{p^2}{2m} + 2gn \right) \right]^{1/2}. \quad (2.24)$$

Here, the quasiparticle with momentum p has wavenumber $k = p/\hbar$, or equivalently, wavelength $\lambda = 2\pi/k$. In the limit of small p , Eq. (2.24) reduces to

$$\varepsilon(p) \approx p \sqrt{\frac{gn}{m}} = pc_s, \quad (2.25)$$

which is a phonon-like dispersion relation, expressed in terms of the *speed of sound*:

$$c_s = \sqrt{\frac{gn}{m}} = \frac{1}{\sqrt{2}} \frac{\hbar}{m\xi}. \quad (2.26)$$

Hence, long wavelength excitations behave like sound waves traveling at velocity c_s . In the contrasting limit of large p , the dispersion relation (2.24) becomes

$$\varepsilon(p) \approx p^2/2m + gn, \quad (2.27)$$

which is the characteristic spectrum of a free particle, but with a mean-field shift gn added. Hence, short wavelength quasiparticles behave as free particles.

Applying the Landau criterion, Eq. (2.6), we note that the critical velocity at which excitations become energetically favourable is:

$$v_c = \min \left(\frac{\varepsilon(p)}{p} \right) = \min \left(\frac{pc_s}{p} \right) = c_s. \quad (2.28)$$

Hence, in a dilute gas BEC, the critical velocity for the onset of dissipation is equal to the speed of sound, and superfluidity is possible, since $c_s > 0$.

7. A quasiparticle is an emergent phenomenon, usually arising in condensed matter systems, which behaves in many ways as if it were a particle.

2.4 Quantised vortices

As discussed in Chapter 1, this thesis will be largely focused on *quantised vortices* in BEC systems. We show here that these topological structures emerge naturally in BECs as a consequence of the fact that the condensate can be described with a single macroscopic classical field ψ . Many of the properties of quantised vortices are also straightforward to derive from the mean-field theory outlined above, as we will show here.

2.4.1 Properties of the superfluid flow

2.4.1.1 The superfluid velocity

We begin by writing the continuity equation for the particle density,

$$\frac{\partial n(\mathbf{r}, t)}{\partial t} + \nabla \cdot \mathbf{j}(\mathbf{r}, t) = 0, \quad (2.29)$$

where \mathbf{j} is the current density, defined by:

$$\mathbf{j}(\mathbf{r}, t) = \frac{i\hbar}{2m} [\psi(\mathbf{r}, t)\nabla\psi^*(\mathbf{r}, t) - \psi^*(\mathbf{r}, t)\nabla\psi(\mathbf{r}, t)], \quad (2.30)$$

where ψ is the classical field describing the condensate within the Gross–Pitaevskii framework. We can decompose the complex valued field ψ into its amplitude \sqrt{n} and phase ϕ using the Madelung transformation:

$$\psi(\mathbf{r}, t) = \sqrt{n(\mathbf{r}, t)}e^{i\phi(\mathbf{r}, t)}. \quad (2.31)$$

Substituting this into Eq. (2.30) leads to an expression for the velocity \mathbf{v}_s of the superfluid:

$$\mathbf{v}_s(\mathbf{r}, t) = \frac{\mathbf{j}(\mathbf{r}, t)}{n(\mathbf{r}, t)} = \frac{\hbar}{m}\nabla\phi(\mathbf{r}, t). \quad (2.32)$$

Hence, the superfluid flows along gradients in the phase of the wavefunction. Consequently, ϕ can be considered as a potential that gives rise to the velocity. It should be noted that this velocity does not describe the motion of the atoms in the condensate. Rather, the superfluid velocity should be thought of as the velocity at which an object immersed in the superfluid would be advected. Eq. (2.32) has far reaching consequences for the types of flows which are physically allowed in a superfluid, as we discuss below.

2.4.1.2 Quantisation of circulation

Firstly, if we calculate the circulation Γ around any closed contour \mathcal{C} in the fluid, it follows from the single-valuedness of the field ψ that

$$\Gamma \equiv \oint_{\mathcal{C}} \mathbf{v}_s \cdot d\mathbf{l} = \frac{\hbar}{m} \oint_{\mathcal{C}} \nabla\phi \cdot d\mathbf{l} = \frac{\hbar}{m} 2\pi s = \kappa s, \quad (2.33)$$

where $s \in \mathbb{Z}$, and we have defined the quantum of circulation $\kappa = h/m$. Thus we find that the circulation must be quantised in units of κ around any closed loop in the superfluid. In other words, any vortices present in the superfluid must be quantised—as a path is traversed around the vortex, the accumulated phase must be equal to a multiple of 2π . The quantity s , which determines the number of 2π phase windings, is usually referred to as the *winding number* or the *charge* of the vortex. By convention, a vortex with negative circulation is often referred to as an *antivortex*. At the vortex core, the phase exhibits a singularity, and hence the wavefunction is forced to vanish there to avoid becoming multi-valued. This geometric requirement reflects the topological nature of quantised vortices; a feature not shared by vortices in classical fluids.

2.4.1.3 Irrotational flow

A second consequence of Eq. (2.32) is that, wherever the phase is non-singular, the vorticity $\boldsymbol{\omega}$ vanishes:

$$\boldsymbol{\omega}(\mathbf{r}, t) \equiv \nabla \times \mathbf{v}_s(\mathbf{r}, t) = \frac{\hbar}{m} \nabla \times \nabla\phi(\mathbf{r}, t) = 0, \quad (2.34)$$

and the velocity field is said to be *irrotational*. However, if there is a vortex line aligned with the z -axis and centred at $\mathbf{r}_{\perp o} = (x_o, y_o)$, then the vorticity can be determined by applying Stokes' theorem to Eq. (2.33), using a contour \mathcal{C} in the xy -plane with area \mathcal{A} that surrounds the core:

$$\oint_{\mathcal{C}} \mathbf{v}_s \cdot d\mathbf{l} = \int_{\mathcal{A}} (\nabla \times \mathbf{v}_s) \cdot d\mathbf{A} = \kappa s, \quad (2.35)$$

which suggests that

$$\boldsymbol{\omega} = \nabla \times \mathbf{v}_s = \kappa s \hat{\mathbf{z}} \delta(\mathbf{r}_{\perp} - \mathbf{r}_{\perp o}), \quad (2.36)$$

due to the phase singularity at the centre of the vortex. Thus, the vorticity of the fluid is confined to the cores of vortices, and vanishes everywhere else.

2.4.1.4 The vortex velocity field

Eq. (2.33) can also be used to determine the velocity field produced by the vortex, assuming azimuthal symmetry around the core:

$$\oint_{\mathcal{C}} \mathbf{v}_s \cdot d\mathbf{l} = v_s \hat{\boldsymbol{\theta}} \cdot 2\pi r \hat{\boldsymbol{\theta}} = \kappa s, \quad (2.37)$$

where \mathcal{C} is chosen to be a circular contour centred on the vortex, and $\hat{\boldsymbol{\theta}}$ is the unit vector pointing tangentially to the contour at every point. This can be rearranged to give the velocity around the vortex:

$$\mathbf{v}_s(r) = \frac{\hbar s}{m r} \hat{\boldsymbol{\theta}}. \quad (2.38)$$

Although the velocity diverges as $r \rightarrow 0$, the mass current \mathbf{j} does not blow up, since the density n drops to zero at the core of the vortex.

2.4.2 Vortex energetics

The velocity field, Eq. (2.38), associated with a vortex produces kinetic energy throughout the condensate, which can be determined by substituting a vortex ansatz wavefunction into the kinetic energy integral in Eq. (2.15a). Using cylindrical co-ordinates, we choose a wavefunction of the form

$$\psi(r, \theta, z) = \sqrt{\tilde{n}} f(r) e^{is\theta}, \quad (2.39)$$

which corresponds to a vortex of circulation s , located at the origin, and embedded in a uniform superfluid with background density \tilde{n} . The dimensionless function $f(r)$ describes the vortex core shape. The kinetic energy per unit length is then:

$$\varepsilon_K = \int \frac{\hbar^2}{2m} |\nabla\psi|^2 d\mathbf{r} = \frac{\hbar^2 \tilde{n}}{2m} \int \left[\left(\frac{df}{dr} \right)^2 + s^2 \frac{f^2}{r^2} \right] d\mathbf{r}. \quad (2.40)$$

The first term is the energy associated with the shape of the vortex core, while the second corresponds to the energy of the vortex velocity field. The function f that minimises this energy for a singly quantised vortex has the approximate form

$$f(r) = \frac{r}{\sqrt{r^2 + 2\xi^2}}. \quad (2.41)$$

In the limit $r \rightarrow 0$, this function linearly approaches zero, while $f \rightarrow 1$ for $r \gg \xi$ (i.e. the density returns to its background value far from the core). Figure 2.2 shows

the function $n(r) = f^2(r)$, which compares well with the numerically obtained core shape.

In a uniform system, the integral Eq. (2.40) is unbounded, and hence the energy is infinite; however, it is still useful to consider the energy within some finite region from the vortex core, particularly since any real system will have some characteristic size R . We therefore integrate Eq. (2.40) between the approximate vortex core size, $|s|\xi$, and the length scale R . For large enough R , the contribution from the first term in the integral becomes negligible, and hence:

$$\begin{aligned}\varepsilon_k &\approx \frac{\hbar^2 \tilde{n}}{2m} \int_{|s|\xi}^R s^2 \frac{f^2}{r^2} r \, dr \\ &\approx s^2 \frac{\pi \hbar^2 \tilde{n}}{m} \log\left(\frac{R}{|s|\xi}\right).\end{aligned}\quad (2.42)$$

Due to the multiplicative factor of s^2 , this expression predicts that a vortex with $|s| > 1$ charge quanta will be energetically unfavourable and should therefore decay into $|s|$ singly charged vortices (since circulation must be conserved). This phenomenon has been observed in experiments [193] and described theoretically [92, 194]. There are, however, specific circumstances in which multi-quantum vortices may remain stable [92, 195, 196].

2.5 Quantum hydrodynamics

In this thesis, we will explore the relationship between quantum and classical fluids, and draw analogies between the two. To facilitate the comparison between these systems, we can begin by expressing the Gross–Pitaevskii equation in the so-called *hydrodynamic form*, which reveals a close resemblance to the equation of motion for an ideal classical fluid. In addition, we can consider the dynamical behaviour of vortices in each type of fluid, which again bear some striking similarities.

2.5.1 Hydrodynamic Gross–Pitaevskii equation

The Gross–Pitaevskii equation can be expressed in hydrodynamic form by substituting the Madelung transformation, Eq. (2.31), into Eq. (2.13), and separating

out the real and imaginary parts of the result. This leaves two coupled equations:

$$\begin{aligned} \frac{\partial \mathbf{v}_s}{\partial t} &= -\nabla \left[\frac{1}{2} \mathbf{v}_s^2 + \frac{1}{m} V_{\text{trap}} + \frac{1}{m} g n - \frac{\hbar^2}{2m^2} \frac{\nabla^2 \sqrt{n}}{\sqrt{n}} \right] \\ \frac{\partial n}{\partial t} + \nabla \cdot (n \mathbf{v}_s) &= 0. \end{aligned} \quad (2.43)$$

The first equation is the *Euler equation* for the fluid. It is effectively Newton's second law applied to a parcel of fluid, and expresses the force experienced by that portion of fluid as the negative gradient of an effective potential energy (the term in brackets). The second equation is simply the continuity equation for the density, Eq. (2.29), which ensures that particle number is conserved. In Chapter 3, we will introduce the equations of motion for a classical incompressible fluid, and see that they are almost equivalent to these [see Eq. (3.3)]. The only differences are the condition of irrotationality, $\nabla \times \mathbf{v}_s = 0$ (except within vortex cores), and the addition of the *quantum pressure* term in Eq. (2.43) (the last term on the right hand side of the upper equation), which appears in a BEC due to the fluid compressibility.

2.5.2 The Helmholtz decomposition

One important difference between dilute gas BECs and many classical fluids is that the former are highly compressible. It is therefore useful to separate the velocity field \mathbf{v}_s into its incompressible and compressible components, \mathbf{v}_s^i and \mathbf{v}_s^c , respectively. This is done by applying a *Helmholtz decomposition*:

$$\mathbf{v}_s = \mathbf{v}_s^i + \mathbf{v}_s^c, \quad (2.44)$$

where $\nabla \cdot \mathbf{v}_s^i = 0$ and $\nabla \times \mathbf{v}_s^c = 0$, by definition. The incompressible component \mathbf{v}_s^i can be thought of as pertaining to the velocity fields produced by vortices, while the compressible part \mathbf{v}_s^c corresponds to the velocity field of the phonons. In doing so, we can also decompose the kinetic energy, Eq. (2.15a), into three contributions:

$$\begin{aligned} E_K &= \int \left[\frac{1}{2} m n \mathbf{v}_s^2 + \frac{\hbar^2}{2m} |\nabla \sqrt{n}|^2 \right] d\mathbf{r} \\ &= \int \left[\frac{1}{2} m n (\mathbf{v}_s^i)^2 + \frac{1}{2} m n (\mathbf{v}_s^c)^2 + \frac{\hbar^2}{2m} |\nabla \sqrt{n}|^2 \right] d\mathbf{r}, \end{aligned} \quad (2.45)$$

where in the second line we have used the fact that $\mathbf{v}_s^i \cdot \mathbf{v}_s^c = 0$. It is then natural to define

$$E_K^i = \frac{1}{2} m \int n(\mathbf{v}_s^i)^2 d\mathbf{r} \quad (2.46a)$$

$$E_K^c = \frac{1}{2} m \int n(\mathbf{v}_s^c)^2 d\mathbf{r} \quad (2.46b)$$

$$E_K^q = \frac{\hbar^2}{2m} \int |\nabla \sqrt{n}|^2 d\mathbf{r}, \quad (2.46c)$$

which are, respectively, the incompressible, compressible and quantum pressure contributions to the kinetic energy.

2.5.3 Vortex dynamics

Given that vortex dynamics are the focus of this thesis, it is worth providing a brief overview of some basic dynamical processes involving these topological defects. The concepts presented here can be thought of as the ‘archetypal’ dynamical processes involving vortices, which will form the basis of the more complicated dynamics that we will be examining throughout this thesis.

2.5.3.1 Interactions between vortices

In an infinite three-dimensional system containing quantised vortex filaments of circulation κ (which is otherwise homogeneous), velocity fields produced by the vortices will permeate the entirety of space. The velocity at a given point \mathbf{r} can be approximated using the Biot–Savart law:

$$\mathbf{v}_s(\mathbf{r}) = \frac{\kappa}{4\pi} \sum_j^{N_v} \int_{\mathcal{L}_j} \frac{(\mathbf{r}' - \mathbf{r}) \times d\mathbf{r}'}{|\mathbf{r}' - \mathbf{r}|^3}, \quad (2.47)$$

which effectively inverts the curl in Eq. (2.36) (this assumes that the vortex cores are infinitesimally thin). The integral here is taken over all vortex lines in the system, denoted by \mathcal{L}_j , where $j \in \{1, 2, 3, \dots, N_v\}$ is an index for each vortex line. Every point along a given vortex filament moves with the background superfluid velocity \mathbf{v}_s , as determined by Eq. (2.47). Given that vortices can bend in 3D, the velocity at any point on a vortex line is affected not only by all points along all other vortices, but also by all other points along the same line. This is depicted in Fig. 2.3(a), which shows how a vortex filament can be affected by itself and by another vortex.

In two dimensions, the problem is simplified, as the vortices are reduced to

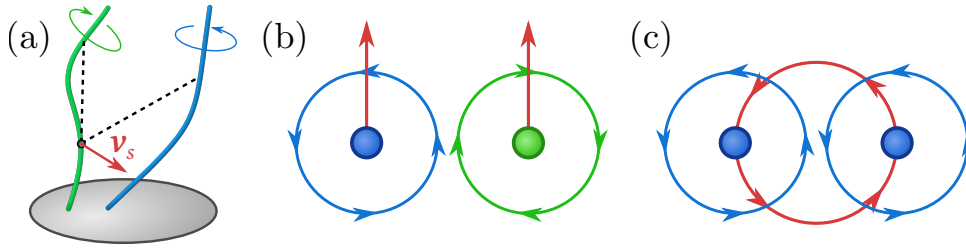


Figure 2.3: Schematic diagram of basic vortex motions. (a) Two vortex filaments in 3D interact. The dashed lines indicate that the velocity at the highlighted point is determined not only by all points on the other vortex, but also by all other points on the same vortex line. (b) The motion of a vortex (blue) and antivortex (green) in 2D. The velocity fields are shown in the corresponding colours, and the direction of motion is indicated by the red lines. (c) The motion of two same-sign vortices in 2D.

points (alternatively, vortices in 3D become effectively two-dimensional if they are all aligned with, say, the z -axis). The velocity at any point in space then simply becomes a discrete sum over the velocity fields produced by every vortex:

$$\mathbf{v}_s(\mathbf{r}) = \frac{\kappa}{2\pi} \sum_j^{N_v} s_j \hat{\mathbf{z}} \times \frac{\mathbf{r} - \mathbf{r}_j}{|\mathbf{r} - \mathbf{r}_j|^2}, \quad (2.48)$$

where the vortices are located at positions $\{\mathbf{r}_j\}$ and have charges $\{s_j\}$, with $j \in \{1, 2, 3, \dots, N_v\}$. From this expression it is straightforward to show two archetypal forms of vortex interaction: a vortex *dipole* (consisting of a vortex and an antivortex) will travel in a straight line perpendicular to their shared axis [Fig. 2.3(b)], and a pair of same-sign vortices will co-rotate about their centre of mass [Fig. 2.3(c)]. The instantaneous velocity in each case is $v = \hbar/md$, where d is the separation between the two vortices.

Equations (2.47) and (2.48) form the basis of two simplified models of vortex dynamics: the *vortex filament model* (in 3D), and the *point-vortex model* (in 2D), respectively. These models have been applied in the context of both classical and quantum turbulence. In the former case, true vortices are not line- or point-like objects, and hence these models are a vast oversimplification. In superfluids, however, quantised vortices may be well approximated as lines or points at distances far from the vortex core. As such, there is hope that vortex filament and point-vortex approaches will prove more fruitful in the latter case. Although we will not discuss the vortex filament model further, the point-vortex model is introduced in detail in Sec. 3.2.

It is worth noting that even an isolated vortex can move. In an infinite uniform system, a lone straight vortex will be stationary. However, if there are local density gradients or boundaries, motion can be induced. An analysis of this behaviour forms the basis of Chapter 5.

2.5.3.2 Kelvin waves

In three dimensions, vortex filaments in both classical and quantum fluids can exhibit excitations known as *Kelvin waves* [197]. These are helical deformations of the vortex line, with frequency ω given by the dispersion relation [83]

$$\omega(k) \approx -\frac{\kappa k^2}{4\pi} \log\left(\frac{1}{k\xi}\right), \quad (2.49)$$

where $k = 2\pi/\lambda$ is the wavenumber associated with the Kelvin wave of wavelength λ . Figure 2.4 shows an example of a Kelvin wave propagating along a vortex filament, with rotation direction opposite to that of the vortex. Indirect evidence for these oscillations in superfluid helium was first obtained by Hall [198], although more recently, direct visualisation of the core deformation has been possible [199]. In 2D systems, all Kelvin wave modes except those of the lowest order are suppressed⁸. It is this ‘anomalous’ mode that gives rise to the motion of a single vortex in a two-dimensionally trapped Bose–Einstein condensate [200] (see Chapter 5). We will also revisit the concept of Kelvin waves in Sec. 3.3 in the context of quantum turbulence.

2.5.3.3 Vortex–sound interactions

When a vortex filament in a superfluid accelerates, it can emit sound waves, thereby converting incompressible into compressible kinetic energy. This process is relevant when multiple vortices approach one another at short distances (see, e.g. [201]), or when a vortex approaches a fluid boundary. Given that both of these processes regularly occur in quantum turbulence, vortex–sound interactions play a large role in this context.

The reverse process is also possible, whereby vortices absorb energy from the sound field [202,203]. However, sound absorption by vortices is understood to play a much smaller role than emission in most dynamical processes. This is especially true in trapped systems, since any sound waves that are produced are repeatedly reflected from the boundaries, eventually resulting in an incoherent background

8. If the endpoints of the vortex line are fixed, the lowest order mode has wavenumber $k = 1/\pi L$, where L is the length of the vortex.

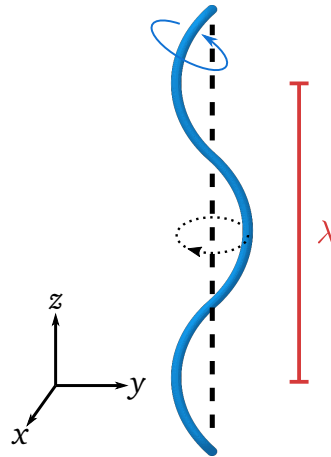


Figure 2.4: Depiction of a Kelvin wave along a three-dimensional vortex filament. The black dotted line indicates the direction of rotation for the helical wave, which is opposite to the circulation of the vortex.

which effectively produces Brownian motion of the vortex line. It is also possible for strong sound waves to cause *pair creation* events, where vortex rings (in 3D) or dipoles (in 2D) form spontaneously [204]. These processes highlight the strong interplay between vortex and sound excitations in a BEC, which takes the role of viscosity in a classical fluid, as we will discuss in Sec. 3.3.

2.5.3.4 Vortex reconnection and annihilation

In three dimensions, when two vortices of locally opposite circulation approach one another, it is possible for a *reconnection* event to take place. When this occurs, the two vortices rapidly approach one another, exchange line ends, and then recoil at high velocity. In the process, Kelvin waves are excited along the filaments, and sound waves are emitted [205, 206]. A reconnection event is depicted in Fig. 2.5. Vortex reconnection is also possible in classical fluids, although the process is driven by viscous effects, and cannot occur in the idealised case where these are ignored. Thus, we see that, despite the vanishing kinematic viscosity of the superfluid, the excitation of sound and Kelvin waves act as an effective energy sink for the reconnection mechanism.

In two dimensions, vortex reconnection reduces to vortex–antivortex *annihilation*, an event where two vortices of opposite circulation approach one another, following a straight trajectory at high velocity, as depicted in Fig. 2.3(b). Once the distance between them decreases beyond a critical value, the pair forms a *vortexonium* [169] or *Jones–Roberts soliton* [207]—a localised rarefaction pulse, and the two phase singularities disappear. This vortexonium state can be sustained

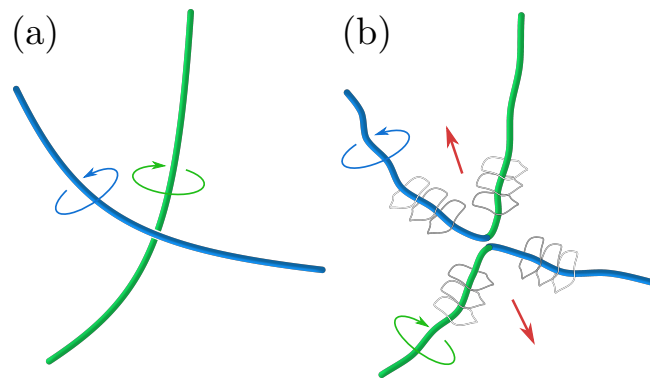


Figure 2.5: Reconnection of two vortex filaments in three dimensions. (a) The two vortices just before reconnection, with circulation directions indicated; (b) the two vortices reconnect and move apart at high velocity, exciting Kelvin waves and emitting sound in the process.

for an extended period of time, and eventually decays via sound emission⁹. At zero temperature, the emission of sound must be catalysed by a collision with either another vortex or a boundary, as we discuss in detail in Chapter 7.

9. It can, however, also reform into the vortex–antivortex pair.

3

TURBULENCE

This chapter begins with a brief digression from Bose–Einstein condensate physics, and instead discusses some important aspects of classical hydrodynamic turbulence theory. We outline a number of known statistical features of turbulence, with a particular focus on cascade processes that are understood to take place in the dynamics. We draw a clear distinction between the cases of three- and two-dimensional turbulence, which display markedly different physics due to the existence of additional conservation laws in the latter case when viscosity is taken to zero. We also describe a simplified model of point-vortices, which becomes applicable in the limit of a dilute configuration of 2D classical vortices. We then return our focus to superfluids, and establish the current base of knowledge regarding turbulence in these systems. In similarity to the classical case, we again emphasise the role of dimensionality on the observed behaviour of the turbulence.

3.1 Classical turbulence

3.1.1 Overview

The phenomenon of hydrodynamic turbulence is ubiquitous throughout physics: the formation of galaxies, the geophysical currents of oceans and atmospheres, the flow of blood through an animal’s circulatory system, and the stirring of a cup of coffee are all examples in which turbulence plays a significant role in the transport of matter, energy and momentum throughout a classical fluid. The scientific study of this universal physical process dates back at least as far as Leonardo da Vinci, who made sketches depicting eddies of circulating flow spanning a range of length scales. This self-similarity across length scales recognised by da Vinci is a fundamental feature of turbulence, and acts as a foundation upon which much of the contemporary understanding of the problem is built. Although our comprehension of fluid dynamics has developed significantly in the time since da Vinci’s rudimentary observations, hydrodynamic turbulence remains a

fundamentally unsolved problem in the sense that physical predictions of dynamics cannot be made, in general, from first principles. As such, turbulence is still an active area of research.

Perhaps surprisingly, even a strict definition of turbulence still eludes fluid dynamicists. Most often, rather than being *defined*, turbulence is *described* in terms of the properties it universally displays. A short list might include (i) strong variability, both spatially and temporally; (ii) ubiquity across length scales; and (iii) a sensitive dependence to initial conditions [208, 209]. This list is not exhaustive, and many more properties could be included. It does, however, capture the basic essence of turbulence: a complicated, seemingly random amalgamation of circulating fluid flows across many length scales.

Naturally, one might ask why turbulence is a problem worth studying at all. Quite apart from the motivations of a fundamental scientist to uncover the laws governing the universe, there are many more practical reasons to study turbulence, since it plays a substantial role in countless engineering applications. For example, the flow of fluids through pipelines, the aerodynamical properties of vehicles, and the efficiency of turbines are all impacted by the presence of turbulence. In such cases, turbulent motion serves to reduce the efficiency of the technology, and must therefore be minimised. By contrast, there are also applications in which turbulence is exploited, since it facilitates the rapid transport of energy, momentum and mass throughout the fluid. This is particularly useful in cases where the aggregation of multiple fluids is required, such as in combustion engines [210], or industrial mixing applications [211].

Any theoretical description of fluid dynamics usually begins with the *Navier–Stokes equation*, which describes the evolution of an incompressible Newtonian fluid, and takes the form:

$$\rho \frac{\partial \mathbf{v}}{\partial t} = -\rho (\mathbf{v} \cdot \nabla) \mathbf{v} - \nabla p + \rho \nu \nabla^2 \mathbf{v} + \mathbf{f}. \quad (3.1)$$

This equation governs the dynamics of the velocity field $\mathbf{v}(\mathbf{r}, t)$ of the fluid, which has constant density ρ , pressure $p(\mathbf{r}, t)$ and kinematic viscosity ν under external forcing $\mathbf{f}(\mathbf{r}, t)$. It is essentially a statement of Newton's second law for an infinitesimal parcel of fluid: on the left hand side is the net force on the fluid parcel, and on the right are the inertial, pressure, viscous and external contributions to the force, respectively. For a fluid to be incompressible (i.e. one whose density is not

affected by changes in pressure)¹, the velocity field must obey the condition

$$\nabla \cdot \mathbf{v} = 0. \quad (3.2)$$

It is widely accepted that Eq. (3.1) may describe all of classical hydrodynamic turbulence, although attempts to extract information directly from it generally prove futile (except via direct numerical simulation).

In the case of an idealised classical fluid with zero thermal conductivity and zero viscosity², the Navier–Stokes equation reduces to the *Euler equation*:

$$\frac{\partial \mathbf{v}}{\partial t} - \mathbf{v} \times (\nabla \times \mathbf{v}) = -\nabla \left[\frac{1}{2} \mathbf{v}^2 + \frac{1}{\rho} V_{\text{ext}} + \frac{1}{\rho} p \right], \quad (3.3)$$

where we have defined $\mathbf{f} = -\nabla V_{\text{ext}}$. Comparing Eqs. (3.3) and (2.43), we can immediately see the similarities between classical and quantum fluid dynamics. As discussed in Sec. 2.5.1, the differences between these equations arise from the compressibility and irrotationality of superfluid flows.

The difficulty in understanding turbulence appears directly in the Navier–Stokes equation: the convective contribution to the fluid forcing introduces strong non-linearity into the problem, thereby making a solution for $\mathbf{v}(\mathbf{r}, t)$ analytically intractable, in general. Even direct numerical simulation of Eq. (3.1) is difficult due to the range of length scales necessary to be modelled [208]. Therefore, rather than trying to understand the microscopic details of the problem, it is often more useful to take a broader approach, and instead study turbulence from a statistical viewpoint. Historically, this strategy has proved fruitful, and many (nearly) universal properties of turbulence have been discovered this way.

3.1.2 Statistical properties of classical turbulence

3.1.2.1 Reynolds number

A turbulent flow can be parameterised in terms of a dimensionless quantity known as the *Reynolds number* [212, 213],

$$\text{Re} = \frac{LU}{\nu}, \quad (3.4)$$

-
1. No fluid is truly incompressible, but for most classical liquids—and in some cases gases—it is an exceptionally good approximation.
 2. Note that here we are *not* describing a superfluid. Rather, we are considering an ‘ideal’, frictionless classical fluid.

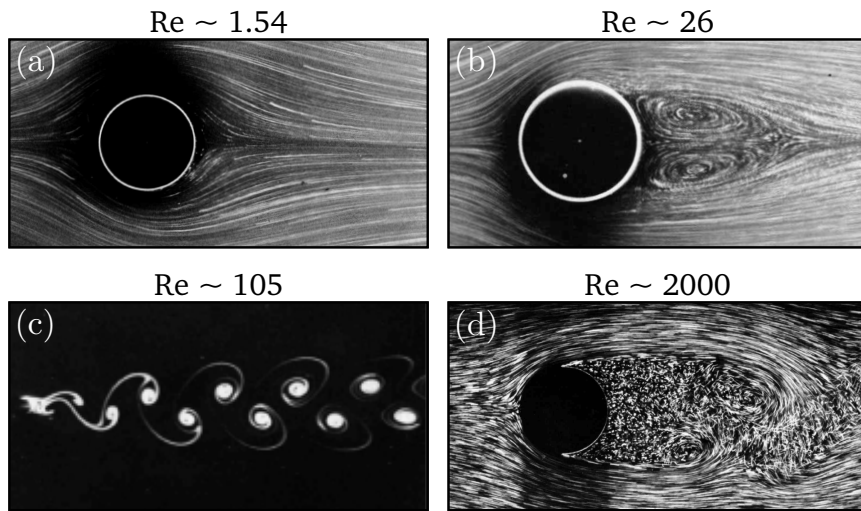


Figure 3.1: The characteristic flow of a fluid past a cylinder at particular values of the Reynolds number (in each frame, the flow is moving left to right). (a) For $Re \lesssim 5$, the flow is laminar. (b) Two counterrotating vortices are formed in the wake of the cylinder when $Re \sim 20$. (c) A vortex street emerges at $Re \sim 100$. (d) A turbulent wake emerges visible for $Re \gtrsim 10^3$. Images adapted from Ref. [214].

which is dependent on the characteristic length (L) and velocity (U) scales relevant to the motion. This parameter is a measure of the ratio of the inertial and viscous forces governing the flow. Remarkably, the Reynolds number alone is sufficient to estimate the behaviour of the flow of an incompressible fluid for a particular choice of geometry, regardless of the values chosen for L and U ³. The Reynolds number therefore exemplifies the scale invariant nature of turbulent phenomena, since the same value of Re can be obtained for a variety of system parameters.

To demonstrate the properties of fluid flow at varying Reynolds number, it is informative to consider the flow of a fluid past a cylindrical obstacle, as shown in Fig. 3.1. In this example, the velocity U is the flow velocity from the left side of each frame, while the scale L is given by the size of the cylinder. It can be seen in panel (a) that, for small Reynolds numbers, the flow is *laminar*—it is steady and predictable, and the streamlines are locally parallel. As the Reynolds number is increased, vortices begin to form behind the object [panel (b)], and eventually a *von Kármán vortex street* emerges [panel (c)], which consists of a series of vortices of alternating circulation. In panel (d), turbulence becomes visible in the wake of the cylinder. This behaviour arises from the *no-slip* condition along the surface of

3. More generally, it should be considered alongside the Mach number, $Ma = U/c_s$, where c_s is the speed of sound in the medium. This gives a measure of the degree of compressibility of the fluid—for $Ma \lesssim 0.3$, the fluid is well approximated to be incompressible.

the cylinder, which ensures the fluid velocity vanishes there. Loosely speaking, the Reynolds number can be thought of as a measure of the ‘degree’ of turbulence—as Re increases, the turbulence becomes stronger and, importantly, involves an ever larger range of length scales.

3.1.2.2 The energy cascade

In 1922, Richardson [215] introduced the concept of the *energy cascade* to the problem of turbulence. His idea hinged on the same observation that had been made by da Vinci centuries earlier—that turbulence is fundamentally comprised of self-similar behaviour across a range of length scales. Specifically, he proposed that any large scale motion of the fluid should gradually break down into smaller scale flows, and hence that energy should ‘cascade’ towards the smallest available length scales in the system, where it could be dissipated via viscous action.

It was not until 1941 that Kolmogorov [216] and Obukhov [217] were able to adapt this concept into a more concrete and quantitative prediction of turbulence. In his seminal work, Kolmogorov put forward a collection of ideas regarding the energy cascade process which have, by and large, stood the test of time. Loosely, these can be summarised as follows [208, 216, 218].

Suppose we have a fluid, which we are stirring at some (presumably large) length scale l_o and producing turbulence. Richardson’s cascade process should transport the energy to small scales, all the way down to the length scale η at which dissipation can begin to take effect. Kolmogorov postulated that, below some small length scale l_{EI} (with $\eta \ll l_{EI} \ll l_o$), the turbulence should become *locally isotropic*—that is, it should have ‘forgotten’ about the details of the largest scale features, such as the stirring and the boundaries. As a result, the symmetries that were broken at those scales should be restored, and any chosen subdomain of the fluid should be statistically invariant under rotations and reflections. Kolmogorov supposed that, at locally isotropic scales (i.e. for lengths $l \lesssim l_{EI}$), the turbulent behaviour should be uniquely determined by the dissipation rate ε and the viscosity ν . He further proposed that, in the subrange $l_{ID} \lesssim l \lesssim l_{EI}$, viscous forces should be negligible, and inertial forces should dominate. Hence, in this *inertial range*, only the dissipation rate ε should be relevant. The scale l_{ID} marks the transition between the inertial range and the *dissipation range*, while l_{EI} subtends the so-called *energy-containing range* and the inertial range.

To quantify this cascade process, it is useful to consider the *energy spectrum* of fully developed, homogeneous turbulence. This spectrum identifies how much energy is contained at each length scale in the system. The details of the derivation

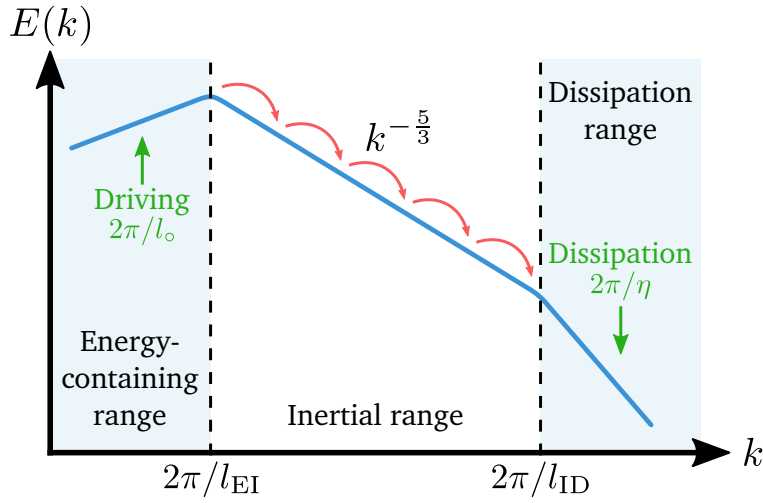


Figure 3.2: Schematic diagram of the kinetic energy spectrum of fully developed, steady-state three-dimensional turbulence at high Reynolds number, on a log–log scale. The approximate driving and dissipation length scales, as well as the upper and lower bounds of the inertial range, are indicated. The arrows in the inertial range show the direction of the cascade.

are not important here, but it is straightforward to show, using dimensional arguments and the arguments outlined above, that the energy spectrum in the inertial range must take the form:

$$E(k) = C\varepsilon^{2/3}k^{-5/3}, \quad (3.5)$$

where $k = 2\pi/l$ is the wavenumber associated with a specific lengthscale l , and C is a dimensionless constant of order unity. A schematic diagram of the full energy spectrum is presented in Fig. 3.2, highlighting the various relevant length scales discussed above. As we will see, restricting the turbulent motion to two spatial dimensions has significant implications for the possible dynamics, a fact which is reflected in the energy spectrum of the fluid.

3.1.3 Classical turbulence in two dimensions

3.1.3.1 The two-dimensional limit

Prior to the 1960s, turbulence in two dimensions was considered by many to be an impossibility. Not only was it thought to be unrealisable in real systems, but some also predicted that could not occur even in theory due to a potentially infinite number of constraints that exist in the limit of zero viscosity [219]. However, following the seminal works of Kraichnan [220] and Batchelor [221], the problem

began to be taken more seriously, and gradually the field of two-dimensional turbulence began to emerge.

We now know that two-dimensional turbulence is not only physically realisable, but is in fact relevant to a number of naturally occurring systems, such as meteorological and oceanic flows. Strictly speaking, fluids such as these have a finite spatial extent in the third dimension, and thus the flow is not completely restricted to a plane. However, external forces acting on the fluid (for example produced by magnetic fields or rotation) can serve to ‘freeze’ the system in the third dimension, thereby improving the 2D approximation [209, 222]. In the laboratory, soap films, plasmas, and electrically conducting fluids have all been used to model two-dimensional behaviour [219, 223].

So what is actually different in the two-dimensional regime? One of the key modifications becomes apparent if we take the curl of the Navier–Stokes equation to obtain an equation of motion for the vorticity $\boldsymbol{\omega} = \nabla \times \mathbf{v}$:

$$\frac{\partial \boldsymbol{\omega}}{\partial t} = (\boldsymbol{\omega} \cdot \nabla) \mathbf{v} - (\mathbf{v} \cdot \nabla) \boldsymbol{\omega} + \nu \nabla^2 \boldsymbol{\omega} + \frac{1}{\rho} \nabla \times \mathbf{f}. \quad (3.6)$$

If the fluid is restricted to two dimensions, the vorticity must take the form $\boldsymbol{\omega} = \omega \hat{\mathbf{z}}$, since it must be everywhere perpendicular to the velocity field, which exists only in the xy -plane. As a result, the first term on the right hand side of Eq. (3.6) must vanish, since the velocity field cannot depend on z . This term, known as the *vortex-stretching* term, is responsible for the production of vorticity in three dimensions. The absence of this term allows for the conservation of not only energy, but also *enstrophy*—defined $\Omega \equiv \int \boldsymbol{\omega}^2(\mathbf{r}) \, d\mathbf{r}$ —in the inviscid limit, $\nu \rightarrow 0$ ⁴. Physically, this conservation law states that, for any point moving with the flow field, the vorticity $\boldsymbol{\omega}$ is constant in time. It turns out that this has major implications for the way in which energy is transferred between length scales in a two-dimensional fluid.

3.1.3.2 Cascades in two-dimensional turbulence

In the late 1960s, Kraichnan [220] and Batchelor [221] independently studied the problem of energy cascades in inviscid two-dimensional turbulence, albeit in two slightly different contexts. Kraichnan considered steady-state turbulence—that is, turbulence with constant forcing and constant dissipation, similar to Kolmogorov’s 3D picture. Batchelor, on the other hand, analysed the case of *decaying* turbulence, where the fluid has been initially stirred and then left to

4. For $\nu > 0$, neither enstrophy nor energy is conserved, and both can only ever decrease unless the fluid is driven.

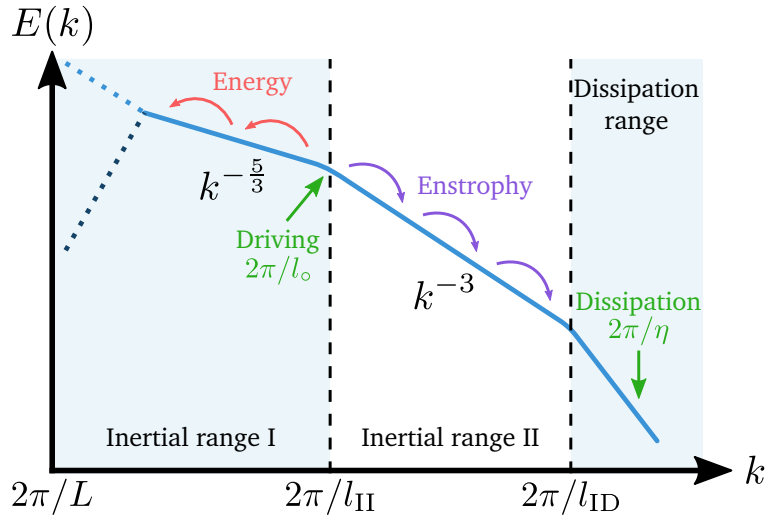


Figure 3.3: Schematic diagram of the kinetic energy spectrum of fully developed, steady-state two-dimensional turbulence at high Reynolds number, on a log–log scale. The approximate driving and dissipation length scales, as well as the bounds of the two inertial ranges, are indicated. The arrows show the directions of the direct enstrophy cascade and the inverse energy cascade. Both possibilities for the energy transported to large scales are depicted: the light dotted line corresponds to a ‘condensate’, while the dark dotted represents applied dissipation at large scales. In the case of freely decaying turbulence, the $k^{-5/3}$ region of the spectrum does not emerge, and only the k^{-3} direct enstrophy cascade remains.

equilibrate. The predictions for the cascade processes in each of these cases were found to be quite different not only from Kolmogorov’s 3D cascade, but also from each other.

Kraichnan proposed that a 2D fluid in a steady state of turbulence should exhibit a *dual cascade*, whereby energy and enstrophy would both be transported through momentum space, but in opposite directions from the driving length scale. While enstrophy should obey the *direct* cascade and flow towards smaller length scales, energy should instead follow an *inverse* cascade and be transported to ever larger sizes.

Based on similar dimensional arguments to Kolmogorov, Kraichnan was able to identify *two* inertial ranges where different power-laws are obtained for the energy spectrum. For a system of size L , these laws can be expressed:

$$E(k) = \begin{cases} C_1 \varepsilon^{2/3} k^{-5/3}, & l_{\text{II}} \lesssim l \lesssim L, \\ C_2 \eta^{2/3} k^{-3}, & l_{\text{ID}} \lesssim l \lesssim l_{\text{II}}, \end{cases} \quad (3.7)$$

where C_1 and C_2 are constants of order unity. In Kraichnan’s picture, the enstrophy is dissipated at small scales, much like the energy in 3D turbulence. By contrast, there are two possible outcomes for the energy that has been transported to system size length scales of order $\sim L$. If there is an ‘applied’ damping at large scales, the energy can be dissipated, and a steady state will be maintained⁵. In this scenario, the inverse cascade becomes equivalent to the direct cascade, except in the direction of the flow. However, if no large scale damping exists, the energy can instead accumulate at the large scales, eventually forming a ‘condensate’⁶, which corresponds to a large scale rotational flow [220]. Thus, the inverse cascade can produce large scale rotational motion from small scale forcing, and it is this prediction which will be the focus of much of our study of 2D turbulence in Bose–Einstein condensates. In Sec. 3.2.2.1 and Chapter 8, we will discuss the vortex ‘condensation’ process in more detail for a system of point-vortices. A schematic diagram of the dual cascade process in driven 2D turbulence is shown in Fig. 3.3, with the relevant length scales identified.

Batchelor predicted that for decaying 2D turbulence, only the direct enstrophy cascade should be present, with the same $E(k) \sim k^{-3}$ scaling law. The inverse energy cascade, by contrast, was predicted to be absent in this context.

Observing both of Kraichnan’s cascades simultaneously—either in experiments or simulations—is a challenging task due to the high Reynolds number (and consequentially the large range of wavenumbers) required for the turbulence [224]. However, appreciable evidence of the dual cascade process has been obtained [225–227], and the direct enstrophy [228, 229] and inverse energy [230, 231] cascades have also been observed independently.

3.2 The point-vortex approximation

3.2.1 Vortices as point-particles

One conceptual advantage of two-dimensional fluid dynamics is that the flow field becomes constrained to a plane, and hence the vortices become parallel and can no longer bend or grow, as in three dimensions. In the limit where the vortices are well separated, they can be reasonably approximated as point-sources of rotating flow. In this scenario, the vorticity of the flow field, which is usually a

5. In an experiment, system-scale damping can be realised by, e.g. friction between the fluid and plates that contain it [219].

6. In analogy with a Bose–Einstein condensate, for which there is a macroscopic occupation of a single momentum state.

continuous function of position, becomes a sum of singularities:

$$\boldsymbol{\omega}(\mathbf{r}) = \sum_j^{N_v} \Gamma_j \hat{\mathbf{z}} \delta(\mathbf{r} - \mathbf{r}_j). \quad (3.8)$$

Here, the *point-vortices* are located at positions $\{\mathbf{r}_j\}$, and have corresponding circulations $\{\Gamma_j\}$, with $j \in \{1, 2, \dots, N_v\}$. The velocity field of a given vortex is given by $\mathbf{v}_j(r) = \Gamma_j / 2\pi r \hat{\boldsymbol{\theta}}$ (with the co-ordinate axes centred on the vortex). We note here the similarity between these point-vortices and the 2D quantised vortices discussed in Secs. 2.4 and 2.5—an analogy that will be expanded upon in Sec. 3.3.3. The resulting equations of motion for these point-vortices are [232, 233]:

$$\frac{d\mathbf{r}_k}{dt} = \frac{1}{2\pi} \sum_{j \neq k} \Gamma_j \hat{\mathbf{z}} \times \frac{\mathbf{r}_k - \mathbf{r}_j}{|\mathbf{r}_k - \mathbf{r}_j|^2}. \quad (3.9)$$

This expression reveals, rather intuitively, that each vortex is advected by the net flow field produced by all the other vortices (the $j = k$ term is omitted from the sum because a given vortex is not affected by its own velocity field). Note that this is simply Eq. (2.48) evaluated at a given vortex core location.

Kirchhoff [234] formulated this problem in terms of a Hamiltonian system of equations with pseudo-Hamiltonian

$$H = -\frac{1}{4\pi} \sum_{j=1}^{N_v} \sum_{k \neq j}^{N_v} \Gamma_j \Gamma_k \log(|\mathbf{r}_k - \mathbf{r}_j|). \quad (3.10)$$

The dynamics are then governed by Hamilton's equations,

$$\Gamma_k \frac{dx_k}{dt} = \frac{\partial H}{\partial y_k}, \quad \Gamma_k \frac{dy_k}{dt} = -\frac{\partial H}{\partial x_k}, \quad (3.11)$$

which simplify to the expression (3.9). We note that Eqs. (3.10) and (3.11) do not define a true Hamiltonian dynamical system, since the canonically conjugate variables are not position and momentum, but x -position and y -position. As such, it is not possible to express both Eqs. (3.10) and (3.11) in the correct units simultaneously. Hence, there is some ambiguity to the choice of dimensional constants which appear in front of each equation (this will be relevant in Chapter 8, where we will use a slightly modified version of these equations). In addition to the Hamiltonian H , there are three conserved quantities under the evolution of

Eq. (3.9):

$$p_x = \sum_j^{N_v} \Gamma_j x_j, \quad p_y = \sum_j^{N_v} \Gamma_j y_j, \quad L = \sum_j^{N_v} \Gamma_j |\mathbf{r}_j|^2. \quad (3.12)$$

These are the linear (p_i) and angular (L) momenta, respectively, which, by Noether's theorem, are conserved due to the symmetries of translation and rotation in an infinite system.

Lin [235, 236] later applied the Hamiltonian formalism to vortices within a multiply-connected, bounded domain, in which case the symmetries may be broken, and thus the quantities p_x , p_y and L may not be conserved. For a bounded system, Eq. (3.10) no longer applies, and instead the Hamiltonian must be derived from the Green's function of the Laplacian, ensuring that the boundary conditions of tangential flow are satisfied [222, 233, 235, 237, 238]. For example, it can be shown that in a circular domain with infinitely sharp boundaries at radius R (a situation of interest in later chapters), the Hamiltonian is given by [237, 239]:

$$H = \frac{1}{4\pi} \sum_j \Gamma_j^2 \log \left(1 - \frac{\mathbf{r}_j^2}{R^2} \right) - \frac{1}{4\pi} \sum_{j < k} \Gamma_j \Gamma_k \log \left(\frac{|\mathbf{r}_k - \mathbf{r}_j|^2}{R^2} \right) + \frac{1}{4\pi} \sum_{j < k} \Gamma_j \Gamma_k \log \left(\frac{|\mathbf{r}_k - \bar{\mathbf{r}}_j|^2 \mathbf{r}_j^2}{R^4} \right), \quad (3.13)$$

where $\bar{\mathbf{r}}_j = \mathbf{r}_j R^2 / |\mathbf{r}_j|^2$ is the position of an *image vortex* outside the boundary of the system. These fictional vortex charges ensure that the boundary conditions are met, and can induce motion of the vortex—this will be discussed further in Chapter 5. The three terms here correspond, respectively, to the interaction between a vortex and its own image, the interaction between real vortices, and the interaction between a vortex and the images of all other vortices. We will use this model (and other, similar forms of point-vortex equations) throughout the thesis.

Although the point-vortex approximation is a vast simplification of a turbulent two-dimensional fluid, it has proved useful in predicting the existence of *coherent states* (long-lived patches of strong vorticity) in 2D classical turbulence [219], and has been applied successfully to the study of 2D plasmas in the guiding-centre approximation [240, 241]. To achieve a greater level of accuracy in classical fluids, point-vortex models have also been generalised to include vortices with finite core size and vorticity [232].

3.2.2 Statistical mechanics of point-vortices

By inspection of the Equations (3.11), we note a rather intriguing feature of the Hamiltonian formulation: as previously mentioned, the canonically conjugate variables are x_k and y_k , and thus the phase space spanned by the vortex ‘particles’ is equivalent to the real space. Onsager [78] pushed this idea a step further by noting that, in a bounded domain, the real space—and hence the phase space—is restricted. The total number of states available to a configuration of N_v vortices is $\mathcal{N} = A^{N_v}$, where A is the area of the two-dimensional domain (i.e. each vortex can be anywhere within the domain). Consequently, the density of states function $w(E)$ is restricted such that it obeys $\lim_{|E| \rightarrow \infty} w(E) = 0$, since

$$\int_{-\infty}^{\infty} w(E) dE = \mathcal{N} = A^{N_v}, \quad (3.14)$$

where E is the energy of a given vortex configuration. Therefore, there must exist a critical energy E_o at which the density of states w reaches a maximum⁷. As an example, a schematic plot of $w(E)$ for the uniform disk system introduced above is depicted in Fig. 3.4.

With this picture in mind, it is now possible to introduce a *vortex temperature* parameter, which will be relevant throughout Chapters 7–9. We stress that this temperature is unrelated to the temperature of the *fluid* (strictly, there is no fluid in the point-vortex model). Rather, it identifies the point along the phase diagram, Fig. 3.4, at which given vortex configuration lies. The vortex temperature T (and corresponding inverse temperature $\beta = 1/k_B T$) is defined in the usual way as follows:

$$k_B \beta = \frac{1}{T} = \frac{\partial S}{\partial E}, \quad (3.15)$$

with Boltzmann entropy $S = k_B \log w$. Bearing in mind the fact that there is a maximum in $S(E)$ at E_o as discussed above, it becomes clear that two temperature regimes exist. For $E < E_o$, the density of states increases with increasing energy, resulting in a positive absolute temperature. However, for $E > E_o$, the temperature becomes *negative*, since the number of available states reduces with increasing energy. In order from coldest to hottest, the temperature scale follows $T = +0\text{ K}, \dots, +\infty\text{ K}, -\infty\text{ K}, \dots, -0\text{ K}$. Figure 3.4 shows schematic diagrams of typical point-vortex configurations in each region of the density of states phase diagram for a circular container. The lowest energy states [i.e. those where Eq. (3.10) is

7. We assume there is only one maximum, although in principle there could be multiple.

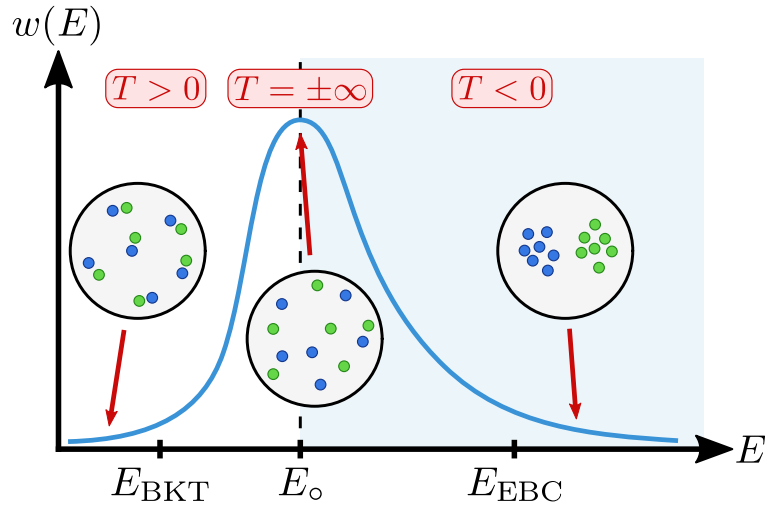


Figure 3.4: Schematic diagram of the density of states for a bounded system of point-vortices, with positive and negative temperature regions labeled. Indicative equilibrium vortex configurations for each temperature regime are shown as insets, with equal numbers of clockwise and anti-clockwise circulations (note that we assume $\Gamma = \pm 1$ for all vortices, although this does not have to be the case in general).

minimised] are populated by *vortex dipoles*, while the highest energy states consist of same-sign *clusters*, also known as *Onsager vortices*. For the ‘intermediate’ energy range, the vortex positions are uncorrelated.

With these observations, Onsager pioneered a new, statistical approach to studying turbulence in two dimensions, where the flows could be characterised using a thermodynamic variable. Evidently, in two dimensional turbulence, there is some link between the negative temperature Onsager vortices and the inverse cascade predicted by Kraichnan to produce ever larger rotational flows; however, the details of the relationship are still unclear.

It is worth noting that negative Boltzmann temperature states are not restricted to the context of 2D point-vortices. They can appear in any system where high energy states are occupied preferentially over those with lower energy (in equilibrium). For example, they have been observed in nuclear spin systems [242, 243], and more recently, in the motional degrees of freedom of cold atoms confined in optical lattices [244]. We also note a distinction between the Boltzmann and the Gibbs definition of temperature, which differ in the way they count energy states [245]. In the former, only the ‘local’ density of states is considered around a given energy E , and this can decrease as energy increases, thus giving rise to negative temperatures, as we have shown. By contrast, in the latter prescription,

the density of states is measured *cumulatively*—from the lowest possible energy all the way up to energy E —and this is a strictly increasing function of energy. As such, the Gibbs temperature can never be negative.

3.2.2.1 Phase transitions of the vortex gas

Based on simple combinatoric arguments, two transition temperatures can be derived, which correspond to the points at which pair collapse and cluster formation become the equilibrium configurations in the positive and negative temperature regimes, respectively. Here, we simply quote the results—for details, see, e.g. Ref. [222].

Assuming equal numbers of vortices and antivortices of circulation $\pm\Gamma$, it can be determined that the pair collapse transition occurs at $\beta_{\text{PC}} = 4\pi/\rho\Gamma^2$ (the same as for a gas of electrically charged particles in two-dimensions [246]), where we remind the reader that ρ is the fluid density. However, Vicelli [239] found that, as the vortex core size⁸ is increased, the transition point shifts towards the Berezinskii–Kosterlitz–Thouless (BKT) [26–28] critical temperature [26–28]:

$$\beta_{\text{BKT}} = \frac{8\pi}{\rho\Gamma^2}. \quad (3.16)$$

It can also be shown that the critical temperature associated with the formation of same-sign clusters—which we refer to as an *Einstein–Bose condensate* (EBC; see Chapter 8)—is given by:

$$\beta_{\text{EBC}} = -\frac{16\pi}{\rho N_v \Gamma^2} \quad (3.17)$$

for a neutral configuration of point-vortices. These two critical temperatures serve as useful reference points for the two temperature extremes.

3.3 Quantum turbulence

3.3.1 Overview

Over the last two decades, quantum turbulence (QT) has emerged as a major field of research in superfluid systems. This dynamical, nonequilibrium state takes the form of a chaotic tangle of quantised vortex lines in 3D, and reduces to a random configuration of point-like vortices in the 2D limit. Although liquid helium has been studied extensively since the 1930s, there were no serious attempts to investigate its turbulent dynamics until the late 1990s [247, 248]. Prior to this, the only

8. The vortex core size is implemented implicitly by ensuring that no two point-vortices come closer than a certain distance to one another.

context in which QT had been considered was the process of *thermal counterflow*, where *mutual friction* between the superfluid and normal fluid components is understood to arise because of the presence of a vortex tangle [79, 249]. In Bose–Einstein condensates, theoretical interest in the problem began to emerge in the mid-2000s [156, 250, 251], and experiments soon followed in both 3D [99, 151] and quasi-2D [103, 152, 154, 155] setups. One of the main focuses of this research has been to uncover the links between classical and quantum turbulence, and we outline some of the major progress towards this goal here.

3.3.2 Quantum–classical analogues

As we have discussed in Secs. 2.5.1 and 3.1.1, the equations of motion governing classical and quantum fluids share many common features. It is therefore natural to ask: How similar are the turbulent dynamics in these two systems? In what scenarios are the properties distinct, and in what way? Here, we outline some of the progress made towards answering these questions.

3.3.2.1 Statistical properties of quantum turbulence

In Sec. 3.1.2.1, we introduced the concept of the Reynolds number for a classical fluid, which was a useful quantity for parameterising the turbulence. For a superfluid, we immediately see a problem when trying to follow the same procedure: the kinematic viscosity ν is zero, and hence Re in Eq. (3.4) becomes undefined [252]. There are, however, propositions of how to resolve this issue. First, we can identify that ν (the kinematic viscosity) and κ (the quantum of circulation) have the same dimensions, and we could therefore define $\text{Re}_s = LU/\kappa$ [253, 254]. In the regime of strong turbulence, $\text{Re}_s \gg 1$, this quantity has been shown to be an adequate descriptor of the flow properties [255, 256]. Recently, this definition was refined by Reeves *et al.* [257], who proposed a slight modification: $\text{Re}_s = L(U - v_c)/\kappa$, where v_c is the superfluid critical velocity determined by the Landau criterion, Eq. (2.6). This latter definition was found to exhibit scale invariant behaviour in the case of a superfluid cylinder wake, in analogy with the classical case discussed in Sec. 3.1.2.1.

It is worth specifically demonstrating how the cylinder wake is altered in the case of a superfluid, as this simultaneously highlights the subtle differences and surprising similarities between classical and quantum fluid dynamics. This problem has been studied in much detail [257–261], and we show an example of some results from Ref. [260] in Fig. 3.5. In this numerical simulation, the cylinder is dragged from left to right across the fluid. The resulting vortex shedding behaviour

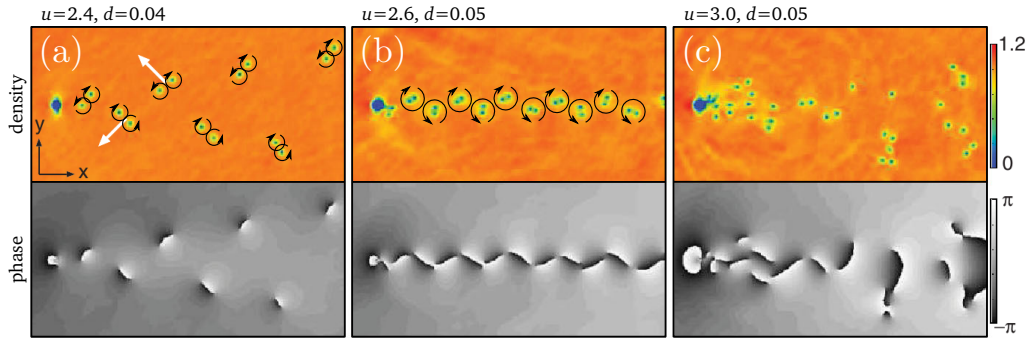


Figure 3.5: Figure adapted from Ref. [260] under the Creative Commons licence. Vortex shedding from a moving obstacle (far left in each panel) in a Gross–Pitaevskii simulation. The density and phase of the wavefunction are shown, and vortex circulation directions are shown in (a) and (b). (a) Dipole shedding regime, (b) von Kármán vortex street regime, (c) irregular regime. The parameter u corresponds to a dimensionless velocity of the repulsive potential, which moves to the left. The parameter d is width of the cylinder, in arbitrary units.

was mapped out as a function of two parameters: the velocity u and width d of the obstacle. In certain low- d regimes, vortex dipoles are shed from the obstacle, and travel outwards in a ‘V’ shape, as seen in panel (a). In a small region of the u – d phase space, a quantum von Kármán vortex street emerges, where pairs of same-sign vortices are shed in an alternating pattern [panel (b)]. For large enough values of u or d , the wake becomes irregular, and turbulence is produced, as shown in panel (c). Evidently, panels (b) and (c) are analogous to panels (c) and (d) in Fig. 3.1, respectively, and demonstrate the similarities between the classical and quantum cases. Panel (a), on the other hand, has no classical equivalent, emphasising that there are also clear differences between these two types of fluids. Recently, Kwon *et al.* [262] experimentally confirmed the possibility of a quantum von Kármán vortex street for the first time in a dilute gas BEC.

Another subject that has received a significant amount of interest is the potential existence of a Richardson-style energy cascade in QT, and additionally the possibility of Kolmogorov-type energy scaling laws. Early experiments in superfluid helium suggested that, not only was there energy scaling behaviour, but that it in fact followed the classical $E(k) \sim k^{-5/3}$ law [247, 248]. Since then, evidence has gradually accumulated in favour of this finding: both Gross–Pitaevskii simulations [157, 255, 263–265] and vortex filament models [266] have obtained energy spectra consistent with this result. One recent experiment was also able to measure the spectral properties of quantum turbulence in a Bose–Einstein condensate

directly [101]. Their data suggested $n(k) \sim k^{-3.5}$ scaling behaviour, where $n(k)$ is the occupation number spectrum, related to the kinetic energy spectrum via $E(k) \sim k^3 n(k)$ [267]. This spectrum compared well with the $n(k) \sim k^{-3}$ prediction for compressible wave turbulence⁹; although comparisons cannot be made with the Kolmogorov scaling law for incompressible, vortex-dominated turbulence. It is worth noting that these studies have all considered decaying, rather than steady-state, turbulence. This is largely because, particularly in dilute gas BECs, the range of length scales available for the injection of energy is many orders of magnitude smaller than in classical systems, since the ratio of the system size to the healing length is only ~ 100 . Hence, an inertial range can only be established over a relatively small region of wavenumber space.

In a three-dimensional classical fluid, the emergence of a self-similar energy cascade is contingent on the mechanism of dissipation at the smallest scales. An obvious question, therefore, is how such a cascade could be possible in a superfluid, where true viscosity is absent¹⁰. It seems that the answer lies in a *Kelvin wave cascade* at the smallest length scales of the system [269, 270]. The physical picture is as follows. At large length scales, the quantum nature of the vortex filaments is insignificant, and they behave much like classical vortices. They are therefore able to follow a Richardson-style cascade, in which vortex lines gradually decrease in length as a result of reconnection events. However, once the scale of the inter-vortex spacing is reached, the superfluid properties of the vortex tangle become evident. At this scale, the Kelvin waves that are excited during each reconnection event become important, and their nonlinear behaviour allows for energy to be transported in a cascade-like process to ever increasing Kelvin wave frequencies. Eventually, the frequencies become high enough for sound waves to be emitted, and thus the incompressible energy of the vortex lines is dissipated into the compressible energy of the fluid [270]. In this Kelvin wave cascade region of wavenumber space, the energy spectrum is predicted to follow a scaling law $E(k) \sim k^\alpha$, much like the classical region; although the exponent α is currently not agreed upon [147, 271, 272].

9. Recent numerical calculations have suggested that the slight deviation likely arose from finite-size effects [268].

10. For nonzero temperatures, mutual friction between the normal and superfluid components can of course act as dissipation, but here we consider the zero temperature limit where this effect is negligible.

3.3.3 Quantum turbulence in two dimensions

Unlike three-dimensional quantum turbulence, the two-dimensional case cannot be easily realised in superfluid helium, due to difficulties with achieving the appropriate confinement. As we have discussed in Sec. 1.1, dilute gas Bose–Einstein condensates, on the other hand, can be straightforwardly prepared in two dimensions; indeed, the regime of 2D QT has been attained in recent BEC experiments [103, 152, 154, 155], and much future work is anticipated. Based on our knowledge of classical fluid dynamics, obvious questions arise in this regime of QT: Does Kraichnan’s dual cascade occur in 2D QT? If so, can it be measured, and what are its underlying properties? Similarly, are Onsager’s predictions of negative temperature states and vortex clusters relevant in these systems? Progress towards answering these questions is hindered partially because of the difficulty of studying steady-state quantum turbulence, as previously discussed. Consequently, decaying turbulence is still the focus of most research, in which case a true steady-state cascade is not possible.

As in the case of 3D QT, significant emphasis has been placed on predicting [273] and measuring [156, 162, 164, 165, 274, 275] the energy spectra of 2D turbulence, since it should in principle be possible to directly observe the transport of energy to large length scales if an inverse cascade is occurring. While most evidence appears to be consistent with such a process, the situation is more subtle than in 2D classical turbulence, since even in a 2D superfluid, energy can be dissipated at the smallest length scales via vortex–antivortex annihilation (in analogy with reconnections in 3D QT). It has been shown that, in certain regimes of 2D QT, this small scale dissipation can lead to a direct energy cascade that dominates over any energy flux to larger scales [158, 276]. In addition, the $E(k) \sim k^{-5/3}$ power-law associated with the inverse energy cascade in 2D classical turbulence appears to be less ubiquitous in QT, and a number of exponents can instead be obtained, depending on the details of the vortex distribution [273].

Due to the ambiguity in interpreting energy spectra—particularly in decaying turbulence—it has become common to instead identify the relative transport of energy to large scales using other observables. To this end, it is useful to draw the rather striking equivalence between quantised vortices in 2D BECs and the point-vortex picture introduced in Sec. 3.2. For scales larger than the vortex core, 2D quantised vortices are described exceedingly well as point-vortices, and should therefore obey similar statistics. It follows that, if energy is being transported to large scales, the dynamical formation of negative temperature Onsager vortex

clusters may be possible, since these correspond to the largest possible flow fields in the system [see, e.g. the streamlines in Fig. 8.2(b) and (c)]. As such, the emergence of these vortex clusters has become the subject of much research, and many metrics of vortex clustering have become widely used to detect their presence [155, 162, 164, 165, 169, 170, 277, 278].

In Ref. [165], the decay of an initially random configuration of vortices and antivortices (i.e. at $T \sim \infty$ K) was simulated using the Gross–Pitaevskii equation, and it was observed that two large scale vortex clusters emerged, indicating that the vortex ‘gas’ had heated towards negative temperatures. This behaviour was interpreted in terms of a vortex *evaporative heating* mechanism. It was noted that, throughout the evolution, vortex–antivortex annihilation events take place, which convert incompressible (vortex) energy into compressible (sound) energy. However, for a vortex and an antivortex to approach one another, they must first transfer a significant amount of their incompressible kinetic energy into the configuration of all the other vortices in the system¹¹. Hence, when they do annihilate, they transfer a comparatively small amount of energy into the sound field, and leave the remaining vortices with a greater average energy. The annihilations therefore act to ‘heat’ the remaining vortices towards negative vortex temperatures. We will discuss this concept further in later chapters.

We stress that the formation of negative temperature Onsager vortices in decaying turbulence does not necessarily imply the existence of an inverse energy cascade. Rather, a *relative* increase of energy at large scales may be possible if energy is removed preferentially at small scales. It is also nontrivial to determine that a true cascade process is occurring, whereby energy is only transferred locally in wavenumber space in the inertial range. Furthermore, rigorously establishing the existence of a cascade requires an inertial range spanning multiple orders of magnitude in wavenumber space—a situation that is not usually realised in 2D QT. We therefore refrain from making any claims regarding the inverse energy cascade when discussing our results.

In addition to the inverse cascade and negative temperature interpretations of decaying 2D, the process has also been described in the context of *non-thermal fixed points* [159–161, 171]. In this description, the emergence of the Onsager vortices corresponds to the critical slowing of the turbulent dynamics, since the annihilations become increasingly infrequent. The system thus remains indefinitely

11. Note that this reasoning only applies to (approximately) microcanonical evolution of the vortices, and thus does not hold if dissipative effects are present.

in a metastable, non-equilibrium state, in which universal scaling dynamics are observed.

Following these recent theoretical developments, the realisation of these Onsager vortex states in the laboratory has become a subject of great interest. However, a number of experimental challenges have impeded progress. Firstly, it was only very recently that a method for determining vortex circulation signs was implemented in an experimental 2D QT setup [155]. This information is essential for observing Onsager vortices, since the two clusters do not necessarily separate spatially. As we discuss in Chapter 7, the trapping potential also plays an important role—in particular, we show that harmonic trapping diminishes the prominence of clusters, making their observation difficult. Thirdly, the emergence of Onsager vortices may be difficult to quantify, especially since only a small number of images of the condensate can be taken during a single experimental run. We address this issue in Chapter 9, where we introduce a thermometry technique that can be used to directly measure the temperature of a vortex configuration. Finally, it is not clear whether the thermal cloud present in an experiment should adversely affect the formation of clusters, since the associated dissipative effects should drive the vortices to the low energy dipole region of Fig. 3.4. Despite these considerable challenges, the creation of same-sign vortex clusters has recently been observed in 2D BECs [279, 280], and indirect evidence of their dynamical formation has also been obtained [280].

4

NUMERICAL TECHNIQUES

This chapter outlines the computational methods used throughout the work presented in this thesis. We describe in detail the numerical procedures implemented to integrate the two differential equations which make up much of our research: the Gross–Pitaevskii equation (GPE) and the point-vortex vortex equations. We then briefly describe our methods of detecting and classifying vortices in our Gross–Pitaevskii simulations, which is essential to studying their dynamics.

4.1 Non-dimensionalisation

In order to numerically simulate the GPE, Eq. (2.13), it is necessary to first express it in a non-dimensional form by choosing a system of units. The key here is to choose a system that depends only on specific properties of the physical problem being studied. In general, this results in values of physical quantities which are within a few orders of magnitude of unity, thus making them simple to deal with and less prone to rounding errors in the numerics.

For the GPE, it suffices to choose units for three physical observables: energy, distance and time. Here, we set these units to be

$$[E] = 2\mu, \quad [d] = \xi, \quad [t] = \frac{\hbar}{2\mu}, \quad (4.1)$$

where $\xi = \hbar/\sqrt{2m\mu}$ is the healing length, and μ is the chemical potential, as defined in Chapter 2. Once these have been chosen, we can ‘extract’ the units from

each dimensional term in the GPE as follows:

$$\begin{aligned}
 \psi &= \psi' [d]^{-2} = \frac{\psi'}{\xi^2} \\
 \nabla^2 &= \nabla'^2 [d]^{-2} = \frac{\nabla'^2}{\xi^2} \\
 V_{\text{trap}} &= V'_{\text{trap}} [E] = V'_{\text{trap}} 2\mu \\
 g &= g' [E][d]^2 = g' 2\mu \xi^2 \\
 \frac{\partial}{\partial t} &= \frac{\partial}{\partial t'} [t]^{-1} = \frac{\partial}{\partial t'} \frac{2\mu}{\hbar}.
 \end{aligned} \tag{4.2}$$

Substituting these into the GPE, all dimensional quantities cancel, and we are left with

$$i \frac{\partial}{\partial t'} \psi'(\mathbf{r}', t') = \left[-\frac{1}{2} \nabla'^2 + V'_{\text{trap}}(\mathbf{r}', t') + g' |\psi'(\mathbf{r}', t')|^2 \right] \psi'(\mathbf{r}', t'). \tag{4.3}$$

In some cases, it is also useful to work in the harmonic oscillator units:

$$[E] = \hbar\omega, \quad [d] = \sqrt{\frac{\hbar}{m\omega}}, \quad [t] = \frac{1}{\omega}. \tag{4.4}$$

This system is particularly useful when considering a harmonically trapped BEC, with potential given by Eq. (2.20) and trapping frequency ω . When working in these units, the non-dimensionalised GPE has the same form as Eq. (4.3).

4.2 Numerical integration of the Gross–Pitaevskii equation

4.2.1 Discretisation

The numerical methods we employ to simulate the dynamics of Bose–Einstein condensates rely on the discretisation of both space and time. To do this for a smooth function $\psi(\mathbf{r}, t)$, we make the association $\psi_{jk}^m \approx \psi(\mathbf{r}_{jk}, t_m)$, where j , k and m are indices denoting the x , y and t location of the discretised value of ψ . In this section, the specific details of the grids required to simulate the GPE will be outlined, as well as a number of important considerations to be aware of when numerically integrating a partial differential equation.

4.2.1.1 Spatial and temporal grids

We begin by creating a grid comprised of N points¹ in each of the two spatial dimensions, using a uniform spacing $\Delta x = \Delta y = L/N$, where L is the physical size of the numerical domain. The discretised \mathbf{x} - and \mathbf{y} -position vectors are therefore defined as

$$\mathbf{x} = \mathbf{y} = \Delta x (-N/2, -N/2 + 1, \dots, N/2 - 2, N/2 - 1). \quad (4.5)$$

Because our integration method requires Fourier transforms, we also require a corresponding momentum-space grid, spanned by the wavenumbers k_x and k_y . To create this grid, we set the spacing $\Delta k = \Delta k_x = \Delta k_y$ equal to the wavenumber corresponding to the longest wavelength sinusoid that we can represent on our real-space grid:

$$\Delta k = \frac{2\pi}{\lambda_{\max}} = \frac{2\pi}{L}, \quad (4.6)$$

since $\lambda_{\max} = L$ is the longest wavelength that fits in the numerical domain. Then, as for the real space grid, we define:

$$\mathbf{k}_x = \mathbf{k}_y = \Delta k (-N/2, -N/2 + 1, \dots, N/2 - 2, N/2 - 1). \quad (4.7)$$

The maximum wavenumber of this grid is therefore $k_{\max} = N\Delta k/2 = \pi/\Delta x$.

To temporally evolve our field ψ , we must take discrete steps of time Δt . Each time step is performed by calculating

$$\psi^{m+1} = \exp(-i\Delta\phi)\psi^m, \quad (4.8)$$

with the change in phase given by $\Delta\phi = \hat{H}'\Delta t'$, where \hat{H}' is the (non-dimensionalised) Hamiltonian of the system. For the solution to remain stable, the magnitude of the phase change must be small, i.e. $\Delta\phi \ll 1$. We therefore find that

$$\Delta t' \ll 1/\hat{H}' \sim 2(\Delta x')^2, \quad (4.9)$$

since the kinetic energy term, $\hat{K}' \sim (\Delta x')^2/2$, should be the dominant contribution to the phase evolution. We use the value $\Delta t' = (\Delta x')^2/6$ throughout our simulations.

1. Since we are implementing fast Fourier transforms (FFTs), we always choose the number of grid points to be a power of two, i.e. $N = 2^n$. This allows the FFTs to be performed most efficiently, because the algorithms rely on breaking the discrete Fourier sum into pairwise terms [281].

4.2.1.2 The Nyquist sampling requirement

When discretely sampling any continuous function, it is essential that all frequencies present in the original signal can be adequately represented using the choice of discretisation. The Nyquist theorem states that, in order for this requirement to be met, the sampling must occur at a minimum of twice the highest wavenumber k_h contained the signal [282, 283]. Below this threshold, there is degeneracy in the choice of sinusoids that can be fitted to the data, and a phenomenon known as *aliasing* can occur.

For our simulations, the Nyquist theorem states that we must use a momentum space grid which extends to $k_{\max} \geq 2k_h$ to avoid aliasing. However, when simulating wavefunctions with vortices, $k_h \rightarrow \infty$, since the vortex core density is radially linear (i.e. $|\psi(r)| \sim r$, where r is measured from the centre of the vortex). Decomposing the vortex core structure into sine waves therefore requires an infinite number of terms in the Fourier series. As a result, aliasing is always present to some degree in our simulations. It therefore becomes a matter of choosing an upper limit of our wavenumber range such that an adequate level of accuracy is obtained. Since the smallest features we need to simulate are vortices, it makes sense to choose $k_h \gtrsim \pi/2\xi$, or equivalently, $\Delta x \lesssim \xi$. This ensures that the physics is well represented on macroscopic scales²; however, the precise details on scales smaller than the vortex core will be lost. For most of our work, the dynamics on scales smaller than ξ are not particularly relevant; however, when studying small-scale features such as dipole contributions to the vortex velocity field (Sec. 5.3.3.3), or vortex–antivortex annihilation events (Sec. 7.3.3), a finer grid would improve quantitative accuracy.

4.2.2 Split-step Fourier method

To numerically integrate the two-dimensional Gross–Pitaevskii equation, we employ a technique known as the split-step Fourier method, an approach commonly used to solve nonlinear Schrödinger equations such as the GPE [284].

To propagate the wavefunction in time from t to $t + \delta t$, a unitary operator is

2. A simple check to confirm this is to decrease the grid spacing by factors of two until the macroscopic dynamics converge.

applied:

$$\psi(\mathbf{r}, t + \delta t) = \exp\left(\frac{-i\hat{H}\delta t}{\hbar}\right)\psi(\mathbf{r}, t) \quad (4.10)$$

$$= \exp\left(\frac{-i(\hat{T} + \hat{V})\delta t}{\hbar}\right)\psi(\mathbf{r}, t), \quad (4.11)$$

where in the second line we have split the Hamiltonian \hat{H} into the kinetic ($\hat{T} = -\hbar^2\nabla^2/2m$) and potential ($\hat{V} = V_{\text{trap}} + g|\psi|^2$) terms of the GPE (2.13). Although this is a conceptually simple equation, it is computationally prohibitive due to the exponentiation of operators, which in discrete form are represented as matrices. In the spatial basis, each element of the matrix corresponds to an (x, y) co-ordinate on the numerical grid. In general, matrix exponentiation is a nontrivial and expensive operation [285], but as we show here it can be avoided in our calculations by splitting up the terms in the exponent. Doing so allows us to diagonalise the operator matrices, and then use the property that the exponential of a diagonal matrix \mathbf{A} is simply the exponential of its elements, i.e. if $\mathbf{B} = \exp(\mathbf{A})$, then $B_{jk} = \exp(A_{jk})\delta_{jk}$, where δ_{jk} is the Kronecker delta.

4.2.2.1 Splitting the operators

Although the operators \hat{T} and \hat{V} do not commute, we can split up the exponential to form an approximate expression of the form [284]

$$\exp[\varepsilon(\hat{T} + \hat{V})] \approx \exp(\varepsilon\beta_j\hat{T})\exp(\varepsilon\alpha_j\hat{V})\dots\exp(\varepsilon\beta_1\hat{T})\exp(\varepsilon\alpha_1\hat{V}), \quad (4.12)$$

with $\sum_j \alpha_j = \sum_j \beta_j = 1$. It is then possible to calculate the coefficients $\{\alpha_j\}$ and $\{\beta_j\}$ such that the approximation is accurate to a particular order in the parameter ε . The second-order accurate formula has $\alpha_1 = \alpha_2 = 1/2$, and $\beta_1 = 1$ (with all other coefficients zero), giving the evolution operator

$$\hat{U}_2(\delta t) = \exp\left(\frac{-i\hat{V}\delta t}{2\hbar}\right)\exp\left(\frac{-i\hat{T}\delta t}{\hbar}\right)\exp\left(\frac{-i\hat{V}\delta t}{2\hbar}\right). \quad (4.13)$$

If greater accuracy is required, higher order operators can be formed by taking products of this second order expression [286, 287]. Using this method, a fourth-order accurate operator can be constructed as follows:

$$\hat{U}_4(\delta t) = \hat{U}_2(p\delta t)\hat{U}_2(p\delta t)\hat{U}_2(q\delta t)\hat{U}_2(p\delta t)\hat{U}_2(p\delta t), \quad (4.14)$$

with coefficients

$$p = \frac{1}{4 - 4^{1/3}}, \quad q = 1 - 4p. \quad (4.15)$$

It is worth noting that the value of q is negative, meaning that the third operator in the above product actually steps *backwards* in time.

4.2.2.2 Potential energy operator

Because the potential energy operator is local, it is diagonal in the spatial basis—i.e. the matrix element ψ_{jk}^{m+1} depends only on \hat{V}_{jk}^m and ψ_{jk}^m . Therefore, we can exponentiate this operator with minimal computational expense.

However, care must be taken each time the potential operator is applied in the expression (4.13), since the nonlinear component of this operator, $g|\psi|^2$, is directly dependent on the wavefunction. This leads to some ambiguity, since for the second application of \hat{V} in Eq. (4.13), there are two versions of ψ available: one at the beginning of the step, and one after applying the two rightmost operations. In general, the value of ψ used in calculating \hat{V} could therefore be a linear combination of both versions of ψ that exist for that portion of the time step. However, it can be shown that the optimal choice is to always use the most recent version of the wavefunction available [284].

4.2.2.3 Kinetic energy operator

Unlike the potential operator, the kinetic energy operator is non-local in space, since it couples the value of ψ_{jk}^{m+1} to its neighbours, $\psi_{j\pm 1, k\pm 1}^m$, as well as ψ_{jk}^m . The matrix \hat{T} therefore contains off-diagonal terms, and matrix exponentiation becomes computationally inhibitive.

To diagonalise the kinetic energy operator in Eq. (4.13), we apply a *spectral method*, in which the wavefunction ψ is expanded in a series of orthonormal basis functions in the domain \mathcal{A} corresponding to our spatial grid: $\psi(\mathbf{r}) = \sum_j a_j \phi_j(\mathbf{r})$, with $\int_{\mathcal{A}} \phi_j(\mathbf{r}) \phi_k(\mathbf{r}) d\mathbf{r} = \delta_{jk}$. Choosing a Fourier basis allows us to take advantage of a particular property of Fourier transforms, known as the Fourier derivative theorem, that converts differentiation in real space into multiplication in Fourier

space:

$$\begin{aligned}
\nabla_{\mathbf{r}}^2 F(\mathbf{r}) &= \nabla_{\mathbf{r}}^2 \mathcal{F}^{-1} \{ \mathcal{F} \{ F(\mathbf{r}) \} \} \\
&= \nabla_{\mathbf{r}}^2 \frac{1}{\sqrt{2\pi}} \int \tilde{F}(\mathbf{k}) e^{-i\mathbf{k}\cdot\mathbf{r}} d\mathbf{k} \\
&= \frac{1}{\sqrt{2\pi}} \int -|\mathbf{k}|^2 \tilde{F}(\mathbf{k}) e^{-i\mathbf{k}\cdot\mathbf{r}} d\mathbf{k} \\
&= \mathcal{F}^{-1} \{ -|\mathbf{k}|^2 \mathcal{F} \{ F(\mathbf{r}) \} \}, \tag{4.16}
\end{aligned}$$

where $\tilde{F}(\mathbf{k}) \equiv \mathcal{F} \{ F(\mathbf{r}) \}$, and \mathcal{F} denotes the Fourier transform. This property also applies to the exponential of the derivative operator, as can be seen by applying a Taylor expansion:

$$\begin{aligned}
e^{\nabla_{\mathbf{r}}^2} F(\mathbf{r}) &= \mathcal{F}^{-1} \left\{ \left(1 + \nabla_{\mathbf{r}}^2 + \frac{1}{2} \nabla_{\mathbf{r}}^4 + \dots \right) \mathcal{F} \{ F(\mathbf{r}) \} \right\} \\
&= \mathcal{F}^{-1} \left\{ \left(1 - |\mathbf{k}|^2 + \frac{1}{2} |\mathbf{k}|^4 - \dots \right) \mathcal{F} \{ F(\mathbf{r}) \} \right\} \\
&= \mathcal{F}^{-1} \left\{ e^{-|\mathbf{k}|^2} \mathcal{F} \{ F(\mathbf{r}) \} \right\}. \tag{4.17}
\end{aligned}$$

Since the matrix $|\mathbf{k}|^2$ is diagonal in the Fourier basis, it is straightforward to numerically exponentiate it and perform the multiplication with $\mathcal{F} \{ F(\mathbf{r}) \}$. The exponentiated Laplacian, which is computationally expensive to perform in real space, therefore becomes a simple multiplication in k -space.

4.2.2.4 The complete algorithm

Putting all of this information together, the algorithm to evolve from time t to $t + \delta t$ takes the form

$$\psi(\mathbf{r}, t + \delta t) = \hat{U}_4 \psi(\mathbf{r}, t), \tag{4.18}$$

where \hat{U}_4 is given by Eq. (4.14). This operator depends on the second order propagator, which we can write explicitly as:

$$\hat{U}_2(\delta t) \psi = \exp\left(\frac{-i\hat{V}'\delta t}{2\hbar}\right) \mathcal{F}^{-1} \left\{ \exp\left(\frac{i|\mathbf{k}|^2\delta t}{\hbar}\right) \mathcal{F} \left\{ \exp\left(\frac{-i\hat{V}\delta t}{2\hbar}\right) \psi \right\} \right\}. \tag{4.19}$$

The first (rightmost) operation on ψ occurs in real space, and the result is then transformed into the Fourier basis, where the second operator (middle) is applied. Transforming back, the final operator (leftmost) is again applied in real space. Note that the potential in this final operator is primed to denote the use of the

intermediate wavefunction ψ' contained in the nonlinear term:

$$\psi' \equiv \mathcal{F}^{-1} \left\{ \exp\left(\frac{i|\mathbf{k}|^2 \delta t}{\hbar}\right) \mathcal{F} \left\{ \exp\left(\frac{-i\hat{V} \delta t}{2\hbar}\right) \psi \right\} \right\}. \quad (4.20)$$

4.2.3 Initial state generation

Our Gross–Pitaevskii simulations require an initial state to seed the dynamics. In general, we generate an initial state by imprinting vortices directly into the ground state wavefunction of the chosen trap. To do this, we apply a *Wick rotation*, $t \rightarrow -it$, to first calculate the ground state, and then to establish the density profile of the vortex cores following a phase imprinting step. The Wick rotation has the effect of turning unitary evolution into exponential decay, $\exp(-i\hat{H}t/\hbar) \rightarrow \exp(-\hat{H}t/\hbar)$, which rapidly drives the system towards the local energy minimum because eigenstates with large values of $\langle \hat{H} \rangle$ decay faster than those with smaller values [288].

4.2.3.1 Ground state calculation

The numerical ground state of the potential is found by evolving an arbitrary ‘guess’ wavefunction in imaginary time, driving it towards the stationary state $\psi(\mathbf{r}, t) = \psi(\mathbf{r}) \exp(-i\mu t)$ which obeys Eq. (2.16). Since the eigenvalue of the ground state should be equal to μ , we can monitor how close to the true ground state the approximation ψ is by calculating the error metric:

$$\varepsilon = \int (\hat{H} - \mu) \psi \, d\mathbf{r}. \quad (4.21)$$

If $\hat{H}\psi = \mu\psi$ is satisfied, then $\varepsilon = 0$ and ψ is a stationary state of the Hamiltonian. Typically, imaginary time evolution will converge to the ground state and result in an error as low as $\varepsilon \sim \mathcal{O}(10^{-15})$.

4.2.3.2 Establishing vortex cores

Imaginary time propagation is also useful for establishing vortex core structures. In many of our simulations, we imprint vortex phase windings into the wavefunction ψ at location (x_0, y_0) by taking the product $\arctan[(y - y_0)/(x - x_0)] \psi(x, y)$. Evolving this state for a small amount of Wick-rotated time causes the density to leave the vortex core region, thereby digging out the density profile of the vortex. This occurs as a result of the velocity divergence in the vortex core region, making it energetically unfavourable for atoms to remain within the vortex core. However,

if the imaginary time evolution continues for too long, the vortex will gradually drift towards either the boundary of the condensate or a vortex of the opposite circulation, eventually causing it to disappear from the system. This is because the vortex has an associated energy cost, so it is energetically favourable to remove it from the system entirely.

4.3 Numerical integration of point-vortex equations

To solve the point-vortex ordinary differential equations, Eq. (3.11), we implement a fourth-order Runge–Kutta–Fehlberg adaptive integrator (unless otherwise stated). In this approach, both a fourth- and a fifth-order Runge–Kutta approximation are calculated, and their difference is used as an error metric to adaptively vary the size of the time step. Because the terms required to calculate the fourth-order approximation are a subset of those required for the fifth-order approximation, there is little extra computation necessary to calculate the former once the latter has been obtained [289].

We begin with the differential equation $\dot{z} = f(z, t)$, which describes the time evolution of the variable $z(t)$, where f is a known function and the dot denotes time differentiation. The Runge–Kutta method allows us to use the function $f(z, t)$ and the known value of $z(t)$ to propagate forward in time by δt to give $z(t + \delta t)$. We denote $z_m = z(t)$ and $z_{m+1} \approx z(t + \delta t)$, where m is an index denoting the time step.

The fifth-order Runge–Kutta formula is given by:

$$z_{m+1}^{(5)} = z_m + \sum_{n=1}^6 c_n k_n + \mathcal{O}(\delta t^6), \quad (4.22)$$

where c_n are a set of predetermined coefficients, and:

$$k_n = f \left(z_m + \sum_{j=1}^{n-1} b_{nj} k_j, t_m + a_n \delta t \right) \delta t, \quad (4.23)$$

where a_n and b_{nj} are additional coefficients, and we set $k_0 = 0$. For all coefficients, we use the values determined by Cash and Karp [290].

The fourth-order integral is then:

$$z_{m+1}^{(4)} = z_m + \sum_{n=1}^6 c_n^* k_n + \mathcal{O}(\delta t^5), \quad (4.24)$$

where c_n^* is another set of coefficients [290]. Note that the fourth- and fifth-order methods use the same set of k_n functions, which means they only need to be calculated once.

To make this integration scheme adaptive, an error estimate is calculated each time step, defined as follows:

$$\varepsilon = z_{m+1}^{(5)} - z_{m+1}^{(4)}. \quad (4.25)$$

If the value of this error ε increases or decreases beyond some chosen bounds, we can update the step size $\delta t \rightarrow \delta t'$ in order to maintain the required error ε' . The new step size is chosen to be

$$\delta t' = \delta t \left| \frac{\varepsilon'}{\varepsilon} \right|^{0.2}. \quad (4.26)$$

This is particularly useful when the timescale of the dynamics varies significantly throughout the evolution. We avoid amassing large errors when fine temporal resolution is required, but also save computational time when the evolution of the system slows down.

4.4 Implementation

4.4.1 Gross–Pitaevskii equation integrator

4.4.1.1 MATLAB implementation

The numerical integration of the zero temperature GPE (using the split-step algorithm described in Sec. 4.2.2) was implemented in MATLAB, using NVIDIA's compute unified device architecture (CUDA) to allow for computation to be parallelised using a graphics card. Most of our simulations were performed on a desktop computer using an NVIDIA Tesla K40c graphics processing unit (GPU). This is particularly advantageous because the split-step integration requires only matrix multiplication, addition and (diagonal) exponentiation, along with the fast Fourier transform, all of which have been optimised for GPU performance within MATLAB.

4.4.2 Point-vortex model integrator

The Runge–Kutta algorithm used to calculate point-vortex dynamics (Sec. 4.3) was implemented in Python. Our simulations were performed using a combination of both a desktop computer and the two Monash high-performance computing clusters, MCC and MonARCH.

4.5 Vortex detection and classification

4.5.1 Detection of vortices

In both the Gross–Pitaevskii and point-vortex approaches, we are primarily interested in tracking the vortex motion and statistical behaviour as a function of time. In the point-vortex numerics, this is straightforward, given that the equations are solved *explicitly* for the vortex locations at each point in time. The GPE, on the other hand, describes the evolution of the wavefunction, while the vortex dynamics are *implicit*. As such, the vortices must be manually detected in the latter case before any analysis of their dynamics can take place.

The detection is performed using an algorithm which locates all positions on the numerical grid about which the phase winds. For each possible square of four neighbouring grid points, a closed loop is created, as depicted in Fig. 4.1. Along each segment of the loop shown, the change in phase $(\Delta\phi)_l$ (with $l = \{1, 2, 3, 4\}$) between the endpoints is calculated (ensuring that the phase is unwrapped so that 2π phase jumps are avoided), and hence the total change in phase around the loop, $\Delta\phi = \sum_l (\Delta\phi)_l$, is determined. If the background phase field is continuous, then $\Delta\phi \approx 0$, since the contributions from opposite sides of the loop approximately cancel each other out. However, if there is a phase singularity within the area defined by the closed loop, all four path segments produce a phase change of the same sign, with a total change equal to $\Delta\phi \approx 2\pi s$ (assuming $\Delta x \lesssim \xi$). If such a phase winding is measured, a vortex of charge s is said to be present within the area bounded by the four grid points.

4.5.2 Classification of vortex configurations

In many scenarios where we are dealing with large numbers of vortices, we make use of a classification algorithm which helps us to analyse the behaviour of the

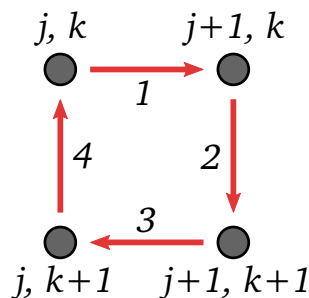


Figure 4.1: The path traversed around a combination of four neighbouring points.

vortex configuration. Specifically, we classify each vortex into one of three groups: *clusters* of same-sign vortices, closely bound *dipole* pairs, and relatively isolated *free vortices*. This section is devoted to explaining in detail how the algorithm works. The method is based on a similar algorithm implemented by Reeves *et al.* [162].

Each vortex in a given configuration of N vortices is assigned a unique and arbitrarily chosen label from the set $\{v_1, v_2, \dots, v_N\}$. The vortex configuration is then described by a corresponding set of positions $\{z_1, z_2, \dots, z_N\}$ (in two-dimensional complex co-ordinates, where $z_j = x_j + iy_j$) and circulation signs $\{s_1, s_2, \dots, s_N\}$, which here take the value $s_j = \pm 1$, denoting clockwise or anticlockwise circulation. The algorithm does not prioritise any vortex and yields the same classification outcome regardless of the choice of vortex labelling. Figure 4.2 shows an example configuration of twelve judiciously numbered point-vortices. The vortex classification algorithm is outlined below.

4.5.2.1 Step one: Find dipole and cluster candidates

For each vortex v_j , we locate the nearest opposite sign (NOS) vortex and label it as $(v_{\text{NOS}})_j$ [i.e. the nearest vortex which satisfies $s_j(s_{\text{NOS}})_j < 0$]. We define the

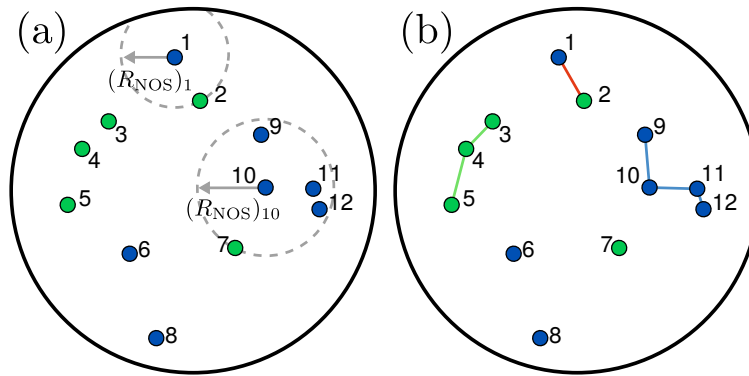


Figure 4.2: A configuration of twelve point-vortices, (a) before and (b) after the classification algorithm has been applied. Vortices are drawn in blue, while antivortices are drawn in green. In panel (a), dashed circles are drawn centered on v_1 and v_{10} , denoting the respective distances $(R_{\text{NOS}})_j$ to the nearest opposite signed vortex. Because v_2 is the closest vortex to v_1 and is of opposite sign, v_2 is labelled as a dipole candidate for v_1 . Vortex v_{10} , on the other hand, is closer to v_9 , v_{11} and v_{12} than it is to v_7 ; hence, these three vortices become cluster candidates for v_{10} . The lines joining clustered vortices in (b) are drawn using a minimum spanning tree algorithm, which is applied once all vortices have been labelled into the sets of clusters, dipoles or free vortices.

distance to this vortex to be $(R_{\text{NOS}})_j \equiv |z_j - (z_{\text{NOS}})_j|$. We then check to see if any other vortices (which are same-sign, by necessity) fall within the disk of radius R_{NOS} centered at vortex v_j .

- (i) *Dipoles*: If not, then $(v_{\text{NOS}})_j$ is labelled as a dipole candidate for v_j [e.g. in Fig. 4.2(a), v_2 is labelled as a dipole candidate for v_1].
- (ii) *Clusters*: If there are $n_j \geq 1$ vortices which are nearer to v_j than $(v_{\text{NOS}})_j$, then these are labelled as cluster candidates for v_j [e.g. vortex v_{10} in Fig. 4.2(a), for which v_9 , v_{11} and v_{12} are cluster candidates].

Each vortex v_j now has a corresponding set of candidate vortex labels, which we denote by \mathbf{l}_j . For case (i), \mathbf{l}_j consists of a single opposite sign vortex, which is a dipole candidate. For case (ii), \mathbf{l}_j is a list of n_j same-sign cluster candidates.

Table 4.1 below displays the lists \mathbf{l}_j that are constructed in Step 1 of the algorithm when it is applied to the configuration shown in Fig. 4.2.

Table 4.1: Collation of \mathbf{l}_j lists for the configuration shown in Fig. 4.2 after dipole and cluster candidates have been identified. Each row corresponds to a particular vortex v_j (leftmost column) and the list of all other vortices, ordered from left to right in increasing distance from v_j . Vortices/antivortices v_k are denoted with blue/green font if $|z_j - z_k| \leq (R_{\text{NOS}})_j$. All vortices for which $|z_j - z_k| > (R_{\text{NOS}})_j$ are colored in gray, as these cannot be dipole or cluster candidates. The lists \mathbf{l}_j consist of either a single opposite sign vortex (e.g. row 1, corresponding to vortex v_1 , which has $\mathbf{l}_1 = \{v_2\}$), or a set of ≥ 1 same-sign vortices (e.g. row 4, corresponding to vortex v_4 , for which $\mathbf{l}_4 = \{v_3, v_5\}$).

v_j	\mathbf{l}_j										
v_1	v_2	v_3	v_9	v_4	v_{10}	v_5	v_{11}	v_7	v_6	v_{12}	v_8
v_2	v_1	v_9	v_3	v_{10}	v_4	v_{11}	v_7	v_{12}	v_5	v_6	v_8
v_3	v_4	v_1	v_2	v_5	v_6	v_9	v_{10}	v_7	v_{11}	v_8	v_{12}
v_4	v_3	v_5	v_6	v_2	v_1	v_9	v_7	v_{10}	v_8	v_{11}	v_{12}
v_5	v_4	v_6	v_3	v_8	v_2	v_7	v_1	v_{10}	v_9	v_{11}	v_{12}
v_6	v_5	v_8	v_7	v_4	v_3	v_{10}	v_2	v_9	v_{12}	v_{11}	v_1
v_7	v_{10}	v_{12}	v_{11}	v_6	v_9	v_8	v_2	v_5	v_3	v_4	v_1
v_8	v_6	v_7	v_5	v_{10}	v_4	v_{12}	v_{11}	v_3	v_9	v_2	v_1
v_9	v_{10}	v_2	v_{11}	v_{12}	v_7	v_1	v_3	v_4	v_6	v_5	v_8
v_{10}	v_{11}	v_9	v_{12}	v_7	v_2	v_6	v_1	v_3	v_8	v_4	v_5
v_{11}	v_{12}	v_{10}	v_9	v_7	v_2	v_1	v_6	v_3	v_8	v_4	v_5
v_{12}	v_{11}	v_{10}	v_7	v_9	v_2	v_6	v_8	v_1	v_3	v_4	v_5

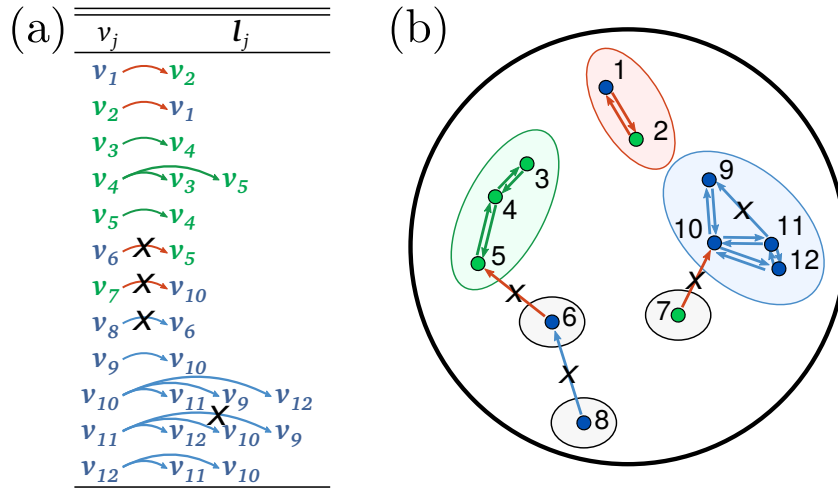


Figure 4.3: The process of identifying mutual neighbours, shown equivalently as (a) a table of candidate lists L_j taken from Table 4.1, and (b) drawn directly onto the example vortex configuration from Fig. 4.2. An arrow is drawn from each vortex v_j to all the members of its candidate list L_j . Only when arrows point in both directions between v_j and v_k are they defined to be mutual neighbours. All arrows that are one-directional have been crossed out in both panels. In panel (b), shaded ovals are drawn around clusters (blue/green for positive/negative), dipoles (red) and free vortices (black).

4.5.2.2 Step two: Find mutually agreeing candidates

In the second step of the algorithm, the lists L_j are checked sequentially for mutual members. This process is shown schematically in Fig. 4.3 for the example configuration shown in Fig. 4.2 and Table 4.1.

- (i) *Dipoles:* If a list L_j consists of a single dipole candidate v_k , then the list L_k is checked to see if it contains (only) the vortex v_j . If so, then the two vortices are mutual nearest neighbours of opposite sign, and are classified as a dipole (e.g. vortices v_1 and v_2 in Fig. 4.3). If not, then the vortices are left unclassified (e.g. vortices v_6 and v_5 in Fig. 4.3).
- (ii) *Clusters:* If a list L_j consists of a set of cluster candidate vortices $\{v_k\}$, then the lists $\{L_k\}$ are all checked to see if they contain the vortex v_j . For each list L_k that does contain v_j , the two vortices v_j and v_k are labelled as belonging to the same cluster (e.g. in Fig. 4.3, vortex v_4 ‘checks’ both L_3 and L_5 to see if it is a member of either. It is found to be a member of both, so all three vortices are placed in a single cluster). For each list L_k that does not contain v_j , neither vortex label is updated (e.g. vortex v_7 and v_{10} in Fig. 4.3). Note that not all

members of a single cluster have to be mutual candidates of one another. In the example shown in Fig. 4.3, v_9 is only a mutual neighbour with v_{10} , but is still placed in the same cluster as v_{11} and v_{12} . As the algorithm proceeds, vortices may be assigned to existing clusters, or previously classified clusters may become merged.

Any vortices left unclassified after this process are classified as free vortices, as they have no mutual dipole or cluster neighbours (e.g. vortex v_6 in Fig. 4.3).

In Fig. 4.3(b), any two vortices that are connected by a two-directional link are part of the same cluster or dipole, while any vortex that has no two-directional links is a free vortex.

To reduce computation, the checking of mutual candidates can be restricted such that it is only initiated for v_j and v_k if $j > k$. Alternatively, once a pair of vortices has been checked, then v_j could be removed from l_k and vice versa.

5

VORTEX DYNAMICS IN NONUNIFORM BOSE–EINSTEIN CONDENSATES

This chapter is dedicated to studying the motion of one and two vortices in a trapped Bose–Einstein condensate. Surprisingly, even this simple dynamical regime is not well understood, despite considerable theoretical efforts devoted to the topic. The main factor complicating analytical treatment of the problem is the varying condensate density, which affects the vortex motion in nontrivial ways. This issue is highly relevant to experiments, since the widely used harmonic traps cause significant inhomogeneity of the fluid. Here, we derive a general and exact equation of motion for a vortex in a two-dimensional BEC, and demonstrate its accuracy using Gross–Pitaevskii simulations. We then identify and discuss a number of weaknesses in the existing literature on the subject, and show how our analysis clarifies these issues. Finally, we use our equation of motion to derive a set of point-vortex equations applicable to harmonically trapped BECs. Compared to the phenomenological model that has previously been used throughout the literature, our newly derived model provides significant improvements for the predictions of few-vortex dynamics. The contents of this chapter form the basis of Ref. [172].

5.1 Motivation

The simplest regime of vortex dynamics is that of a single vortex in a trapped BEC. An off-axis vortex has been experimentally observed to orbit the centre of a harmonically trapped condensate at a constant radius and frequency [110, 114, 116, 127, 291], and similar dynamics have been observed for vortices in superfluid Fermi gases [292, 293]. Although conceptually simple, this motion has proved nontrivial to describe theoretically due to the inhomogeneous density profile, which results from the harmonic trapping. Many attempts have been made to

derive analytical expressions for the velocity of a single quantised vortex in these nonuniform systems [111, 112, 294–302]; however, there is no consensus on the correct form of such an expression. In fact, even the specific physics responsible for the orbital motion is not universally agreed upon—there are conflicting descriptions of how density and phase gradients affect the vortex motion [111, 299, 301], and there has been extensive debate over the relevance of image vortices to systems with soft boundaries [94, 111, 298, 302–304]. The effects of more general fluid inhomogeneity on vortex motion have also been studied theoretically [303–306]—a problem which will become increasingly relevant as experiments begin to utilise more complex trapping geometries [36–38, 101].

Despite the theoretical complications resulting from fluid inhomogeneity, focus has recently shifted towards increasingly complex regimes of vortex motion. Experiments have been performed to investigate configurations such as vortex dipoles [102, 127, 128], few-vortex clusters [130, 131], and quantum turbulence [103, 152, 155]. To theoretically model the dynamics of these systems, it has become common to apply point-vortex approximations, in which the vortices are treated as point-particles whose motion is described by a set of coupled differential equations [128, 131, 136–138, 140, 154, 165, 307], as discussed in Sec. 3.2. These models, which are both conceptually and computationally simple, have been used to provide qualitative predictions of the dynamical and statistical behaviour observed in both experiments [128, 131, 132, 154] and Gross–Pitaevskii simulations [138, 165, 275]. However, current point-vortex models cannot take general fluid inhomogeneity into account. In the case of harmonic trapping, a phenomenological term is commonly included to capture the vortex orbital motion (e.g. [128, 131]), but it only provides a quantitatively accurate prediction of the dynamics for vortices near the trap centre, where the density is approximately uniform [94, 111].

In this chapter, we use the Gross–Pitaevskii equation to derive a general and exact expression for the velocity of a vortex, applicable in generic Bose–Einstein condensates. Although this expression has appeared in previous BEC literature [301, 302, 308], its importance has been understated. To demonstrate its accuracy and generality, we simulate the motion of a single vortex in both harmonic and hard-walled disk-shaped trapping potentials using the GPE. We find excellent agreement between the simulated dynamics and those predicted by the analytics. We also examine other models from the literature, and find that the expression derived here provides the best prediction of the vortex velocity. In addition, we show that it

is possible to derive point-vortex equations of motion for arbitrary fluid geometries directly from this general equation, although approximations are necessary to account for ambient velocity fields that are induced by the inhomogeneous density.

This chapter is structured as follows. In Sec. 5.2, we derive the vortex equation of motion, before verifying its accuracy using GPE simulations in Sec. 5.3. Section 5.4 reviews past literature on the subject, and attempts to clarify a number of misconceptions present throughout previous works. In Sec. 5.5, we derive and test an improved point-vortex model for a harmonically trapped BEC. Finally, we summarise our main results in Sec. 5.6.

5.2 The vortex velocity in an inhomogeneous superfluid

We begin with the nonlinear Schrödinger equation $i\hbar\partial_t\psi = \hat{H}\psi$ with the Hamiltonian

$$\hat{H} = -\frac{\hbar^2}{2m}\nabla^2 + \hat{U}(\mathbf{r}, t), \quad (5.1)$$

where \hat{U} is, in general, a complex operator. For the non-dissipative, zero temperature Gross–Pitaevskii model used throughout this chapter, $\hat{U}(\mathbf{r}, t) = V(\mathbf{r}, t) + gn(\mathbf{r}, t)$, as defined in Sec. 2.3.1. However, for the purposes of this derivation, the precise form of \hat{U} turns out to be unimportant and could include terms due to thermal atom density or non-Hermitian growth and decay terms. Hence, the resulting equation for the vortex velocity is exceptionally general and its applicability is not limited to BECs.

We begin by assuming that at time $t = 0$ there is a singly quantised vortex in a 2D condensate at the location $\mathbf{r}_o = (x_o, y_o)$, which we express in complex notation as $z_o = x_o + iy_o$. By definition, this means that $\psi(x_o, y_o) = 0$, since there must be zero atomic density at the vortex core. Such a vortex state may be described, with no loss of generality, by the wavefunction

$$\psi_o \equiv \psi(\mathbf{r}, t = 0) = (z - z_o)\tilde{\rho}e^{i\tilde{\phi}}, \quad (5.2)$$

where $\tilde{\rho}(\mathbf{r}, t)$ and $\tilde{\phi}(\mathbf{r}, t)$ are real functions which, respectively, describe the background magnitude and phase of the wavefunction after the vortex has been factored out. The function $z = x + iy$ accounts for both the density and phase of the condensate close to the vortex core.

We may use the Gross–Pitaevskii equation to propagate the wavefunction for-

ward an infinitesimal time δt by applying the unitary evolution operator:

$$\psi_{\text{new}} \equiv \psi(\mathbf{r}, t = \delta t) = \exp\left(-\frac{i}{\hbar}\hat{H}\delta t\right)\psi_{\circ} \quad (5.3a)$$

$$\approx \left(1 - \frac{i}{\hbar}\hat{H}\delta t\right)\psi_{\circ}, \quad (5.3b)$$

where in the second line we have expanded the exponential term in a Taylor series to first order in δt . Substituting the Hamiltonian, Eq. (5.1), and the vortex ansatz wavefunction, Eq. (5.2), into this expression results in

$$\psi_{\text{new}} \approx (z - z_{\circ})\tilde{\rho}e^{i\tilde{\phi}} - \frac{i}{\hbar}\delta t \left(-\frac{\hbar^2}{2m}\nabla^2 + \hat{U}\right)(z - z_{\circ})\tilde{\rho}e^{i\tilde{\phi}}. \quad (5.4)$$

The Laplacian term may be expanded to yield

$$\begin{aligned} \nabla^2[(z - z_{\circ})\tilde{\rho}e^{i\tilde{\phi}}] = & \left[(z - z_{\circ})\nabla^2\tilde{\rho} + 2(1, i) \cdot \nabla\tilde{\rho} + 2i \{(z - z_{\circ})\nabla\tilde{\rho} + \tilde{\rho}(1, i)\} \cdot \nabla\tilde{\phi} \right. \\ & \left. + (z - z_{\circ})\tilde{\rho} \{i\nabla^2\tilde{\phi} - (\nabla\tilde{\phi})^2\} \right] e^{i\tilde{\phi}}, \end{aligned} \quad (5.5)$$

where we have used $\nabla(z - z_{\circ}) = (1, i)$ and $\nabla^2(z - z_{\circ}) = 0$. Substituting Eq. (5.5) into Eq. (5.4), we evaluate ψ_{new} at $z = z_{\circ} + \delta z = (x_{\circ} + \delta x) + i(y_{\circ} + \delta y)$, which is the new location of the vortex after time δt . Because ψ_{new} must vanish at the new core location, we find that

$$\begin{aligned} 0 \approx & \left\{ \delta z\tilde{\rho} - \frac{i}{\hbar}\delta t \left[-\frac{\hbar^2}{2m} \left(\delta z\nabla^2\tilde{\rho} + 2i(\delta z\nabla\tilde{\rho} + \tilde{\rho}(1, i)) \cdot \nabla\tilde{\phi} \right. \right. \right. \\ & \left. \left. + 2(1, i) \cdot \nabla\tilde{\rho} + \delta z\tilde{\rho}(i\nabla^2\tilde{\phi} - (\nabla\tilde{\phi})^2) \right) + \delta z\hat{U}\tilde{\rho} \right] \right\} e^{i\tilde{\phi}}. \end{aligned} \quad (5.6)$$

The $e^{i\tilde{\phi}}$ term is nonzero in general, and hence the term inside the braces must be equal to zero. We take the limit of the resulting expression as $\delta z \rightarrow 0$ and $\delta t \rightarrow 0$, leaving only terms which are first order in δz and δt :

$$0 \approx \delta z\tilde{\rho} + \frac{i\hbar}{2m}\delta t \left(2i\tilde{\rho}(1, i) \cdot \nabla\tilde{\phi} + 2(1, i) \cdot \nabla\tilde{\rho} \right). \quad (5.7)$$

Rearranging, we obtain an expression

$$v_x + iv_y \equiv \frac{\delta z}{\delta t} = \frac{\hbar}{m} \left((1, i) \cdot \nabla\tilde{\phi} + (-i, 1) \cdot \frac{\nabla\tilde{\rho}}{\tilde{\rho}} \right), \quad (5.8)$$

for the vortex velocity $\mathbf{v}_v = (v_x, v_y)$ to first order accuracy, which becomes exact

in the limit of adiabatic vortex motion [309, 310]. Expressed in vector form, the velocity of the vortex is

$$\mathbf{v}_v(\mathbf{r}_o) = \frac{\hbar}{m} (\nabla \tilde{\phi} - \hat{\boldsymbol{\kappa}} \times \nabla \log \tilde{\rho}) \Big|_{\mathbf{r}_o} \quad (5.9a)$$

$$\equiv \mathbf{v}_s(\mathbf{r}_o) + \mathbf{v}_d(\mathbf{r}_o). \quad (5.9b)$$

Here we have identified two independent contributions to the vortex velocity: the background superfluid velocity due to ambient phase gradients $\mathbf{v}_s = (\hbar/m)\nabla\tilde{\phi}$, and a density gradient velocity $\mathbf{v}_d = -(\hbar/m)\hat{\boldsymbol{\kappa}} \times \nabla \log \tilde{\rho}$. In Eq. (5.9a), we have explicitly included the dependence on the unit vector $\hat{\boldsymbol{\kappa}}$ which points in the direction of the vortex circulation vector $\boldsymbol{\kappa} = \kappa \hat{\mathbf{z}}$. It is straightforward to verify this dependence on $\hat{\boldsymbol{\kappa}}$ by repeating the above calculation with $z \rightarrow z^*$, $z_o \rightarrow z_o^*$ and $\delta z \rightarrow \delta z^*$ (i.e. an antivortex). We explicitly show in Sec. 5.3.3.4 that \mathbf{v}_d is only dependent on the direction, not the magnitude, of $\boldsymbol{\kappa}$.

We note that Eq. (5.9) is an entirely local expression—the vortex velocity is not directly affected by global features of the condensate, such as its overall density profile, the presence of boundaries, or the existence of other vortices in the system. All such effects modify the motion of the vortex phase singularity implicitly through the changes in the ambient condensate density and phase. Furthermore, the vortex velocity derives exclusively from the kinetic energy term in the Hamiltonian, and hence the velocity of the vortex does not explicitly depend on \hat{U} (although there is an implicit dependence via the wavefunction). Equation (5.9) is therefore generic and applies even for more general forms of \hat{U} , such as those which include dynamics of thermal atom densities, higher order nonlinear terms and dissipative effects.

5.3 Numerical study of the velocity of a single vortex

5.3.1 The motion of a single vortex in an axisymmetric trap

The goal of Sec. 5.3 is to verify the expression, Eq. (5.9), for the vortex velocity by numerically simulating the motion of a single vortex in a trapped BEC using the Gross–Pitaevskii equation. In doing so, we uncover a number of interesting features underlying the vortex motion, including the effects of varying density on the ambient superfluid velocity, and multipole moments induced in the vortex velocity field. We consider two cylindrically symmetric geometries: a harmonic trap and a uniform disk-shaped trap with hard walls. It is well documented that,

in each of these cases, a single off-centred vortex will orbit around the centre of the trap at a constant radius $r_o \equiv |\mathbf{r}_o|$ with a radially dependent velocity¹ $v_{\text{orb}}(r_o)$ [94, 110, 111, 127]. However, this motion is typically thought to derive from different physical effects in each of these two cases.

In the uniform disk trap, the vortex motion is understood to arise from the Bernoulli effect, whereby the warping of the flow field due to the boundary leads to a pressure gradient, and hence a radial force, which drives the vortex in a circular path due to the gyroscopic effect of the rotating fluid. Equivalently, the motion can be described using the mathematical construction of image vortices—hypothetical vortex charges that exist outside the condensate and alter the fluid velocity field such that the boundary conditions of zero radial flow are satisfied [94, 239]. These images generate a phase gradient within the fluid, and thus induce vortex motion via the first term in Eq. (5.9).

By contrast, in the harmonic trap, the vortex orbital motion is usually attributed to the inhomogeneity of the condensate [111], while the effect of the ambient superfluid velocity \mathbf{v}_s has often been disregarded [111] or treated inadequately [299, 301] (see Secs. 5.3.3.2 and 5.4 for further discussion on previous results). However, our simulations reveal that both terms in Eq. (5.9) contribute significantly to the vortex velocity in the harmonic trap, as we show in Sec. 5.3.3.

5.3.2 Numerical methods

We numerically solve the GPE using a 512×512 grid, with a spacing approximately equal to the healing length ξ . To obtain the harmonic and uniform disk geometries, we use trapping potentials $V_h(r) = \mu_h(r/R_h)^2$ and $V_u(r) = \mu_u(r/R_u)^{50}$, respectively, where the chemical potential in the harmonic trap is chosen to be four times that in the uniform trap, $\mu_h = 4\mu_u$. We set the interaction parameter in the GPE to $g = 1.28 \times 10^4 \hbar^2/m$, and use a trap radius of $R = 128 \xi_h = 64 \xi_u$, with $\xi_h = \xi_u/2$. For each trap, we first calculate the ground state using imaginary time propagation. We then imprint a vortex of charge s at location \mathbf{r}_o by multiplying this ground state wavefunction by $f(|\mathbf{r} - \mathbf{r}_o|)e^{i\phi_v(\mathbf{r})}$, where $\phi_v(\mathbf{r}) = s \arctan[(y - y_o)/(x - x_o)]$, and the approximate density profile of a vortex is given by Eq. (2.41). This initial state is evolved to $t = 5 \times 10^4 \hbar/\mu$ using the GPE (long enough to see at least four orbits of the vortex around the trap centre at the lowest frequencies). We identify the vortex location using the phase singularity detection algorithm described in Sec. 4.5.1.

1. Unless there is dissipation, in which case it will drift radially outward [311].

Throughout the time evolution, we independently measure each of the three terms in Eq. (5.9):

- (i) The total orbital velocity [the left-hand side of Eq. (5.9)] is calculated from the angular frequency of the vortex orbital motion as $v_v = v_{\text{orb}} = \omega_{\text{orb}} r_o$.
- (ii) To measure the ambient superfluid velocity field $\mathbf{v}_s(\mathbf{r}_o) = (\hbar/m)\nabla\tilde{\phi}(\mathbf{r})|_{\mathbf{r}_o}$, we first calculate the ambient phase $\tilde{\phi}(\mathbf{r})$ by subtracting the axisymmetric vortex phase field from the total phase of the condensate: $\tilde{\phi}(\mathbf{r}) = \phi(\mathbf{r}) - \phi_v(\mathbf{r})$. This subtraction must be done carefully to minimise numerical fluctuations at the vortex core. We then average the resulting velocity field $\mathbf{v}_s(\mathbf{r})$ within a series of annuli $r_a - \xi < |\mathbf{r} - \mathbf{r}_o| < r_a + \xi$ around the vortex core, where r_a is varied between 2ξ and 11ξ . Due to fluctuations in the velocity within $|\mathbf{r} - \mathbf{r}_o| \lesssim \xi$ (and contributions from a multipole velocity field—see Sec. 5.3.3.3), we extrapolate the measurements from the larger annuli to determine the velocity at \mathbf{r}_o .
- (iii) The density-dependent velocity $\mathbf{v}_d(\mathbf{r}_o) = -(\hbar/m)\hat{\mathbf{k}} \times \nabla\tilde{\rho}/\tilde{\rho}|_{\mathbf{r}_o}$ is measured numerically around the vortex core by fitting a plane $P(x, y) = A + Bx + Cy$ to $\rho(\mathbf{r}) = |\psi(\mathbf{r})|$ within the annuli $r_a - \xi < |\mathbf{r} - \mathbf{r}_o| < r_a + \xi$, where r_a is varied between 6ξ and 11ξ . We then calculate the density terms as: $\tilde{\rho}(\mathbf{r}_o) = \langle A \rangle$, $|\nabla\tilde{\rho}|_{\mathbf{r}_o} = \sqrt{\langle B \rangle^2 + \langle C \rangle^2}$, where the average is taken over both time and the radii r_a . For comparison, we also calculate \mathbf{v}_d using the ground state density profile, and find very good agreement between the two methods.

5.3.3 Results

5.3.3.1 Vortex orbital dynamics

The numerically measured velocity curves for a vortex located at variable radius r_o in a harmonically trapped system are shown in Fig. 5.1. As predicted by Eq. (5.9), the sum of the density and phase gradient terms gives excellent agreement with the total vortex velocity. For improved clarity at small values of r_o , we have also included the orbital frequency measurements in the inset of the Figure. This data clearly shows that, for all radii, the ambient superfluid velocity is actually the dominant contribution to the vortex motion, while the density-dependent effect only becomes significant near the boundary. This finding is in contradiction with much of the literature on the topic, as we discuss in Sec. 5.4.

Figure 5.2 shows the measured velocity data for a single vortex in the uniform trap. Once again, we find that the total velocity is well described by the sum of the

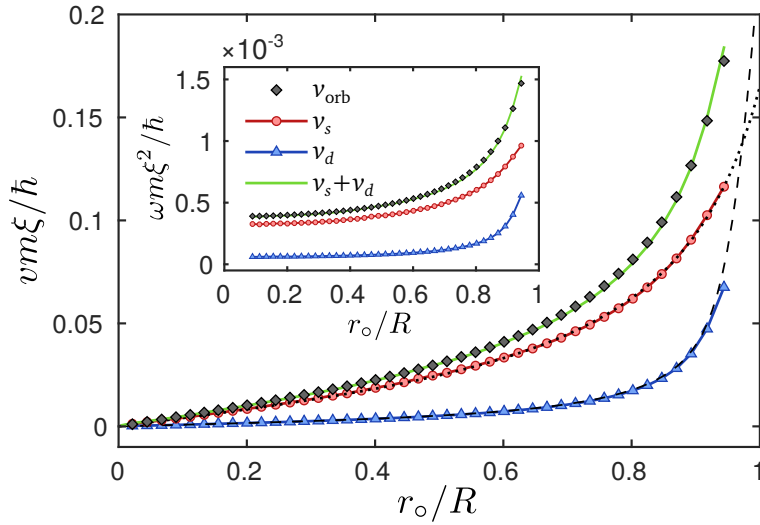


Figure 5.1: The contributions to the vortex orbital velocity and frequency (inset) in a harmonically trapped condensate, for a vortex initiated at variable radius r_o . In the main frame the black diamonds denote the measured orbital velocity v_{orb} , while the two terms on the right hand side of Eq. (5.9), v_s and v_d , are plotted as red circles and blue triangles, respectively. The sum $v_s + v_d$ is also shown as a solid green line for comparison with v_{orb} . All corresponding frequencies are plotted equivalently in the inset. In the main frame, the dotted line shows the fit $v(r_o) = (\hbar/m)\alpha r_o / (\beta R^2 - r_o^2)$, a generalised image vortex velocity, to $v_s(r_o)$, where $\alpha = 6.79$, $\beta = 1.32$ (see Sec. 5.5.2). The dashed curve is the result of calculating v_d using the ground state density profile. In the inset, the data for the lowest four radii have been omitted due to numerical noise.

phase and density terms, as Eq. (5.9) predicts. We also observe that, in this system, the overwhelming contribution to the vortex velocity for radii $r_o \lesssim 0.9R$ is the phase gradient. The sudden increase in v_d near the boundary is due to the finite width of the wall—in an infinite cylindrical well, this term would remain negligible everywhere. We also find that, for small radii, $v_s(r_o)$ agrees well with the velocity field produced by an image vortex outside the condensate at radius $\bar{r}_o = r_o R^2 / |r_o|^2$, the expected image location for a disk-shaped system with infinitely hard walls (as discussed in Sec. 3.2.1). As the vortex approaches the edge of the fluid, the phase gradient velocity becomes stronger than the image vortex predicts. This can be attributed to the fact that neither the vortex nor the wall are infinitesimally narrow features and consequently the ideal point-vortex image picture fails near the boundary of the condensate.

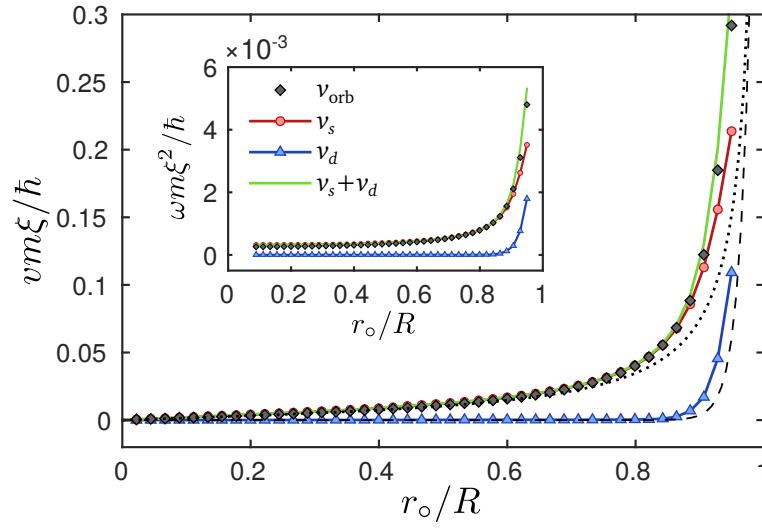


Figure 5.2: The contributions to the vortex orbital velocity and frequency (inset) in a uniform, disk-shaped condensate, for a vortex imprinted at variable radius r_o . The data are labelled as in Fig. 5.1, except that the dotted curve shown here is the velocity $v(r_o) = (\hbar/m)r_o/(R^2 - r_o^2)$ produced by an image vortex at $\bar{r}_o = R^2/r_o$. As in Fig. 5.1, the frequency data at the lowest four radii have been omitted due to numerical noise.

5.3.3.2 Contributions to the ambient velocity field

Whereas the density gradient velocity in Eq. (5.9) is straightforward to measure from ground state properties, the ambient velocity field $\mathbf{v}_s(\mathbf{r})$ induced by the vortex is, in general, more complicated. To demonstrate this, we measure the background velocity field everywhere in the condensate for a vortex at radius $r_o \approx 0.75R$ in each of our two traps. The inset of Fig. 5.3(b) shows the y -component of each measured velocity field over the entire condensate when the vortex is located at $\mathbf{r}_o \approx (0.75R, 0)$, while the main frame of panel (b) shows a one-dimensional slice through this field along the x -axis. Panel (a) shows the corresponding density profiles, normalised to n_o , the maximum density in the harmonic trap.

In the uniform trap, the background velocity field is well described by an image vortex located at $\bar{\mathbf{r}}_o \approx (0.75^{-1}R, 0)$ (the expected location for a hard-walled disk trap), although the agreement becomes worse near the boundary closest to the vortex, due to the finite core size and boundary width. By contrast, the velocity field in the harmonic trap is more complicated. A peak in the background velocity in the region around the vortex core is clearly visible, and has been previously identified and discussed in Ref. [302]. It was suggested in Ref. [302] that the background velocity field $\mathbf{v}_s(\mathbf{r})$ could be split into two independent contributions:

an image vortex field arising from the presence of the boundary, plus an additional contribution due to the fluid inhomogeneity at the vortex location. In fact, Sheehy and Radzihovsky [299] derived an approximate expression for this second contribution,

$$\mathbf{v}_{\text{peak}}(\mathbf{r}) = \frac{\hbar}{m} \hat{\mathbf{z}} \times \frac{\nabla \tilde{\rho}(\mathbf{r}_o)}{\tilde{\rho}(\mathbf{r}_o)} \log \left(\frac{|\mathbf{r} - \mathbf{r}_o| |\nabla \tilde{\rho}(\mathbf{r}_o)|}{|\tilde{\rho}(\mathbf{r}_o)|} \right), \quad (5.10)$$

which is responsible for the peak in the region around the vortex (however, it was assumed in their derivation that this was the only contribution to the vortex orbital velocity, which we have shown is not the case). For comparison, we show in Fig. 5.3(b) the sum of the image velocity field and Eq. (5.10), as suggested

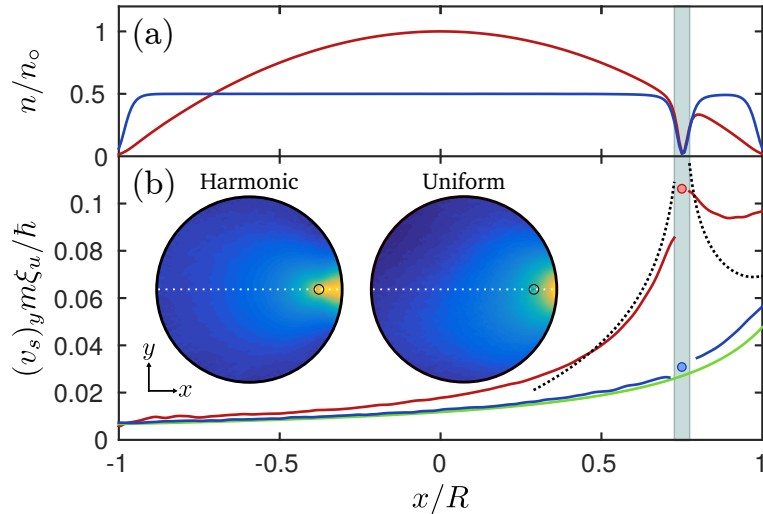


Figure 5.3: The (a) one-dimensional density profile $n(x) = |\psi(x, 0)|^2$ and (b) y -component of the background velocity field $\mathbf{v}_s = \nabla \tilde{\phi}$ along the x -axis in both the harmonic (red) and uniform disk (blue) traps for a vortex at position $x_o \approx 0.75 R$ (highlighted by the vertical shaded region). In the inset of panel (b), the y -component of \mathbf{v}_s has been plotted across the whole condensate for each trap, with a dotted line indicating the cross-section shown in the main frame, and a black circle denoting the vortex location. The colour scales in the inset are the same as the y -axis of (b). All numerical data has been averaged over ≈ 130 dynamical frames in each geometry. The solid green line in (b) is the velocity field produced by an image vortex at $\bar{x}_o \approx 0.75^{-1} R$, while the black dotted line shows the sum of Eq. (5.10) and the image vortex velocity field. For comparison with Figs. 5.1 and 5.2, the measurements of v_s at $r_o \approx 0.75 R$ in each trap are also shown as filled circles (note that there is a factor of two difference for the velocity in the harmonic trap due to the scaling with ξ_u).

in Ref. [302]. While qualitatively reasonable, this approach does not provide quantitative accuracy. Moreover, Eq. (5.10) is only valid near, but outside of, the core region, and therefore fails at greater distances.

Interpreting these observations in light of Eq. (5.9), we emphasise that a density gradient at the vortex location produces two distinct effects on the vortex motion:

- (i) A ‘direct’ effect on the vortex produced by \mathbf{v}_d [which does not contribute to the ambient velocity field \mathbf{v}_s shown in Fig. 5.3(b)].
- (ii) An ‘indirect’ effect via a warping of the phase field that enters \mathbf{v}_s in addition to an image effect due to the boundary, and which manifests as a peak in the azimuthal velocity field around the vortex in the harmonically trapped condensate [shown in Fig. 5.3(b)].

Unlike for the uniform trap, we do not expect the background ‘image vortex’ field in an inhomogeneous system to be described by a single image point-vortex located outside the fluid. Instead, we expect the softness of the boundary to delocalise the image, much like a spherical aberration produced by a soft mirror [312]. It may therefore be possible to approximate the image field more accurately using a configuration of multiple image vortices; however, doing so would destroy the simplified physical picture that makes the image representation appealing.

5.3.3.3 Induced multipole moments

In addition to the effects of boundaries and varying condensate density on the background velocity field $\mathbf{v}_s(\mathbf{r})$ (discussed in Sec. 5.3.3.2), dipole, and higher multipole, moments in the velocity field $\mathbf{v}_i(\mathbf{r})$ of the vortex have been predicted to emerge as a result of the internal structure of the defect. This effect arises due to the dynamical excitation of the $n_z = 0$ kelvon quasiparticles localised within the vortex core [191, 313–317]. Because the vortices considered here are two-dimensional, kelvons with axial quantum numbers $n_z > 0$ are suppressed [318].

In Ref. [319], it was predicted that a vortex moving relative to the background superflow should exhibit an altered intrinsic velocity field $\mathbf{v}_i(\mathbf{r})$ which is no longer circularly symmetric. Outside of the vortex core, the corrections can be expressed in terms of a multipole expansion [319]:

$$\begin{aligned} \mathbf{v}_i(\mathbf{r}) &= \mathbf{v}_i^{(1)}(\mathbf{r}) + \mathbf{v}_i^{(2)}(\mathbf{r}) + \dots \\ &= \frac{\hbar}{m} \left[\hat{\mathbf{z}} \times \frac{\mathbf{r} - \mathbf{r}_o}{|\mathbf{r} - \mathbf{r}_o|^2} + \frac{(\mathbf{r} - \mathbf{r}_o)^2 \mathbf{d} - 2[\mathbf{d} \cdot (\mathbf{r} - \mathbf{r}_o)](\mathbf{r} - \mathbf{r}_o)}{|\mathbf{r} - \mathbf{r}_o|^4} + \dots \right], \end{aligned} \quad (5.11)$$

where the dipole moment

$$\mathbf{d} \equiv \mathbf{v}_{\text{rel}} \frac{m\xi^2}{\hbar} \left(\log \left| \frac{\mathbf{r} - \mathbf{r}_o}{\xi} \right| - a \log \left| \frac{m\xi \mathbf{v}_{\text{rel}}}{\hbar} \right| \right). \quad (5.12)$$

Here, $a \approx 1.49$ is a numerical constant, and \mathbf{v}_{rel} is the velocity of the vortex relative to the superfluid in the vortex frame of reference.

To investigate the possibility of such multipole effects in our Gross–Pitaevskii simulations, we have performed further numerical calculations in the disk-shaped trap, using an increased resolution of 4096×4096 grid points, and a smaller interaction parameter, $g = 148 \hbar^2/m$. This reduces the condensate radius to $R \approx 21 \xi$, and increases the number of grid points per healing length to ~ 64 . After imprinting the vortex phase winding into the ground state of the trap and evolving for a short amount of imaginary time, a quadrupole-like structure becomes visible in the flow field, once both the monopole field $\mathbf{v}_i^{(1)}(\mathbf{r})$ and the local mean

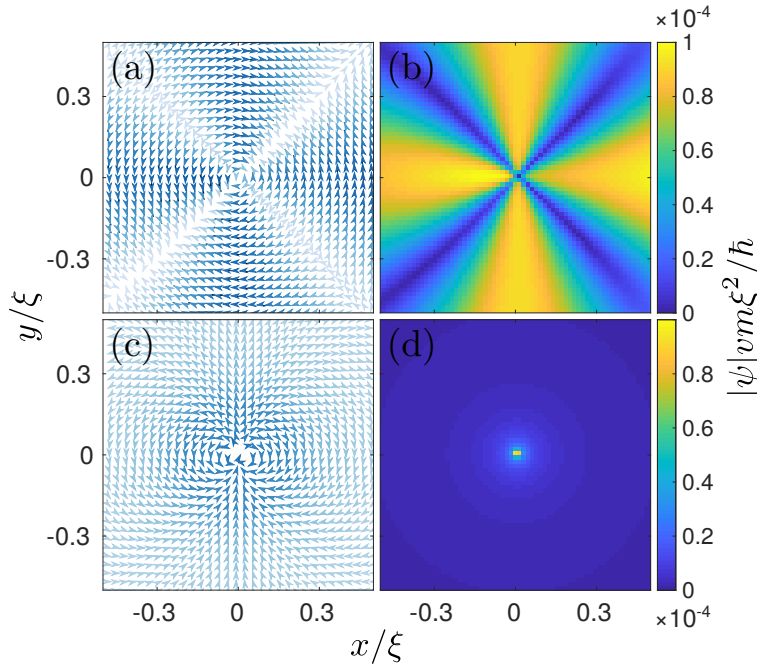


Figure 5.4: Comparison between the numerical [(a)/(b)] and predicted [(c)/(d)] density-weighted velocity fields within the vortex core, left over after subtracting out the vortex monopole field $\mathbf{v}_i^{(1)}(\mathbf{r})$ and the local background velocity $\langle \mathbf{v}_s \rangle$ (averaged over the region shown). The left and right columns, respectively, show the direction and magnitude of each velocity field. The vortex is located at $x_o \approx 0.5R$, and will travel in the positive y -direction under real time evolution.

background velocity $\langle \mathbf{v}_s \rangle$ have been subtracted away². Figure 5.4(a)–(b) shows this numerically measured velocity field for a vortex initiated at $\mathbf{r}_o \approx (0.5R, 0)$. Although the data shown has been obtained using imaginary time propagation, the same structure develops during real time evolution, and is 1-2 orders of magnitude weaker than the background superflow \mathbf{v}_s driving the vortex motion.

We are only able to reproduce a dipole field—such as the prediction of Eqs. (5.11) and (5.12) shown in Fig. 5.4(c)–(d)—as a numerical artifact arising from an inaccurate subtraction of the monopole field, which essentially imprints a vortex–antivortex dipole in the wavefunction. Further investigation into the vortex core localised multipolar velocity fields is a topic of future work.

5.3.3.4 The velocity of a vortex with multiple circulation quanta

To confirm that Eq. (5.9) applies equally well for higher charge vortices, we have repeated our numerical analysis of the vortex velocity in a harmonic trap using a single $s = 2$ vortex. Due to the inherent energetic instabilities of this vortex state, the singularity immediately splits into two singly-charged vortices, which continuously emit phonons and gradually drift apart, causing the centre-of-mass velocity to decrease (for approximately one trap orbit, however, the two vortex cores are indiscernible). To minimise the effects of this splitting on our velocity data, we cut off our measurements once the distance d_v between the two singularities becomes greater than 8ξ , and only calculate the background fields for the early times when $d_v \leq 3\xi$. The obtained velocity and frequency curves are shown in Fig. 5.5, demonstrating that Eq. (5.9) still holds for a multi-quantum vortex. Surprisingly, if the derivation in Sec. 5.2 is repeated using an ansatz wavefunction with $(z - z_o) \rightarrow (z - z_o)^{|s|}$ (i.e. a multi-quantum vortex of charge $s > 0$), then the velocity in Eq. (5.9) becomes $\mathbf{v}_v \rightarrow |s|(\mathbf{v}_s + \mathbf{v}_d)$, which does not match with our numerical results.

For all radii, the total orbital velocity of the vortex is approximately 1.6 times greater than the velocity obtained for a charge $s = 1$ vortex at the same radius. This increase comes entirely from the phase gradient term, which grows by ≈ 1.8 times—slightly lower than the factor of two one would expect from a simple image vortex picture. We have confirmed that, in the uniform disk trap, the v_s component does scale by a factor of two, suggesting that the slightly smaller value observed

2. Strictly, the induced multipole moments are intrinsic to the vortex ‘particle’ and could therefore be removed from the phase field before calculating the smooth background field $\mathbf{v}_s = \nabla \tilde{\phi}$ which drives the vortex motion. However, since we have only subtracted the circularly symmetric monopole component $\mathbf{v}_i^{(1)}(\mathbf{r})$, the higher order multipole contributions remain in our measured ‘background’ field $\mathbf{v}_s(\mathbf{r})$.

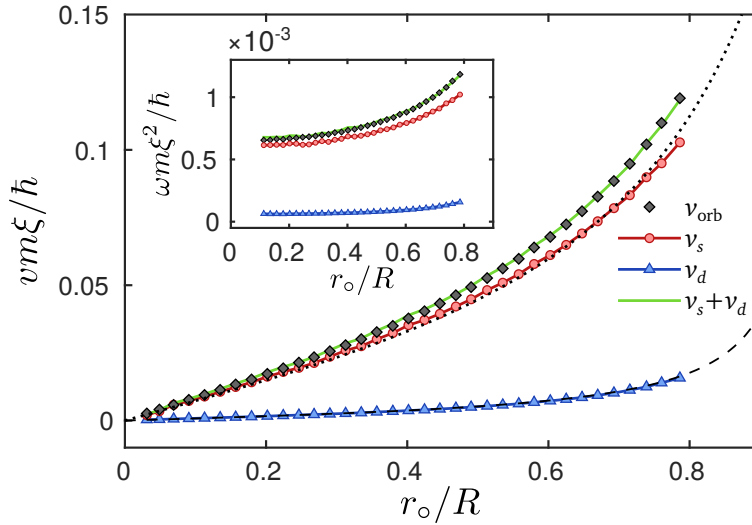


Figure 5.5: The contributions to the orbital velocity and frequency (inset) for a charge $s = 2$ vortex in a harmonic trap, initiated at variable radius r_o . The data are labelled as in Figs. 5.1 and 5.2. The dotted curve shown in the main frame is a fit to $v(r_o) = (\hbar/m)\alpha r_o / (1.32R^2 - r_o^2)$, which gives $\alpha = 12.26$, which is ≈ 1.81 times larger than the value obtained from the single vortex fit. Frequency data at the lowest radii have been omitted due to numerical fluctuations.

in the harmonic trap is related to the shape of the induced velocity peak discussed in Sec. 5.3.3.2. It is interesting to note that, for vortices with large circulation, the phase gradient term in Eq. (5.9) becomes increasingly dominant, since v_d does not scale with $|s|$.

5.4 Comparison with results in the literature

Many expressions describing the motion of vortices in inhomogeneous fluids to varying degree of accuracy are found in the literature. We find that, unlike our analytical solution Eq. (5.9), none of the other models agree precisely with the numerically measured orbital velocity of a single vortex. In the following, we discuss the two most widely used approaches, and briefly review some more recent results.

5.4.1 The two standard approaches

The first of the two common methods from the literature invokes a force balancing argument whereby the negative gradient of the energy $E(\mathbf{r}_o)$ is equated to the

‘Magnus force’ on the vortex [293, 294, 297, 299, 320]:

$$\mathbf{F}_{\text{Mag}} \stackrel{?}{=} m\tilde{n}\boldsymbol{\kappa} \times \mathbf{v}_v = \nabla E(\mathbf{r}_o), \quad (5.13)$$

where $\tilde{n} \equiv \tilde{\rho}^2$, and the gradient $\nabla E(\mathbf{r}_o)$ is taken with respect to the vortex location \mathbf{r}_o . The same formula has also been obtained using a variational Lagrangian approach [111, 295]. The advantage of this expression is that the vortex velocity can be calculated directly from the total energy E of the fluid, which is straightforward to measure numerically, and can be approximated analytically for a single vortex [111, 294, 295, 297]. However, we argue that this approach also has a number of significant shortcomings. Firstly, Eq. (5.13) requires knowledge of the global properties of the condensate, making it less general than the local description of Eq. (5.9). Moreover, as suggested by the $\stackrel{?}{=}$ notation, the Magnus force, rather than being proportional to the vortex velocity, should be proportional to the velocity of the vortex *relative* to the background superflow³ [322–324]:

$$\mathbf{F}_{\text{Mag}} = m\tilde{n}\boldsymbol{\kappa} \times (\mathbf{v}_v - \mathbf{v}_s) = m\tilde{n}\boldsymbol{\kappa} \times \mathbf{v}_d, \quad (5.14)$$

where Eq. (5.9) has been used to obtain the second equality. Comparing expressions (5.13) and (5.14), it thus becomes apparent that the force which appears in the former is not the Magnus force, but rather the total force on the vortex, $\mathbf{F}_v = m\tilde{n}\boldsymbol{\kappa} \times \mathbf{v}_v = m\tilde{n}\boldsymbol{\kappa} \times (\mathbf{v}_s + \mathbf{v}_d)$, which is responsible for its total velocity \mathbf{v}_v [325]. Equation (5.13) therefore states that the change in condensate energy induced by radially shifting the vortex is redistributed into the vortex motion. However, this is only an approximation, since a small amount of energy will, in general, also be distributed into the phonon (compressible) and quantum pressure components.

The second approach is to use a matched asymptotic expansion [326, 327], where analytic solutions of the Gross–Pitaevskii equation are found both within and far from the vortex core. The two solutions are then matched at an intermediate length scale, providing an analytic expression for the vortex velocity of the form [111]:

$$\mathbf{v}_v = \frac{3\hbar}{4m\mu} \log\left(\frac{R}{\xi}\right) \hat{\mathbf{k}} \times \nabla V_{\text{trap}} = \frac{3}{2} \log\left(\frac{R}{\xi}\right) \mathbf{v}_d. \quad (5.15)$$

3. This is in direct analogy with the Magnus force per unit length on a rotating cylinder in a classical fluid, which has the form $\mathbf{F}_{\text{Mag}}/L = \rho\boldsymbol{\kappa} \times (\mathbf{v} - \mathbf{v}_b)$, where L is the length of the cylinder, ρ is the mass density of the fluid, $\boldsymbol{\kappa}$ is the circulation of the rotating cylinder, \mathbf{v} is its velocity, and \mathbf{v}_b is the velocity of the background flow [321].

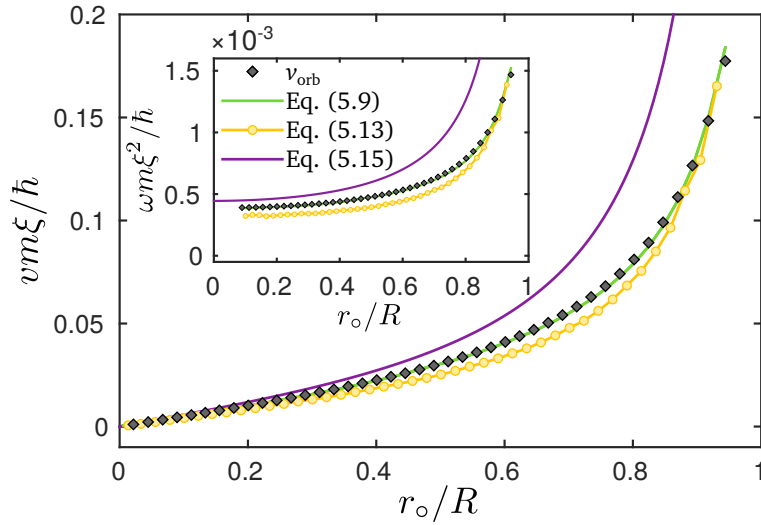


Figure 5.6: Comparison between our numerically obtained orbital velocity (from Fig. 5.1) and the predictions of Eqs. (5.9), (5.13) and (5.15) for a single vortex in a harmonically trapped BEC. The inset shows the corresponding orbital frequencies, where the data for the lowest radii have been excluded due to numerical noise.

Since $\nabla V_{\text{trap}} \propto \nabla \tilde{n}$ and $\mu \propto \tilde{n}$, this expression can be reduced to the same functional form as the velocity \mathbf{v}_d in Eq. (5.9); the only difference being a dimensionless factor $(3/2) \log(R/\xi)$ which is introduced by the matched asymptotic expansion [299,301]. Equation (5.15) is therefore not in agreement with Eq. (5.9), since the contribution from the phase gradient velocity \mathbf{v}_s is missing. The dimensionless factor multiplying \mathbf{v}_d approximately accounts for this missing term, but only provides an adequate result when the vortex is near the trap centre.

For comparison between our model and those which appear in the literature, Fig. 5.6 shows the orbital velocity and frequency (inset) of a vortex in a harmonic trap as calculated from Eqs. (5.9), (5.13) and (5.15) using our numerical results. Figure 5.6 shows that Eq. (5.9) gives the best agreement with the observed orbital velocity from the GPE, although Eq. (5.13) also provides a good approximation. The discrepancy in the latter case is due to some of the condensate energy [the right hand side of Eq. (5.13)] being distributed into degrees of freedom other than the vortex motion.

5.4.2 Potential sources of confusion

In a harmonic trap, it is possible to simplify Eqs. (5.13) and (5.15) using a number of approximations, thereby reducing them to the same approximate expression

for the vortex velocity:

$$\mathbf{v}_v \propto \frac{\hbar}{m} \frac{r_o}{R^2 - r_o^2} \hat{\boldsymbol{\theta}}. \quad (5.16)$$

This is done substituting the Thomas–Fermi density profile $n(r) = n_o(1 - r^2/R^2)$ and local chemical potential $\mu(r) = gn(r)$, where n_o is the density at the trap centre [94, 111, 295, 297, 299]. The agreement between these two approaches has previously been interpreted as confirmation of their validity [94], despite the shortcomings of each method. To further confound the problem, it has also previously been assumed that Eqs. (5.10) and (5.15) are equivalent, due to their similar functional forms [94, 299]. However, as clarified in Sec. 5.3.3.2, these two expressions describe different physics: while Eq. (5.10) approximates an induced phase gradient around the vortex, Eq. (5.15) [or equivalently, the velocity \mathbf{v}_d in Eq. (5.9)] describes a component of the vortex velocity that does not appear in the superfluid phase.

An additional source of potential confusion in the harmonically trapped system is that all three velocity terms in Eq. (5.9) have approximately the same radial dependence, as shown in Fig. 5.1. Therefore, the density gradient term \mathbf{v}_d may provide a reasonable estimate for the total velocity if multiplied by a suitable constant, as in Eq. (5.15). However, this approach ignores the essential physics of the induced background velocity field and image effects, and will therefore not yield quantitatively accurate results in general (as seen for large r_o in Fig. 5.6).

It is also worth noting that, due to the specific shape of the harmonic trapping potential, Eq. (5.16) has the same functional form as predicted by the point-vortex approximation for a uniform disk of incompressible fluid; a system that corresponds to the exactly soluble electrostatic problem of a point charge inside a disk with conducting boundaries. As discussed throughout Sec. 5.3.3, however, the vortex velocities in these two systems arise from different physical sources, and therefore should not be conflated.

5.4.3 Image vortices

In deriving the above expressions, Eqs. (5.13) and (5.15), it is usually assumed that image vortices do not play a role in bounded inhomogeneous systems [94, 111]. Assuming conservation of particle number, the boundary condition for the mass current is $\hat{\mathbf{n}} \cdot \mathbf{j} = \hat{\mathbf{n}} \cdot n\mathbf{v}_s = 0$, where $\hat{\mathbf{n}}$ is the unit vector normal to the fluid boundary. Because the density $n(\mathbf{r})$ gradually approaches zero at a soft wall, this condition is automatically satisfied regardless of the value of \mathbf{v}_s at the edge of the

system. By contrast, for a hard-walled system, the density is finite even near the boundary of the fluid, and therefore image vortices must be introduced to ensure $\hat{\mathbf{n}} \cdot \mathbf{v}_s = 0$. However, as we have argued in Sec. 5.3.3.2, there is a component of the background superfluid velocity field arising from boundary effects even in the harmonic trap, although it does not appear to be well approximated using a single localised image vortex, as is the case in the uniform disk geometry [see the dashed line in Fig. 5.3(b)].

5.4.4 Further comparisons

Here we briefly discuss a number of other related works, whose results seem to have been largely neglected throughout the BEC literature since they were published, as most authors have instead opted to use the methods described in Sec. 5.4.1.

Nilsen, Baym and Pethick [301] obtained the same general expression for the vortex velocity in an inhomogeneous fluid, Eq. (5.9), via an equivalent derivation as presented here. However, they proceeded by assuming that $\mathbf{v}_d = 0$ and replaced \mathbf{v}_s with $\nabla \log(\tilde{\rho})$ for a single vortex in a harmonic trap. Essentially, this lead to a model which is equivalent to Eq. (5.15), and which neglects important contributions to the vortex velocity.

Jezeq and Cataldo [302, 305] also derived Eq. (5.9) using a different approach, although their model included a phenomenological correction factor multiplying \mathbf{v}_d —a factor which we have found to be unity. They also performed a detailed analysis of the induced background velocity field around a vortex in a harmonic trap [302], as we have done in Sec. 5.3.3.2.

Various forms of Eq. (5.9) have also appeared in the context of optical vortex motion in nonlinear media [328–330], since the dynamics in these optical systems are governed by a nonlinear Schrödinger equation similar to the Gross–Pitaevskii model used here.

5.5 Generalising the point-vortex model

Equipped with an improved understanding of the motion of a vortex in an inhomogeneous superfluid, we now turn to an application of this theory—namely, a generalised model for describing the dynamics of point-vortices in arbitrary geometries. In particular, we will examine how our findings apply to a harmonically trapped BEC, although the approach we outline here could be applied to more general geometries. To our knowledge, all previous work considering point-

vortex dynamics in harmonic traps has ignored the ambient phase gradient effects discussed throughout Secs. 5.2–5.4. Rather, the orbital motion of a single vortex has always been modelled using the simplified form in Eq. (5.16) [131, 137, 331], where a multiplicative constant is included to set the timescale of the dynamics. In this section we will show that this simplifying assumption results in a model that provides a poor quantitative description of the vortex dynamics, and that some minor adjustments based on our findings above can improve the model significantly. However, we conclude that, due to the complicated nature of the induced ambient velocity field discussed in Sec. 5.3.3.2, a fully general and efficient point-vortex description seems unachievable.

5.5.1 Requirements of a point-vortex model

We first wish to specify what we consider to be the requirements of a point-vortex model. Namely:

- (i) The model must be simple, both computationally and conceptually. Specifically, it must be more efficient to solve numerically than the GPE, otherwise there is no improvement over the standard approach to simulating BEC dynamics. To gain the improvement, however, it may be necessary to perform initial calibrations for the model using the GPE.
- (ii) The predictions for the velocities of each vortex in the system must only depend on their circulations and instantaneous positions.
- (iii) The dynamics predicted by the point-vortex model must be quantitatively accurate.

5.5.2 The point-vortex model

We consider a configuration of N_v vortices at positions $\mathbf{r}_j(t)$ with integer charges $\{s_j\}$, where $j = \{1, 2, \dots, N_v\}$. To obtain a point-vortex model from Eq. (5.9), we need to substitute in the phase field produced by this vortex configuration, as well as the background density profile of the condensate, as a function of \mathbf{r}_j . This approach is quite general, provided a reasonable approximation for the phase field is obtainable for the geometry under consideration. Here, we begin by demonstrating that the point-vortex model for a uniform disk can be derived exactly using Eq. (5.9). We then turn to the harmonically trapped case, where an exact derivation is not possible. Instead, to arrive at a point-vortex model, we

make some simplifying approximations to account for the ambient velocity fields which arise from the inhomogeneous density profile.

5.5.2.1 The uniform disk system

In the case of the uniform disk geometry, each vortex induces a single image vortex of charge $\bar{s}_j = -s_j$ located beyond the fluid boundary at position $\bar{\mathbf{r}}_j = \mathbf{r}_j R^2 / |\mathbf{r}_j|^2$ [237, 239]. Hence, the total superfluid phase is given by:

$$\phi(\mathbf{r}, t) = \sum_{j=1}^{N_v} \left\{ s_j \arctan \left[\frac{y - y_j(t)}{x - x_j(t)} \right] + \bar{s}_j \arctan \left[\frac{y - \bar{y}_j(t)}{x - \bar{x}_j(t)} \right] \right\}, \quad (5.17)$$

where the first term is produced by the physical vortices, while the second term arises from the images. The gradient of this scalar field is:

$$\nabla \phi(\mathbf{r}, t) = \sum_{j=1}^{N_v} \left[s_j \hat{\mathbf{z}} \times \frac{(\mathbf{r} - \mathbf{r}_j)}{|\mathbf{r} - \mathbf{r}_j|^2} + \bar{s}_j \hat{\mathbf{z}} \times \frac{(\mathbf{r} - \bar{\mathbf{r}}_j)}{|\mathbf{r} - \bar{\mathbf{r}}_j|^2} \right]. \quad (5.18)$$

Substituting this into Eq. (5.9), and using the fact that $\nabla \log(\bar{\rho}) = 0$ (due to the constant density), we find that the velocity of vortex k at position \mathbf{r}_k is given by:

$$\mathbf{v}_k = \frac{\hbar}{m} \left[\sum_{j \neq k}^{N_v} s_j \hat{\mathbf{z}} \times \frac{(\mathbf{r}_k - \mathbf{r}_j)}{|\mathbf{r}_k - \mathbf{r}_j|^2} + \sum_j^{N_v} \bar{s}_j \hat{\mathbf{z}} \times \frac{(\mathbf{r}_k - \bar{\mathbf{r}}_j)}{|\mathbf{r}_k - \bar{\mathbf{r}}_j|^2} \right], \quad (5.19)$$

where the $j = k$ term in the first sum has been excluded because a vortex is not affected by its own velocity field. This is the standard point-vortex model for a disk-shaped system [237, 239], with corresponding Hamiltonian, Eq. (3.13). The first term describes the vortex–vortex interactions, while the second corresponds to vortex–image interactions, necessary for keeping the vortex particles within the physical boundary and ensuring that the continuity equation is satisfied there.

5.5.2.2 The harmonically trapped system

We now move on to the more complicated case of a harmonically trapped condensate. As discussed in Sec. 5.3.3.2, the phase field induced by a vortex in an inhomogeneous condensate is nontrivial, and hence obtaining a fully general point-vortex model for this geometry is most likely not possible. Instead, our goal here is to provide improvements on the model currently used throughout the literature, without introducing significant complexity.

As shown in Fig. 5.3(b), the ambient velocity field produced far from the vortex

core for an off-centred vortex is well approximated using a standard image description [left side of Fig. 5.3(b)]. It is only in the vicinity of the vortex core that this approximation fails, as the contributions from Eq. (5.10) become important (we ignore entirely the small effect of the multipole field discussed in Sec. 5.3.3.3). Based on this, we propose a correction to the phase field in a harmonic trap that distinguishes between self-image and non-self-image interactions. To do this, we introduce an additional set of image vortices, $\{\bar{\mathbf{r}}'_j, \bar{s}'_j\}$, to produce the self-induced part of the phase field at the vortex locations $\mathbf{r} = \mathbf{r}_j$. In the infinitesimal region around the k th vortex, the phase is approximated to be:

$$\begin{aligned} \phi_k(\mathbf{r}, t) = & \sum_{j=1}^{N_v} s_j \arctan \left[\frac{y - y_j(t)}{x - x_j(t)} \right] + \sum_{j \neq k}^{N_v} \bar{s}_j \arctan \left[\frac{y - \bar{y}_j(t)}{x - \bar{x}_j(t)} \right] \\ & + \bar{s}'_k \arctan \left[\frac{y - \bar{y}'_k(t)}{x - \bar{x}'_k(t)} \right], \end{aligned} \quad (5.20)$$

while at all other locations in the fluid, the phase field is given by Eq. (5.17). We stress that this approach is only viable in the dilute-vortex limit when the vortices are separated well enough that the induced background velocity peak around each vortex does not significantly affect any other vortex. Alternatively, if the vortices only approach one another in relatively uniform regions of the fluid (e.g. at the centre of the harmonic trap), the effect of Eq. (5.10) should be small, and hence this approach should remain valid. To apply this double-image approximation, we substitute Eq. (5.20) into Eq. (5.9), which yields the following point-vortex model:

$$\begin{aligned} \mathbf{v}_k = & \frac{\hbar}{m} \left[\sum_{j \neq k}^{N_v} s_j \hat{\mathbf{z}} \times \frac{(\mathbf{r}_k - \mathbf{r}_j)}{|\mathbf{r}_k - \mathbf{r}_j|^2} + \sum_{j \neq k}^{N_v} \bar{s}_j \hat{\mathbf{z}} \times \frac{(\mathbf{r}_k - \bar{\mathbf{r}}_j)}{|\mathbf{r}_k - \bar{\mathbf{r}}_j|^2} \right. \\ & \left. + \bar{s}'_k \hat{\mathbf{z}} \times \frac{(\mathbf{r}_k - \bar{\mathbf{r}}'_k)}{|\mathbf{r}_k - \bar{\mathbf{r}}'_k|^2} - \hat{\mathbf{k}} \times \nabla \log \tilde{\rho}(r_k) \right]. \end{aligned} \quad (5.21)$$

Note that we have retained the density term, since the fluid is now inhomogeneous. We approximate $\tilde{\rho}(r_k)$ using a parabolic Thomas–Fermi profile.

To obtain the generalised image description, we introduce an effective charge α and system radius $\sqrt{\beta}R$ for the self-images by setting $\bar{s}'_j = \alpha \bar{s}_j$ and $\bar{\mathbf{r}}'_j = \beta \bar{\mathbf{r}}_j$, respectively. For a vortex at radius r_o , this modified image will produce a velocity $v(r_o) = (\hbar/m)\alpha r_o/(\beta R^2 - r_o^2)$. Fitting this generalised image model to the $v_s(r_o)$ data in Fig. 5.1, we obtain $\alpha = 6.79$, $\beta = 1.32$, which gives very good agreement

with the obtained data. The values of these parameters (in particular the effective charge α) are so large because we are modelling the localised peak visible in Fig. 5.3 using image vortices, when in fact this is not an image effect at all. We note that these parameters are specific to our choice of system, and that the calibration would need to be repeated for other configurations. We therefore have all of the parameters required to test Eq. (5.21).

5.5.3 Testing the model

Having derived and calibrated a new point-vortex model, we may test its accuracy for a few simple two-vortex scenarios to see how well it reproduces the dynamics predicted by our Gross–Pitaevskii simulations. In each scenario, we compare the performance of our model to the model used throughout the literature for a harmonically trapped BEC:

$$\mathbf{v}_k = \frac{\hbar}{m} \left[\sum_{j \neq k}^{N_v} s_j \hat{\mathbf{z}} \times \frac{(\mathbf{r}_k - \mathbf{r}_j)}{|\mathbf{r}_k - \mathbf{r}_j|^2} + \Omega_o \hat{\mathbf{z}} \times \frac{s_k \mathbf{r}_k}{R^2 - r_k^2} \right], \quad (5.22)$$

where $\Omega_o = (3/2) \log(R/\xi)$ [94, 131, 136, 331]. The second term here corresponds to Eq. (5.16), and is responsible for the circular motion of each vortex in the system. We find that replacing $\Omega_o \rightarrow 0.88 \Omega_o$ gives a better prediction for the orbital frequency at the trap centre, so we use this value instead. The key differences between Eqs. (5.21) and (5.22) are that (i) we include image vortex effects, and (ii) our single vortex orbital behaviour arises from the sum of the density gradient and the self-image term.

We have already examined the single vortex case in Secs. 5.3.3 and 5.4.1. Since we have calibrated our model using the data in Fig. 5.1, we find very good agreement in this case. Equation (5.22), on the other hand, reduces to Eq. (5.15) for a single vortex, which provides a significantly less accurate prediction, as shown in Fig. 5.6.

5.5.3.1 Test 1: Two symmetric same-sign vortices

The first two-vortex case we consider is initialised with condition $s_1 = s_2 = 1$, $\mathbf{r}_1 = -\mathbf{r}_2 = (x_o, 0)$. In this case, the two vortices symmetrically orbit around the trap centre at a constant frequency and radius. We calculate the velocity of each vortex as a function of r_o using the GPE, and plot the separate contributions to the velocity in Fig. 5.7(b). Here, we have split the ambient velocity measurement \mathbf{v}_s into $\mathbf{v}_{\text{int}}(r_o) = 1/2r_o \hat{\boldsymbol{\theta}}$, the contribution from the other vortex, and $\mathbf{v}_{\text{im}}(r_o)$,

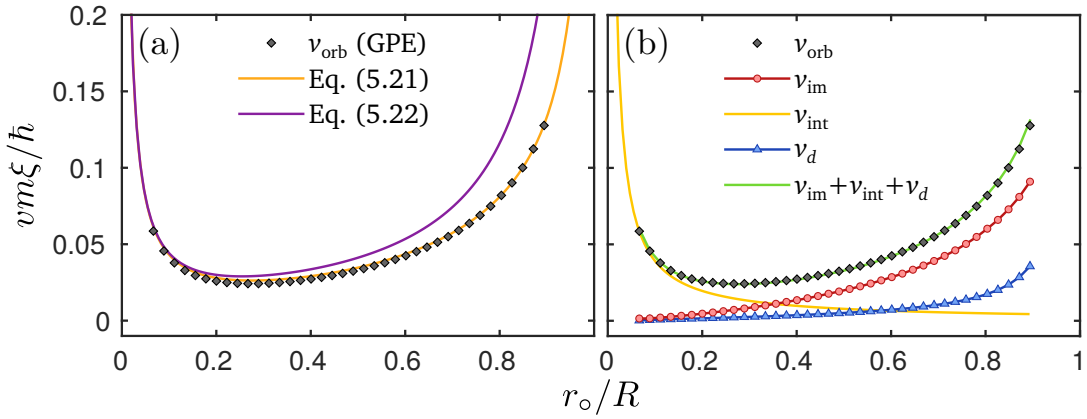


Figure 5.7: The azimuthal velocity of two same-sign vortices in a harmonically trapped BEC as a function of their symmetric radius r_o . (a) Comparison of the orbital velocity predictions from the two point-vortex models, Eqs. (5.21) and (5.22), and the GPE. (b) Contributions to the total orbital velocity of each vortex, as measured using the GPE. We have split the ambient velocity field into $\mathbf{v}_s = \mathbf{v}_{\text{im}} + \mathbf{v}_{\text{int}}$, where \mathbf{v}_{im} is the velocity produced by the image and the density-induced phase warping, and \mathbf{v}_{int} is the velocity resulting from the vortex–vortex interaction.

the velocity due to images and the density-induced phase warping. Figure 5.7(a) shows how well each point-vortex model [Eqs. (5.21) and (5.22)] predicts the total orbital velocity measured in the GPE. For small radii, where the vortex–vortex interaction dominates, the two predictions are equivalent; however, at larger radii our improved model is significantly more accurate.

5.5.3.2 Test II: Symmetric vortex dipole

The second case we examine is a symmetrically placed vortex dipole, with $s_1 = -s_2 = 1$ and initial condition $\mathbf{r}_1 = -\mathbf{r}_2 = (x_o, 0)$. For this configuration, the vortices undergo symmetric counter-rotating orbits on opposite sides of the trap, which are concentric with one another as x_o is varied. In addition, the orbits vary in frequency as a function of x_o . In Fig. 5.8, we present both the orbits (inset) and their frequency (main frame) as a function of x_o , obtained using the GPE. For comparison, we also show the predictions from both point-vortex models, Eqs. (5.21) and (5.22). For almost all values of x_o , we obtain only a minor improvement for both the orbital shapes and their frequencies using our point-vortex model. This is not surprising, however, since this configuration violates the requirement that the vortices remain well separated while in inhomogeneous regions of the trap.

When $x_o \approx 0.24R$, the dipole configuration is a stationary state, in which all

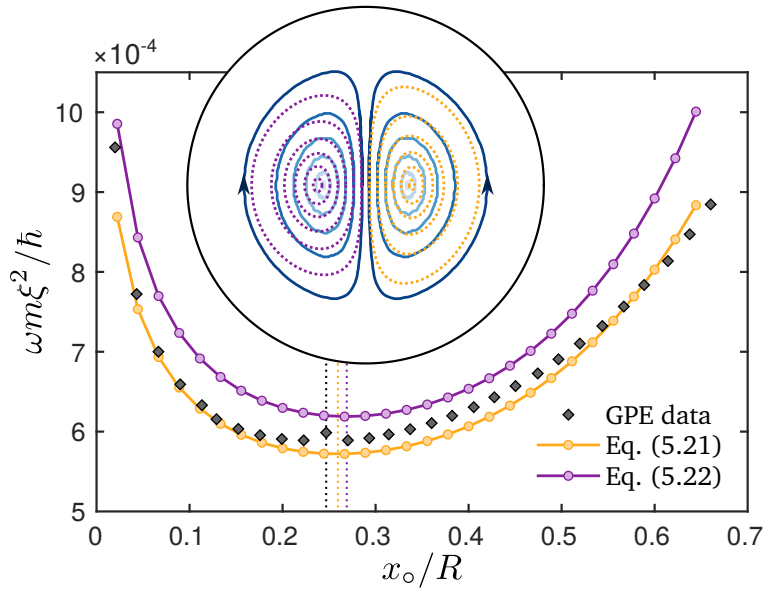


Figure 5.8: Numerically calculated orbital frequency for a vortex dipole initiated at $\pm(x_0, 0)$ in a harmonically trapped BEC. The orbital frequencies calculated from the two point-vortex models, Eqs. (5.21) and (5.22), are shown alongside the Gross–Pitaevskii data for comparison. In the inset, the symmetric orbits observed in the GPE are shown as solid blue lines for the initial positions $x_0/R \approx \{0.02, 0.07, 0.11, 0.16, 0.20, 0.24\}$. The corresponding orbits predicted by each point-vortex model for the same initial conditions are shown as dotted lines, with Eq. (5.21) on the right, and Eq. (5.22) on the left. Dashed vertical lines in the main frame show the position of the stationary point in each model.

contributions to the vortex velocity cancel. Using the two point-vortex models, Eqs. (5.21) and (5.22), this point is overestimated to be $x_0 \approx 0.260R$ and $x_0 \approx 0.269R$, respectively. Also absent from the point-vortex models is the frequency resonance observed around the stationary point in the Gross–Pitaevskii data. This resonance is the result of the compressibility not accounted for in the simplified models.

5.6 Summary

We have derived a general and exact expression, Eq. (5.9), for the velocity of a quantised vortex in a spatially inhomogeneous superfluid. Using Gross–Pitaevskii simulations, we have found that this equation provides highly accurate predictions of the velocity of vortices in some simple one- and two-vortex scenarios, both in harmonic and uniform disk-shaped traps. In doing so, we have clarified precisely how density and phase gradients affect the motion of a vortex in each of these sys-

tems. In addition, we have found a clear signature of a multipole moment induced in the velocity field of the vortex due to its internal core structure. Although past literature has made significant progress in describing vortex dynamics in nonuniform fluids, many misconceptions and erroneous assumptions exist throughout. The Magnus force has often been attributed to the total vortex velocity; however, we have shown here that it is in fact only responsible for the density gradient velocity \mathbf{v}_d in Eq. (5.9). We have also found in agreement with Ref. [302] that image vortices, which have often been disregarded in harmonically trapped BECs, are relevant even for systems with soft boundaries.

Using our findings, we have been able to derive a new point-vortex model for a harmonically trapped BEC, which provides significant improvements for one- and two-vortex dynamics over the model currently in use throughout the literature. However, for our approach to remain quantitatively accurate, the vortices must remain dilute while in regions of varying density, since our simplified model does not rigorously account for induced ambient velocity fields in regions of varying density. Due to this stringent requirement, even with our improvements, the point-vortex model fails to provide quantitative accuracy even for simple two-vortex scenarios. Of course, the model could easily be improved by introducing more accurate approximations for the induced ambient velocity fields around each vortex; however, any added complexity may rapidly negate the simplicity required of the point-vortex model. We therefore conclude that a quantitatively accurate point-vortex treatment for arbitrary trap shapes is not possible in general due to the difficulties of modelling ambient velocity fields that fundamentally arise from the compressibility of the fluid. For a qualitative or statistically satisfactory point-vortex model, on the other hand, the approach presented here should be straightforward to apply in a wide variety of inhomogeneous systems.

6

DYNAMICS OF TWO SAME-SIGN POINT-VORTICES

This chapter is devoted to studying the motion of two same-sign point-vortices, a dynamical regime which serves as a natural bridge between the comparatively simple scenario of a single vortex examined in the previous chapter, and the more complicated dynamics of quantum turbulence, a topic which will be the focus of subsequent chapters. The work presented here is based on Ref. [140]. We expand on the results of Ref. [131], in which both theoretical analysis and experimental observations were used to investigate a bifurcation in the dynamics of two same-sign vortices in a harmonically trapped BEC. Upon attempting to reproduce the findings of Ref. [131], we discovered that the authors' conclusions regarding the specific details of this bifurcation were incomplete, and hence we sought to expand on their results.

6.1 Motivation

Recent experiments [127, 128, 131, 132, 154, 332] have shown that vortices in superfluid gases are amenable to a point-vortex approach, opening up possibilities for quantitative studies of vortex dynamics such as Kelvin waves [116, 316, 317, 333, 334], Crow instabilities [335–337], and Tkachenko vortex waves [120–122, 338]. Understanding such few-vortex phenomena forms the basis for solving more complex problems involving vortices, such as quantum turbulence in 2D systems [103, 152, 156, 157, 162, 164, 165, 273, 275, 339, 340] and the emergence of Onsager vortices and negative Boltzmann temperatures for vortices in disk-shaped traps [165, 169, 170], which will be examined in later chapters.

In 2D superfluids, strong turbulence is tantamount to chaotic dynamics of the quantised vortices in the system. For three or more vortices in an effectively 2D Bose–Einstein condensate confined by a harmonic trap, the vortex dynamics

can become chaotic. However, a two-vortex problem is integrable due to two conservation laws related to the energy and angular momentum of the system, as discussed in Sec. 3.2.1. As a precursor to studying the onset of turbulence, we focus here on the problem of two vortices of the same circulation. Our work is motivated by recent BEC experiments that discovered a bifurcation of rigidly rotating stationary states in the two-vortex case [131]. Here we find that the phase space of the two-vortex system is divided into two topologically distinct regions corresponding to two radically different types of two-vortex motion: In one region the individual orbits of the two vortices overlap, whereas in the other region the orbits never cross each other.

This chapter is organised as follows. In Sec. 6.2, we outline the point-vortex model we use for describing the effectively 2D dynamics of vortices in a highly oblate harmonically trapped BEC. Section 6.3 presents our results using two complementary descriptions: the position-space representation and the velocity-space representation. These are used for revealing the phase-space boundary that separates the system dynamics into two topologically distinct classes. We then summarise our conclusions in Sec. 6.4.

6.2 Point-vortex model

In this chapter, we restrict our theoretical analysis to the point-vortex model. Despite the shortcomings of this approach (as discussed in the previous chapter), it can still be used to provide qualitative predictions of vortex dynamics.

The point-vortex model used in this work is equivalent to Eq. (5.22):

$$-i\dot{z}_k = R^2\Omega_0 \frac{s_k z_k}{R^2 - |z_k|^2} + R^2\Omega_{\text{int}} \sum_{j \neq k}^{N_v} s_j \frac{z_k - z_j}{|z_k - z_j|^2}, \quad (6.1)$$

where $z_k = x_k + iy_k$ is the position coordinates of the k th vortex in complex notation, $s_k \in \mathbb{Z}$ is its circulation number, and $k \in \{1, \dots, N_v\}$. However, the qualitative findings were verified using our improved point-vortex model, Eq. (5.21), and the Gross–Pitaevskii equation. The vortices are constrained to move within the Thomas–Fermi radius of the condensate, $R > |z_k|$. Furthermore, Ω_0 is the orbital angular frequency of a solitary unit-strength vortex infinitesimally close to the trap centre [127, 341], and Ω_{int} is an angular frequency determining the effective strength of the vortex–vortex interaction [131].

Equations (6.1) are equivalent to Hamilton's equations of motion,

$$s_k \dot{x}_k = \frac{\partial H}{\partial y_k}, \quad s_k \dot{y}_k = -\frac{\partial H}{\partial x_k}, \quad (6.2)$$

corresponding to the Hamiltonian

$$H = \frac{R^2 \Omega_0}{2} \sum_{k=1}^{N_v} s_k^2 \ln \left(1 - \frac{|z_k|^2}{R^2} \right) - R^2 \Omega_{\text{int}} \sum_{k=1}^{N_v} \sum_{j>k}^{N_v} s_k s_j \log \frac{|z_k - z_j|}{R}. \quad (6.3)$$

In addition to H , the model also has another integral of motion, $L = \sum_k s_k |z_k|^2$, due to the underlying rotational symmetry, as discussed in Sec. 3.2.1. In analogy to point particles, this quantity is referred to as the point-vortex angular momentum; note, however, that it should not be confused with the orbital angular momentum that the vortex induces in the flow of the surrounding superfluid. In fact, whereas the point-vortex angular momentum $s_k |z_k|^2$ of a single vortex increases as the vortex moves away from the symmetry axis, the angular momentum of the superfluid decreases under such circumstances.

By denoting $z_k = r_k \exp(i\theta_k)$, we obtain the radial and angular vortex velocities \dot{r}_k and $\dot{\theta}_k$, respectively, from the Cartesian velocities as

$$\begin{bmatrix} \dot{r}_k \\ r_k \dot{\theta}_k \end{bmatrix} = \begin{bmatrix} \cos\theta_k & \sin\theta_k \\ -\sin\theta_k & \cos\theta_k \end{bmatrix} \begin{bmatrix} \dot{x}_k \\ \dot{y}_k \end{bmatrix}. \quad (6.4)$$

The velocity space $\{(\dot{r}_k, \dot{\theta}_k)\}$ turns out to be extremely useful for representing the vortex dynamics in subsequent analysis (Sec. 6.3.2).

From here on, we focus on a system of two vortices with equal circulations, setting $N_v = 2$ and $s_1 = s_2 = 1$. We measure lengths in units of R and time in units of Ω_0^{-1} . Up to a rotation of the coordinate system, all possible two-vortex configurations are spanned by three variables: the angle $\phi = \tan^{-1}(r_2/r_1)$, the point-vortex angular momentum $L = r_1^2 + r_2^2$, and the azimuthal angle $\theta_{21} = \theta_2 - \theta_1$ between the two vortices. Recently, Navarro *et al.* [131] investigated this system both theoretically and experimentally for two-vortex configurations with $\theta_{21} = \pi$. They demonstrated that when $\Omega_{\text{int}}/\Omega_0 = 0.1$ (a value that we adopt throughout this chapter), the system exhibits a pitchfork bifurcation at $L = L_{\text{cr}} \approx 0.273 R^2$ that induces the emergence and stabilisation of asymmetric ($r_1 \neq r_2$) rigidly rotating vortex configurations and the destabilisation of symmetric ($r_1 = r_2$, i.e., $\phi = \pi/4$) rigidly rotating states at $L > L_{\text{cr}}$.

We have solved Eqs. (6.1) numerically using the ode113 function in MATLAB with a relative tolerance of 10^{-13} , absolute tolerance of 10^{-15} , and a variable time step. As the initial conditions (ϕ, L, θ_{21}) , we consider 20 equidistant values from $\phi = 0.238\pi$ to $\phi = 0.466\pi$ and from $L = 0.1R^2$ to $L = 0.955R^2$, and 10 equidistant values from $\theta_{21} = 0.1\pi$ to $\theta_{21} = \pi$. For trajectories that have exactly symmetric initial conditions ($\phi = \pi/4$ and $\theta_{21} = \pi$) and exhibit stable rigid-body rotation ($L < L_{\text{cr}}$), our simulations show deviations from the initial radius $r_k(0)$, initial Hamiltonian energy H , and initial L of at most 10^{-6} in the respective units of each over time intervals under consideration.

6.3 Results

In this section, we present our numerical results on the dynamics of two same-sign point-vortices and, in particular, describe the emergence of the two distinct classes of motion in the system. These two dynamical regimes are separated by a

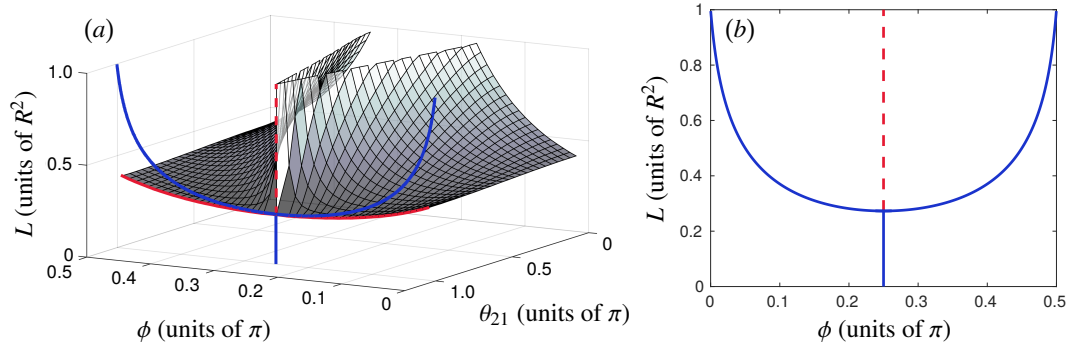


Figure 6.1: (a) Phase-space-dividing wall, and [(a) and (b)] the curve of rigidly rotating states. In panel (a), the full three-dimensional parameter space (ϕ, L, θ_{21}) of possible two-vortex configurations is shown. Above the surface, the individual orbits of the two vortices never cross each other, whereas below it the orbits intersect. Here $\phi = \tan^{-1}(r_2/r_1)$, $L = r_1^2 + r_2^2$, and $\theta_{21} = \theta_2 - \theta_1$, with $\{(r_k, \theta_k)\}$ denoting the polar coordinates of the vortices. The blue solid curve corresponding to rigidly rotating states lies in the plane $\theta_{21} = \pi$ shown in (b); see also Fig. 6.9. The red dashed line marks the unstable rigidly rotating states occurring for $L > L_{\text{cr}} \approx 0.273R^2$. Panel (b) corresponds to Fig. 1(c) in Ref. [131]. Notice that the rigidly rotating states trace a one-dimensional curve in the three-dimensional parameter space (a), whereas the red curves are the boundary curves of the two-dimensional phase-space-dividing wall for $\theta_{21} = \pi$. As in Ref. [131], all results are for $\Omega_{\text{int}}/\Omega_0 = 0.1$ [Eqs. (6.1)].

surface which exists in the phase space of possible two-vortex configurations.

Figure 6.1 summarises the main findings. The wall that divides the two-vortex phase space mapped by (ϕ, L, θ_{21}) is shown in Fig. 6.1(a), indicating a sharp transition between the two types of motion as the initial vortex positions are varied. This transition boundary is impenetrable in the sense that any two-vortex state located on one side of the boundary at any one time will always remain on that side of the boundary as the system evolves in time. Furthermore, and contrary to the findings of Ref. [131], our simulations reveal that this phase space division is not related to a set of asymmetric rigidly rotating states, which exist only for $\theta_{21} = \pi$. The distinction between these two phase-space curves is made in Fig. 6.1.

To relate our results to the findings of Ref. [131], we limit the specific examples examined in the rest of the chapter to the case $\theta_{21} = \pi$, corresponding to vortices that are initially located on opposite sides of the centre of the harmonic trap. However, we emphasise that the two distinct phase-space regions persist for all values of θ_{21} [Fig. 6.1(a)]. We first consider the position-coordinate representation (Sec. 6.3.1) in order to provide a physically intuitive picture, but subsequently switch to using the radial and angular velocities as our coordinates (Sec. 6.3.2) because the emergence of the two types of motion is most apparent in this representation.

6.3.1 Position-space representation

Consider first two same-sign vortices placed at equal distances on opposite sides of the trap centre (i.e., $\phi = \pi/4$ and $\theta_{21} = \pi$) in terms of their position coordinates $(x_k, y_k) \in \mathbb{R}^2$, $r_k < R$. These states lie on the solid vertical line segment in Fig. 6.1. As long as $L < L_{\text{cr}} \approx 0.273R^2$ [131], the resulting motion will consist of stable rigid-body rotation as exemplified in Fig. 6.2(a). The dynamics of this state show no major divergence from rigid rotation over time scales of $\sim 4000\Omega_0^{-1}$ and satisfy $|r_k(t) - r_k(0)|/R < 10^{-10}$ during the entire simulation.

On the other hand, it was recently found by Navarro *et al.* [131] that when $L > L_{\text{cr}}$, the symmetric rigidly rotating states with $\theta_{21} = \pi$ and $\phi = \pi/4$ are dynamically unstable due to a symmetry-breaking pitchfork bifurcation, and stable rigid-body rotation is instead exhibited by *asymmetric* states with $\theta_{21} = \pi$ and $\phi = \pi/4 \pm \delta$, where the specific value of δ is determined by L . In Fig. 6.1(b), the stable rigidly rotating two-vortex states lie on the solid curve, whereas the unstable symmetric rigidly rotating states are indicated by the dashed line segment. An example of an asymmetric rigidly rotating state is shown in Fig. 6.2(b). Figure 6.3,

in turn, illustrates the destabilisation of the symmetric configuration for $L > L_{\text{cr}}$: the initial configuration is perfectly symmetric, but after a sufficiently long simulation time, the state becomes nonrigidly rotating since even the smallest numerical deviation pushes the vortices out of the rigidly rotating trajectories.

Next, we turn to the general case of two-vortex dynamics with any ϕ , L , and θ_{21} , considering the full 3D configuration space [Fig. 6.1(a)]. Two possible types of general stable dynamics in the nonrigidly rotating configurations are observed. Figure 6.4(a) shows the first type, in which the vortices trace out orbits that are confined to the same spatial region of the trap and intersect each other at different times. If we define the closed intervals $I_k \equiv [\min_t r_k(t), \max_t r_k(t)]$, which describe the smallest annuli inside which each vortex moves, the first type of motion is characterised by $I_1 = I_2$. Figure 6.4(b), in turn, is an example of the other general type of dynamics, in which the two vortices are confined to separate spatial regions and their orbits never intersect. In this case, $I_1 \cap I_2 = \emptyset$. The equivalence of the coordinate space $\{(x_k, y_k)\}$ to the Hamiltonian phase space of the system [Eq. (6.2)] suggests that this difference between shared and separate trap regions represents a change in the topology of the system's accessible phase space.

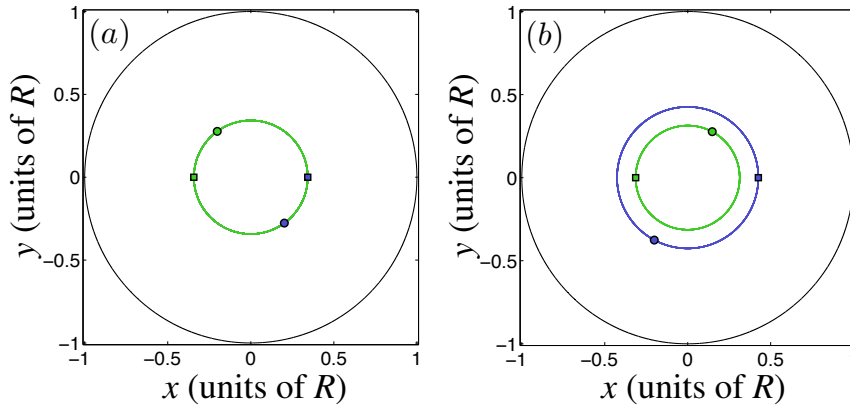


Figure 6.2: Dynamics of rigidly rotating configurations of two same-sign point-vortices. (a) Symmetric rigidly rotating configuration with the initial conditions $\phi/\pi = 0.25$, $L = 0.235 R^2$, and $\theta_{21} = \pi$, corresponding to panel B17 in Fig. 6.9. In this and all other figures, the total simulation time is $60 \Omega_0^{-1}$. (b) Asymmetric rigidly rotating state with $L = 0.28 R^2$, $\phi/\pi = 0.298$, and $\theta_{21} = \pi$ (panel F16). The initial and final position of each vortex are denoted by square and circular markers, respectively. Approximately 15 orbits have occurred in these simulations. The orbit of vortex 1 is shown in dark (blue) color and that of vortex 2 in light (green) color. In panel (a), the individual orbits of the two vortices are the same.

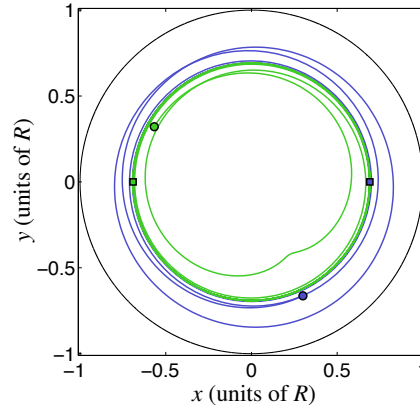


Figure 6.3: Simulated dynamics of an unstable symmetric rigidly rotating two-vortex configuration with the initial conditions $\phi/\pi = 0.25$, $L = 0.955R^2$, and $\theta_{21} = \pi$, corresponding to panel B1 in Fig. 6.9. Although in theory the configuration rotates rigidly, the instability causes even the smallest numerical errors to result in large deviations from the rigid rotation.

The mixing of two time scales due to the orbital and relative motion of the vortices makes it difficult to quantify the periodic motion of the vortices. To elucidate the relative motion of the vortices, we can transform to a rotating frame of reference. In this frame, the coordinate axes x' and y' are rotating relative to the laboratory frame with the time-dependent angular velocity $(\dot{\theta}_1 + \dot{\theta}_2)/2$, i.e., the instantaneous average angular velocity of the two vortices.

The fixed and rotating frames of reference are compared for the case of intersecting orbits in Fig. 6.5 and for noncrossing orbits in Fig. 6.6 (here again both

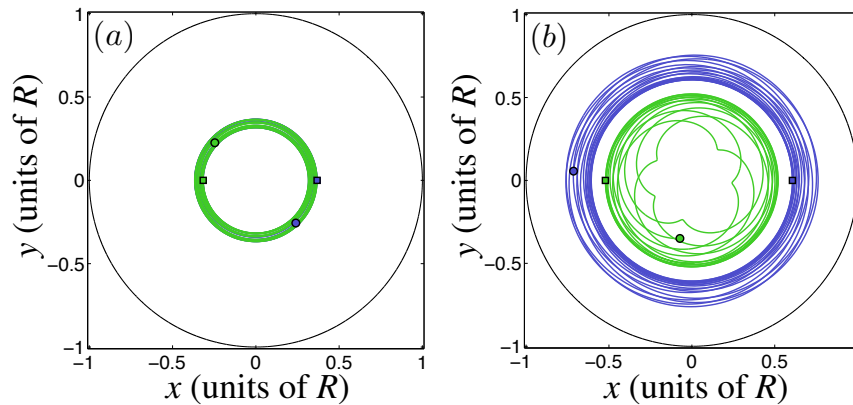


Figure 6.4: (a) Two-vortex dynamics with overlapping orbits and initial conditions $\phi/\pi = 0.274$, $L = 0.235R^2$, and $\theta_{21} = \pi$ (panel D17 in Fig. 6.9). (b) Dynamics for which the vortex orbits never intersect; here $\phi/\pi = 0.274$, $L = 0.64R^2$, and $\theta_{21} = \pi$ (panel D8).

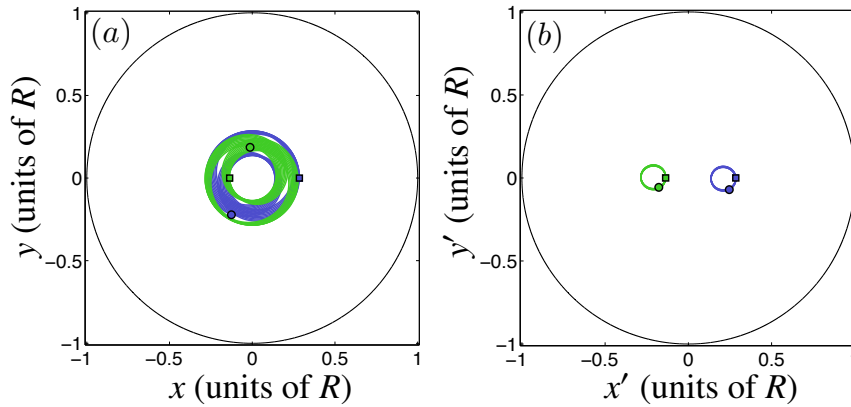


Figure 6.5: Comparison of laboratory- and rotating-frame perspectives with the initial conditions $\phi/\pi = 0.358$, $L = 0.1R^2$, and $\theta_{21} = \pi$, corresponding to panel K20 in Fig. 6.9. (a) Laboratory-frame representation showing intersecting single-vortex orbits. (b) Rotating-frame view of the same dynamics showing orbits that are the same shape but at opposite sides of the trap. The coordinate axes x' and y' rotate with the instantaneous average angular velocity of the two vortices.

examples start with $\theta_{12} = \pi$). When the orbits cross in the laboratory frame [Fig. 6.5(a)], they form similarly shaped closed curves in the rotating frame [Fig. 6.5(b)], which are centred at equal distances but at opposite sides of the trap centre. For noncrossing orbits in the laboratory frame [Fig. 6.6(a)], the rotating frame yields two closed curves that have different shapes and are located at differ-

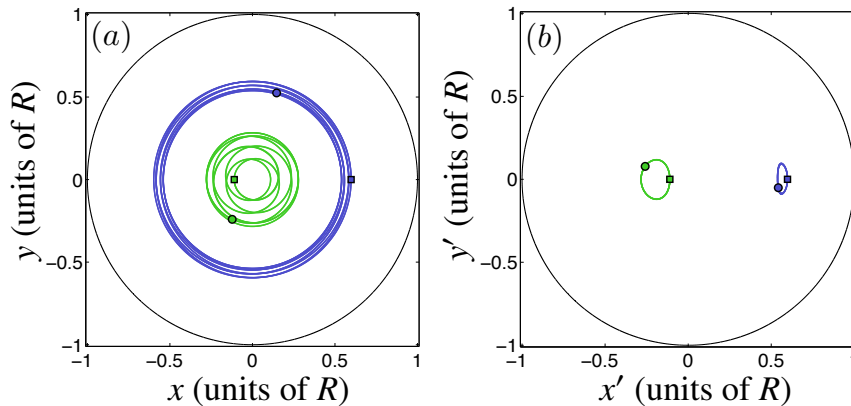


Figure 6.6: Comparison of laboratory- and rotating-frame perspectives for the initial conditions $\phi/\pi = 0.442$, $L = 0.37R^2$, and $\theta_{21} = \pi$, corresponding to panel R14 in Fig. 6.9. (a) Laboratory-frame representation showing vortices moving in separate regions of the trap. (b) Rotating-frame view of the same dynamics showing orbits that are of different shape and at different distances from the trap centre.

ent distances from the trap centre [Fig. 6.6(b)]. We conclude that although the overall vortex motion always reduces to relatively simple orbits in the rotating frame [128], distinguishing between the two general classes of dynamics is not particularly simple. In addition, the small numerical errors in determining the correct frame-rotation frequency are prone to accumulate for long simulation times, leading to deviations from the simple closed curves.

6.3.2 Velocity-space representation

The two types of dynamics of the two-vortex system become particularly evident when one inspects the motion in terms of the radial and angular velocities $\{(\dot{r}_k, \dot{\theta}_k)\}$ [Eq. (6.4)]. This method is invariant under the rotation of the vortex configuration about the trap centre, and we refer to it as the *velocity-space representation*. The two general types of two-vortex dynamics are illustrated using this representation in Fig. 6.7. Figure 6.7(a) shows the orbits that the vortices trace out in the 2D velocity space $(\dot{r}, \dot{\theta})$ in the case where their individual real-space orbits intersect and $I_1 = I_2$. We observe that in this case both vortices always trace identical simple loops in the velocity space (for stable symmetric rigidly rotating states this loop contracts into a single point). Since the conservation of H and L guarantee that $(\dot{r}_1, \dot{\theta}_1) \neq (\dot{r}_2, \dot{\theta}_2)$ whenever $\dot{r}_k \neq 0$, the vortices traverse the joint velocity-space

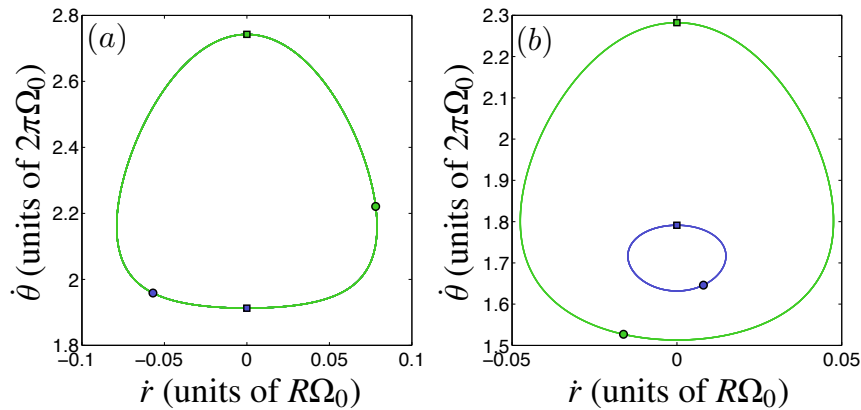


Figure 6.7: Two-vortex dynamics in the velocity-space representation. (a) Overlaid orbits showing that each vortex has exactly the same dynamics, albeit out of phase from the other. The initial conditions are $\phi/\pi = 0.358$, $L = 0.1R^2$, and $\theta_{21} = \pi$, corresponding to Fig. 6.5 (panel K20 in Fig. 6.9). (b) Vortex orbits for the initial conditions $\phi/\pi = 0.442$, $L = 0.37R^2$, and $\theta_{21} = \pi$ (Fig. 6.6 and panel R14 in Fig. 6.9) showing that the two vortices trace separate loops in the polar velocity space.

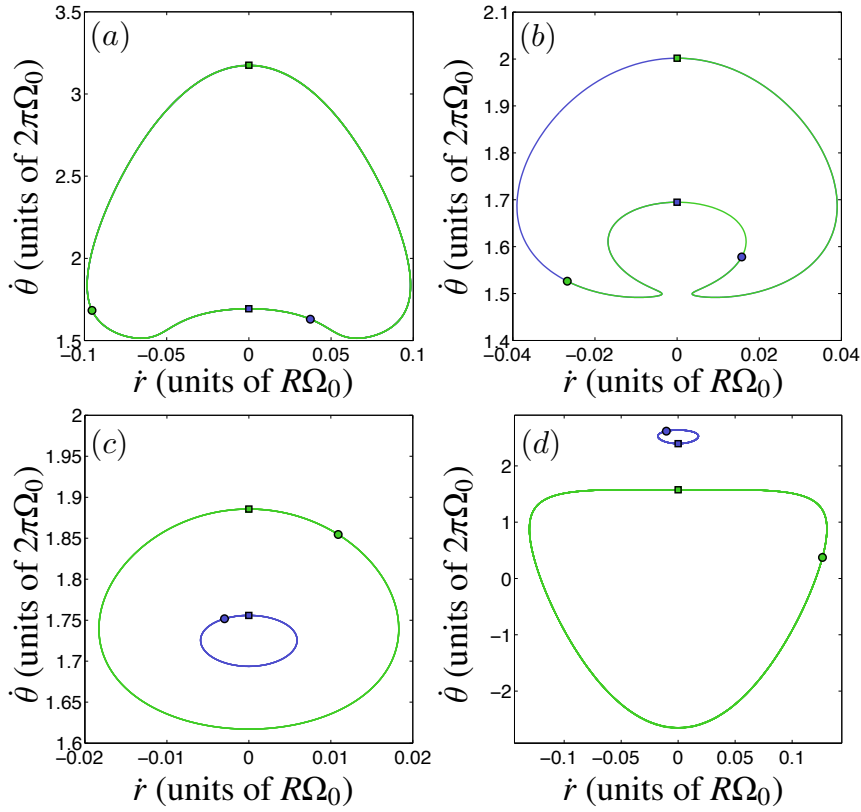


Figure 6.8: Comparison of different types of observed dynamics in the polar velocity space. (a) Shared-space dynamics far from the phase transition with the initial conditions $\phi/\pi = 0.454$ and $L = 0.28R^2$ (panel S16 in Fig. 6.9). (b) Shared-space dynamics near the transition with $\phi/\pi = 0.418$ and $L = 0.325R^2$ (panel P15). (c) Noncrossing dynamics near the transition with $\phi/\pi = 0.418$ and $L = 0.37R^2$ (panel P14). (d) Noncrossing dynamics far from the transition with $\phi/\pi = 0.418$ and $L = 0.595R^2$ (panel P9). In each panel, the initial separation angle is $\theta_{21} = \pi$.

loop out of phase. The other type of general two-vortex motion, where their coordinate-space orbits never cross and $I_1 \cap I_2 = \emptyset$, is illustrated in the velocity space in Fig. 6.7(b). In this case, the two vortices trace separate loops in the velocity space that do not intersect each other.

Let us next consider in detail what happens in the velocity-space when one crosses over from one type of motion to the other, i.e., crosses over the separating boundary in the initial configuration space (ϕ, L, θ_{21}) [Fig. 6.1(a)]. We stress that such a crossover can never occur during the dynamics; instead, one should think of varying the parameters (ϕ, L, θ_{21}) manually. Again, we consider the case $\theta_{21} = \pi$, due to its relevance to Ref. [131].

At sufficiently low L values, the motion corresponds to overlapping orbits, and the single velocity-space loop traced by both vortices encloses a convex area [Fig. 6.7(a)]. In the rotating coordinate-space representation, the individual orbits are identically shaped ellipses as in Fig. 6.5(b). The change induced in the dynamics when the initial point-vortex angular momentum L is gradually increased is illustrated in Fig. 6.8. As L is increased, the closed velocity-space orbit deforms and becomes concave, with the single minimum in the angular velocity splitting into two minima, each with the same angular velocity and opposite radial velocities [Fig. 6.8(a)]. In the rotating coordinate space, this corresponds to the development of a sharp point in the vortex paths near the edge of the trap, deforming the ellipses into droplets with their tips pointing away from the trap centre. On further increasing L , this sharp point develops into a second loop in the path, creating a figure-eight curve in the rotating-frame coordinate space. In the velocity-space representation, the figure-eight stage corresponds to concave closed curves of the type shown in Fig. 6.8(b). Eventually a critical value of L is reached at which the single loop in the velocity space self-intersects at zero radial velocity and a finite value of angular velocity, and subsequently separates into two nonintersecting simple loops [Fig. 6.8(c)]. Depending on the values of L and ϕ , one of the separated loops may lie inside the other [Fig. 6.8(c)], or they may not enclose any points in common [Fig. 6.8(d)]. As L is varied continuously between the configurations shown in panels (c) and (d) of Fig. 6.8, the second (green) vortex passes through $r = 0$ during the dynamics, causing the green loop to extend to $\dot{\theta} \rightarrow \infty$, before crossing over to $\dot{\theta} \rightarrow -\infty$. For values of L beyond this singular point, the blue velocity loop is no longer enclosed by the green loop, as seen in Fig. 6.8(d).

Figure 6.9 demarcates the different types of two-vortex dynamics in the parameter space (ϕ, L) of different initial configurations with $\theta_{21} = \pi$. Sampling of this (ϕ, L) space was done by scanning the parameters on a 20-by-20 grid of 400 initial conditions and integrating the system over a time interval of $60\Omega_0^{-1}$. Each grid cell in Fig. 6.9 shows the resulting dynamics in the position-coordinate space. The transition from a shared velocity-space loop (shaded region in Fig. 6.9) to separated loops—i.e., from $I_1 = I_2$ to $I_1 \cap I_2 = \emptyset$ —is represented by the dark (red) solid line in Fig. 6.9. For fixed $\phi = \phi_0$, values of L above this transition point always result in distinct, nonintersecting orbits in both the coordinate-space [Figs. 6.2(b), 6.4(b), and 6.6] and the velocity-space representation [Figs. 6.7(b), 6.8(c), and 6.8(d)]. This critical value of L increases slightly with increasing ϕ .

The asymmetric rigidly rotating configurations are also indicated in Fig. 6.9 (upper, blue solid curve). We note in particular that these configurations lie inside the region of separated-phase-space dynamics and do not occur at the transition point between the two types except at a single point $(\phi, L, \theta_{21}) = (\pi/4, L_{\text{cr}}, \pi)$. The symmetric rigidly rotating states, and the critical value L_{cr} of the point-vortex angular momentum at which the bifurcation occurs along the line $(\phi, \theta_{21}) = (\pi/4, \pi)$, are in agreement with previous predictions [131]. However, the topological change in the accessible phase space, where the vortex orbits

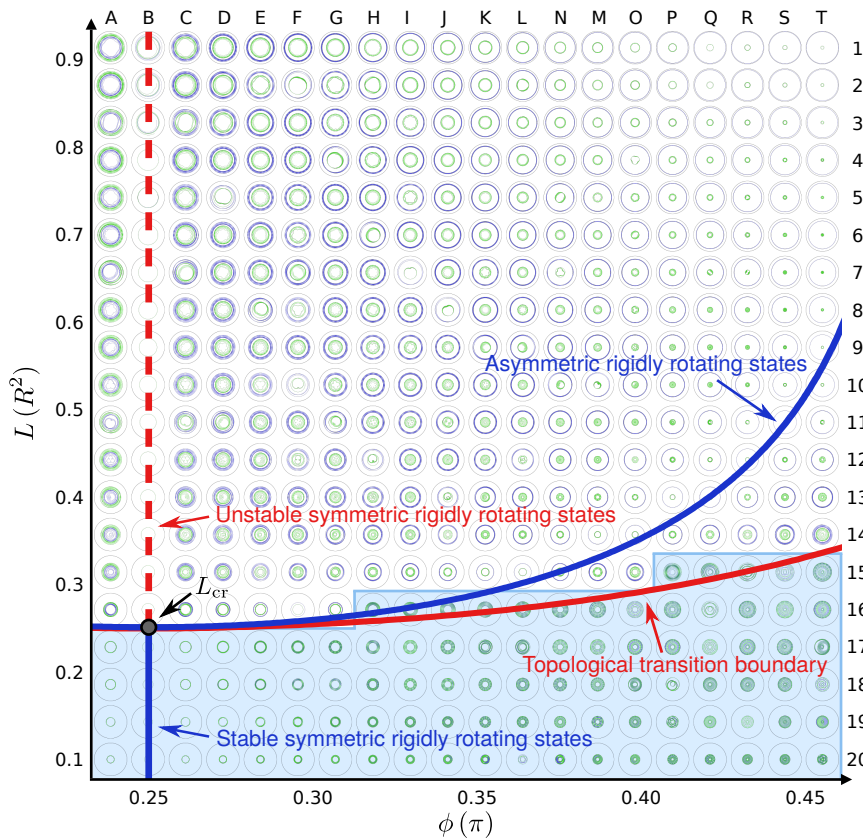


Figure 6.9: Laboratory-frame views of two-vortex dynamics, positioned according to their initial conditions in the 2D parameter space (ϕ, L) ; here the initial angle between the vortices is set to $\theta_{21} = \pi$. The blue solid vertical line represents stable symmetric rigidly rotating states and the red dashed vertical line represents unstable symmetric rigidly rotating states. The blue (upper) curve represents the asymmetric rigidly rotating states, while the red (lower) curve denotes the topological transition between shared and separated phase spaces. In the shaded region below the red curve, the two vortices exhibit shared phase spaces. This figure should be compared with Fig. 1(c) in Ref. [131]. A high-resolution version of the diagram is provided in the supplemental material of Ref. [140].

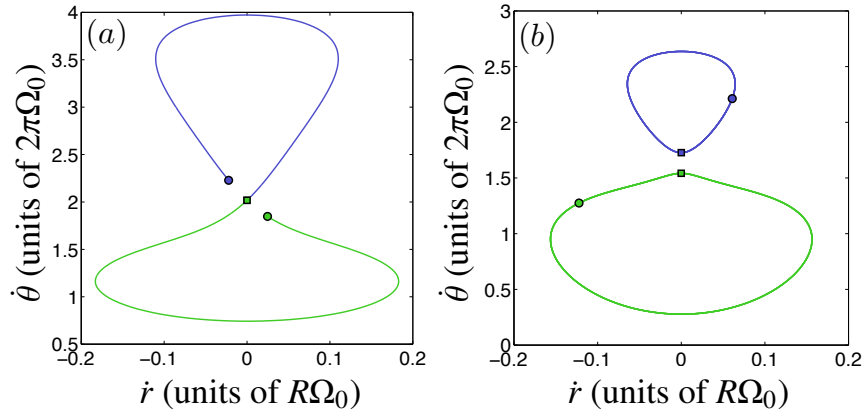


Figure 6.10: Comparison of (a) an unstable symmetric rigidly rotating state, with the initial conditions $\phi/\pi = 0.25$, $L = 0.955R^2$, and $\theta_{21} = \pi$ (panel B1 in Fig. 6.9), and (b) an asymmetric nonrigidly rotating state, with $\phi/\pi = 0.274$, $L = 0.64R^2$, and $\theta_{21} = \pi$ [Fig. 6.4(b) and panel D8 in Fig. 6.9].

become nonintersecting, was not reported in Ref. [131].

The change from stable rigidly rotating states to nonrigidly rotating ones can be understood by closely examining the symmetric rigidly rotating state that destabilises at the bifurcation point L_{cr} . The unstable symmetric state with $L = 0.955R^2 > L_{\text{cr}}$ (Fig. 6.3) yields the simulated dynamics shown in Fig. 6.10(a) using the velocity-space representation. Qualitatively, it resembles the velocity-space representations of states with $\phi \gtrsim \pi/4$ and $L \gtrsim L_{\text{cr}}$ but in the latter the orbits of the two vortices in the velocity space become separated as shown in Fig. 6.10(b).

For initial states near the phase-space transition (solid red curve in Fig. 6.9), the two-vortex system may, during its dynamics, approach the unstable rigidly rotating state (red dashed line in Fig. 6.9), but it is then pushed away from it by the instability of the configuration. If the dynamics exhibit shared phase spaces, this results in a swapping of the outside and inside vortices. For separated phase spaces, the radial velocity of each vortex changes sign, and the outside and inside vortices are pushed back into their respective zones. This suggests that at the bifurcation point $(\phi, L, \theta_{21}) = (\pi/4, L_{\text{cr}}, \pi)$, the symmetric rigidly rotating states (vertical blue line in Fig. 6.9) separate into two antisymmetric branches of asymmetric rigidly rotating states (blue curve in Fig. 6.9) and two symmetric branches of states on the phase-space-dividing boundary (red curve in Fig. 6.9). The branches of asymmetric rigidly rotating states are antisymmetric in the sense that the dynamics of the two rigidly rotating states with $\phi = \pi/4 \pm \delta$ map to each other by interchanging the two vortices. The phase-space-dividing branches are

symmetric in the sense that, for values of L at and below the branches, the initial states with $\phi = \pi/4 \pm \delta$ and same L represent essentially the same dynamics (due to time-translation and rotational symmetry of the model).

When the two vortices are not initially located at opposite sides of the trap, i.e., when $\theta_{21} \neq \pi$, the rigidly rotating states become entirely absent but the phase-space separation transition persists. This is illustrated in Fig. 6.1(a): the symmetric and asymmetric rigidly rotating states form a bifurcating curve in the 2D plane $\theta_{21} = \pi$ of the 3D parameter space (ϕ, L, θ_{21}) of possible two-vortex configurations. The phase-space-dividing boundary, on the other hand, constitutes a 2D surface. In the (ϕ, L, θ_{21}) space, all possible two-vortex orbits are planar curves (which may be single points) that are perpendicular to the L axis (since L is conserved) and never penetrate the phase-space wall.

6.4 Summary

We have numerically studied the dynamics of two same-sign point-vortices in a harmonically trapped superfluid using a point-vortex model. We discovered an impenetrable wall in the 3D phase space of possible two-vortex configurations that divides the ensuing vortex dynamics into two distinct types. In the first type, the two vortices move inside the same annular regions in the trap, whereas in the second type their orbits never intersect. The two types are particularly easy to distinguish in the 2D parameter space spanned by the angular and radial velocities of the vortices, where the first type results in one closed curve along which both vortices travel and the second type yields separate loops for each vortex. This phase-space wall is distinct from the bifurcation of rigidly rotating two-vortex configurations found by Navarro *et al.* [131]. Importantly, the phase-space wall also persists for configurations where the two vortices are not initially at opposite sides of the trap centre, unlike the rigidly rotating states.

Introducing the velocity-space representation opens a number of ways to extend the investigations of point-vortex dynamics in future studies. One obvious question is how the introduction of asymmetry between the vortices, i.e., $s_1 \neq s_2$, would affect the transition phenomena in the phase space; the archetypal example of such a configuration is the vortex–antivortex pair ($s_2 = -s_1$), which is known to exhibit stationary solutions in the harmonically trapped system [127, 128, 137, 332]. On the other hand, increasing the number of vortices to three in Eqs. (6.1) results in the emergence of chaotic vortex dynamics in a particularly simple yet experimentally relevant setup; in the absence of the trap [i.e., for $\Omega_0 = 0$ in Eqs. (6.1)], chaos can

reign only if $N \geq 4$. In fact, already the two-vortex case is likely to exhibit *chaotic advection* [342]: if one formally introduces a third vortex with $s_3 = 0$, its motion in the flow field of the two genuine vortices may be chaotic. Chaotic advection is known to exist in the presence of three genuine vortices for $\Omega_0 = 0$ [232].

Repeating the calculations presented here using Gross–Pitaevskii simulations may give rise to some interesting additional features in the dynamics due to the fluid compressibility not accounted for in the point-vortex model. Preliminary calculations have, however, demonstrated that the phase space wall discovered in this work is qualitatively unchanged in the Gross–Pitaevskii approach. We therefore conclude that, despite its simplifications, the point-vortex model is valuable for providing a qualitative picture of the possible dynamics of the system.

Ultimately, the point-vortex model will serve as an efficient tool for modelling 2D quantum turbulence, a regime of highly chaotic motion of a large number of point-vortices. As such, it shows promise in further elucidating such phenomena as the inverse energy cascade and direct enstrophy cascade, the emergence of Onsager vortices, and negative absolute Boltzmann temperatures associated with 2D turbulence in superfluids.

7

ONSAGER VORTEX FORMATION IN DECAYING QUANTUM TURBULENCE

In this chapter, we begin our examination of turbulence in two-dimensional Bose–Einstein condensates. We investigate the effects of trapping geometry on both the macroscopic and microscopic behaviour of vortices in decaying 2D quantum turbulence. We identify a strong relationship between the shape of the trap and the spontaneous formation of Onsager vortices—a finding which clarifies an apparent contradiction that had existed in the literature prior to this work. We also examine in detail vortex–antivortex annihilation events, and discover that, in our zero temperature Gross–Pitaevskii model, they rarely involve just two vortices; rather, they usually occur via three- and four-vortex annihilation channels. Finally, we model the effects of thermal atoms using a damped Gross–Pitaevskii equation, and introduce a rate equation to describe the vortex number decay for turbulent systems at varying temperatures. These results form the basis of the publication Ref. [169].

7.1 Motivation

Non-equilibrium physics of quantum gases has attracted significant activity recently [343]. Quantum turbulence (QT) is an archetype of non-equilibrium dynamics which features an intriguing interplay between chaos and order. Remarkably, despite the fact that the microscopic behaviour of three-dimensional QT is driven by Kelvin waves [116, 197, 199, 317, 334], Crow instabilities [335–337], vortex reconnections [79, 199, 344], phonon radiation [201, 345] and mutual friction between the normal and superfluid components [346], statistically the dynamics is thought to yield the same Kolmogorov scaling of incompressible kinetic energy as in classical fluid turbulence, as discussed in Sec. 3.3.

In the regime of two-dimensional QT, the debate continues regarding whether or

not an inverse cascade and associated Onsager vortices should emerge [103, 152, 158, 162, 164, 165, 267, 275, 277, 340, 347–349]. Numasato *et al.* [158] simulated quantum turbulence in a uniform 2D superfluid and found evidence of a direct cascade pushing incompressible kinetic energy towards small length scales. In accordance with this finding, recent experiments [103, 155] and simulations [340] using turbulent harmonically trapped highly oblate BECs did not find evidence for the formation of Onsager vortices. By contrast, Simula *et al.* [165] observed strong evidence of vortex clustering in their quasi-2D simulations in a flat trap with steep walls.

One key difference between these studies which could explain the disparity between their findings is the trapping potential used for confining the condensate. The aim of this work is therefore to investigate the role of the trap geometry with regard to the emergence of Onsager vortices. We focus on numerical studies of decaying two-dimensional quantum turbulence in power-law traps, with a particular emphasis on comparing harmonically trapped condensates to those in uniform disk potentials with steep walls. A variety of techniques now exist for producing such steep-walled trapping potentials experimentally [38–42], as has been mentioned in Sec. 1.1.

We simulate BEC dynamics using the Gross–Pitaevskii model and also study their thermodynamic properties using a Markov Chain Monte Carlo technique, interpreting the vortex dynamics in each trap in terms of the vortex evaporative heating mechanism outlined in Sec. 3.3.3 [165]. In addition, we examine in detail the microscopic process of vortex–antivortex annihilation, an essential aspect of the decaying turbulence in these systems.

The outline of this chapter is as follows. In Sec. 7.2, we specify the details of the numerics. In Sec. 7.3, we present the key findings from our simulations of decaying superfluid turbulence in different trapping potentials and interpret our observations using a statistical mechanics framework. We then examine the vortex dynamics on a microscopic scale, focusing in particular on vortex–antivortex annihilation in 2D QT, showing it to be a four-vortex process. Finally, we present our conclusions in Sec. 7.4.

7.2 Model

7.2.1 System parameters

We simulate the dynamics of the condensate wavefunction $\psi(\mathbf{r}, t)$ using the GPE, Eq. (2.13). We consider general power-law trapping potentials of the form

$$V_{\text{trap}}(\mathbf{r}) = \mu_h \left(\frac{|\mathbf{r}|}{R_o} \right)^\alpha, \quad (7.1)$$

where α is a parameter which defines the steepness of the trap walls, R_o is the effective system radius, and $\mu_h = m\omega_r^2 R_o^2/2$ is the chemical potential calculated for the harmonic trap, which depends on the radial trapping frequency ω_r . For $\alpha = 2$ this potential is a standard harmonic trap $V(\mathbf{r}) = m\omega_r^2 |\mathbf{r}|^2/2$ with Thomas–Fermi radius $R_{\text{TF}} = R_o$. In the limit of infinite steepness ($\alpha \rightarrow \infty$) it approaches a cylindrically symmetric well of radius R_o .

Our system parameters correspond to a two-dimensional ^{23}Na BEC with a radial trapping frequency of $\omega_r = 2\pi \times 15 \text{ Hz}$, and a Thomas–Fermi radius of $R_{\text{TF}} \approx 70 \mu\text{m} \approx 12.79 a_{\text{osc}}$, where the radial harmonic oscillator length scale is defined as $a_{\text{osc}} = \sqrt{\hbar/m\omega_r}$. To this end we choose $g = 21\,000 \hbar^2/m$. Hence, the radial extent of our system is similar to those used in the recent experiment by Kwon *et al.* [103] and simulations by Stagg *et al.* [340].

7.2.2 Numerical techniques

As described in Sec. 4.2.3, we solve for the approximate ground state of the system using imaginary time evolution of the GPE and imprint vortices by multiplying the wavefunction ψ by a phase factor $\prod_k^{N_v} \exp(i\phi_k)$, with $\phi_k(x, y) = s_k \arctan[(y - y_k)/(x - x_k)]$. We choose $N_v(t = 0) = 120$ vortices with equal numbers of vortices ($s_k = 1$) and antivortices ($s_k = -1$). The co-ordinate (x_k, y_k) defines the position of the k th vortex, whose circulation sign is s_k .

We choose initial conditions which approximate high entropy, highly randomised states which could be produced by stirring the condensate. To this end, we first construct a density of states distribution $w(E)$ for our chosen vortex number by iteratively generating random vortex configurations and calculating their energy E using the point-vortex Hamiltonian, Eq. (3.13) [see Fig. 3.4 for a schematic of $w(E)$]. The maximum entropy state corresponds to the peak of this distribution; hence, we ensure that all initial conditions generated have an energy lying within

10% of this maximum entropy value¹.

After the vortex imprinting step, the wavefunction is evolved further in imaginary time for $0.05 \omega_r^{-1}$ to establish the structure of the vortex cores. This can lead to the annihilation of vortices near the boundary, as well as vortex–antivortex pairs if they were imprinted very close together. The number of vortices at the start of the real-time evolution is therefore $N_v \approx 113$.

We solve the GPE using our fourth-order split-step Fourier algorithm (Sec. 4.2.2) using a 1024×1024 spatial grid with spacing $\Delta x \approx 0.05 a_{\text{osc}}$ (approximately 0.65 condensate healing lengths) unless otherwise stated. The locations of the vortices in the system are detected at predetermined time intervals using the method outlined in Sec. 4.5.1. Vortices are only measured in the region $|\mathbf{r}| < 0.9R_0$ in order to avoid detection of ghost vortices [350] in the low density region of the traps with lower α values.

7.3 Results

7.3.1 Macroscopic dynamical behaviour

We first compare the results of decaying turbulence in the two traps discussed in the literature: a harmonic trap ($\alpha = 2$) and a uniform trap with steep walls ($\alpha = 100$), which has constant density to within ~ 5 healing lengths of the boundary. For each simulation, we monitor the number of vortices $N_v(t)$, which decreases over time due to vortex annihilation events. We also measure the dipole moment $d(t)$ of the vortex distribution, defined as $d = |\mathbf{d}| = \left| \sum_i q_i \mathbf{r}_i \right|$, where \mathbf{r}_i is the position of the i th vortex, and $q_i = s_i \kappa = s_i \hbar / m$ is its charge. For the confined systems being studied here, it is convenient to scale d with the system size R_0 and the number of vortices N_v . If the vortices are randomly distributed, d will approach zero for large systems. A large d , on the other hand, signals the presence of two Onsager vortex clusters in our system.

Figure 7.1 shows the characteristic time evolution of the vortex distribution in the two traps, along with the respective dipole moments. In agreement with previous simulations and experiments [103, 340], we observe no significant vortex clustering in the $\alpha = 2$ harmonic trap. However, and also in agreement with previous 3D simulations [165], the uniform trap exhibits a strong tendency to form Onsager vortices, as indicated by the increasing dipole moment. Thus, we

1. The evaporative heating mechanism does not rely on starting with a specific vortex configuration—the initial condition simply determines how much heating is required to reach the clustered Onsager vortex states.

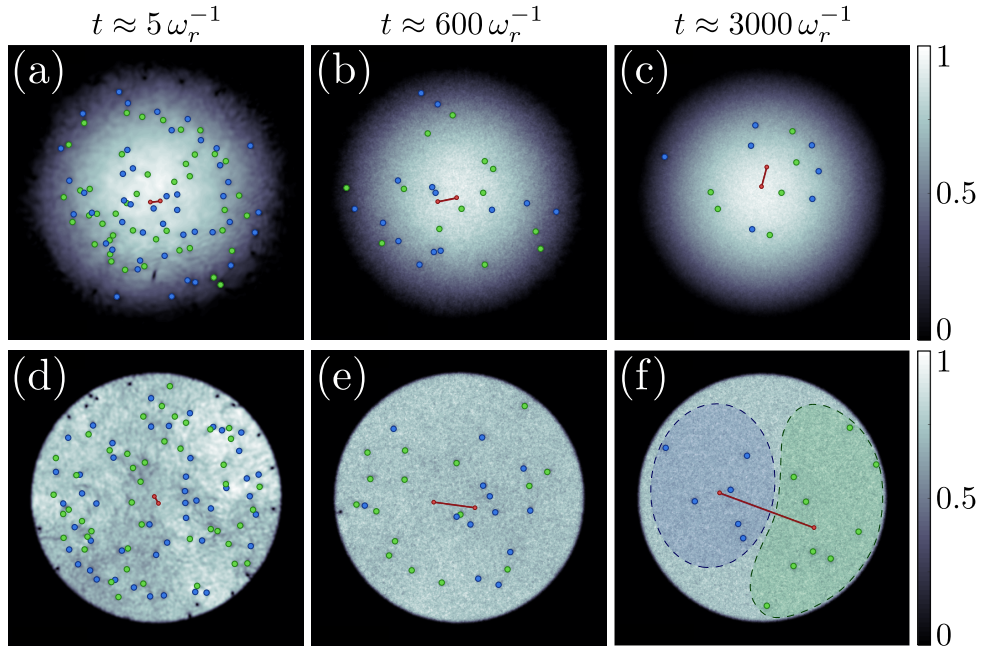


Figure 7.1: Comparison of the time evolution of the vortex configuration between the $\alpha = 2$ harmonic trap (a)–(c) and $\alpha = 100$ uniform trap (d)–(f). The greyscale value represents the superfluid density $|\psi|^2$, and the colorbars are normalised to the maximum density: $4.3 \times 10^{-3} a_{\text{osc}}^{-2}$ and $2.7 \times 10^{-3} a_{\text{osc}}^{-2}$ for the top and bottom rows, respectively. Vortices and antivortices are denoted by blue and green circles, respectively. The red line denotes the dipole moment of the vortex distribution. For full movies of the dynamics of each simulation, see the supplemental materials of Ref. [169].

conclude that the shape of the trapping potential has a strong influence on the vortex clustering behaviour, partially resolving the apparent contradiction in the existing literature.

7.3.2 Statistical mechanics interpretation

The spontaneous formation of Onsager vortices found in Ref. [165] was attributed to the evaporative heating mechanism of vortices outlined in Sec. 3.3.3. When enough heating has occurred for the mean incompressible kinetic energy per vortex, E_K^i/N_v , to increase beyond a critical value, a transition into the Onsager vortex state is possible² [165].

The absence of strong clustering in the harmonic trap could be due to (i) the rate of evaporative heating per annihilation event being too low, leading to inefficient

2. Here we treat the ‘transition’ as being the point at which the two vortex signs spatially separate into opposite sides of the trap; we will, however, refine this definition in Chapter 8.

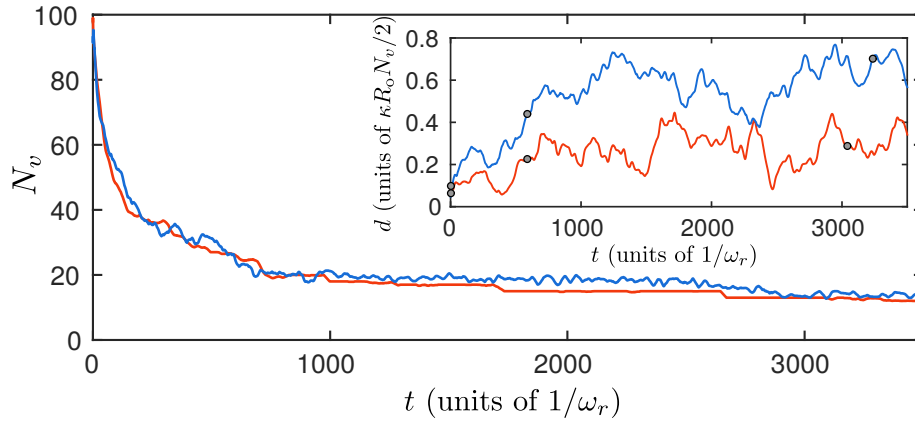


Figure 7.2: Comparison of the vortex number decay and dipole moment evolution (inset) for the harmonic (red) and uniform (blue) traps. The black circles in the inset correspond to the timeframes displayed in Fig. 7.1. The fluctuations in the vortex number are due to vortices crossing the counting radius of $0.9R_0$, in addition to occasional vortex–antivortex pair creation.

evaporative heating of the vortex gas, (ii) the critical energy per vortex for the Onsager vortex transition in a harmonic trap being out of reach despite the vortices being evaporatively heated, or (iii) the critical value of the dipole moment for harmonic traps being too small to allow a clear distinction to be made between the disordered and clustered vortex configurations. In the following we argue that the combined effect of (ii) and (iii) may explain the observed behaviour.

7.3.2.1 Dynamical statistical behaviour

Figure 7.2 shows little difference between the vortex number decay in the two traps. This suggests that the evaporation of vortices is only weakly affected by the details of the trapping potential. However, the dipole moment shows quantitatively different behaviour between the two traps, and indicates strongly enhanced clustering in the uniform trap. To better understand this difference, we construct a probability distribution of different vortex configurations generated by the dynamics in the space spanned by the dipole moment and energy per vortex number squared by taking the vortex configuration at each time step to correspond to an independently sampled microstate. We choose to normalise the energy to the square of the vortex number to cancel out the N_v^2 scaling which occurs in the high energy limit when the system tends towards a multi-quantum vortex dipole configuration [c.f. Eq. (3.10), with $\Gamma_1\Gamma_2 \sim N_v^2$]. Figure 7.3 shows the resulting histograms for each trap. In the harmonic trap (a), the dipole moment shows no significant variation over the measured range of energy per vortex number

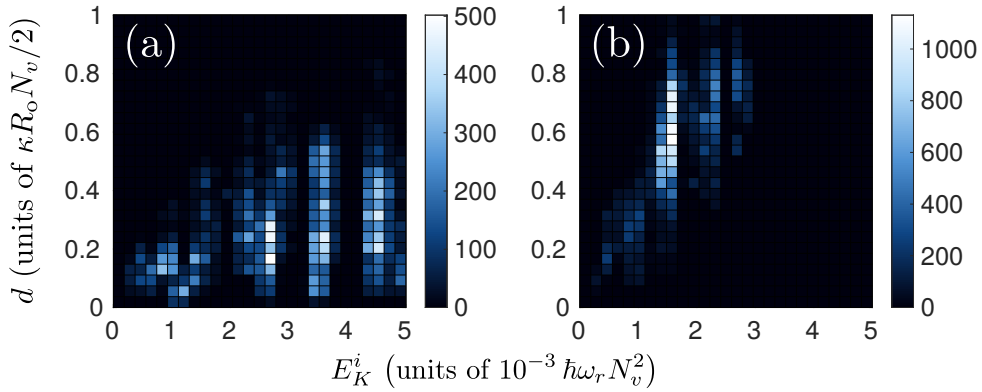


Figure 7.3: Comparison of statistical behaviour between (a) the harmonic trap and (b) the uniform trap. For each dynamical simulation, the dipole moment of the vortex configuration is shown as a function of the incompressible kinetic energy per vortex number squared. The initial state in each plot is the bottom-left corner, and the evaporative heating increases the energy per vortex number squared over time. The data appears as columns because each vortex annihilation increases the energy per vortex number squared by a discrete amount.

squared, and hence there is no evidence that the system crosses the Onsager vortex transition. Conversely, the trend in the uniform trap (b) is a clear indication that the evaporative heating is on average increasing the dipole moment, causing the system to evolve towards the Onsager vortex state.

7.3.2.2 Monte Carlo thermodynamics

In order to determine the statistical behaviour of the vortex gas beyond the range accessible via the dynamics, we implement a Markov Chain Monte Carlo (MCMC) algorithm for the two traps on a 256×256 grid. The algorithm is initialised by imprinting a random configuration of N_v vortices into the condensate ground state using the imaginary time propagation method described in Sec. 7.2.2. We set $N_v = 12$ (six vortices of each sign) to approximate the late time configurations of the dynamical simulations presented in Figs. 7.1 and 7.2. Keeping N_v fixed, each step in the algorithm shifts a single randomly chosen vortex in the configuration and calculates the value of a predetermined weighting function η . This new configuration is then either accepted or rejected based on the change in the weighting function. Here, we use a Boltzmann factor $\eta = \exp(-E_K^i/k_B T)$ as our weighting function, defining T to be the statistical temperature of the vortex gas (which in this case is negative, as discussed in Chapter 3). The equilibrium behaviour of the vortex gas is dictated by the choice of T ; hence, varying T allows us to ‘manually’ observe the transition to the Onsager vortex state. To characterise

the temperature dependence, we measure three observables: the incompressible kinetic energy per vortex number squared, the dipole moment and the specific heat, defined as $c_v = \text{var}(E_K^i)/(N_v T)^2$. The system is evolved for 110 000 Monte Carlo steps, the first 10 000 of which are disregarded as the initial condition is, in general, unrepresentative of the chosen temperature. The results for both traps are shown in Fig. 7.4. This MCMC data shows the transition from the disordered state to the Onsager vortex state in each trap, characterised most obviously by a maximum in the respective specific heat curves in Fig. 7.4(a). In addition, both the

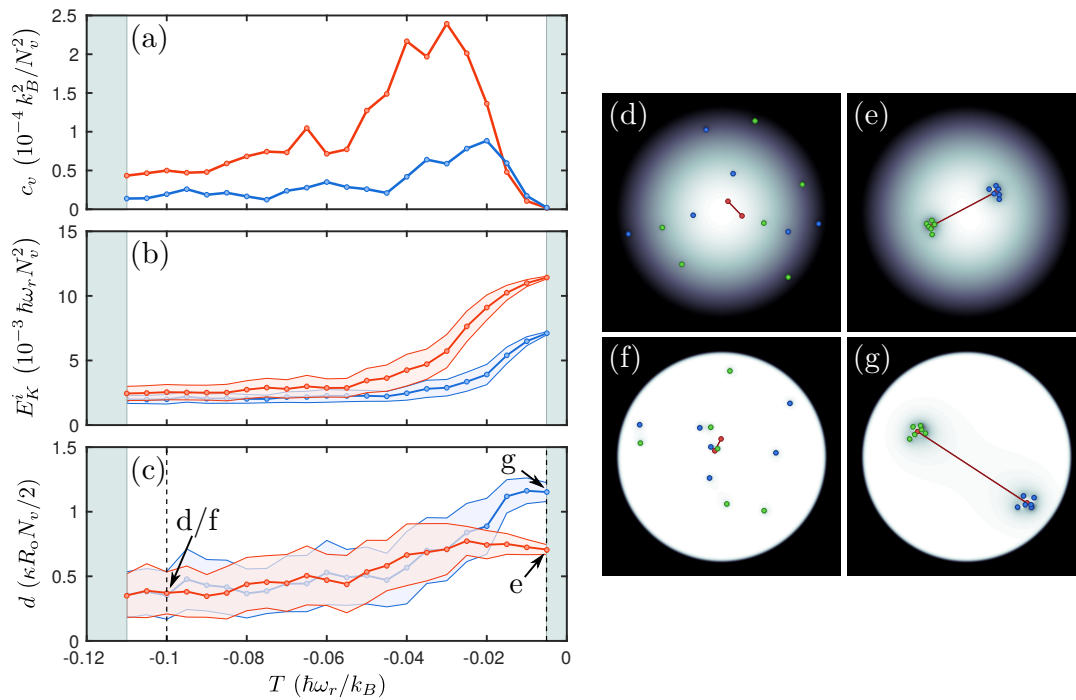


Figure 7.4: Statistical data obtained from 100 000-step Markov Chain Monte Carlo simulations for a harmonic (red) and a uniform (blue) trap for a total of 12 vortices with equal numbers of vortices and antivortices. The subfigures show (a) the specific heat, (b) the incompressible kinetic energy per vortex number squared, and (c) the dipole moment of the configuration, each plotted as a function of the statistical temperature. The shaded regions in (b) and (c) correspond to the standard deviation of each observable at a given temperature. The maximum in the specific heat indicates the transition to the Onsager vortex state in each trap, and is accompanied by an increase in both the energy per vortex number squared and the dipole moment. Frames (d) & (e) and (f) & (g) show typical vortex configurations at the temperature extremes in the harmonic and uniform traps, respectively, with labelling as in Fig. 7.1. The temperatures shown in these frames are indicated in (c) with vertical dashed lines.

energy per vortex number squared [Fig. 7.4(b)] and dipole moment [Fig. 7.4(c)] begin to rapidly climb around this critical temperature, signalling the formation of vortex clusters. For a uniform system with superfluid density ρ_s , the critical temperature is predicted to be $T_{\text{EBC}} = -\pi N_v \rho_s \hbar^2 / 4m^2 k_B \approx -0.019 \hbar \omega_r / k_B$ for a neutral vortex gas (see Sec. 3.2.2), which is in good agreement with our data. In a harmonically trapped system, Fig. 7.4 shows that T_{EBC} is shifted towards lower temperatures compared to the uniform system. In Chapter 8, we investigate the extreme negative temperature region beyond this critical point, and observe the *condensation* of vortices which takes place.

The key differences between the two traps are evident in Fig. 7.4. Figure 7.4(c) shows that the dipole moment climbs to a significantly higher value at the highest temperatures in the uniform trap compared to the harmonic trap—the respective vortex configurations are displayed in frames (e) and (g). In fact, the dipole moment shows only a weak temperature dependence in the harmonic trap, the most marked effect being a decrease in its variance at high temperatures. This suggests that, even if the harmonically trapped system transitions to the Onsager state, the resulting dipole moment would remain relatively small when compared to the steeper traps. Figure 7.4(b) also shows that the energy per vortex number squared required to cross the transition is significantly higher in the harmonic trap. This provides further support for the absence of clustering in the GPE dynamics in the harmonic trap, as the evaporative heating does not supply enough energy to drive the system to these temperatures.

7.3.2.3 Maximum achievable dipole moment

We can predict numerically the maximal separation of the two Onsager vortex clusters in a given system by calculating the energy of a vortex dipole as a function of the separation between the vortex and the antivortex. This yields further insight as to why the two traps show different clustering behaviour. In an infinite system, increasing the dipole separation will logarithmically increase the energy of the Onsager dipole without bound. However, for a bounded system, there exists a separation which maximises the energy. For a harmonic trap, this maximum energy configuration also corresponds to a stationary state [127, 136, 142, 332]. The dipole energy landscapes obtained for various trap steepnesses are presented in Fig. 7.5, showing that the energy-maximising separation increases as a function of the steepness. This result explains why the MCMC dipole moments in Fig. 7.4(c) asymptote to different values in the high temperature limit, as the two systems reach their highest energy at differing cluster separations. In addition to various

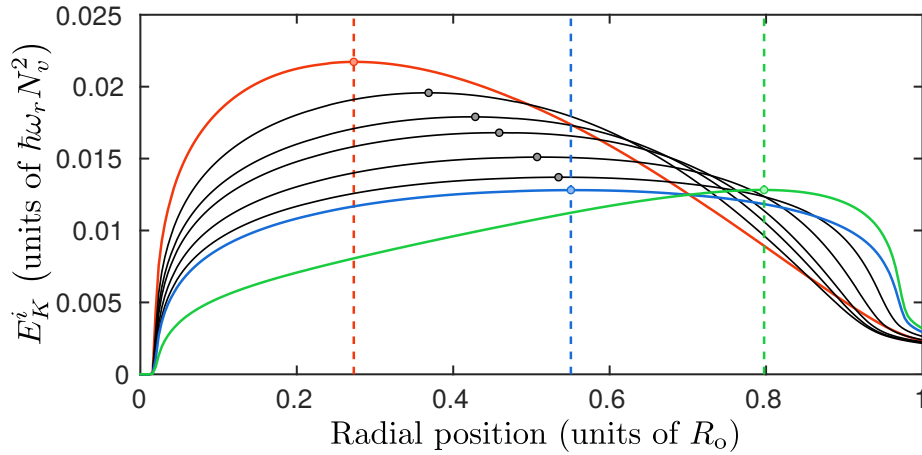


Figure 7.5: Incompressible kinetic energies of a vortex–antivortex pair for a range of power-law traps computed using the GPE. The pair is placed symmetrically in the trap and both vortices are an equal radial distance from the center. In order of peak location from left to right, the power-law exponents are $\alpha = 2$ (red), $\alpha = \{4, 6, 8, 14, 30\}$ (thin black lines) and $\alpha = 100$ (blue). In addition, the dipole energy for an inverted trap (as described in the main text) is shown in light green. The maximal separation is indicated on each curve with a circle, and is emphasised further on the two extreme power-law traps, as well as the inverted trap (described in the text), with a vertical dashed line.

power-law traps, Fig. 7.5 shows the dipole energy in an ‘inverted’ trap. This trap consists of a steep wall ($\alpha = 100$) with an additional repulsive Gaussian potential of width $R_o/3$ in the centre which pushes the condensate density radially outwards. In this configuration, the energy-maximising separation of a vortex dipole increases significantly, suggesting that an Onsager state in this trap should have an even greater dipole moment than such a state in the $\alpha = 100$ trap. We have confirmed this prediction with a dynamical GPE simulation (available in the supplemental materials of Ref. [169]).

7.3.3 Vortex annihilation is a many-vortex process

The microscopic underpinning of the evaporative heating mechanism of vortices is vortex–antivortex annihilation [165]. Scalar Bose–Einstein condensates with quantised vortices have two types of low-lying excitations—Bogoliubov phonons and vortex waves [333, 351, 352]. Such modes can resonate, mediating vortex–sound interactions [205, 206]. In principle such vortex–phonon interactions could cause vortex–antivortex pairs to annihilate via soundwave emission, which would account for the conservation of energy and momentum. However, for a single

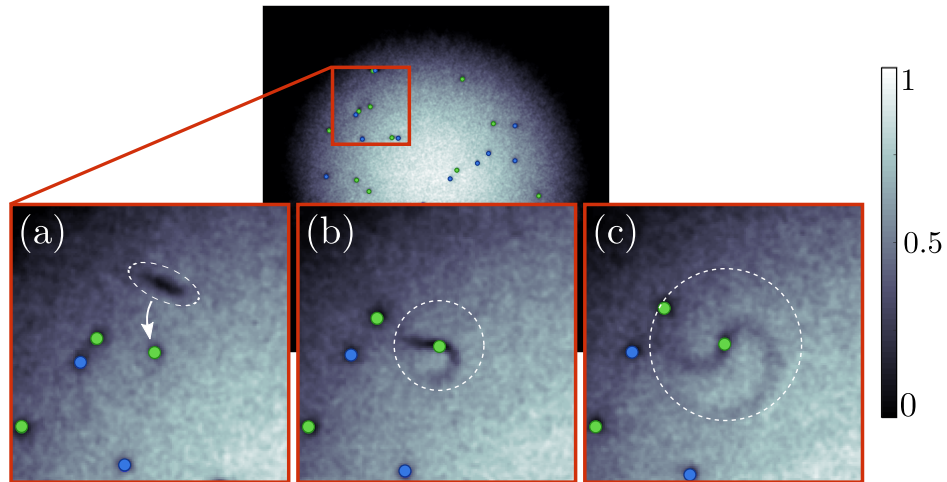


Figure 7.6: A vortexonium state (formed from a vortex–antivortex pair) highlighted in (a) with a dashed oval colliding with an antivortex and dissipating into fluid soundwaves which disperse radially, indicated in (b) and (c) with dashed circles. The vortices and colorbar are labelled as per Fig. 7.1. A movie of this event is available in the supplement of Ref. [169].

vortex–antivortex pair this does not occur, as has been supported experimentally [102] and shown theoretically [353]. If such vortex–antivortex pair annihilations are forbidden, this raises the question of how the vortex number can decay over time as observed both in the simulations and experiments [103, 155].

The answer must be that vortex–antivortex annihilation is a many-vortex process. Figure 7.6 shows a three-vortex process whereby a vortex–antivortex pair has formed a neutral *vortexonium* state (a rarefaction pulse also known as a Jones–Roberts soliton [207]), in which the individual vortex phase singularities are no longer discernible yet the excitation retains its identity as a spatially localised bound state. This excitation is reminiscent of positronium—a neutral bound state of an electron and a positron. The vortexonium, which is identifiable by a phase step, travels close to the speed of sound until it eventually scatters off an additional vortex or antivortex, as shown in Fig. 7.6(b) and (c). This decay process irreversibly disperses the energy and momentum of the vortexonium into sound waves [354, 355]. Until this secondary process occurs, the vortexonium can also re-form as a vortex–antivortex pair, an event which frequently occurs when a vortexonium state travels into the low density region near the boundary of the trap. The formation of vortexonium as a precursor to the vortex–antivortex annihilation process in 2D BECs has been discussed previously [103, 340, 356, 357]. Here, we identify the three-vortex collision to be an essential part of the annihilation process

in 2D superfluid turbulence.

The question remains how these vortexonium states form to begin with. In a uniform system free from dissipation, an isolated vortex–antivortex pair will travel with constant velocity and inter-vortex separation. Therefore, some mechanism other than sound induced interaction must be responsible for reducing the pair’s separation and forming vortexonium. In our simulations, we observe two ways this bound state can form. Firstly, a vortex–antivortex pair travelling towards a higher density region will reduce its separation in order to satisfy energy conservation, often forming a vortexonium state. However, this process only occurs in traps with soft walls, where the density variation is significant. The second process we observe is the shrinking of a vortex–antivortex pair via a long-range interaction with a third vortex. By giving up some of its energy to this catalyst vortex, the pair can reduce their separation, ultimately resulting in a vortex–antivortex fusion event and the formation of a vortexonium state. We note that this latter process is ubiquitous in all traps studied. However, in the presence of dissipation, both the formation and annihilation of vortexonium would be possible without additional interactions, as the loss of energy would gradually drive vortex dipoles closer together regardless.

Combining these observations, we obtain a complete picture of the vortex–antivortex annihilation process. Figure 7.7 depicts the process as a Feynman diagram, showing how four vortices are involved in the annihilation. Movie S4 in the supplemental materials of Ref. [169] shows one such four-vortex process. In the first stage, a vortex–antivortex pair interacts with a catalyst vortex to produce a

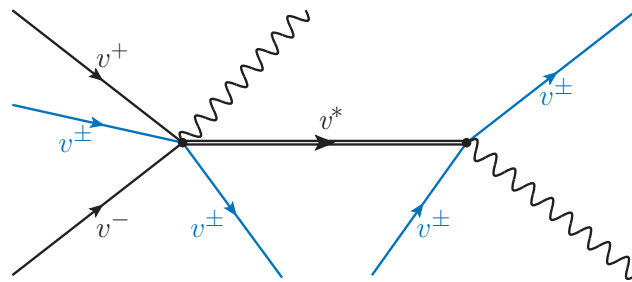


Figure 7.7: Feynman diagram depicting the entire vortex–antivortex annihilation process observed, with time flowing from left to right. The straight lines represent vortices (v^+) and antivortices (v^-), the double line represents vortexonium (v^*), and the wavy lines denote the sound waves emitted at each vertex (the magnitude of the second burst of sound is far greater than the first). The blue lines indicate participating catalyst vortices, which are not annihilated during the process.

vortexonium state, and in the second stage, the vortexonium scatters off a catalyst vortex, leading to the ultimate destruction of the vortex–antivortex pair and the emission of sound. The catalysts can be any vortex or antivortex in the system.

7.3.4 Rate equation for evaporative heating of vortices

Attempts have previously been made to fit a universal law to the vortex number decay [103, 160, 340, 358]. Kwon *et al.* [103] proposed a phenomenological model of the form $dN_v/dt = -\Gamma_1 N_v - \Gamma_2 N_v^2$, comprised of a linear term to model vortex drift out of the condensate and a nonlinear term to account for vortex–antivortex annihilation, where the Γ_1 and Γ_2 are the one-body and two-body decay constants, respectively.

We find that, due to the zero temperature of the GPE simulations, this equation does not provide an adequate fit to our vortex number decay curves. Instead, for $t \gtrsim 30 \omega_r^{-1}$, the vortex number decay is well described by a power law of the form $N_v(t) \propto (\omega_r t)^{-1/3}$ in all traps. This is evident in Fig. 7.8, which shows the number decay in a harmonic trap averaged over five simulations at 512×512 resolution. This power law was also observed by Schole *et al.* [160], who further suggested that the vortex number rate equation should have the form $dN_v/dt \sim -N_v^4$. This would reflect the importance of a four-body loss process at zero temperature, in contrast to the one- and two-body loss observed in Kwon *et al.*'s experiments [103]. The four-vortex annihilation events discussed in Sec. 7.3.3 are consistent with this four-body loss mechanism.

To study the effect of the thermal cloud, we model non-zero condensate temperatures using a damped Gross–Pitaevskii equation [359]:

$$(i - \gamma)\hbar \frac{\partial}{\partial t} \psi(\mathbf{r}, t) = \left[\frac{-\hbar^2}{2m} \nabla^2 + V_{\text{trap}}(\mathbf{r}) + g_{2D} |\psi(\mathbf{r}, t)|^2 + i\gamma\mu \right] \psi(\mathbf{r}, t), \quad (7.2)$$

where γ is the temperature dependent dimensionless damping parameter, and μ is the chemical potential. We propose a general rate equation for vortex loss at all temperatures:

$$\frac{dN_v}{dt} = -\Gamma_1 N_v - \Gamma_2 N_v^2 - \Gamma_3 N_v^3 - \Gamma_4 N_v^4 - \dots, \quad (7.3)$$

where Γ_n is the decay constant corresponding to a particular n -body loss mechanism. This model combines the one- and two-body loss processes observed in experiments [103] with the higher order three- and four-vortex loss processes observed in our zero temperature simulations. Strictly, a three-vortex decay process is not possible since it would violate the vortex charge conservation law. We instead interpret

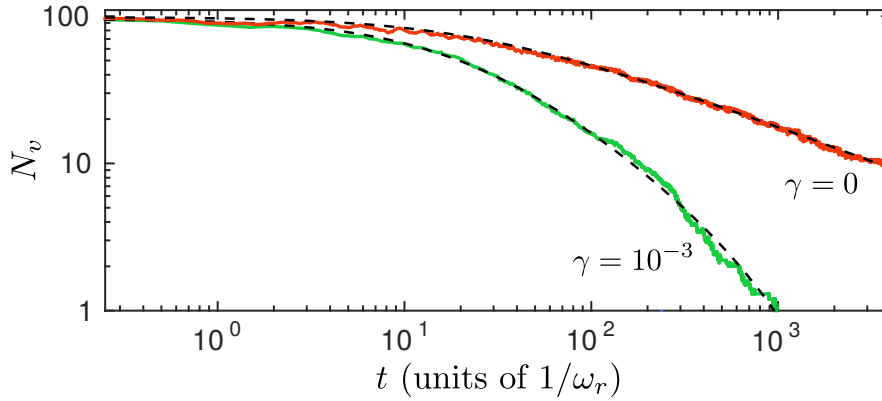


Figure 7.8: Ensemble averaged vortex number decay curves for harmonically trapped systems at zero temperature ($\gamma = 0$, solid red/dark line) and non-zero temperature ($\gamma = 10^{-3}$, solid green/light line). The fits for each curve to Eq. (7.3) are shown as black dashed lines, with $\Gamma_1 = 0.14 \text{ s}^{-1}$, $\Gamma_2 = 0.044 \text{ s}^{-1}$, $\Gamma_3 = \Gamma_4 = 0$ for the non-zero temperature case, and $\Gamma_1 = \Gamma_2 = 0$, $\Gamma_3 = 1.2 \times 10^{-4} \text{ s}^{-1}$, $\Gamma_4 = 8.1 \times 10^{-7} \text{ s}^{-1}$ for the zero temperature case.

the three-body term as the loss of two vortices arising from the collision of three (i.e. a vortexonium colliding with a catalyst vortex, as discussed in Sec. 7.3.3).

We have chosen the damping parameter $\gamma = 10^{-3}$ to study the vortex number decay behaviour at non-zero temperature. Figure 7.8 shows the decay curves for zero temperature ($\gamma = 0$) and non-zero temperature ($\gamma = 10^{-3}$), each averaged over five simulations in a harmonic trap using a 512×512 numerical grid. We model both cases using Eq. (7.3). For the $\gamma = 10^{-3}$ case, we find that the decay is best described by a one- and two-body model, with $\Gamma_1 = 0.14 \text{ s}^{-1}$, $\Gamma_2 = 0.044 \text{ s}^{-1}$ and $\Gamma_3 = \Gamma_4 = 0$. These values are in good agreement with those found by Kwon *et al.* [103]. By contrast, the $\gamma = 0$ case is best described by a three- and four-body decay model with decay constants $\Gamma_1 = \Gamma_2 = 0$, $\Gamma_3 = 1.2 \times 10^{-4} \text{ s}^{-1}$ and $\Gamma_4 = 8.1 \times 10^{-7} \text{ s}^{-1}$. We conclude that the three- and four-body vortex loss processes are characteristic of zero temperature systems, and that one- and two-body events become dominant at sufficiently high temperature.

The appropriate vortex decay law is still a topic of discussion in the literature, and the precise form is not universally agreed upon. Recently, it has been suggested that an n -body decay process should actually give rise to scaling of the form $dN_v/dt \sim -N_v^{n+1/2}$ due to the vortex-density dependent velocity of the vortices, which introduces an additional factor of $N_v^{1/2}$ [171, 358]. We find that the data in Fig. 7.8 are consistent with Eq. (7.3), with or without this additional factor of $N_v^{1/2}$.

7.3.5 Interaction between vortices and boundaries

In our harmonic trap simulations, the multi-vortex collision process described in Sec. 7.3.3 is the only mechanism of vortex annihilation, excluding a small proportion of vortices which drift out of the condensate. By contrast, the presence of a hard boundary in the steeper traps allows for a number of additional phenomena relating to the dynamics and decay of vortex–antivortex pairs. In particular, we observe three distinct vortex–boundary collision processes, two of which give rise to additional vortex decay channels.

When a single vortex is near the boundary, it will pair up with its image vortex of opposite sign beyond the wall and travel around the circumference of the trap at high velocity. If the separation reduces sufficiently, this vortex–image pair can form a vortexonium with a phase step along the tangent of the wall. As this bound state travels around the boundary, it can either unbind and reform the vortex–image pair, or it can annihilate in much the same way as a vortexonium in the fluid

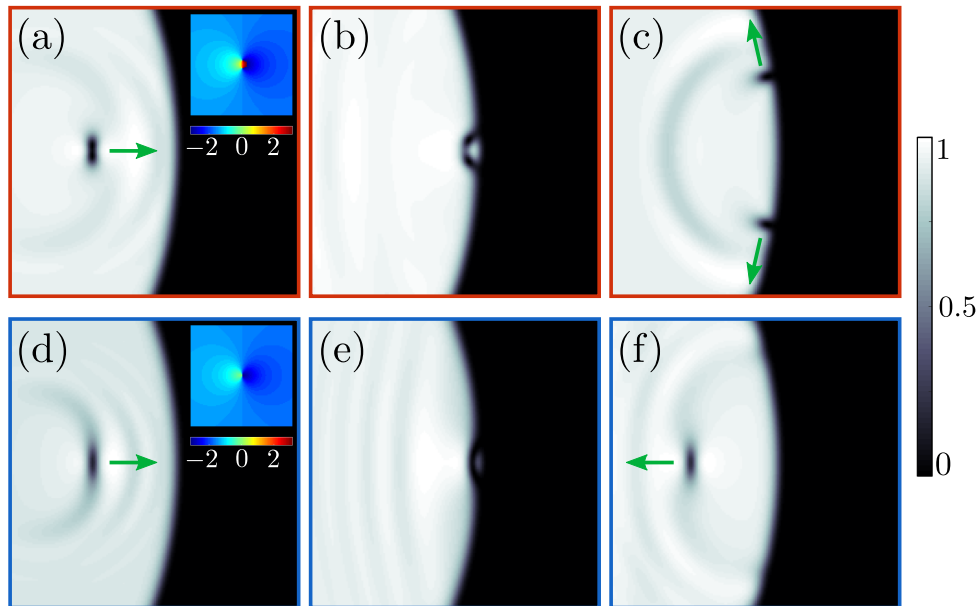


Figure 7.9: (a)–(c) Unbinding of a vortex pair and (d)–(f) reflection of a vortexonium state at the boundary in the uniform trap. The green arrows show the direction each excitation is travelling. The insets in (a) and (d) show the phase of the wavefunction in the corresponding frame—the two singularities are visible in (a), while only a phase step remains in (d). The soundwave produced by each collision event propagates outwards in (c) and (f). The colorbar is normalised to the maximum condensate density, as in Fig. 7.1. Movies S6 and S7 in the supplemental materials of Ref. [169] show each event in full.

bulk—by colliding with another vortex.

We observe a similar process involving the collision of a vortex–antivortex pair with the boundary. When the pair collides with the wall, it unbinds into two separate vortex–image pairs, which then travel around the boundary in opposite directions, as shown in Fig. 7.9(a)–(c). If travelling at high enough velocity, one or both of these new vortex–image pairs can form vortexonium excitations, which can then decay as described above. Often, the collision will be violent enough to cause one of the vortices in the initial pair to annihilate immediately, while the other one is left to travel around the boundary.

If the initial conditions are such that the vortex–antivortex pair which is incident on the boundary has already fused and formed a vortexonium excitation, the collision dynamics become markedly different. Figure 7.9(d)–(f) shows that the vortexonium will not separate at the boundary, but rather reflect from it, reversing its propagation direction. This effectively changes the sign of the vortices in the bound state, and can be understood as an exchange of locations with the image vortices beyond the boundary. Effectively, the image vortexonium travels into the condensate, while the real vortexonium leaves.

Remarkably, for the steepest potentials, the proportion of vortices annihilated at the boundary (i.e. via one of the first two processes described above) accounts for approximately half of the total vortex loss. Despite this clear spatial dependence of annihilation behaviour which is absent in the harmonic trap, the vortex number decays at the same rate (see Fig. 7.2) and the efficiency of the evaporative heating appears to be unaffected. It seems plausible that boundary annihilations would increase evaporative heating efficiency, since less incompressible kinetic energy should be lost per annihilation (as the energy of a vortex in the low density close to the system’s boundary is less than in the fluid bulk), leaving more for the remaining vortices. However, we have not been able to quantify this effect.

7.3.6 Onsager vortex formation as a function of trap steepness

We repeated our Gross–Pitaevskii simulations of decaying turbulence for a number of trap steepnesses ranging between the two extremes examined in Secs. 7.3.1 and 7.3.2 by varying the value of α in Eq. (7.1). Five GPE simulations were performed in each of the chosen trap geometries using a 512×512 grid, and the dipole moment curves obtained for each steepness were combined by taking averages at each point in time. These averaged dipole moment curves are shown in Fig. 7.10. On average, a steeper trap produces a larger dipole moment and thus

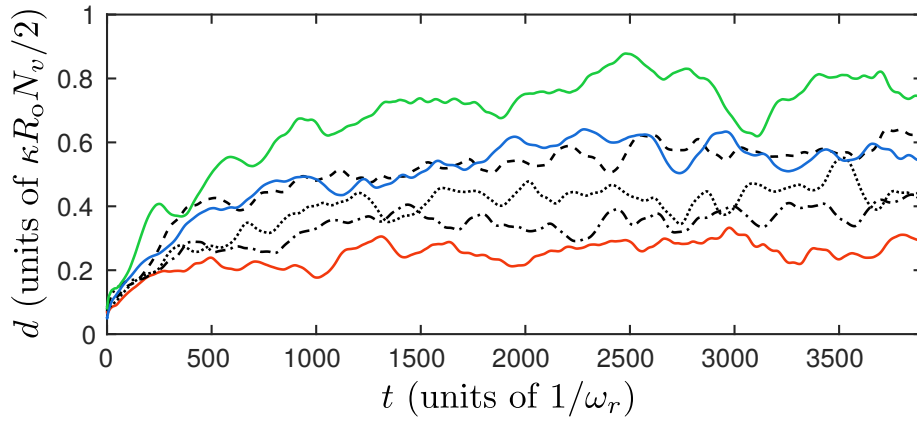


Figure 7.10: Comparison of dipole moment evolution in traps of varying steepness, with each curve averaged over five simulations. The trap steepnesses are (from bottom to top) $\alpha = 2$ (solid red line), $\alpha = 8$ (dot-dashed black line), $\alpha = 14$ (dotted black line), $\alpha = 30$ (dashed black line), $\alpha = 100$ (solid blue line) and an $\alpha = 100$ inverted trap (solid green line).

a greater separation of vortex charge. As predicted from energy considerations in Sec. 7.3.2, an inverted trap produces even stronger clustering than any of the power-law traps. For the power-law traps, it appears that the clustering behaviour saturates beyond a steepness of $\alpha \approx 30$. The dipole moments in Fig. 7.10 should be compared with their predicted maximum values shown in Fig. 7.5.

7.4 Summary

We have studied decaying two-dimensional quantum turbulence using the Gross–Pitaevskii model. We have considered Bose–Einstein condensates confined in generic power-law traps which, in particular, enables a comparison to be made between vortex dynamics in harmonically trapped condensates and in condensates confined in (nearly) uniform density disk traps. When an initially disordered vortex configuration is left to decay, we find that in uniform traps the vortices and antivortices arrange into Onsager vortex clusters due to the evaporative heating mechanism posited in Ref. [165]. However, when a harmonic trapping potential is used, the emergence of Onsager vortices is not obvious—a finding which agrees with experimental observations [103]. To verify that these results are not specific to our randomly sampled initial vortex configurations, we repeated our simulations in both traps using a repulsive Gaussian laser potential to stir the fluid and produce the initial state vortex configuration, as in Ref. [340]. Considering both lateral and circular stirring motions, the qualitative vortex clustering behaviour in the

harmonic and uniform traps was unaffected. This result was expected since a turbulent system should rapidly forget its history, washing out any initial state dependence.

We also performed Monte Carlo calculations to study equilibrium vortex configurations in harmonic and uniform traps. These calculations showed that the transition from disordered vortex configurations to the clustered Onsager vortex states exist also in harmonic traps but the resulting vortex dipole moment is significantly smaller than for uniform traps, which partially explains why the Onsager vortex clusters have not been observed to emerge in harmonically trapped Bose–Einstein condensates.

To obtain an improved understanding of the vortex evaporative heating mechanism [165], we carefully tracked the vortex–antivortex annihilation events in the simulations. At zero temperature, we found that vortex–antivortex pair annihilation in these quantum turbulent systems is essentially a three- or four-body loss process involving up to two catalyst vortices in addition to the annihilating pair. First, a vortex–antivortex pair interacts with a catalyst vortex forming a *vortexonium* bound state, which then has to interact again with a catalyst vortex for it to irreversibly decay into phonons. Indeed, it has been shown both experimentally [102] and theoretically [353] that an isolated vortex–antivortex pair is resistant to sound induced decay. By adding dissipation to the Gross-Pitaevskii model, we simulated a non-zero temperature system and found that the four-body annihilation mechanism becomes less important, and instead one- and two-body annihilation events begin to dominate, in agreement with experimental observations [103].

By considering power-law traps of varying steepnesses, we found that the vortex clustering tendency becomes stronger as the trap steepness is increased. Finally, we found that a locally and weakly anti-trapping potential [360–362] should provide the most promising route to experimental observation of the emergence of the Onsager vortices.

8

VORTEX CONDENSATION

In this chapter, we investigate the equilibrium properties of a two-dimensional point-vortex gas in the high energy limit. We introduce a parallel between the 2D configuration of vortices and a 1D gas of particles. Using this equivalence, we identify a process of *condensation* of Onsager vortices in the high energy limit, which we quantify using an observable which plays the role of a condensate fraction, in analogy to a Bose–Einstein condensate. Using our definition, we are able to draw a sharp distinction between the clustering of vortices observed in the previous chapter and their condensation—a difference that becomes clearest when only one sign of vortices is present. We determine that, in the dynamical simulations of decaying 2D quantum turbulence presented in Chapter 7, the transition to an Onsager vortex condensate does not occur, despite the clear formation of large scale clusters. These results comprise Ref. [173].

8.1 Motivation

The inverse energy cascade in two-dimensional classical turbulence, discussed in Chapter 3, dynamically transports incompressible kinetic energy to the largest available spatial scales. Kraichnan [220] conjectured that, as a result of this process, energy should begin to accumulate in the lowest available momentum states, assuming the absence of dissipation at large scales. He referred to this pile up of energy as a *condensate*, stating explicitly that “*the phenomenon is analogous to the Einstein–Bose condensation of a finite two-dimensional quantum gas*” [220]. According to this picture, the condensate should correspond to the highest accessible energy states of the vortices, a suggestion that is concurrent with the negative temperature vortex clusters identified by Onsager [78].

We recall from Sec. 3.2.2.1 that, in a neutral system with N_{tot} vortices in total, the condensation of Onsager vortices occurs at a critical negative temperature $T_{\text{EBC}} = -\alpha N_{\text{tot}}/4$ [165, 222, 239], where $\alpha = \rho_s \kappa^2 / 4\pi k_B = T_{\text{PC}}$ is the critical

positive temperature for the Hauge–Hemmer pair-collapse transition [246], which in the case of non-zero vortex core size becomes renormalised to the Berezinskii–Kosterlitz–Thouless (BKT) [26–28] critical temperature $T_{\text{BKT}} = T_{\text{PC}}/2$. Here, ρ_s is the (super)fluid density. Inspired by Kraichnan’s insight, we here refer to the critical temperature of condensation of Onsager vortices with the acronym EBC. We note that, in non-neutral systems there are two condensation temperatures with the majority species of vortices condensing first at $T_{\text{maj}} = -\alpha N_{\text{maj}}/2$.

In addition to visual inspection, the presence of Onsager vortices in two-dimensional quantum turbulence has been associated with indicators such as the vortex dipole moment used in the previous chapter [165, 169], vortex clustering measures [155, 162, 277, 278], or a peak in the power spectral density of incompressible kinetic energy [164, 165, 363]. However, a measurable that would distinguish between vortex clustering and their condensation has been lacking. Here we use a *vortex–particle duality* to define a condensate fraction that enables quantitative measurements of condensation of Onsager vortices in these two-dimensional systems. This is made possible by using the vortex classification algorithm described in Sec. 4.5.2. We find that the condensate fraction exhibits universal behavior independent of the number of vortices in the bounded circular system and that strong vortex clustering is prevalent already at temperatures far from the transition. Such vortex clustering is a precursor to the condensation of Onsager vortices and is reminiscent of the quasi-condensation that precedes the superfluid phase transitions in low-dimensional quantum gas systems [29, 30, 364, 365].

In the next section, we introduce the link between 2D vortices and 1D particles, upon which the rest of the chapter is based. In Secs. 8.3 and 8.4, we introduce an effective Hamiltonian to describe a gas of point-vortices. Following this, we define the vortex condensate fraction in Sec. 8.5, and then apply it to Monte Carlo simulation data in Secs. 8.6 and 8.7, demonstrating that vortex clustering and condensation are not equivalent. We then show in Sec. 8.8 that condensation does not occur in our dynamical simulations from Chapter 7. Finally, we summarise our findings in Sec. 8.9.

8.2 Vortex–particle duality

We consider N_{tot} singly quantised point-like vortices with a hard core of radius ξ and equal numbers of clockwise and anticlockwise circulations confined in a circular disk of radius R_0 , unless stated otherwise. The Hamiltonian describing

our system is [165, 237]:

$$\begin{aligned}
 H = & \alpha k_B \sum_j s_j^2 \log(1 - r_j^2) - \alpha k_B \sum_{i < j} s_i s_j \log(r_{ij}^2) \\
 & + \alpha k_B \sum_{i < j} s_i s_j \log(1 - 2x_i x_j - 2y_i y_j + r_i^2 r_j^2), \quad (8.1)
 \end{aligned}$$

where $r_j^2 = x_j^2 + y_j^2$, and x_j and y_j are the dimensionless Cartesian coordinates of the j th vortex measured in units of the system radius R_o and $s_j = \pm 1$ determines the circulation direction of the j th vortex. Note that we have expressed the Hamiltonian in a slightly different form to Eq. (3.13), since we have now ensured that the Hamiltonian has units of energy.

The dynamics of the point-like vortices are determined by the equations of motion [78]

$$h s_j \frac{\partial x_j}{\partial t} = \frac{\partial H}{\partial y_j} \quad \text{and} \quad h s_j \frac{\partial y_j}{\partial t} = -\frac{\partial H}{\partial x_j}, \quad (8.2)$$

which again take on a slightly different form to Eq. (3.11). To draw a closer correspondence with Hamiltonian mechanics, we may assign for each vortex a canonical coordinate $q_j = R_o x_j$ and momentum $p_j = -m_o \omega_o R_o y_j$, where m_o is the vortex mass [325] and ω_o is an angular frequency. Thus the set of vortex coordinates $\{x_j, y_j\}$ in the real space are mapped onto points in the phase space $\{q_j, p_j\}$ spanned by the canonical conjugate variables. In this Hamiltonian description the vortex particles move in one-dimensional real space tracing out orbits in the two-dimensional phase space, which is bounded by the circular wall of radius R_o . Equation (8.2) establishes the *vortex-particle duality*—that a vortex in a two-dimensional (2D) fluid may behave as a particle in a one-dimensional (1D) space. Hence, in contrast to Kraichnan's conjecture, we anticipate the condensation of Onsager vortices to be analogous to the Bose-Einstein condensation of a finite *one-dimensional* quantum gas. Interestingly, in the 2D fluid picture the vortex condensate corresponds to maximum kinetic energy states of the fluid whereas in the 1D dual picture the condensate corresponds to zero momentum state of the 1D vortex particles.

8.3 Ideal vortex gas approximation

By ignoring the vortex-vortex interactions we obtain an ideal-gas model of vortex particles. A Maclaurin series expansion of the single vortex term in Eq. (8.1) with

respect to r_j formally yields a one-dimensional harmonic oscillator Hamiltonian

$$H_0 = \alpha k_B \sum_j s_j^2 \log(1 - r_j^2) \approx -\frac{\rho_s \kappa^2}{2\pi} \frac{1}{m_0 \omega_0^2 R_0^2} \sum_j \left(\frac{p_j^2}{2m_0} + \frac{1}{2} m_0 \omega_0^2 q_j^2 \right) \quad (8.3)$$

with an inverted energy spectrum with respect to the canonical case. Within the harmonic approximation, a single vortex ν of this system will travel along a periodic phase space orbit $\{q_\nu, p_\nu\} = \{R_\nu \cos(\omega_\nu t), -m_0 \omega_0 R_\nu \sin(\omega_\nu t)\}$, with orbital angular frequency ω_ν and semi-axis R_ν .

The Einstein–Brillouin–Keller semiclassical quantisation rule [366]

$$\oint p_\nu dq_\nu = \left(n + \frac{k}{4} \right) h, \quad (8.4)$$

where n is the principal quantum number and k is the Keller–Maslov index then evaluates to

$$\int_0^T p_\nu dq_\nu = \int_0^{\frac{2\pi}{\omega_\nu}} \omega_\nu m_0 \omega_0 R_\nu^2 \sin^2(\omega_\nu t) dt = \pi m_0 \omega_0 R_\nu^2, \quad (8.5)$$

where we have integrated over one period, $T = 2\pi/\omega_\nu$, of the vortex orbit. The one-dimensional oscillatory motion has two classical turning points, $k = 2$, and therefore the quantisation rule, the combination of Eqs. (8.4) and (8.5), yields the energy spectrum $E_n = (n + \frac{1}{2})\hbar\omega_0 = \frac{1}{2}m_0\omega_0^2 R_\nu^2$. This implies a minimum semi-axis $\min(R_\nu) = \xi$ for the vortex trajectories and yields the zero-point energy $E_0 = \frac{1}{2}m_0\omega_0^2 \xi^2$. In correspondence with the Heisenberg uncertainly relation, $\Delta q \Delta p \gtrsim \hbar/2$, the zero-point energy carries the information that the area A of the phase space is quantised in units of $\hbar = m_0\omega_0 \xi^2$. This reflects the fact that it is not possible to localize the position of the vortex inside an area smaller than the vortex core.

8.4 Interacting vortex gas approximation

The velocity fields produced by the vortices give rise to strong and long-ranged vortex–vortex interactions such that the ideal-vortex approximation is strictly only valid for one vortex near the centre of the disk. However, the second term in Eq. (8.1) may be approximated as a mean-field potential by integrating out the spatial scales smaller than the inter-vortex spacing.

If a neutral superfluid is locally rotated at angular frequency Ω , and contains N_ν

vortices of the same sign, a vortex lattice is formed in equilibrium, and the vortex number density is given by

$$n_v = \frac{N_v}{\pi R^2} = \frac{m\Omega}{\pi\hbar}. \quad (8.6)$$

Hence, the superfluid velocity varies as $v(r) = \Omega r$, where r is the distance measured from the centre of such a rotating cluster of vortices. In contrast, for a high-winding number vortex with N_v circulation quanta, the superfluid velocity field outside the core is given by $v(r) = (\hbar/m)N_v/r$, which is the gradient of the condensate phase. In general, the velocity field is therefore

$$v(r) = \begin{cases} N_v \frac{\hbar}{m} \frac{r}{R_c^2} & r < R_c \\ N_v \frac{\hbar}{m} \frac{1}{r} & r > R_c, \end{cases} \quad (8.7)$$

which is a combination of solid body rotation and potential flow. The kinetic energy associated with such a flow field may therefore be approximated by a mean-field interaction

$$\begin{aligned} H_{\text{int}} &= -\alpha k_B \sum_{i<j} s_i s_j \log(r_{ij}^2) \\ &\approx \int_0^{2\pi} \int_0^{R_o} \frac{1}{2} \rho_s v^2(r) r \, dr \, d\theta \\ &= \pi \rho_s N_v^2 \frac{\hbar^2}{m^2} \left(\frac{1}{4} + \log\left(\frac{R}{R_c}\right) \right). \end{aligned} \quad (8.8)$$

The final term in the point-vortex Hamiltonian, Eq. (8.1), describes the remaining interaction with image vortices and yields an energy shift:

$$-\mu = \alpha k_B \sum_{i<j} s_i s_j \log(1 - 2x_i x_j - 2y_i y_j + r_i^2 r_j^2). \quad (8.9)$$

Combining Eqs. (8.3), (8.8), and (8.9), we thus arrive at the effective 1D vortex-particle Hamiltonian,

$$\begin{aligned} H_{\text{eff}} &= H_0 + H_{\text{int}} - \mu \\ &\approx -\frac{\rho_s \kappa^2}{2\pi} \left[\frac{1}{m_0 \omega_0^2 R_o^2} \sum_j \left(\frac{p_j^2}{2m_0} + \frac{1}{2} m_0 \omega_0^2 q_j^2 \right) \right. \\ &\quad \left. - \frac{1}{2} N_v^2 \left(\frac{1}{4} + \log\left(\frac{R}{R^*}\right) \right) \right] - \mu \end{aligned} \quad (8.10)$$

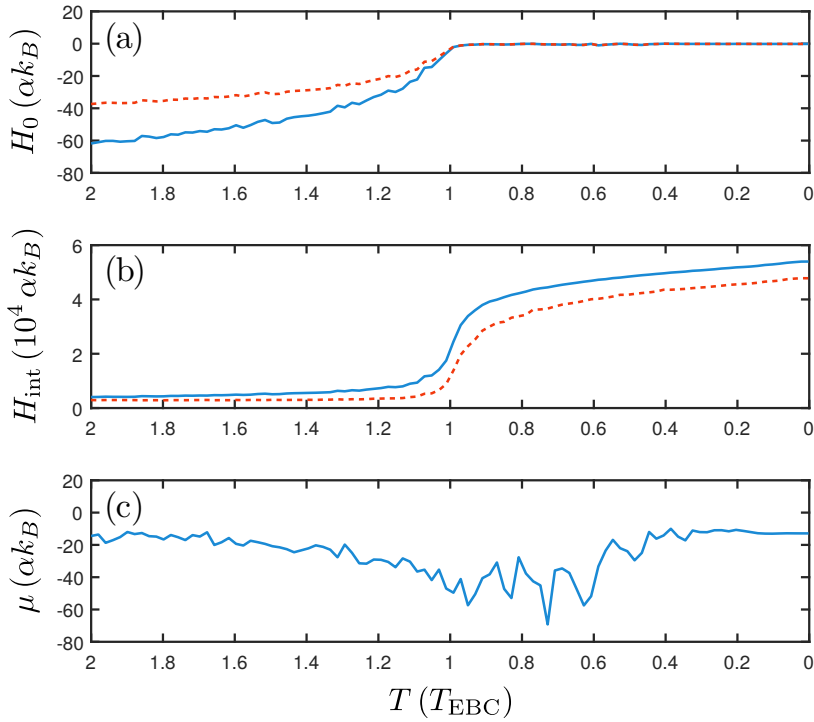


Figure 8.1: Contributions to the Hamiltonian for a system of $N_v = 100$ single species ($s = +1$) vortices in a circular, hard-walled trap. The three energy terms of Eq. (8.1) are shown as solid lines in panels (a)–(c), respectively, as functions of reduced temperature. The corresponding approximations, Eq. (8.3) and Eq. (8.8), are shown as dashed lines in (a) and (b), respectively. The values are obtained by taking the mean over 1000 uncorrelated equilibrium configurations at each chosen value of T . We remind the reader that $T_{\text{EBC}} = -\alpha N_v/4$, and $\alpha = \rho_s \kappa^2/4\pi k_B$.

that describes a system of one-dimensional strongly interacting harmonic oscillators.

Figure 8.1 shows the independent contributions of the three terms in the Hamiltonian, Eq. (8.1), for a system of 100 like-signed vortices as functions of reduced temperature. The details of this calculation are described in Sec. 8.7. For comparison, the energy contributions due to the harmonic oscillator and mean-field approximations, Eq. (8.3) and Eq. (8.8), respectively, are shown by dashed lines. The harmonic oscillator approximation, Eq. (8.3), is better at lower effective temperatures because the vortices clump close to the centre of the disk, as seen in Fig. 8.4(b)–(c). However, since the mean-field term, Eq. (8.8), is proportional to N_v^2 , it is overwhelmingly larger than the single-vortex terms, which are proportional to N_v . These results establish that the mean-field Hamiltonian Eq. (8.10) is a reasonable approximation for Eq. (8.1).

8.5 Fraction of condensed vortices

We anticipate condensation of Onsager vortices when the phase space density $n_v \lambda_v \gtrsim 1$. Here n_v is the mean vortex density and

$$\lambda_v = h/\langle p \rangle \sim 2\pi\xi^2/\langle R_v \rangle \quad (8.11)$$

is the thermal vortex de Broglie wavelength, which in the vortex dual is inversely proportional to the size of an average temperature-dependent vortex orbit in the phase space. For N^* vortices confined within length $2R^*$ the condensation criterion becomes

$$\pi N^* \xi^2 / \langle R_v \rangle R^* \sim 1, \quad (8.12)$$

which shows that condensation is expected when the vortices concentrate into a phase-space cluster with size of the order of $\sqrt{N^*} \xi$.

These considerations lead us to define the fraction of condensed vortices as the ratio, N_0/N , of N_0 vortices of a given sign in a single many-vortex cluster to the total number of vortices N of that same sign in the system. The highest density of vortices is found within clusters and by denoting N^* to be the number of vortices in the largest cluster and $A^0 = N^* m_0 \omega_0 \xi^2$ and A^* to be, respectively, the minimum possible phase space area occupied by the N^* vortices and the phase space area actually covered by them, we obtain

$$\frac{N_0}{N} = \frac{N^* A^0}{N A^*} = \frac{N^*}{N} \frac{\xi^2}{\langle r_{nn} \rangle^2}. \quad (8.13)$$

Thus the condensate fraction is the product of the largest cluster fraction N^*/N and the square of the ratio of single vortex core radius ξ to the mean radius $\langle r_{nn} \rangle$ of the effective area occupied by a vortex within the cluster, where r_{nn} is one half of the distance between nearest neighbour vortices. Although for single vortex species systems $N^*/N = 1$, in general, the system contains both vortices and antivortices and to measure $N^* < N$, clusters of like-signed vortices must first be identified by the vortex classification algorithm outlined in Sec. 4.5.2.

8.6 Two-species Monte Carlo results

To study the thermodynamics of the condensation of Onsager vortices, we have performed Monte Carlo calculations using a Metropolis algorithm to find the equilibrium vortex configurations as functions of temperature for systems with

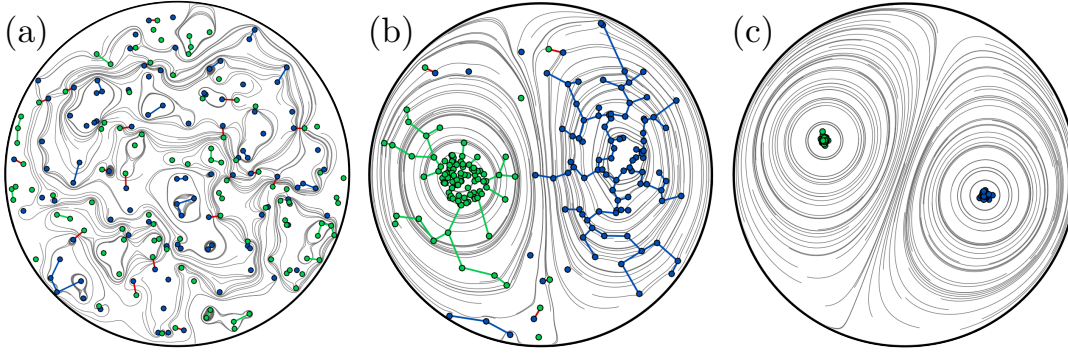


Figure 8.2: Representative neutral vortex configurations (a)–(c) at respective temperatures $T/T_{\text{EBC}} = \{10^6, 1.02, 0.78\}$, with $T_{\text{EBC}} = -0.25\alpha N_{\text{tot}}$ and $N_{\text{tot}} = 200$. Vortices in vortex and antivortex clusters are connected by blue and green lines, respectively, vortex–antivortex dipoles are connected by red lines and free vortices are marked by isolated filled circles. The streamlines illustrate the velocity field generated by the collection of vortices.

10, 20, 50, 100, 200, 300 and 400 vortices [165, 239]. A hard core diameter of $2\xi = 0.001 R_0$ was imposed on each vortex. The Monte Carlo samplings were performed for temperatures in the range $T \in (-\infty, -0)$, with 10^6 microstates at each temperature after an initial burn in of 10^6 steps. Out of the 10^6 microstates, 1000 uniformly spaced configurations were recorded and used for vortex classification analysis.

Figure 8.2 shows typical vortex configurations of disordered and clustered neutral vortex states of $N_{\text{tot}} = 200$ vortices obtained from the Monte Carlo calculations at different temperatures. The same-sign clusters, dipoles and free vortices are identified using the vortex classification algorithm described in Sec. 4.5.2 and the velocity field streamlines are included to visualise the superflow around the vortices. Figure 8.2(a) shows a vortex configuration at a high negative temperature, $T = 10^6 T_{\text{EBC}}$, revealing a fairly disordered configuration of vortices with an abundance of vortex dipoles and small clusters. Figure 8.2(b) shows a vortex configuration at $T = 1.02 T_{\text{EBC}}$ just above the critical temperature. Note how nearly all the vortices have already clustered into two Onsager vortices although the condensate fraction remains zero. This clearly shows that vortex clustering precedes the condensation and that the presence of Onsager vortices is not a sufficient criterion for the existence of a condensate of Onsager vortices in the system. Figure 8.2(c) shows Onsager vortices at temperature $T = 0.78 T_{\text{EBC}}$ where the system has a condensate fraction of ≈ 0.1 . The qualitative similarity between the streamlines in Figs. 8.2(b) and (c) is striking despite the states lying on different

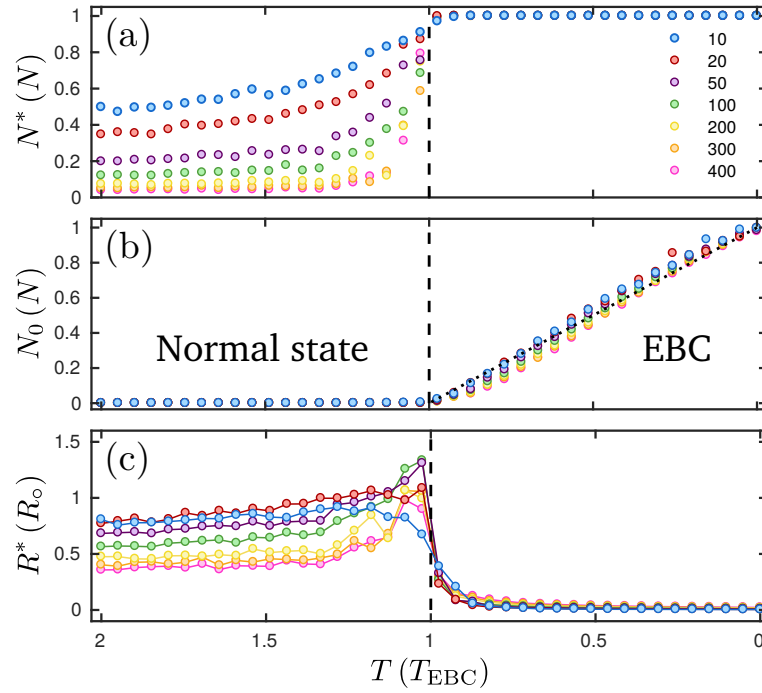


Figure 8.3: Two-species Monte Carlo simulation results. Shown as functions of temperature are: (a) The fraction of vortices in the largest cluster, (b) the condensate fraction, Eq. (8.13), and (c) the mean cluster radius $R^* = 4 \text{Std}(r_j)$, where \mathbf{r}_j is the vector of positions of the vortices in the largest cluster. Data is shown for systems with different vortex numbers as indicated in the legend. The function $1 - T/T_{\text{EBC}}$, where $T_{\text{EBC}} = -0.25\alpha N_{\text{tot}}$, is shown as a dotted line in (b) for $|T| < |T_{\text{EBC}}|$ and the vertical dashed line marks the critical point. All quantities are ensemble averaged.

sides of the transition.

As shown below in Sec. 8.7, the transition occurs even in a maximally imbalanced case where only one type of vortex is present in the system, in which case the dipole moment is identically zero at all temperatures. In the general imbalanced case with N_+ vortices and N_- antivortices with $N_{\text{tot}} = N_+ + N_- = N_{\text{maj}} + N_{\text{min}}$ and $N_{\text{maj}} > N_{\text{min}}$, there are two critical temperatures. When the temperature approaches negative zero, the majority species condenses first at $T_{\text{maj}} = -\alpha N_{\text{maj}}/2$, followed by the condensation of the minority species at $T_{\text{min}} \approx -\alpha N_{\text{min}}/2$, where the latter is shifted slightly toward negative zero due to the interaction with the condensate of the majority species.

Figure 8.3 shows (a) the largest cluster fraction, (b) the condensate fraction, and (c) the mean radius of the largest cluster in the system as functions of temperature in units of the critical temperature $T_{\text{EBC}} = -0.25\alpha N_{\text{tot}}$. As mentioned previously,

Fig. 8.3 reveals that the system becomes completely clustered before the critical point is reached. The largest cluster fraction Fig. 8.3(a) is strongly dependent on the total number of vortices in the system. In contrast, the condensate fraction, shown in Fig. 8.3(b), remains zero at all temperatures $|T| > |T_{\text{EBC}}|$ and thereafter increases as the absolute negative zero is approached. Figure 8.3(c) shows the mean radii of the largest vortex clusters as functions of temperature. As the critical temperature is approached from the disordered side, the largest cluster tends to grow in size as ever more vortices are joining in. In the condensed phase the cluster rapidly shrinks as the phase-space density, and hence the condensate fraction, increases. Importantly, the condensate fraction shows universality in the sense that it is consistent with data collapsing onto a single curve, indicating that the condensate fraction becomes a vortex number independent quantity in the large vortex number limit.

8.7 One-species Monte Carlo results

As we have stated previously, the clustering of vortices and their condensation are two separate phenomena. To make this explicitly clear, we have performed Monte Carlo calculations for a charge-polarised case where only one species of vortex is present in the system, i.e. $\sum_{i=1}^{N_{\text{tot}}} s_i = N_{\text{tot}}$. Figure 8.4 shows the vortex configurations at three different temperatures under this constraint. As can be seen in panels (b)–(c), the vortex positions suddenly collapse when the radius of the cluster reaches a critical value, R_c . As such, the transition illustrated in Fig. 8.2 simply corresponds to the independent condensation of two spatially separated clusters of vortices, which happens to occur at the same temperature because each cluster contains the same number of vortices or antivortices. In vortex number imbalanced systems, there are two different, vortex number dependent, critical temperatures, as discussed above.

The critical temperature for the condensation of an Onsager vortex in a single vortex species system may be predicted by a similar free energy argument as for two vortex species systems [165]. The Helmholtz free energy, $F = E - TS$, of a vortex configuration where all N_v vortices are clustered inside a circular region of radius R^* is

$$F \approx \frac{\rho_s \kappa^2}{4\pi} N_v^2 \log\left(\frac{R}{R^*}\right) - T k_B \log\left(\frac{R^*}{R}\right)^{2N_v} \quad (8.14)$$

where the energy E is that of a multiply quantised vortex of core radius R^* , and the entropy S is obtained as the logarithm of the statistical weight of the configuration.

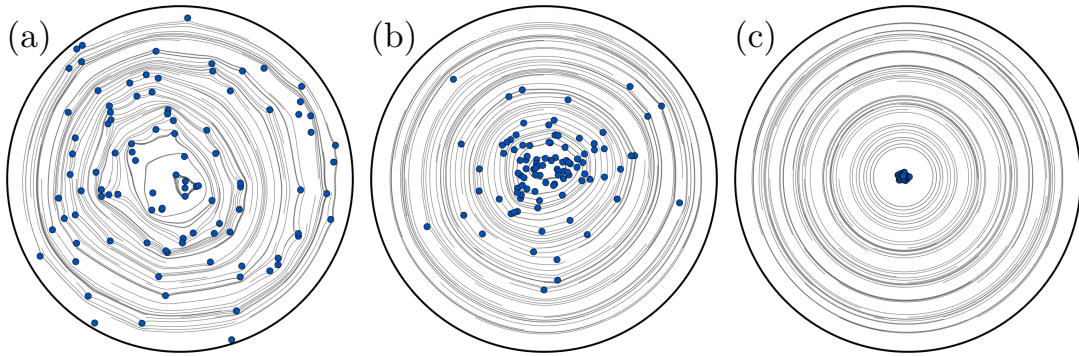


Figure 8.4: Representative charge-polarised vortex configurations (a)–(c) at respective temperatures $T/T_{\text{EBC}} = \{2, 1.03, 0.77\}$, with $T_{\text{EBC}} = -0.5\alpha N_{\text{tot}}$ and $N_{\text{tot}} = 100$. The streamlines illustrate the velocity field generated by the collection of vortices.

A change in the sign of the free energy signifies that the probability $p_F \propto e^{-F/k_B T}$ of observing such a configuration becomes exceedingly high and predicts a critical temperature

$$T_{\text{EBC}} = -\frac{\alpha N_v}{2}. \quad (8.15)$$

The condensation of Onsager vortices is the result of competition between solid body rotation within the core of the vortex cluster and potential flow outside the cluster, see Eqs. (8.7). Equating the kinetic energy contributions of these two velocity fields in the mean-field interaction energy term in Eq. (8.10) thus predicts a critical cluster radius

$$R_c = e^{-1/4} R_o \approx 0.78 R_o, \quad (8.16)$$

such that for $T/T_{\text{EBC}} > 1$ the whole system prefers to mimic solid body rotation of a classical fluid, whereas for $T/T_{\text{EBC}} < 1$ the system prefers to mimic the velocity field of a quantised superfluid vortex. With this insight, it is interesting to recall the structure of a simple vortex in a superfluid or a superconductor. Outside of the vortex core the superfluid or superconducting order parameter is at its bulk value whereas in the vortex core region the superfluid order parameter vanishes and the original symmetry of the full Hamiltonian is locally restored. A local observer spatially traversing a vortex core in such systems thus measures a superfluid–normal–superfluid transition along the path.

Figure 8.5 shows the condensate fraction, measured using Eq. (8.13), and the radius of the vortex cluster. Above the critical temperature, vortices are found scattered everywhere within the circular boundary, and the condensate fraction is strictly zero. Near the transition, the vortices begin to clump and at critical

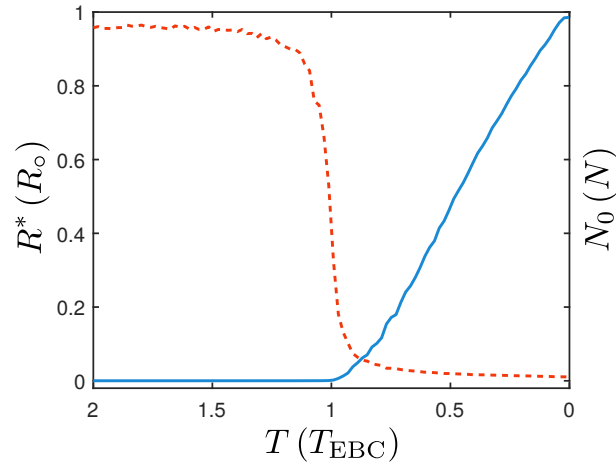


Figure 8.5: Condensate fraction of $N_v = 100$ single species, $s = +1$, vortices (right axis, blue solid line) and the radius, R^* , of the vortex cluster, (left axis, red dashed line), as functions of reduced temperature.

radius R_c the vortex cluster suddenly collapses. Accompanied by the rapid spatial shrinking of the vortex cluster, the condensate fraction grows almost linearly with the reduced temperature.

Figure 8.6(a) shows the phase space density, $n_v \langle \lambda_v \rangle$ of the vortices as functions of both position and reduced temperature. The one-dimensional vortex-particle density $n(x)$ is obtained by modeling each vortex-particle by a normalised Gaussian wave packet of waist λ_v . The frames (b)–(d) show the 1D density of the vortex gas for three different temperatures $T/T_{\text{EBC}} = \{2, 1.03, 0.77\}$. Above the condensation temperature the vortex density is spread over the whole system while below the transition the vortex density becomes localised both in real space and in vortex momentum space.

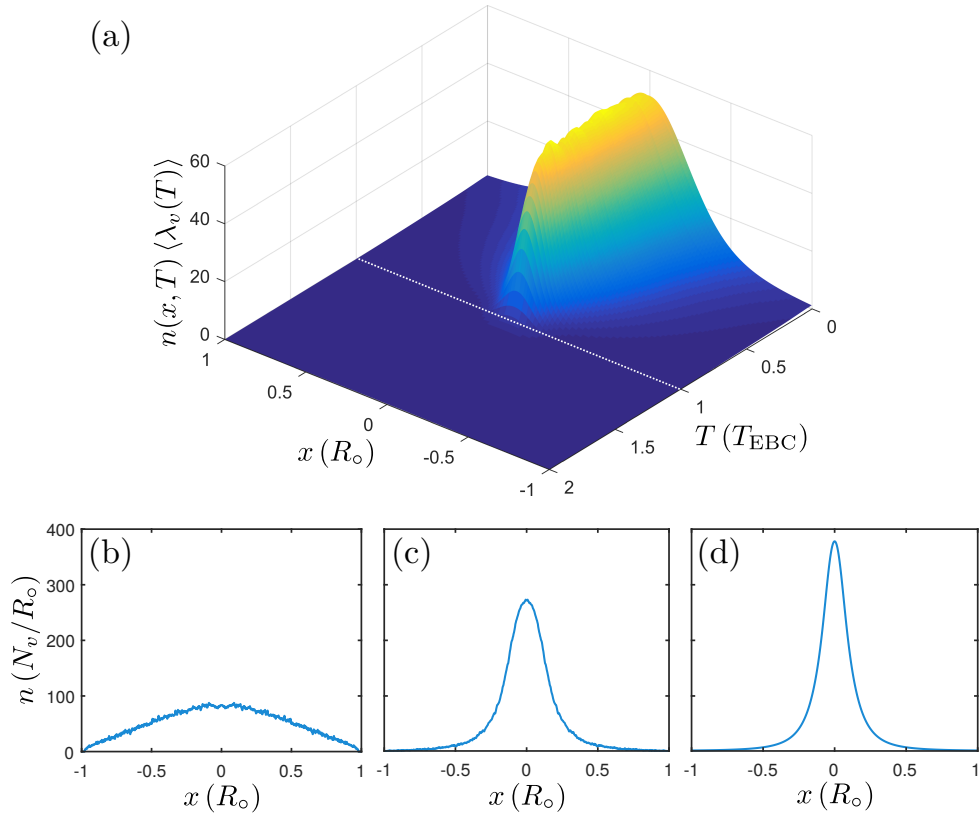


Figure 8.6: (a) Phase space density as a function of both position and reduced temperature, (b)–(d) the one-dimensional density of the vortices at respective temperatures $T/T_{\text{EBC}} = \{2, 1.03, 0.77\}$, for $N_v = 100$, with $T_{\text{EBC}} = -0.5\alpha N_v$.

8.8 Evaporative heating of vortices

With the ability to quantify the condensation of Onsager vortices, we have revisited the dynamical mean-field simulations of Chapter 7. Figure 8.7 shows a typical result, revealing that in this neutral vortex system, the largest cluster fraction and vortex dipole moment are practically equivalent observables. However, although the system is continually evaporatively heated, the condensate fraction remains zero for all times. The initial vortex number in this simulation is ≈ 100 and it decays to the final value of 12. Comparing the largest cluster fraction in Fig. 8.7 with Fig. 8.3(a) shows that this system is initially at temperature $|T| \gg |T_{\text{EBC}}|$ and evaporatively heats, eventually reaching a final temperature of $|T| \gtrsim |T_{\text{EBC}}|$ at late times. Quantitatively, the temperature of the vortex system could be determined using the vortex thermometry technique that we will introduce in Chapter 9. However, once the system becomes fully clustered and is at the verge of the transition, the evaporative heating mechanism switches off [165] and the condensation is unable to proceed.

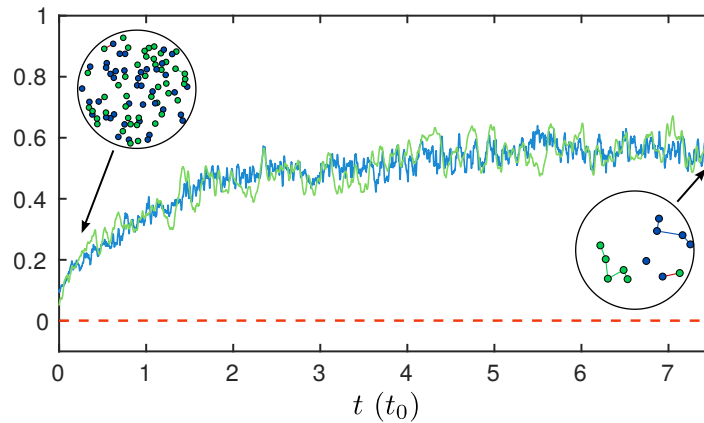


Figure 8.7: Vortex dipole moment (blue solid line) expressed in units of $d_0 = \kappa R_0 N$, largest cluster fraction (green solid line) and condensate fraction (red dashed line) as functions of time calculated from a dynamical mean-field simulation with a trapping potential of steepness $\sim r^{50}$ (c.f. Fig. 7.10). The unit of time is $t_0 = \hbar/\mu$, where μ is the chemical potential. The initial vortex number is ≈ 100 and as the system evaporatively heats up, the vortex number decays to a value of 12 at the end of the simulation (see Chapter 7 for details).

8.9 Summary

In conclusion, we have employed a vortex–particle duality to establish a correspondence between two-dimensional fluid vortices and a one-dimensional gas of vortex particles. This mapping has allowed us to define a quantitative measure of the condensation Onsager vortices, and we have used this to show the clear difference between a condensate of Onsager vortices and a quasi-condensate of vortex clusters. Furthermore, we have shown that the dynamical evaporative heating of vortices does not lead to the spontaneous crossing of the critical point.

The condensation process described here bears resemblance to rapidly rotating neutral superfluids that are predicted to undergo phase changes when the vortex cores begin to significantly overlap and the filling factor, or the number of fluid particles per vortex, approaches unity [94, 367].

In steady-state two-dimensional incompressible fluid turbulence the inverse energy cascade of the Kraichnan model predicts a spectral power-law kinetic energy spectrum. However, once large Onsager vortices form in the system, the energy spectrum changes drastically and would no longer be consistent with the structure of the inverse energy cascade. In particular, the system scale Onsager vortices that form before they can condense facilitate energy transport across all spatial scales in the system. Hence, we postulate that even the inverse energy

cascade mechanism of driven classical two-dimensional turbulence may not supply a sufficient amount of energy for condensation, and that instead a direct forcing at the Onsager vortex scale may be required to realise and observe the condensed states of Onsager vortices. Ultimately, deep in the condensed phase a phase-space Wigner crystallisation of vortices with hard cores takes place [165], while true point-vortices would condense into multiply quantised vortex states [195].

9

VORTEX THERMOMETRY FOR TURBULENT TWO-DIMENSIONAL FLUIDS

In this chapter, we introduce a thermometry technique which allows us to directly measure the statistical temperature of a turbulent configuration of vortices in two dimensions. The thermometer is calibrated using Monte Carlo simulations and a vortex classification algorithm (described in Sec. 4.5.2). We find that there is a unique mapping between the temperature of the vortex gas and the proportion of clusters and dipoles identified by our algorithm; thus, if we know one, we can infer the other. We test our thermometer by applying it to dynamical simulations of decaying turbulence in a Bose–Einstein condensate, and find that, as predicted in Ref. [165], the vortex gas is evaporatively heating towards negative temperatures. We also find previously unidentified vortex power-law distributions which emerge from the dynamics, signalling that the vortex gas is in a state of dynamical equilibrium as it decays. This chapter forms the basis of Ref. [170].

9.1 Motivation

As outlined in Sec. 3.3.3, a number of obstacles currently hinder the experimental realisation of Onsager vortices in decaying 2D quantum turbulence. We demonstrated in Chapter 7 that harmonic trapping is one such obstacle, as vortex clusters appear to be suppressed in this geometry [103, 169, 340]. In addition, the detection of vortex circulation signs is experimentally difficult, and it is only recently that techniques have been proposed [368] and implemented [155] to achieve this. Analysis of turbulent dynamics is made even more challenging by current condensate imaging methods, which only allow a small number of frames to be captured for a single experimental realisation [135]. It is therefore not possible to observe the turbulent dynamics in real time. As such, it is desirable to be able to characterise the state of a turbulent fluid using a robust statistical

analysis that links the instantaneous microscopic configuration of the system to its macroscopic behaviour. Here we propose to use Onsager’s vortex temperature as an observable for this purpose.

The chapter is structured as follows. We first describe our method for measuring the temperature of the vortex gas in Sec. 9.2, before examining a specific case of decaying superfluid turbulence using mean-field Gross–Pitaevskii simulations in Sec. 9.3. In the dynamics, we observe that the vortex gas undergoes rapid equilibration before settling into a quasi-equilibrium state where it continues to heat adiabatically via vortex evaporation [165]. We have discovered that in this evolution, the numbers of clusters, dipoles and free vortices follow robust power-laws with respect to the total vortex number. The existence of this quasi-equilibrium allows quantitative thermometry of the turbulent fluid, which we use to directly measure the effects of evaporative heating. To conclude, we summarise these results in Sec. 9.4.

9.2 Monte Carlo thermometry

To calibrate the vortex thermometer, we use Monte Carlo (MC) simulations to map out the equilibrium vortex configurations as a function of the inverse temperature $\beta = 1/k_B T$, as we did in the previous chapter. We do this for a system of $N_v = 50$ point-vortices with equal numbers of clockwise and anticlockwise circulations. We use a point-vortex Hamiltonian corresponding to a uniform fluid within a circular boundary of radius R , Eq. (3.13) [165, 237], and set a hard core of radius $0.003R$ to prevent energy divergences. As we vary the temperature across both positive and negative regimes, we quantify the effect on the vortex configuration using our vortex classification algorithm (see Sec. 4.5.2). We then calculate the numbers of clusters N_c , dipoles N_d and free vortices N_f as functions of temperature, and the resulting fractional population curves are presented in Fig. 9.1.

The resulting phase diagram can be compared with the density of states schematic, Fig. 3.4. At low positive absolute temperatures (left hand side of Fig. 9.1), the vortex gas is at its ‘coldest’, as both the energy and entropy are minimised. In this regime, bound vortex–antivortex dipole pairs dominate the configuration. Above the Berezinskii–Kosterlitz–Thouless critical temperature β_{BKT} [26–28], the vortex dipoles dissociate, causing an increase in both the energy and entropy. At $\beta = 0$, the entropy is maximised, but begins decreasing again with temperature in the negative region. In this regime, clusters of like-sign

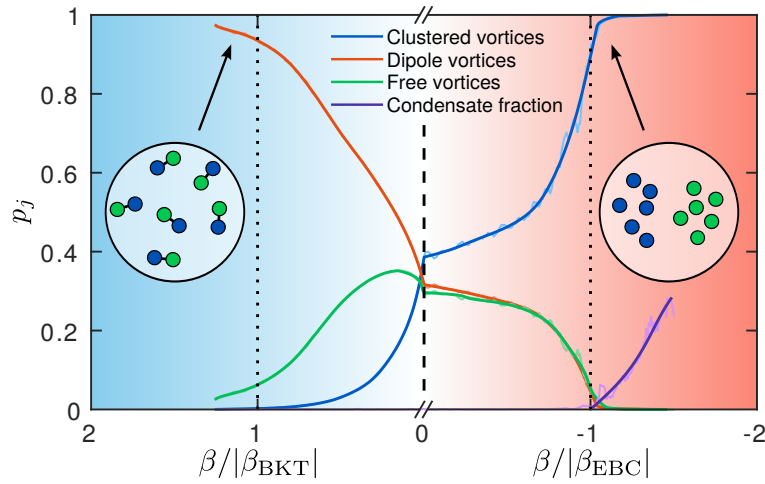


Figure 9.1: Fractional population $p_j = N_j/N_v$ of each component of the vortex gas (where $j \in \{c: \text{clustered vortices}, d: \text{dipole vortices}, f: \text{free vortices}\}$) and Einstein–Bose condensate fraction (described in text), as functions of inverse temperature β . The fluctuating faint lines show the raw data, while the smooth dark lines show cubic spline fits. The negative temperature axis is scaled by the critical temperature $|\beta_{\text{EBC}}|$, and the positive temperature axis by $|\beta_{\text{BKT}}|$, causing an apparent discontinuity in the slopes at $\beta = 0$. The vertical dashed line indicates $\beta = 0$ and the dotted vertical lines highlight the two critical temperatures. The shaded background represents the energy of the system (red and blue correspond to ‘hot’/high energy and ‘cold’/low energy, respectively). Schematic vortex configurations at each temperature extreme are depicted in the insets, where vortices (antivortices) are shown as blue (green) filled circles.

vortices tend to form. Above the critical temperature β_{EBC} , the vortices form an Einstein–Bose condensate (EBC), as discussed in Chapter 8 [165, 173, 348]. The two aforementioned critical temperatures are defined in Sec. 3.2.2.1.

Figure 9.1 demonstrates that the dipole and cluster populations are monotonic functions of β —this is the key observation enabling thermometry of the vortex gas. Given an arbitrary vortex configuration in thermal equilibrium, we may determine its temperature by calculating the populations of clusters and/or dipoles and comparing the obtained values to the curves in Fig. 9.1. Strictly, the $p_j(\beta)$ curves in the negative temperature region of Fig. 9.1 are dependent on the vortex number. However, we repeated our MC simulations for $N_v = 100$ and $N_v = 200$ vortices and found that, for the vortex numbers relevant to the dynamical simulations presented here, the change to the thermometry curves is not significant.

Also shown in Fig. 9.1 is the Einstein–Bose condensate fraction, Eq. (8.13), which quantifies the density of vortices in the largest cluster. For $\beta > \beta_{\text{EBC}}$, the

condensate fraction is zero, but when $\beta < \beta_{\text{EBC}}$ it rises sharply. In this extreme temperature region, the other thermometers saturate and the condensate fraction becomes the relevant order parameter.

9.3 Thermometry of decaying two-dimensional turbulence

9.3.1 System parameters

As an application of our vortex thermometer, we use it to characterise decaying turbulence in a disk-shaped BEC, as in Chapter 7. We simulate the two-dimensional time-dependent Gross–Pitaevskii equation (GPE), Eq. (2.13), using a potential of the form $V_{\text{tr}} = \mu(r/R)^{50}$ to obtain the uniform circular geometry. Here, $r = \sqrt{x^2 + y^2}$ is the radial distance from the axis of the trap, μ is the chemical potential, and $R \approx 171 \xi$ is the radius of the trap, measured in units of the healing length ξ . The interaction parameter is set to $g = 4.6 \times 10^4 \hbar^2/m$. We solve the GPE on a 1024×1024 numerical grid with spacing $\approx \xi/2$. We detect vortices and their circulation signs within $r < 0.98R$ using the algorithm described in Sec. 4.5.1.

9.3.2 Emergence of vortex equilibria

The initial state for our GPE simulations has $N_v = 800$ vortices imprinted at random locations with equal numbers of each circulation sign. The short imaginary time evolution causes the loss of ≈ 40 vortices, and a further ≈ 25 are initiated beyond the detection radius. As the turbulence decays, the vortices annihilate and the vortex gas evaporatively heats, resulting in the emergence of two large Onsager vortices at late times [165, 169]. Three sample frames from a single simulation are shown in Fig. 9.2, where panels (a)–(c) show the density $|\psi|^2$ of the fluid, and panels (d)–(f) show the corresponding vortex configuration after the detection and classification steps. A Helmholtz decomposition (see Sec. 2.5.2) has been used to extract the divergence-free component of the condensate velocity field, and the resulting streamlines are also shown in the lower panels. The Onsager vortex clusters are clearly visible in panel (f).

The number of clusters, dipoles and free vortices are shown in Fig. 9.3 as functions of both time t (inset) and the total number of vortices $N_v(t)$. The time-dependent populations (inset) do not follow any simple function. However, the populations as functions of the total number of vortices (main frame) show clear power-law scaling behaviour. The corresponding power-laws are: $N_c \propto N_v^\alpha$, $N_d \propto N_v^\gamma$, $N_f \propto N_v^\delta$ and $N_{vc} \propto N_v^\varepsilon$, with measured values $\alpha = 0.79$, $\gamma = 1.21$, $\delta = 1.18$, and $\varepsilon = -0.25$. These are suggestive of rational value power-laws

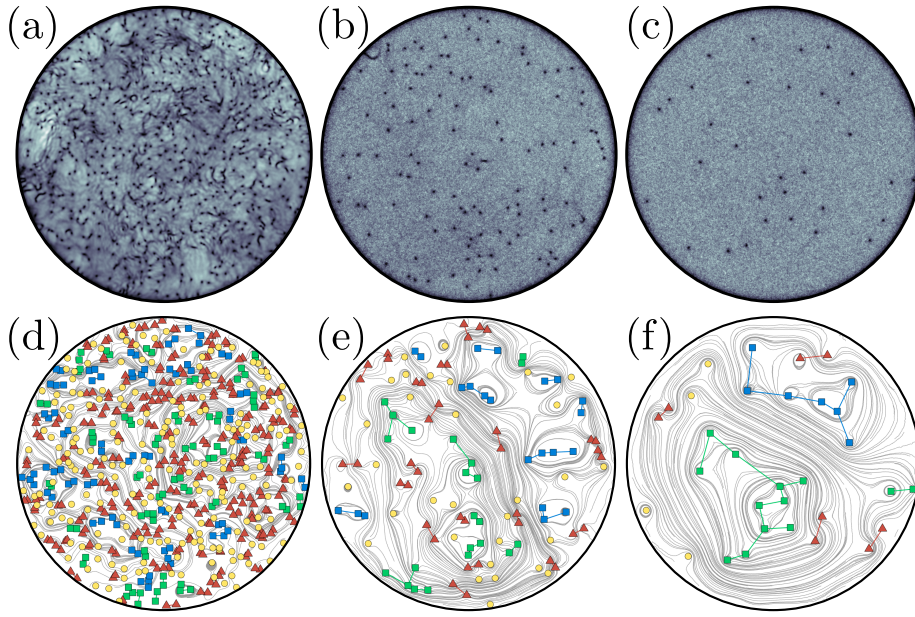


Figure 9.2: Freely decaying two-dimensional quantum turbulence. Panels (a)–(c) show the classical field density $|\psi|^2$, for respective times $t \approx (25, 7500 \text{ and } 74000) \hbar/\mu$. The grey scale in each panel is normalised to the respective peak value of $|\psi|^2$. Panels (d)–(f) correspond to panels (a)–(c), respectively, and show the vortices in positive (negative) clusters as blue (green) squares, dipoles as red triangles, and free vortices as yellow circles. Note that each vortex dipole contains one vortex and one antivortex. The streamlines in (d)–(f) are obtained by calculating the incompressible component of the velocity field of the classical field describing the Bose gas.

with exponents $\alpha = 4/5$, $\gamma = \delta = 6/5$ and $\varepsilon = -1/4$. The mean number of vortices per cluster $N_{vc} \equiv N_c/N_{cl}$, where N_{cl} is the total number of clusters of any size at a given time. To study the effects of system size on these power-laws, we have also considered two smaller disk-shaped systems of radii $R \approx 49 \xi$ and $R \approx 85 \xi$ respectively, each with $N_v = 100$ vortices initially imprinted. We find that the scaling behaviour is unchanged in these smaller systems, suggesting that the evolution of the vortex gas is underpinned by a universal microscopic process.

In this system, the primary cause of vortex number decay is the annihilation of vortex–antivortex dipoles. Despite this, the populations of dipoles and free vortices follow approximately the same power-law, demonstrating an interconversion between the vortex populations. However, a distinct power-law emerges for the vortex clusters. This behaviour points toward a two-fluid model, where the dipoles and free vortices behave as a weakly interacting thermal cloud, while the clusters act as a quasi-condensate whose relative weight grows over time as a result of

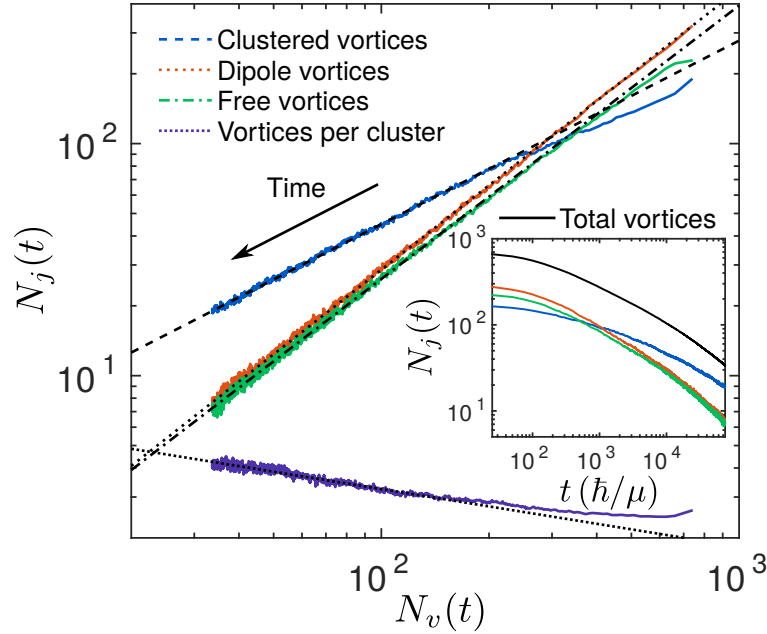


Figure 9.3: Decay of the vortex populations $N_j(t)$ (where $j \in \{c: \text{clustered vortices}, d: \text{dipole vortices}, f: \text{free vortices}\}$) in each component of the vortex gas, and the growth of the number of vortices per cluster $N_{vc}(t)$, as functions of the total vortex number $N_v(t)$. The data has been averaged over 80 simulations, with power-law fits shown as straight lines. Note that time flows from right to left in this figure. The inset shows the total number of vortices and the number of vortices in each component of the vortex gas as functions of time.

vortex evaporative heating. This behaviour is a precursor to the Einstein–Bose condensation observed for $\beta < \beta_{\text{EBC}}$, which is described in detail in Ref. [173]. Extrapolating the data toward $N_v \rightarrow 0$ leads to the inevitable decay of all dipoles and free vortices, leaving only Onsager vortex clusters remaining. At this point, the rate of pair annihilation becomes insignificant in the dynamics due to the very low probability of vortex–antivortex collisions.

9.3.3 Dependence on initial condition

To assess the sensitivity of the observed power-laws to the choice of initial vortex configuration, we have run simulations with a diverse range of initial conditions. In addition to the randomly sampled initial condition (case I) described above, we consider four other initial states. The cases II and III are configurations with lower kinetic energy created by imprinting the vortices as dipole pairs with sizes 8ξ and 12ξ , respectively. For case IV, the vortex creation is simulated dynamically by stirring an initially unperturbed condensate with a repulsive Gaussian potential

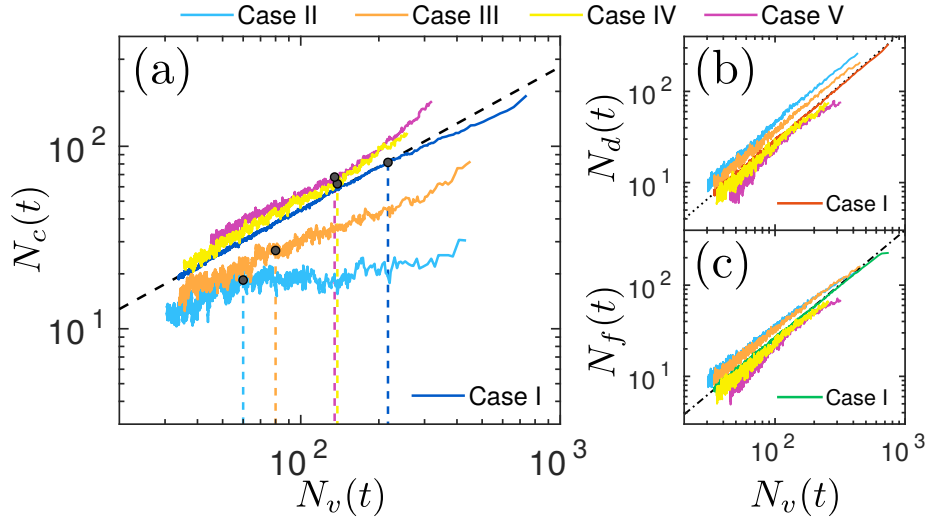


Figure 9.4: Vortex decay curves for initial conditions I–V described in the text. Each curve for case II–V has been averaged over ten simulations. The three panels separately show (a) clusters, (b) dipoles, and (c) free vortices. Note that the curves for case I are identical to those in Fig. 9.3. In panel (a), dashed vertical lines and filled circles indicate the value of N_v at which each cluster decay curve begins to approximate the $N_c \sim N_v^{4/5}$ power-law.

of waist 30ξ and amplitude 5μ . The stirring potential is moved back and forth with centroid position $x_o(t) = 100 \xi \cos(2\pi \mu t / 1050 \hbar)$ for four periods, and then ramped down to zero over a fifth period. Finally, a large kinetic energy in case V is initiated by imprinting a periodic square array of vortex clusters with alternating circulation sign, each with a radius of $\approx 43 \xi$ and containing ≈ 50 vortices.

The resulting number decay curves for each vortex type are shown in Fig. 9.4(a)–(c). The dipole and free vortex decay curves [panels (b) and (c), respectively] remain relatively unchanged across different initial configurations. By contrast, the clusters [panel (a)] show clear variation across the set of initial conditions, suggesting that initially the system is in fact behaving very differently under each constraint. However, despite initial differences (at large N_v), all cluster decay curves eventually exhibit behaviour consistent with the power-laws obtained in Fig. 9.3, demonstrating a loss of memory of the initial vortex configuration. This suggests that these power-laws correspond to a state of quasi-equilibrium in which the vortex gas should have a well-defined temperature, which we can determine using the thermometers established in Fig. 9.1.

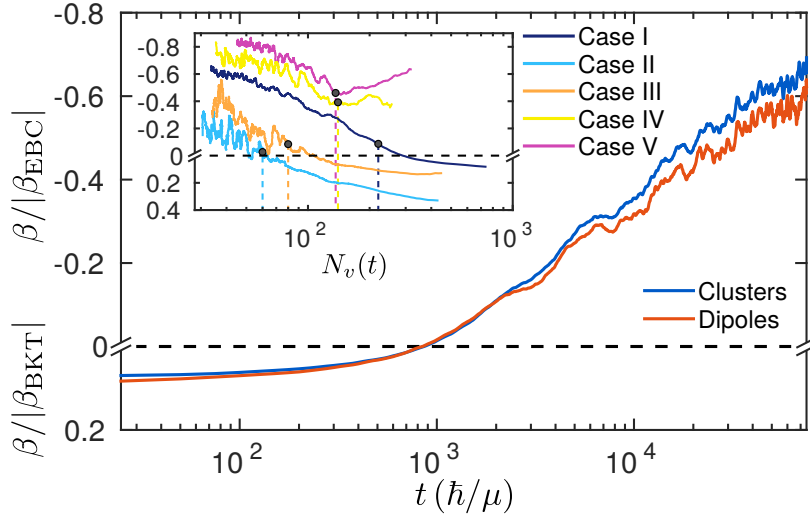


Figure 9.5: Inverse temperature of the vortex gas as a function of time, averaged over a set of dynamical GPE simulations for case I. The temperature is measured independently using the populations of both clusters and dipoles. In the inset, the mean temperature readings from both thermometers for all five initial conditions (as described in the text) are shown as a function of the total vortex number $N_v(t)$. The vertical dashed lines and filled circles are from Fig. 9.4(a). As in Fig. 9.1, the positive and negative temperature regions have been scaled by their respective critical temperatures, and a dashed horizontal line denotes $\beta = 0$. The vertical axis of the inset is the same as for the main frame.

9.3.4 Evaporative heating of the vortex gas

We now have an algorithm to assign a vortex temperature to the dynamical GPE simulations. We determine the fractional populations of vortex dipoles and clusters as a function of time, and use each of these to read off a temperature from the curves in Fig. 9.1. The two resulting measurements of $\beta(t)$ for case I are presented in the main frame of Fig. 9.5. Both measurements show that the temperature of the vortex gas is spontaneously increasing as Onsager vortex clusters form, thereby confirming the evaporative heating scenario posited in Ref. [165]. At late times, a small discrepancy between the two temperature readings emerges, which we attribute to the compressibility of the fluid not accounted for in the MC model.

The inset of Fig. 9.5 shows the mean temperature readings for all five cases. These curves show a clear dependence on initial condition, with the low energy configurations (cases II and III) being consistently colder than those with high energy (cases IV and V). The random initial configuration (case I) lies between the two extremes. The approximate value of N_v at which the vortex gas appears to reach equilibrium in each case [see Fig. 9.4(a)] is also shown in the inset. Even

before this point (i.e. for larger N_v), the vortex thermometer provides a plausible temperature reading, but the measurement is not reliable if the vortex gas is out of equilibrium. In cases IV and V, the equilibration point corresponds to a turning point in the temperature curve, providing further evidence for our interpretation of the vortex gas equilibrium condition.

9.4 Summary

We have developed a methodology that allows the temperature of point-vortices in two-dimensional fluids to be determined using only the information about the vortex positions and their signs of circulation. We have applied the vortex gas thermometers to freely decaying two-dimensional quantum turbulent systems and quantitatively shown the transition to negative temperatures and the emergence of Onsager vortices due to the evaporative heating of the vortex gas [165, 169]. Our vortex thermometers may also be useful for characterisation of turbulent classical fluids, as the continuous vorticity distributions can be approximated accurately by a discretised set of point-vortices before performing the vortex classification and thermometry. This methodology may therefore open new pathways to quantitative studies of two-dimensional turbulence.

10

CONCLUSIONS AND OUTLOOK

10.1 Summary

In this thesis, we have presented an investigation into the problems of vortex motion and turbulence in two-dimensional scalar Bose–Einstein condensates. We have studied both the microscopic and the macroscopic, building our understanding from the absolute basics of vortex motion all the way to the chaotic, untameable dynamics that constitute quantum turbulence.

We have established our knowledge from the ground up, beginning in Chapter 5 with the simplest case of a single vortex in a trapped BEC. By comprehensively studying this problem, we identified all contributions to the motion of a vortex in an inhomogeneous 2D BEC. In doing so, we were able to identify a number of shortcomings that were present in the existing literature when describing the vortex dynamics in this scenario. We clarified the issue of the Magnus force acting on a vortex, which has often been misidentified, and determined that image vortices are relevant even for systems with soft boundaries. We also measured for the first time the induced multipole velocity field of a moving vortex. Our dynamical formalism allowed us to obtain refined point-vortex equations for inhomogeneous systems, which we have demonstrated to give significant improvements over existing models.

Despite the shortcomings of the point-vortex model in terms of its quantitative accuracy, we applied it in Chapter 6 to study the qualitative trajectories of two same-sign vortices in a harmonically trapped BEC. By studying a precursor to turbulence—a pitchfork bifurcation in the two-vortex dynamics observed in recent experiments—we discovered a previously unidentified impenetrable boundary in the phase space of possible initial conditions, a feature which was unknown before this work. We have also discovered that the bifurcation is most readily visible in a velocity-space—rather than a real-space—representation of the dynamics.

In Chapter 7, we began our exploration of two-dimensional quantum turbulence.

Motivated by an apparent contradiction that recently emerged in the literature, we investigated the effects of geometry on vortex clustering and found that the commonly used harmonic traps inhibit the formation of large scale vortex clusters. Increasing the steepness and uniformity of the trap was found to produce more distinct clusters, due to a shift in the equilibrium position of the Onsager vortex dipole. By studying the microscopic details of such turbulent states, we discovered the importance of three- and four-body annihilation events at zero temperature.

We then took a brief detour from dynamics in Chapter 8, and instead studied in detail the equilibrium properties of the vortex gas in the regime of extreme negative temperatures. We identified a process of vortex condensation, in analogy with Bose–Einstein condensation, and were able to quantify it by defining a condensate fraction. Importantly, this work draws a clear distinction between the clustering of vortices observed in dynamical simulations and the condensation of Onsager vortices, which occurs in the extreme negative temperature region. Using our condensate fraction observable, we were able to show that the dynamics of decaying 2D quantum turbulence never reach a temperature at which the condensate forms.

Finally, in Chapter 9, we introduced a novel method of thermometry for a turbulent configuration of quantised vortices in two dimensions, which requires only the vortex location and sign information. Our technique provided the first direct quantitative measurement of Onsager’s vortex temperature parameter, and simultaneously proved that vortex evaporative heating is responsible for the dynamical evolution towards negative vortex temperatures. Importantly, we were also able to identify a state of statistical quasi-equilibrium in the decaying turbulence, thereby providing evidence that the vortex gas should have a well-defined temperature as it adiabatically evolves.

10.2 Outlook

Throughout the work presented here, many questions regarding vortex dynamics and quantum turbulence have been addressed. However, as is the case in any worthwhile scientific endeavour, myriad potential future directions have revealed themselves along the way. We cannot reasonably list them all, but we present here an outline of arguably the most promising among them.

Our detailed examination of the velocity field of a moving vortex in Chapter 5 revealed the existence a vortex multipole field, which has received little attention prior to this work. The specific properties—and potential experimental measurement—of such a multipole field are of primary interest, especially in light

of a potential analogy with the elusive electric dipole moment of the electron [369]. Our measurements of vortex orbits and dynamical bifurcations in Chapter 6 could be extended to a multitude of other vortex configurations, and the transition to chaos as the vortex number is increased could be studied in detail. Countless other geometries for two-dimensional vortex motion and turbulence could be studied beyond those examined in Chapter 7—some more exotic examples include constraining the fluid to the surface of a cylinder [370], Möbius strip, or spherical shell. The ensuing dynamics may reveal new, interesting features of the motion not attainable in other configurations. We have already begun an investigation into the effects of finite condensate temperature on both the number decay and clustering behaviour of decaying 2D quantum turbulence using a stochastic projected Gross–Pitaevskii formalism [371], and obtained results consistent with the phenomenological damped GPE data presented here. The realisation of Einstein–Bose condensation in 2D quantum turbulence remains an experimentally open problem: even if vortex clusters are observed to emerge in 2D quantum turbulence in the near future, our dynamical simulations suggest that vortex condensation cannot take place spontaneously. It may be possible to continue the vortex heating towards the EBC transition by introducing locally dissipative pinning potentials to the centre of the vortex clusters, thereby causing them to ‘spin up’ [109]—indeed, we have already performed some preliminary simulations to this end. Our results presented in Chapter 9 open up a number of future possibilities. Firstly, it would be interesting to determine whether the vortex number power-laws are universal, or whether they depend on system parameters such as geometry. To elucidate these power-laws, attempts could be made to predict the exponents directly from statistical arguments regarding the microscopics of the vortex gas. Arguably the most pertinent test of our proposed thermometry technique would be to apply it to 2D classical fluid turbulence, especially since this would be the first ever measurement of a negative temperature state in its initially theorised context.

With regards to the broader outlook, the future of 2D quantum turbulence research has much in store. Experimentally, technology and methodology are both constantly improving, and it should soon be possible to image vortices *in situ* with vortex sign detection, and possibly in real time. This should greatly improve the ability to interpret results, since the vortex dynamics could be observed directly, in contrast to the small number of images that can now be taken over a given experimental run. Ultimately, the goal would be to move towards steady-state turbulence, which requires optimisation of stirring techniques that prevent the

condensate from heating too rapidly. For the foreseeable future, however, one of the major impediments in studying turbulence in BECs experimentally is the restriction on the system size, and the correspondingly small range of length scales over which any turbulent flow can exist. Numerically, however, system sizes can continue to grow, and ever more powerful computers will undoubtedly be taken advantage of to perform these increasingly demanding calculations. With the ability to numerically model such large systems, the crossover between quantum and classical turbulence could be explored in detail, clarifying the link between the two. Finally, fascinating regimes of vortex dynamics and turbulence may be realisable in other types of BECs. There is growing interest in the possibilities of turbulence in spinor [372, 373], dipolar [374], and fermionic [375] systems, each of which promise their own varieties of as yet unexplored physics.

In truth, a universal ‘theory of turbulence’ seems, at this point, like an impossibility. It remains to be seen whether superfluids hold the answers to this ongoing problem, but regardless, quantum turbulence presents its own rich and diverse field of physics, which will no doubt captivate researchers for decades to come.

REFERENCES

- [1] M. H. Anderson, J. R. Ensher, M. R. Matthews, C. E. Wieman, and E. A. Cornell, ‘*Observation of Bose-Einstein condensation in a dilute atomic vapor*’, *Science* **269**, 198 (1995).
- [2] K. B. Davis, M.-O. Mewes, M. R. Andrews, N. J. van Druten, D. S. Durfee, D. M. Kurn, and W. Ketterle, ‘*Bose-Einstein Condensation in a Gas of Sodium Atoms*’, *Physical Review Letters* **75**, 3969 (1995).
- [3] C. C. Bradley, C. A. Sackett, J. J. Tollett, and R. G. Hulet, ‘*Evidence of Bose-Einstein Condensation in an Atomic Gas with Attractive Interactions*’, *Physical Review Letters* **75**, 1687 (1995).
- [4] V. S. Bagnato, D. J. Frantzeskakis, P. G. Kevrekidis, B. A. Malomed, and D. Mihalache, ‘*Bose-Einstein condensation: Twenty years after*’, *Romanian Reports in Physics* **67**, 5 (2015).
- [5] F. Dalfovo, S. Giorgini, L. Pitaevskii, and S. Stringari, ‘*Theory of Bose-Einstein condensation in trapped gases*’, *Reviews of Modern Physics* **71**, 463 (1999).
- [6] A. J. Leggett, ‘*Bose-Einstein condensation in the alkali gases: Some fundamental concepts*’, *Reviews of Modern Physics* **73**, 307 (2001).
- [7] J. O. Andersen, ‘*Theory of the weakly interacting Bose gas*’, *Reviews of Modern Physics* **76**, 599 (2004).
- [8] L. Pitaevskii and S. Stringari, *Bose-Einstein condensation and superfluidity*, vol. 164 of *International Series of Monographs on Physics*, Oxford University Press (2003).
- [9] A. J. Leggett, *Quantum liquids: Bose condensation and Cooper pairing in condensed-matter systems*, Oxford University Press (2006).
- [10] C. J. Pethick and H. Smith, *Bose-Einstein condensation in dilute gases*, Cambridge University Press (2008).
- [11] W. D. Phillips, ‘*Nobel Lecture: Laser cooling and trapping of neutral atoms*’, *Reviews of Modern Physics* **70**, 721 (1998).
- [12] C. N. Cohen-Tannoudji, ‘*Nobel Lecture: Manipulating atoms with photons*’, *Reviews of Modern Physics* **70**, 707 (1998).
- [13] S. Chu, ‘*Nobel Lecture: The manipulation of neutral particles*’, *Reviews of Modern Physics* **70**, 685 (1998).
- [14] W. Ketterle and N. J. van Druten, ‘*Evaporative Cooling of Trapped Atoms*’, in B. Bederson and H. Walther (eds.), ‘*Advances In Atomic, Molecular, and Optical Physics*’, vol. 37, 181–236, Academic Press (1996).
- [15] I. Bloch, J. Dalibard, and S. Nascimbène, ‘*Quantum simulations with ultracold quantum gases*’, *Nature Physics* **8**, 267 (2012).

- [16] P. Hauke, F. M. Cucchietti, L. Tagliacozzo, I. Deutsch, and M. Lewenstein, ‘*Can one trust quantum simulators?*’, *Reports on Progress in Physics* **75**, 082401 (2012).
- [17] I. M. Georgescu, S. Ashhab, and F. Nori, ‘*Quantum simulation*’, *Reviews of Modern Physics* **86**, 153 (2014).
- [18] T. H. Johnson, S. R. Clark, and D. Jaksch, ‘*What is a quantum simulator?*’, *EPJ Quantum Technology* **1**, 10 (2014).
- [19] J. Estève, C. Gross, A. Weller, S. Giovanazzi, and M. K. Oberthaler, ‘*Squeezing and entanglement in a Bose–Einstein condensate*’, *Nature* **455**, 1216 (2008).
- [20] S. Boixo, A. Datta, M. J. Davis, A. Shaji, A. B. Tacla, and C. M. Caves, ‘*Quantum-limited metrology and Bose-Einstein condensates*’, *Physical Review A* **80**, 032103 (2009).
- [21] C. Gross, ‘*Spin squeezing, entanglement and quantum metrology with Bose–Einstein condensates*’, *Journal of Physics B: Atomic, Molecular and Optical Physics* **45**, 103001 (2012).
- [22] G. K. Brennen, C. M. Caves, P. S. Jessen, and I. H. Deutsch, ‘*Quantum Logic Gates in Optical Lattices*’, *Physical Review Letters* **82**, 1060 (1999).
- [23] J. K. Pachos and P. L. Knight, ‘*Quantum Computation with a One-Dimensional Optical Lattice*’, *Physical Review Letters* **91**, 107902 (2003).
- [24] T. Byrnes, K. Wen, and Y. Yamamoto, ‘*Macroscopic quantum computation using Bose-Einstein condensates*’, *Physical Review A* **85**, 040306 (2012).
- [25] A. Görlitz, J. M. Vogels, A. E. Leanhardt, C. Raman, T. L. Gustavson, J. R. Abo-Shaeer, A. P. Chikkatur, S. Gupta, S. Inouye, T. Rosenband, and W. Ketterle, ‘*Realization of Bose-Einstein Condensates in Lower Dimensions*’, *Physical Review Letters* **87**, 130402 (2001).
- [26] V. L. Berezinskii, ‘*Destruction of long-range order in one-dimensional and two-dimensional systems having a continuous symmetry group I. Classical systems*’, *Soviet Journal of Experimental and Theoretical Physics* **32**, 493 (1971).
- [27] V. L. Berezinskii, ‘*Destruction of long-range order in one-dimensional and two-dimensional systems possessing a continuous symmetry group II. Quantum systems*’, *Soviet Journal of Experimental and Theoretical Physics* **34**, 610 (1972).
- [28] J. M. Kosterlitz and D. J. Thouless, ‘*Ordering, metastability and phase transitions in two-dimensional systems*’, *Journal of Physics C: Solid State Physics* **6**, 1181 (1973).
- [29] Z. Hadzibabic, P. Krüger, M. Cheneau, B. Battelier, and J. Dalibard, ‘*Berezinskii–Kosterlitz–Thouless crossover in a trapped atomic gas*’, *Nature* **441**, 1118 (2006).
- [30] P. Cladé, C. Ryu, A. Ramanathan, K. Helmerson, and W. D. Phillips, ‘*Observation of a 2D Bose Gas: From Thermal to Quasicondensate to Superfluid*’, *Physical Review Letters* **102**, 170401 (2009).
- [31] S. Hofferberth, I. Lesanovsky, B. Fischer, T. Schumm, and J. Schmiedmayer, ‘*Non-equilibrium coherence dynamics in one-dimensional Bose gases*’, *Nature* **449**, 324 (2007).
- [32] T. Kinoshita, T. Wenger, and D. S. Weiss, ‘*Observation of a One-Dimensional Tonks–Girardeau Gas*’, *Science* **305**, 1125 (2004).

- [33] O. Morsch and M. Oberthaler, ‘Dynamics of Bose-Einstein condensates in optical lattices’, *Reviews of Modern Physics* **78**, 179 (2006).
- [34] D. Jaksch, C. Bruder, J. I. Cirac, C. W. Gardiner, and P. Zoller, ‘Cold Bosonic Atoms in Optical Lattices’, *Physical Review Letters* **81**, 3108 (1998).
- [35] M. Greiner, O. Mandel, T. Esslinger, T. W. Hänsch, and I. Bloch, ‘Quantum phase transition from a superfluid to a Mott insulator in a gas of ultracold atoms’, *Nature* **415**, 39 (2002).
- [36] K. Henderson, C. Ryu, C. MacCormick, and M. G. Boshier, ‘Experimental demonstration of painting arbitrary and dynamic potentials for Bose-Einstein condensates’, *New Journal of Physics* **11**, 043030 (2009).
- [37] G. Gauthier, I. Lenton, N. M. Parry, M. Baker, M. J. Davis, H. Rubinsztein-Dunlop, and T. W. Neely, ‘Direct imaging of a digital-micromirror device for configurable microscopic optical potentials’, *Optica* **3**, 1136 (2016).
- [38] A. L. Gaunt, T. F. Schmidutz, I. Gotlibovych, R. P. Smith, and Z. Hadzibabic, ‘Bose-Einstein Condensation of Atoms in a Uniform Potential’, *Physical Review Letters* **110**, 200406 (2013).
- [39] L. Chomaz, L. Corman, T. Bienaimé, R. Desbuquois, C. Weitenberg, S. Nascimbène, J. Beugnon, and J. Dalibard, ‘Emergence of coherence via transverse condensation in a uniform quasi-two-dimensional Bose gas’, *Nature Communications* **6**, 6162 (2015).
- [40] S. Eckel, J. G. Lee, F. Jendrzejewski, C. J. Lobb, G. K. Campbell, and W. T. Hill III, ‘Contact resistance and phase slips in mesoscopic superfluid-atom transport’, *Physical Review A* **93**, 063619 (2016).
- [41] T. A. Bell, J. A. P. Glidden, L. Humbert, M. W. J. Bromley, S. A. Haine, M. J. Davis, T. W. Neely, M. A. Baker, and H. Rubinsztein-Dunlop, ‘Bose-Einstein condensation in large time-averaged optical ring potentials’, *New Journal of Physics* **18**, 035003 (2016).
- [42] S. Tempone-Wiltshire, S. Johnstone, and K. Helmerson, ‘High efficiency, low cost holographic optical elements for ultracold atom trapping’, *Optics Express* **25**, 296 (2017).
- [43] M. Edwards, P. A. Ruprecht, K. Burnett, R. J. Dodd, and C. W. Clark, ‘Collective Excitations of Atomic Bose-Einstein Condensates’, *Physical Review Letters* **77**, 1671 (1996).
- [44] S. Stringari, ‘Collective Excitations of a Trapped Bose-Condensed Gas’, *Physical Review Letters* **77**, 2360 (1996).
- [45] D. S. Jin, J. R. Ensher, M. R. Matthews, C. E. Wieman, and E. A. Cornell, ‘Collective Excitations of a Bose-Einstein Condensate in a Dilute Gas’, *Physical Review Letters* **77**, 420 (1996).
- [46] M.-O. Mewes, M. R. Andrews, N. J. van Druten, D. M. Kurn, D. S. Durfee, C. G. Townsend, and W. Ketterle, ‘Collective Excitations of a Bose-Einstein Condensate in a Magnetic Trap’, *Physical Review Letters* **77**, 988 (1996).
- [47] M. R. Andrews, D. M. Kurn, H.-J. Miesner, D. S. Durfee, C. G. Townsend, S. Inouye, and W. Ketterle, ‘Propagation of Sound in a Bose-Einstein Condensate’, *Physical Review Letters* **79**, 553 (1997).

- [48] R. Onofrio, D. S. Durfee, C. Raman, M. Köhl, C. E. Kuklewicz, and W. Ketterle, ‘*Surface Excitations of a Bose-Einstein Condensate*’, *Physical Review Letters* **84**, 810 (2000).
- [49] D. J. Frantzeskakis, ‘*Dark solitons in atomic Bose-Einstein condensates: from theory to experiments*’, *Journal of Physics A: Mathematical and Theoretical* **43**, 213001 (2010).
- [50] S. Burger, K. Bongs, S. Dettmer, W. Ertmer, K. Sengstock, A. Sanpera, G. V. Shlyapnikov, and M. Lewenstein, ‘*Dark Solitons in Bose-Einstein Condensates*’, *Physical Review Letters* **83**, 5198 (1999).
- [51] J. Denschlag, J. E. Simsarian, D. L. Feder, C. W. Clark, L. A. Collins, J. Cubizolles, L. Deng, E. W. Hagley, K. Helmerson, W. P. Reinhardt, S. L. Rolston, B. I. Schneider, and W. D. Phillips, ‘*Generating Solitons by Phase Engineering of a Bose-Einstein Condensate*’, *Science* **287**, 97 (2000).
- [52] Z. Dutton, M. Budde, C. Slowe, and L. V. Hau, ‘*Observation of Quantum Shock Waves Created with Ultra-Compressed Slow Light Pulses in a Bose-Einstein Condensate*’, *Science* **293**, 663 (2001).
- [53] K. E. Strecker, G. B. Partridge, A. G. Truscott, and R. G. Hulet, ‘*Formation and propagation of matter-wave soliton trains*’, *Nature* **417**, 150 (2002).
- [54] L. Khaykovich, F. Schreck, G. Ferrari, T. Bourdel, J. Cubizolles, L. D. Carr, Y. Castin, and C. Salomon, ‘*Formation of a Matter-Wave Bright Soliton*’, *Science* **296**, 1290 (2002).
- [55] G. A. Swartzlander, D. R. Andersen, J. J. Regan, H. Yin, and A. E. Kaplan, ‘*Spatial dark-soliton stripes and grids in self-defocusing materials*’, *Physical Review Letters* **66**, 1583 (1991).
- [56] B. Denardo, W. Wright, S. Putterman, and A. Larraza, ‘*Observation of a kink soliton on the surface of a liquid*’, *Physical Review Letters* **64**, 1518 (1990).
- [57] A. Weller, J. P. Ronzheimer, C. Gross, J. Esteve, M. K. Oberthaler, D. J. Frantzeskakis, G. Theocharis, and P. G. Kevrekidis, ‘*Experimental Observation of Oscillating and Interacting Matter Wave Dark Solitons*’, *Physical Review Letters* **101**, 130401 (2008).
- [58] J. H. V. Nguyen, P. Dyke, D. Luo, B. A. Malomed, and R. G. Hulet, ‘*Collisions of matter-wave solitons*’, *Nature Physics* **10**, 918 (2014).
- [59] B. P. Anderson, P. C. Haljan, C. A. Regal, D. L. Feder, L. A. Collins, C. W. Clark, and E. A. Cornell, ‘*Watching Dark Solitons Decay into Vortex Rings in a Bose-Einstein Condensate*’, *Physical Review Letters* **86**, 2926 (2001).
- [60] T.-L. Ho, ‘*Spinor Bose Condensates in Optical Traps*’, *Physical Review Letters* **81**, 742 (1998).
- [61] T. Ohmi and K. Machida, ‘*Bose-Einstein Condensation with Internal Degrees of Freedom in Alkali Atom Gases*’, *Journal of the Physical Society of Japan* **67**, 1822 (1998).
- [62] C. K. Law, H. Pu, and N. P. Bigelow, ‘*Quantum Spins Mixing in Spinor Bose-Einstein Condensates*’, *Physical Review Letters* **81**, 5257 (1998).
- [63] C. Wang, C. Gao, C.-M. Jian, and H. Zhai, ‘*Spin-Orbit Coupled Spinor Bose-Einstein Condensates*’, *Physical Review Letters* **105**, 160403 (2010).

- [64] Y.-J. Lin, K. Jiménez-García, and I. B. Spielman, ‘*Spin-orbit-coupled Bose-Einstein condensates*’, *Nature* **471**, 83 (2011).
- [65] J. Stenger, S. Inouye, D. M. Stamper-Kurn, H.-J. Miesner, A. P. Chikkatur, and W. Ketterle, ‘*Spin domains in ground-state Bose-Einstein condensates*’, *Nature* **396**, 345 (1998).
- [66] Y. Kawaguchi and M. Ueda, ‘*Spinor Bose-Einstein condensates*’, *Physics Reports* **520**, 253 (2012).
- [67] T. Lahaye, T. Koch, B. Fröhlich, M. Fattori, J. Metz, A. Griesmaier, S. Giovanazzi, and T. Pfau, ‘*Strong dipolar effects in a quantum ferrofluid*’, *Nature* **448**, 672 (2007).
- [68] M. Lu, N. Q. Burdick, S. H. Youn, and B. L. Lev, ‘*Strongly Dipolar Bose-Einstein Condensate of Dysprosium*’, *Physical Review Letters* **107**, 190401 (2011).
- [69] T. Lahaye, J. Metz, B. Fröhlich, T. Koch, M. Meister, A. Griesmaier, T. Pfau, H. Saito, Y. Kawaguchi, and M. Ueda, ‘*d-Wave Collapse and Explosion of a Dipolar Bose-Einstein Condensate*’, *Physical Review Letters* **101**, 080401 (2008).
- [70] I. Ferrier-Barbut, H. Kadau, M. Schmitt, M. Wenzel, and T. Pfau, ‘*Observation of Quantum Droplets in a Strongly Dipolar Bose Gas*’, *Physical Review Letters* **116**, 215301 (2016).
- [71] L. Chomaz, S. Baier, D. Petter, M. J. Mark, F. Wächtler, L. Santos, and F. Ferlaino, ‘*Quantum-Fluctuation-Driven Crossover from a Dilute Bose-Einstein Condensate to a Macrodroplet in a Dipolar Quantum Fluid*’, *Physical Review X* **6**, 041039 (2016).
- [72] M. Greiner, C. A. Regal, and D. S. Jin, ‘*Emergence of a molecular Bose-Einstein condensate from a Fermi gas*’, *Nature* **426**, 537 (2003).
- [73] S. Giorgini, L. P. Pitaevskii, and S. Stringari, ‘*Theory of ultracold atomic Fermi gases*’, *Reviews of Modern Physics* **80**, 1215 (2008).
- [74] J. Kasprzak, M. Richard, S. Kundermann, A. Baas, P. Jeambrun, J. M. J. Keeling, F. M. Marchetti, M. H. Szymańska, R. André, J. L. Staehli, V. Savona, P. B. Littlewood, B. Deveaud, and L. S. Dang, ‘*Bose-Einstein condensation of exciton polaritons*’, *Nature* **443**, 409 (2006).
- [75] H. Deng, H. Haug, and Y. Yamamoto, ‘*Exciton-polariton Bose-Einstein condensation*’, *Reviews of Modern Physics* **82**, 1489 (2010).
- [76] S. O. Demokritov, V. E. Demidov, O. Dzyapko, G. A. Melkov, A. A. Serga, B. Hillebrands, and A. N. Slavin, ‘*Bose-Einstein condensation of quasi-equilibrium magnons at room temperature under pumping*’, *Nature* **443**, 430 (2006).
- [77] J. Klaers, J. Schmitt, F. Vewinger, and M. Weitz, ‘*Bose-Einstein condensation of photons in an optical microcavity*’, *Nature* **468**, 545 (2010).
- [78] L. Onsager, ‘*Statistical hydrodynamics*’, *Il Nuovo Cimento* **6**, 279 (1949).
- [79] R. Feynman, ‘*Chapter II Application of Quantum Mechanics to Liquid Helium*’, in ‘*Progress in Low Temperature Physics*’, vol. 1, 17–53, Elsevier (1955).
- [80] E. J. Yarmchuk, M. J. V. Gordon, and R. E. Packard, ‘*Observation of Stationary Vortex Arrays in Rotating Superfluid Helium*’, *Physical Review Letters* **43**, 214 (1979).

- [81] G. P. Bewley, D. P. Lathrop, and K. R. Sreenivasan, 'Superfluid Helium: Visualization of quantized vortices', *Nature* **441**, 588 (2006).
- [82] W. F. Vinen, 'The Detection of Single Quanta of Circulation in Liquid Helium II', *Proceedings of the Royal Society of London A: Mathematical, Physical and Engineering Sciences* **260**, 218 (1961).
- [83] R. J. Donnelly, *Quantized vortices in helium II*, Cambridge University Press (1991).
- [84] L. M. Pismen, *Vortices in Nonlinear Fields: From Liquid Crystals to Superfluids, from Non-equilibrium Patterns to Cosmic Strings*, Clarendon Press (1999).
- [85] G. Blatter, M. V. Feigel'man, V. B. Geshkenbein, A. I. Larkin, and V. M. Vinokur, 'Vortices in high-temperature superconductors', *Reviews of Modern Physics* **66**, 1125 (1994).
- [86] J. F. Nye and M. V. Berry, 'Dislocations in Wave Trains', *Proceedings of the Royal Society of London A: Mathematical, Physical and Engineering Sciences* **336**, 165 (1974).
- [87] P. Coullet, L. Gil, and F. Rocca, 'Optical vortices', *Optics Communications* **73**, 403 (1989).
- [88] M. R. Dennis, K. O'Holleran, and M. J. Padgett, 'Singular optics: Optical vortices and polarization singularities', *Progress in Optics* **53**, 293 (2009).
- [89] M. Uchida and A. Tonomura, 'Generation of electron beams carrying orbital angular momentum', *Nature* **464**, 737 (2010).
- [90] J. Verbeeck, H. Tian, and P. Schattschneider, 'Production and application of electron vortex beams', *Nature* **467**, 301 (2010).
- [91] K. Y. Bliokh, I. P. Ivanov, G. Guzzinati, L. Clark, R. Van Boxem, A. Béch e, R. Juchtmans, M. A. Alonso, P. Schattschneider, F. Nori, and J. Verbeeck, 'Theory and applications of free-electron vortex states', *Physics Reports* **690**, 1 (2017).
- [92] H. Pu, C. K. Law, J. H. Eberly, and N. P. Bigelow, 'Coherent disintegration and stability of vortices in trapped Bose condensates', *Physical Review A* **59**, 1533 (1999).
- [93] M. R. Matthews, B. P. Anderson, P. C. Haljan, D. S. Hall, C. E. Wieman, and E. A. Cornell, 'Vortices in a Bose-Einstein Condensate', *Physical Review Letters* **83**, 2498 (1999).
- [94] A. L. Fetter, 'Rotating trapped Bose-Einstein condensates', *Reviews of Modern Physics* **81**, 647 (2009).
- [95] B. P. Anderson, 'Resource Article: Experiments with Vortices in Superfluid Atomic Gases', *Journal of Low Temperature Physics* **161**, 574 (2010).
- [96] A. E. Leanhardt, A. G rlitz, A. P. Chikkatur, D. Kielpinski, Y. Shin, D. E. Pritchard, and W. Ketterle, 'Imprinting Vortices in a Bose-Einstein Condensate using Topological Phases', *Physical Review Letters* **89**, 190403 (2002).
- [97] K. W. Madison, F. Chevy, W. Wohlleben, and J. Dalibard, 'Vortex Formation in a Stirred Bose-Einstein Condensate', *Physical Review Letters* **84**, 806 (2000).
- [98] P. C. Haljan, I. Coddington, P. Engels, and E. A. Cornell, 'Driving Bose-Einstein-Condensate Vorticity with a Rotating Normal Cloud', *Physical Review Letters* **87**, 210403 (2001).

- [99] E. A. L. Henn, J. A. Seman, G. Roati, K. M. F. Magalhães, and V. S. Bagnato, ‘*Generation of Vortices and Observation of Quantum Turbulence in an Oscillating Bose-Einstein Condensate*’, *Journal of Low Temperature Physics* **158**, 435 (2009).
- [100] S. Kang, J. Choi, S. W. Seo, W. J. Kwon, and Y. Shin, ‘*Rotating a Bose-Einstein condensate by shaking an anharmonic axisymmetric magnetic potential*’, *Physical Review A* **91**, 013603 (2015).
- [101] N. Navon, A. L. Gaunt, R. P. Smith, and Z. Hadzibabic, ‘*Emergence of a turbulent cascade in a quantum gas*’, *Nature* **539**, 72 (2016).
- [102] T. W. Neely, E. C. Samson, A. S. Bradley, M. J. Davis, and B. P. Anderson, ‘*Observation of Vortex Dipoles in an Oblate Bose-Einstein Condensate*’, *Physical Review Letters* **104**, 160401 (2010).
- [103] W. J. Kwon, G. Moon, J. Choi, S. Seo, and Y. Shin, ‘*Relaxation of superfluid turbulence in highly oblate Bose-Einstein condensates*’, *Physical Review A* **90**, 063627 (2014).
- [104] W. J. Kwon, G. Moon, S. W. Seo, and Y. Shin, ‘*Critical velocity for vortex shedding in a Bose-Einstein condensate*’, *Physical Review A* **91**, 053615 (2015).
- [105] T. W. B. Kibble, ‘*Topology of cosmic domains and strings*’, *Journal of Physics A: Mathematical and General* **9**, 1387 (1976).
- [106] W. H. Zurek, ‘*Cosmological experiments in superfluid helium?*’, *Nature* **317**, 505 (1985).
- [107] C. N. Weiler, T. W. Neely, D. R. Scherer, A. S. Bradley, M. J. Davis, and B. P. Anderson, ‘*Spontaneous vortices in the formation of Bose-Einstein condensates*’, *Nature* **455**, 948 (2008).
- [108] D. R. Scherer, C. N. Weiler, T. W. Neely, and B. P. Anderson, ‘*Vortex Formation by Merging of Multiple Trapped Bose-Einstein Condensates*’, *Physical Review Letters* **98**, 110402 (2007).
- [109] P. Engels, I. Coddington, P. C. Haljan, V. Schweikhard, and E. A. Cornell, ‘*Observation of Long-Lived Vortex Aggregates in Rapidly Rotating Bose-Einstein Condensates*’, *Physical Review Letters* **90**, 170405 (2003).
- [110] B. P. Anderson, P. C. Haljan, C. E. Wieman, and E. A. Cornell, ‘*Vortex Precession in Bose-Einstein Condensates: Observations with Filled and Empty Cores*’, *Physical Review Letters* **85**, 2857 (2000).
- [111] A. A. Svidzinsky and A. L. Fetter, ‘*Stability of a Vortex in a Trapped Bose-Einstein Condensate*’, *Physical Review Letters* **84**, 5919 (2000).
- [112] A. A. Svidzinsky and A. L. Fetter, ‘*Dynamics of a vortex in a trapped Bose-Einstein condensate*’, *Physical Review A* **62**, 063617 (2000).
- [113] P. C. Haljan, B. P. Anderson, I. Coddington, and E. A. Cornell, ‘*Use of Surface-Wave Spectroscopy to Characterize Tilt Modes of a Vortex in a Bose-Einstein Condensate*’, *Physical Review Letters* **86**, 2922 (2001).
- [114] E. Hodby, S. A. Hopkins, G. Hechenblaikner, N. L. Smith, and C. J. Foot, ‘*Experimental Observation of a Superfluid Gyroscope in a Dilute Bose-Einstein Condensate*’, *Physical Review Letters* **91**, 090403 (2003).

- [115] P. Rosenbusch, V. Bretin, and J. Dalibard, ‘Dynamics of a Single Vortex Line in a Bose-Einstein Condensate’, *Physical Review Letters* **89**, 200403 (2002).
- [116] V. Bretin, P. Rosenbusch, F. Chevy, G. V. Shlyapnikov, and J. Dalibard, ‘Quadrupole Oscillation of a Single-Vortex Bose-Einstein Condensate: Evidence for Kelvin Modes’, *Physical Review Letters* **90**, 100403 (2003).
- [117] A. A. Abrikosov, ‘Magnetic properties of superconductors of the second group’, *Soviet Journal of Experimental and Theoretical Physics* **5** (1957).
- [118] C. Raman, J. R. Abo-Shaeer, J. M. Vogels, K. Xu, and W. Ketterle, ‘Vortex Nucleation in a Stirred Bose-Einstein Condensate’, *Physical Review Letters* **87**, 210402 (2001).
- [119] J. R. Abo-Shaeer, C. Raman, J. M. Vogels, and W. Ketterle, ‘Observation of vortex lattices in Bose-Einstein condensates’, *Science* **292**, 476 (2001).
- [120] V. K. Tkachenko, ‘On vortex lattices’, *Soviet Journal of Experimental and Theoretical Physics* **22**, 1282 (1966).
- [121] V. K. Tkachenko, ‘Stability of vortex lattices’, *Soviet Journal of Experimental and Theoretical Physics* **23**, 1049 (1966).
- [122] I. Coddington, P. Engels, V. Schweikhard, and E. A. Cornell, ‘Observation of Tkachenko Oscillations in Rapidly Rotating Bose-Einstein Condensates’, *Physical Review Letters* **91**, 100402 (2003).
- [123] V. Schweikhard, I. Coddington, P. Engels, V. P. Mogendorff, and E. A. Cornell, ‘Rapidly Rotating Bose-Einstein Condensates in and near the Lowest Landau Level’, *Physical Review Letters* **92**, 040404 (2004).
- [124] P. Engels, I. Coddington, P. C. Haljan, and E. A. Cornell, ‘Nonequilibrium Effects of Anisotropic Compression Applied to Vortex Lattices in Bose-Einstein Condensates’, *Physical Review Letters* **89**, 100403 (2002).
- [125] N. R. Cooper, N. K. Wilkin, and J. M. F. Gunn, ‘Quantum Phases of Vortices in Rotating Bose-Einstein Condensates’, *Physical Review Letters* **87**, 120405 (2001).
- [126] J. Sinova, C. B. Hanna, and A. H. MacDonald, ‘Quantum Melting and Absence of Bose-Einstein Condensation in Two-Dimensional Vortex Matter’, *Physical Review Letters* **89**, 030403 (2002).
- [127] D. V. Freilich, D. M. Bianchi, A. M. Kaufman, T. K. Langin, and D. S. Hall, ‘Real-Time Dynamics of Single Vortex Lines and Vortex Dipoles in a Bose-Einstein Condensate’, *Science* **329**, 1182 (2010).
- [128] S. Middelkamp, P. J. Torres, P. G. Kevrekidis, D. J. Frantzeskakis, R. Carretero-González, P. Schmelcher, D. V. Freilich, and D. S. Hall, ‘Guiding-center dynamics of vortex dipoles in Bose-Einstein condensates’, *Physical Review A* **84**, 011605 (2011).
- [129] W. J. Kwon, S. W. Seo, and Y. Shin, ‘Periodic shedding of vortex dipoles from a moving penetrable obstacle in a Bose-Einstein condensate’, *Physical Review A* **92**, 033613 (2015).

- [130] J. A. Seman, E. A. L. Henn, M. Haque, R. F. Shiozaki, E. R. F. Ramos, M. Caracanhas, P. Castilho, C. Castelo Branco, P. E. S. Tavares, F. J. Poveda-Cuevas, G. Roati, K. M. F. Magalhães, and V. S. Bagnato, ‘*Three-vortex configurations in trapped Bose-Einstein condensates*’, *Physical Review A* **82**, 033616 (2010).
- [131] R. Navarro, R. Carretero-González, P. J. Torres, P. G. Kevrekidis, D. J. Frantzeskakis, M. W. Ray, E. Altuntaş, and D. S. Hall, ‘*Dynamics of a Few Corotating Vortices in Bose-Einstein Condensates*’, *Physical Review Letters* **110**, 225301 (2013).
- [132] G. Moon, W. J. Kwon, H. Lee, and Y. Shin, ‘*Thermal friction on quantum vortices in a Bose-Einstein condensate*’, *Physical Review A* **92**, 051601 (2015).
- [133] E. C. Samson, K. E. Wilson, Z. L. Newman, and B. P. Anderson, ‘*Deterministic creation, pinning, and manipulation of quantized vortices in a Bose-Einstein condensate*’, *Physical Review A* **93**, 023603 (2016).
- [134] S. Tung, V. Schweikhard, and E. A. Cornell, ‘*Observation of Vortex Pinning in Bose-Einstein Condensates*’, *Physical Review Letters* **97**, 240402 (2006).
- [135] K. E. Wilson, Z. L. Newman, J. D. Lowney, and B. P. Anderson, ‘*In situ imaging of vortices in Bose-Einstein condensates*’, *Physical Review A* **91**, 023621 (2015).
- [136] S. Middelkamp, P. G. Kevrekidis, D. J. Frantzeskakis, R. Carretero-González, and P. Schmelcher, ‘*Bifurcations, stability, and dynamics of multiple matter-wave vortex states*’, *Physical Review A* **82**, 013646 (2010).
- [137] P. J. Torres, P. G. Kevrekidis, D. J. Frantzeskakis, R. Carretero-González, P. Schmelcher, and D. S. Hall, ‘*Dynamics of vortex dipoles in confined Bose-Einstein condensates*’, *Physics Letters A* **375**, 3044 (2011).
- [138] P. J. Torres, R. Carretero-González, S. Middelkamp, P. Schmelcher, D. J. Frantzeskakis, and P. G. Kevrekidis, ‘*Vortex interaction dynamics in trapped Bose-Einstein condensates*’, *Communications on Pure and Applied Analysis* **10**, 1589 (2011).
- [139] T. Aoi, T. Kadokura, T. Kishimoto, and H. Saito, ‘*Controlled Generation and Manipulation of Vortex Dipoles in a Bose-Einstein Condensate*’, *Physical Review X* **1**, 021003 (2011).
- [140] A. V. Murray, A. J. Groszek, P. Kuopanportti, and T. Simula, ‘*Hamiltonian dynamics of two same-sign point vortices*’, *Physical Review A* **93**, 033649 (2016).
- [141] L.-C. Crasovan, V. Vekslerchik, V. M. Pérez-García, J. P. Torres, D. Mihalache, and L. Torner, ‘*Stable vortex dipoles in nonrotating Bose-Einstein condensates*’, *Physical Review A* **68**, 063609 (2003).
- [142] M. Möttönen, S. M. M. Virtanen, T. Isoshima, and M. M. Salomaa, ‘*Stationary vortex clusters in nonrotating Bose-Einstein condensates*’, *Physical Review A* **71**, 033626 (2005).
- [143] V. Pietilä, M. Möttönen, T. Isoshima, J. A. M. Huhtamäki, and S. M. M. Virtanen, ‘*Stability and dynamics of vortex clusters in nonrotated Bose-Einstein condensates*’, *Physical Review A* **74**, 023603 (2006).
- [144] V. M. Lashkin, A. S. Desyatnikov, E. A. Ostrovskaya, and Y. S. Kivshar, ‘*Azimuthal vortex clusters in Bose-Einstein condensates*’, *Physical Review A* **85**, 013620 (2012).

- [145] A. C. White, B. P. Anderson, and V. S. Bagnato, ‘*Vortices and turbulence in trapped atomic condensates*’, *Proceedings of the National Academy of Sciences* **111**, 4719 (2014).
- [146] C. F. Barenghi, L. Skrbek, and K. R. Sreenivasan, ‘*Introduction to quantum turbulence*’, *Proceedings of the National Academy of Sciences* **111**, 4647 (2014).
- [147] M. Tsubota, ‘*Turbulence in quantum fluids*’, *Journal of Statistical Mechanics: Theory and Experiment* **2014**, P02013 (2014).
- [148] N. G. Parker, A. J. Allen, C. F. Barenghi, and N. P. Proukakis, ‘*A quantum storm in a teacup*’, arXiv:1511.07064 (2015).
- [149] M. C. Tsatsos, P. E. S. Tavares, A. Cidrim, A. R. Fritsch, M. A. Caracanhas, F. E. A. dos Santos, C. F. Barenghi, and V. S. Bagnato, ‘*Quantum turbulence in trapped atomic Bose–Einstein condensates*’, *Physics Reports* **622**, 1 (2016).
- [150] M. Tsubota, K. Fujimoto, and S. Yui, ‘*Numerical Studies of Quantum Turbulence*’, *Journal of Low Temperature Physics* **188**, 119 (2017).
- [151] E. A. L. Henn, J. A. Seman, G. Roati, K. M. F. Magalhães, and V. S. Bagnato, ‘*Emergence of Turbulence in an Oscillating Bose-Einstein Condensate*’, *Physical Review Letters* **103**, 045301 (2009).
- [152] T. W. Neely, A. S. Bradley, E. C. Samson, S. J. Rooney, E. M. Wright, K. J. H. Law, R. Carretero-González, P. G. Kevrekidis, M. J. Davis, and B. P. Anderson, ‘*Characteristics of Two-Dimensional Quantum Turbulence in a Compressible Superfluid*’, *Physical Review Letters* **111**, 235301 (2013).
- [153] P. E. S. Tavares, A. R. Fritsch, G. D. Telles, M. S. Hussein, F. Impens, R. Kaiser, and V. S. Bagnato, ‘*Chaotic nature of turbulent Bose-Einstein condensates*’, arXiv:1606.01589 (2016).
- [154] J. H. Kim, W. J. Kwon, and Y. Shin, ‘*Role of thermal friction in relaxation of turbulent Bose-Einstein condensates*’, *Physical Review A* **94**, 033612 (2016).
- [155] S. W. Seo, B. Ko, J. H. Kim, and Y. Shin, ‘*Observation of vortex-antivortex pairing in decaying 2D turbulence of a superfluid gas*’, *Scientific Reports* **7**, 4587 (2017).
- [156] N. G. Parker and C. S. Adams, ‘*Emergence and Decay of Turbulence in Stirred Atomic Bose-Einstein Condensates*’, *Physical Review Letters* **95**, 145301 (2005).
- [157] M. Kobayashi and M. Tsubota, ‘*Kolmogorov Spectrum of Superfluid Turbulence: Numerical Analysis of the Gross-Pitaevskii Equation with a Small-Scale Dissipation*’, *Physical Review Letters* **94**, 065302 (2005).
- [158] R. Numasato, M. Tsubota, and V. S. L’vov, ‘*Direct energy cascade in two-dimensional compressible quantum turbulence*’, *Physical Review A* **81**, 063630 (2010).
- [159] B. Nowak, D. Sexty, and T. Gasenzer, ‘*Superfluid turbulence: Nonthermal fixed point in an ultracold Bose gas*’, *Physical Review B* **84**, 020506 (2011).
- [160] J. Schole, B. Nowak, and T. Gasenzer, ‘*Critical dynamics of a two-dimensional superfluid near a nonthermal fixed point*’, *Physical Review A* **86**, 013624 (2012).

- [161] B. Nowak, J. Schole, D. Sexty, and T. Gasenzer, ‘*Nonthermal fixed points, vortex statistics, and superfluid turbulence in an ultracold Bose gas*’, *Physical Review A* **85**, 043627 (2012).
- [162] M. T. Reeves, T. P. Billam, B. P. Anderson, and A. S. Bradley, ‘*Inverse Energy Cascade in Forced Two-Dimensional Quantum Turbulence*’, *Physical Review Letters* **110**, 104501 (2013).
- [163] M. Karl, B. Nowak, and T. Gasenzer, ‘*Universal scaling at nonthermal fixed points of a two-component Bose gas*’, *Physical Review A* **88**, 063615 (2013).
- [164] T. P. Billam, M. T. Reeves, B. P. Anderson, and A. S. Bradley, ‘*Onsager–Kraichnan Condensation in Decaying Two-Dimensional Quantum Turbulence*’, *Physical Review Letters* **112**, 145301 (2014).
- [165] T. Simula, M. J. Davis, and K. Helmerson, ‘*Emergence of Order from Turbulence in an Isolated Planar Superfluid*’, *Physical Review Letters* **113**, 165302 (2014).
- [166] B. Nowak, J. Schole, and T. Gasenzer, ‘*Universal dynamics on the way to thermalization*’, *New Journal of Physics* **16**, 093052 (2014).
- [167] T. Gasenzer, L. McLerran, J. M. Pawłowski, and D. Sexty, ‘*Gauge turbulence, topological defect dynamics, and condensation in Higgs models*’, *Nuclear Physics A* **930**, 163 (2014).
- [168] S. Mathey, T. Gasenzer, and J. M. Pawłowski, ‘*Anomalous scaling at nonthermal fixed points of Burgers’ and Gross–Pitaevskii turbulence*’, *Physical Review A* **92**, 023635 (2015).
- [169] A. J. Groszek, T. P. Simula, D. M. Paganin, and K. Helmerson, ‘*Onsager vortex formation in Bose–Einstein condensates in two-dimensional power-law traps*’, *Physical Review A* **93**, 043614 (2016).
- [170] A. J. Groszek, M. J. Davis, D. M. Paganin, K. Helmerson, and T. P. Simula, ‘*Vortex Thermometry for Turbulent Two-Dimensional Fluids*’, *Physical Review Letters* **120**, 034504 (2018).
- [171] M. Karl and T. Gasenzer, ‘*Strongly anomalous non-thermal fixed point in a quenched two-dimensional Bose gas*’, *New Journal of Physics* **19**, 093014 (2017).
- [172] A. J. Groszek, D. M. Paganin, K. Helmerson, and T. P. Simula, ‘*Motion of vortices in inhomogeneous Bose–Einstein condensates*’, *Physical Review A* **97**, 023617 (2018).
- [173] R. N. Valani, A. J. Groszek, and T. P. Simula, ‘*Condensation of Onsager Vortices*’, arXiv:1612.02930 (2016).
- [174] T. Guénault, *Statistical Physics*, Springer Netherlands (1995).
- [175] A. Einstein, ‘*Quantentheorie des einatomigen idealen Gases*’, *Sitzungsberichte der Preussischen Akademie der Wissenschaften, Physikalisch-mathematische Klasse* **1**, 261 (1924).
- [176] A. Einstein, ‘*Quantentheorie des einatomigen idealen Gases: Zweite Abhandlung*’, *Sitzberichte der Preussischen Akademie der Wissenschaften, Physikalisch-mathematische Klasse* **1**, 3 (1925).
- [177] S. N. Bose, ‘*Plancks Gesetz und Lichtquantenhypothese*’, *Zeitschrift für Physik* **26**, 178 (1924).
- [178] S. Giorgini, L. P. Pitaevskii, and S. Stringari, ‘*Condensate fraction and critical temperature of a trapped interacting Bose gas*’, *Physical Review A* **54**, R4633 (1996).

- [179] J. R. Ensher, D. S. Jin, M. R. Matthews, C. E. Wieman, and E. A. Cornell, ‘*Bose-Einstein Condensation in a Dilute Gas: Measurement of Energy and Ground-State Occupation*’, *Physical Review Letters* **77**, 4984 (1996).
- [180] A. J. Leggett, ‘*Superfluidity*’, *Reviews of Modern Physics* **71**, S318 (1999).
- [181] F. London, ‘*The Lambda-Phenomenon of Liquid Helium and the Bose-Einstein Degeneracy*’, *Nature* **141**, 643 (1938).
- [182] P. Kapitza, ‘*Viscosity of Liquid Helium below the λ -Point*’, *Nature* **141**, 74 (1938).
- [183] J. F. Allen and A. D. Misener, ‘*Flow Phenomena in Liquid Helium II*’, *Nature* **142**, 643 (1938).
- [184] L. Tisza, ‘*Transport phenomena in helium II*’, *Nature* **141**, 913 (1938).
- [185] L. Landau, ‘*Theory of the Superfluidity of Helium II*’, *Physical Review* **60**, 356 (1941).
- [186] N. Bogoliubov, ‘*On the theory of superfluidity*’, *Journal of Physics* **11**, 23 (1947).
- [187] O. Penrose, ‘*On the quantum mechanics of Helium II*’, *Philosophical Magazine* **42**, 1373 (1951).
- [188] O. Penrose and L. Onsager, ‘*Bose-Einstein Condensation and Liquid Helium*’, *Physical Review* **104**, 576 (1956).
- [189] M. S. Paoletti, R. B. Fiorito, K. R. Sreenivasan, and D. P. Lathrop, ‘*Visualization of Superfluid Helium Flow*’, *Journal of the Physical Society of Japan* **77**, 111007 (2008).
- [190] E. P. Gross, ‘*Structure of a quantized vortex in boson systems*’, *Il Nuovo Cimento* **20**, 454 (1961).
- [191] L. P. Pitaevskii, ‘*Vortex lines in an imperfect Bose gas*’, *Soviet Journal of Experimental and Theoretical Physics* **13**, 451 (1961).
- [192] E. A. Donley, N. R. Claussen, S. L. Cornish, J. L. Roberts, E. A. Cornell, and C. E. Wieman, ‘*Dynamics of collapsing and exploding Bose-Einstein condensates*’, *Nature* **412**, 295 (2001).
- [193] Y. Shin, M. Saba, M. Vengalattore, T. A. Pasquini, C. Sanner, A. E. Leanhardt, M. Prentiss, D. E. Pritchard, and W. Ketterle, ‘*Dynamical Instability of a Doubly Quantized Vortex in a Bose-Einstein Condensate*’, *Physical Review Letters* **93**, 160406 (2004).
- [194] J. A. M. Huhtamäki, M. Möttönen, T. Isoshima, V. Pietilä, and S. M. M. Virtanen, ‘*Splitting Times of Doubly Quantized Vortices in Dilute Bose-Einstein Condensates*’, *Physical Review Letters* **97**, 110406 (2006).
- [195] T. P. Simula, S. M. M. Virtanen, and M. M. Salomaa, ‘*Stability of multiquantum vortices in dilute Bose-Einstein condensates*’, *Physical Review A* **65**, 033614 (2002).
- [196] J. A. M. Huhtamäki, M. Möttönen, and S. M. M. Virtanen, ‘*Dynamically stable multiply quantized vortices in dilute Bose-Einstein condensates*’, *Physical Review A* **74**, 063619 (2006).
- [197] W. Thomson, ‘*XXIV. Vibrations of a columnar vortex*’, *The London, Edinburgh, and Dublin Philosophical Magazine and Journal of Science* **10**, 155 (1880).

- [198] H. E. Hall, *'An Experimental and Theoretical Study of Torsional Oscillations in Uniformly Rotating Liquid Helium II'*, Proceedings of the Royal Society of London A: Mathematical, Physical and Engineering Sciences **245**, 546 (1958).
- [199] E. Fonda, D. P. Meichle, N. T. Ouellette, S. Hormoz, and D. P. Lathrop, *'Direct observation of Kelvin waves excited by quantized vortex reconnection'*, Proceedings of the National Academy of Sciences **111**, 4707 (2014).
- [200] D. L. Feder, A. A. Svidzinsky, A. L. Fetter, and C. W. Clark, *'Anomalous Modes Drive Vortex Dynamics in Confined Bose-Einstein Condensates'*, Physical Review Letters **86**, 564 (2001).
- [201] C. F. Barenghi, N. G. Parker, N. P. Proukakis, and C. S. Adams, *'Decay of quantised vorticity by sound emission'*, Journal of Low Temperature Physics **138**, 629 (2005).
- [202] S. V. Nazarenko, *'Absorption of Sound by Vortex Filaments'*, Physical Review Letters **73**, 1793 (1994).
- [203] N. G. Parker, A. J. Allen, C. F. Barenghi, and N. P. Proukakis, *'Coherent cross talk and parametric driving of matter-wave vortices'*, Physical Review A **86**, 013631 (2012).
- [204] N. G. Berloff and C. F. Barenghi, *'Vortex Nucleation by Collapsing Bubbles in Bose-Einstein Condensates'*, Physical Review Letters **93**, 090401 (2004).
- [205] M. Leadbeater, T. Winiecki, D. C. Samuels, C. F. Barenghi, and C. S. Adams, *'Sound Emission due to Superfluid Vortex Reconnections'*, Physical Review Letters **86**, 1410 (2001).
- [206] S. Zuccher, M. Caliari, A. W. Baggaley, and C. F. Barenghi, *'Quantum vortex reconnections'*, Physics of Fluids **24**, 125108 (2012).
- [207] C. A. Jones and P. H. Roberts, *'Motions in a Bose condensate. IV. Axisymmetric solitary waves'*, Journal of Physics A: Mathematical and General **15**, 2599 (1982).
- [208] S. B. Pope, *Turbulent flows*, Cambridge University Press (2001).
- [209] P. A. Davidson, *Turbulence: An introduction for scientists and engineers*, Oxford University Press (2015).
- [210] Z. Han and R. D. Reitz, *'Turbulence Modeling of Internal Combustion Engines Using RNG κ - ϵ Models'*, Combustion Science and Technology **106**, 267 (1995).
- [211] H. E. A. Van den Akker, *'The Details of Turbulent Mixing Process and their Simulation'*, Advances in Chemical Engineering **31**, 151 (2006).
- [212] O. Reynolds, *'An experimental investigation of the circumstances which determine whether the motion of water shall be direct or sinuous, and of the law of resistance in parallel channels.'*, Proceedings of the Royal Society of London **35**, 84 (1883).
- [213] O. Reynolds, *'On the dynamical theory of incompressible viscous fluids and the determination of the criterion.'*, Proceedings of the Royal Society of London **56**, 40 (1894).
- [214] M. Van Dyke, *An album of fluid motion*, The Parabolic Press (1982).
- [215] L. F. Richardson, *Weather prediction by numerical process*, Cambridge University Press (1922).

- [216] A. N. Kolmogorov, 'The local structure of turbulence in incompressible viscous fluid for very large Reynolds numbers', in 'Dokl. Akad. Nauk SSSR', vol. 30, 299–303 (1941).
- [217] A. M. Obukhov, 'On the distribution of energy in the spectrum of turbulent flow', in 'Dokl. Akad. Nauk SSSR', vol. 32, 22–24 (1941).
- [218] U. Frisch, *Turbulence: The legacy of A. N. Kolmogorov*, Cambridge University Press (1995).
- [219] P. Tabeling, 'Two-dimensional turbulence: A physicist approach', *Physics Reports* **362**, 1 (2002).
- [220] R. H. Kraichnan, 'Inertial Ranges in Two-Dimensional Turbulence', *Physics of Fluids* **10**, 1417 (1967).
- [221] G. K. Batchelor, 'Computation of the Energy Spectrum in Homogeneous Two-Dimensional Turbulence', *The Physics of Fluids* **12**, II-233 (1969).
- [222] R. H. Kraichnan and D. Montgomery, 'Two-dimensional turbulence', *Reports on Progress in Physics* **43** (1980).
- [223] H. Kellay and W. I. Goldburg, 'Two-dimensional turbulence: A review of some recent experiments', *Reports on Progress in Physics* **65**, 845 (2002).
- [224] G. Boffetta and R. E. Ecke, 'Two-dimensional turbulence', *Annual Review of Fluid Mechanics* **44**, 427 (2012).
- [225] M. A. Rutgers, 'Forced 2D Turbulence: Experimental Evidence of Simultaneous Inverse Energy and Forward Enstrophy Cascades', *Physical Review Letters* **81**, 2244 (1998).
- [226] C. H. Bruneau and H. Kellay, 'Experiments and direct numerical simulations of two-dimensional turbulence', *Physical Review E* **71**, 046305 (2005).
- [227] G. Boffetta and S. Musacchio, 'Evidence for the double cascade scenario in two-dimensional turbulence', *Physical Review E* **82**, 016307 (2010).
- [228] H. Kellay, X.-l. Wu, and W. I. Goldburg, 'Experiments with Turbulent Soap Films', *Physical Review Letters* **74**, 3975 (1995).
- [229] C. Pasquero and G. Falkovich, 'Stationary spectrum of vorticity cascade in two-dimensional turbulence', *Physical Review E* **65**, 056305 (2002).
- [230] J. Sommeria, 'Experimental study of the two-dimensional inverse energy cascade in a square box', *Journal of Fluid Mechanics* **170**, 139 (1986).
- [231] J. Paret and P. Tabeling, 'Experimental Observation of the Two-Dimensional Inverse Energy Cascade', *Physical Review Letters* **79**, 4162 (1997).
- [232] H. Aref, 'Integrable, Chaotic, and Turbulent Vortex Motion in Two-Dimensional Flows', *Annual Review of Fluid Mechanics* **15**, 345 (1983).
- [233] P. K. Newton, *The N-Vortex Problem: Analytical Techniques*, Springer-Verlag (2001).
- [234] G. R. Kirchhoff, *Vorlesungen über mathematische Physik: Mechanik*, vol. 1, Teubner (1876).
- [235] C. C. Lin, 'On the Motion of Vortices in Two Dimensions', *Proceedings of the National Academy of Sciences of the United States of America* **27**, 570 (1941).

- [236] C. C. Lin, *On the Motion of Vortices in Two Dimensions*, Number 5 in University of Toronto studies, University of Toronto Press (1943).
- [237] Y. B. Pointin and T. S. Lundgren, ‘*Statistical mechanics of two-dimensional vortices in a bounded container*’, *Physics of Fluids* **19**, 1459 (1976).
- [238] G. L. Eyink and K. R. Sreenivasan, ‘*Onsager and the theory of hydrodynamic turbulence*’, *Reviews of Modern Physics* **78**, 87 (2006).
- [239] J. A. Vieceili, ‘*Equilibrium properties of the condensed states of a turbulent two-dimensional neutral vortex system*’, *Physics of Fluids* **7**, 1402 (1995).
- [240] G. Joyce and D. Montgomery, ‘*Negative temperature states for the two-dimensional guiding-centre plasma*’, *Journal of Plasma Physics* **10**, 107 (1973).
- [241] D. Montgomery and G. Joyce, ‘*Statistical mechanics of “negative temperature” states*’, *Physics of Fluids* **17**, 1139 (1974).
- [242] E. M. Purcell and R. V. Pound, ‘*A Nuclear Spin System at Negative Temperature*’, *Physical Review* **81**, 279 (1951).
- [243] N. F. Ramsey, ‘*Thermodynamics and statistical mechanics at negative absolute temperatures*’, *Physical Review* **103**, 20 (1956).
- [244] S. Braun, J. P. Ronzheimer, M. Schreiber, S. S. Hodgman, T. Rom, I. Bloch, and U. Schneider, ‘*Negative Absolute Temperature for Motional Degrees of Freedom*’, *Science* **339**, 52 (2013).
- [245] J. Dunkel and S. Hilbert, ‘*Consistent thermostatics forbids negative absolute temperatures*’, *Nature Physics* **10**, 67 (2014).
- [246] E. H. Hauge and P. C. Hemmer, ‘*2-Dimensional coulomb gas*’, *Physica Norvegica* **5**, 209 (1971).
- [247] J. Maurer and P. Tabeling, ‘*Local investigation of superfluid turbulence*’, *EPL (Europhysics Letters)* **43**, 29 (1998).
- [248] S. R. Stalp, L. Skrbek, and R. J. Donnelly, ‘*Decay of Grid Turbulence in a Finite Channel*’, *Physical Review Letters* **82**, 4831 (1999).
- [249] W. F. Vinen, ‘*An Introduction to Quantum Turbulence*’, *Journal of Low Temperature Physics* **145**, 7 (2006).
- [250] S. Nazarenko and M. Onorato, ‘*Wave turbulence and vortices in Bose–Einstein condensation*’, *Physica D: Nonlinear Phenomena* **219**, 1 (2006).
- [251] M. Kobayashi and M. Tsubota, ‘*Quantum turbulence in a trapped Bose-Einstein condensate*’, *Physical Review A* **76**, 045603 (2007).
- [252] C. F. Barenghi, ‘*Is the Reynolds number infinite in superfluid turbulence?*’, *Physica D: Nonlinear Phenomena* **237**, 2195 (2008).
- [253] A. P. Finne, T. Araki, R. Blaauwgeers, V. B. Eltsov, N. B. Kopnin, M. Krusius, L. Skrbek, M. Tsubota, and G. E. Volovik, ‘*An intrinsic velocity-independent criterion for superfluid turbulence*’, *Nature* **424**, 1022 (2003).

- [254] V. S. L'vov, L. Skrbek, and K. R. Sreenivasan, 'Viscosity of liquid ^4He and quantum of circulation: Are they related?', *Physics of Fluids* **26**, 041703 (2014).
- [255] C. Nore, M. Abid, and M. E. Brachet, 'Kolmogorov Turbulence in Low-Temperature Superflows', *Physical Review Letters* **78**, 3896 (1997).
- [256] C. Nore, C. Huepe, and M. E. Brachet, 'Subcritical Dissipation in Three-Dimensional Superflows', *Physical Review Letters* **84**, 2191 (2000).
- [257] M. Reeves, T. Billam, B. Anderson, and A. Bradley, 'Identifying a Superfluid Reynolds Number via Dynamical Similarity', *Physical Review Letters* **114**, 155302 (2015).
- [258] T. Frisch, Y. Pomeau, and S. Rica, 'Transition to dissipation in a model of superflow', *Physical Review Letters* **69**, 1644 (1992).
- [259] T. Winiecki, J. F. McCann, and C. S. Adams, 'Pressure Drag in Linear and Nonlinear Quantum Fluids', *Physical Review Letters* **82**, 5186 (1999).
- [260] K. Sasaki, N. Suzuki, and H. Saito, 'Bénard-von Kármán Vortex Street in a Bose-Einstein Condensate', *Physical Review Letters* **104**, 150404 (2010).
- [261] G. W. Stagg, N. G. Parker, and C. F. Barenghi, 'Quantum analogues of classical wakes in Bose-Einstein condensates', *Journal of Physics B: Atomic, Molecular and Optical Physics* **47**, 095304 (2014).
- [262] W. J. Kwon, J. H. Kim, S. W. Seo, and Y. Shin, 'Observation of von Kármán Vortex Street in an Atomic Superfluid Gas', *Physical Review Letters* **117**, 245301 (2016).
- [263] C. Nore, M. Abid, and M. E. Brachet, 'Decaying Kolmogorov turbulence in a model of superflow', *Physics of Fluids* **9**, 2644 (1997).
- [264] M. Kobayashi and M. Tsubota, 'Kolmogorov Spectrum of Quantum Turbulence', *Journal of the Physical Society of Japan* **74**, 3248 (2005).
- [265] J. Yopez, G. Vahala, L. Vahala, and M. Soe, 'Superfluid Turbulence from Quantum Kelvin Wave to Classical Kolmogorov Cascades', *Physical Review Letters* **103**, 084501 (2009).
- [266] T. Araki, M. Tsubota, and S. K. Nemirovskii, 'Energy Spectrum of Superfluid Turbulence with No Normal-Fluid Component', *Physical Review Letters* **89**, 145301 (2002).
- [267] C. Ewerz, T. Gasenzer, M. Karl, and A. Samberg, 'Non-thermal fixed point in a holographic superfluid', *Journal of High Energy Physics* **2015**, 70 (2015).
- [268] I. Chantesana, A. P. Orioli, and T. Gasenzer, 'Kinetic theory of non-thermal fixed points in a Bose gas', arXiv:1801.09490 (2018).
- [269] D. Kivotides, J. C. Vassilicos, D. C. Samuels, and C. F. Barenghi, 'Kelvin Waves Cascade in Superfluid Turbulence', *Physical Review Letters* **86**, 3080 (2001).
- [270] W. F. Vinen, M. Tsubota, and A. Mitani, 'Kelvin-Wave Cascade on a Vortex in Superfluid ^4He at a Very Low Temperature', *Physical Review Letters* **91**, 135301 (2003).
- [271] E. Kozik and B. Svistunov, 'Kelvin-Wave Cascade and Decay of Superfluid Turbulence', *Physical Review Letters* **92**, 035301 (2004).

- [272] V. S. L'vov and S. Nazarenko, 'Spectrum of Kelvin-wave turbulence in superfluids', *JETP Letters* **91**, 428 (2010).
- [273] A. S. Bradley and B. P. Anderson, 'Energy Spectra of Vortex Distributions in Two-Dimensional Quantum Turbulence', *Physical Review X* **2**, 041001 (2012).
- [274] T. Kusumura, H. Takeuchi, and M. Tsubota, 'Energy Spectrum of the Superfluid Velocity Made by Quantized Vortices in Two-Dimensional Quantum Turbulence', *Journal of Low Temperature Physics* **171**, 563 (2013).
- [275] T. P. Billam, M. T. Reeves, and A. S. Bradley, 'Spectral energy transport in two-dimensional quantum vortex dynamics', *Physical Review A* **91**, 023615 (2015).
- [276] R. Numasato and M. Tsubota, 'Possibility of Inverse Energy Cascade in Two-Dimensional Quantum Turbulence', *Journal of Low Temperature Physics* **158**, 415 (2009).
- [277] A. C. White, C. F. Barenghi, and N. P. Proukakis, 'Creation and characterization of vortex clusters in atomic Bose-Einstein condensates', *Physical Review A* **86**, 013635 (2012).
- [278] A. Skaugen and L. Angheluta, 'Vortex clustering and universal scaling laws in two-dimensional quantum turbulence', *Physical Review E* **93**, 032106 (2016).
- [279] S. P. Johnstone, A. J. Groszek, P. T. Starkey, C. J. Billington, T. P. Simula, and K. Helmerson, 'Negative absolute temperatures of vortices in a two-dimensional superfluid', arXiv:1801.06952 (2018).
- [280] G. Gauthier, M. T. Reeves, X. Yu, A. S. Bradley, M. Baker, T. A. Bell, H. Rubinsztein-Dunlop, M. J. Davis, and T. W. Neely, 'Negative-Temperature Onsager Vortex Clusters in a Quantum Fluid', arXiv:1801.06951 (2018).
- [281] T. Pang, *An Introduction to Computational Physics*, Cambridge University Press (2006).
- [282] H. Nyquist, 'Certain Topics in Telegraph Transmission Theory', *Transactions of the American Institute of Electrical Engineers* **47**, 617 (1928).
- [283] C. Shannon, 'Communication in the Presence of Noise', *Proceedings of the IRE* **37**, 10 (1949).
- [284] J. Javanainen and J. Ruostekoski, 'Symbolic calculation in development of algorithms: split-step methods for the Gross-Pitaevskii equation', *Journal of Physics A: Mathematical and General* **39**, L179 (2006).
- [285] C. Moler and C. Van Loan, 'Nineteen dubious ways to compute the exponential of a matrix, twenty-five years later', *SIAM review* **45**, 3 (2003).
- [286] M. Suzuki, 'General theory of fractal path integrals with applications to many-body theories and statistical physics', *Journal of Mathematical Physics* **32**, 400 (1991).
- [287] B. I. Schneider and L. A. Collins, 'The discrete variable method for the solution of the time-dependent Schrödinger equation', *Journal of Non-Crystalline Solids* **351**, 1551 (2005).
- [288] M. L. Chiofalo, S. Succi, and M. P. Tosi, 'Ground state of trapped interacting Bose-Einstein condensates by an explicit imaginary-time algorithm', *Physical Review E* **62**, 7438 (2000).
- [289] W. H. Press, S. A. Teukolsky, W. T. Vetterling, and B. P. Flannery, *Numerical recipes in C: The art of scientific computing*, Cambridge University Press (2002).

- [290] J. R. Cash and A. H. Karp, 'A Variable Order Runge-Kutta Method for Initial Value Problems with Rapidly Varying Right-hand Sides', *ACM Trans. Math. Softw.* **16**, 201 (1990).
- [291] S. Serafini, M. Barbiero, M. Debortoli, S. Donadello, F. Larcher, F. Dalfovo, G. Lamporesi, and G. Ferrari, 'Dynamics and Interaction of Vortex Lines in an Elongated Bose-Einstein Condensate', *Physical Review Letters* **115**, 170402 (2015).
- [292] T. Yefsah, A. T. Sommer, M. J. H. Ku, L. W. Cheuk, W. Ji, W. S. Bakr, and M. W. Zwierlein, 'Heavy solitons in a fermionic superfluid', *Nature* **499**, 426 (2013).
- [293] M. J. H. Ku, W. Ji, B. Mukherjee, E. Guardado-Sanchez, L. W. Cheuk, T. Yefsah, and M. W. Zwierlein, 'Motion of a Solitonic Vortex in the BEC-BCS Crossover', *Physical Review Letters* **113**, 065301 (2014).
- [294] B. Jackson, J. F. McCann, and C. S. Adams, 'Vortex line and ring dynamics in trapped Bose-Einstein condensates', *Physical Review A* **61**, 013604 (1999).
- [295] E. Lundh and P. Ao, 'Hydrodynamic approach to vortex lifetimes in trapped Bose condensates', *Physical Review A* **61**, 063612 (2000).
- [296] A. L. Fetter and J.-k. Kim, 'Vortex Precession in a Rotating Nonaxisymmetric Trapped Bose-Einstein Condensate', *Journal of Low Temperature Physics* **125**, 239 (2001).
- [297] S. A. McGee and M. J. Holland, 'Rotational dynamics of vortices in confined Bose-Einstein condensates', *Physical Review A* **63**, 043608 (2001).
- [298] J. R. Anglin, 'Vortices near surfaces of Bose-Einstein condensates', *Physical Review A* **65**, 063611 (2002).
- [299] D. E. Sheehy and L. Radzihovsky, 'Vortices in spatially inhomogeneous superfluids', *Physical Review A* **70**, 063620 (2004).
- [300] U. Al Khawaja, 'Vortex dynamics near the surface of a Bose-Einstein condensate', *Physical Review A* **71**, 063611 (2005).
- [301] H. M. Nilsen, G. Baym, and C. J. Pethick, 'Velocity of vortices in inhomogeneous Bose-Einstein condensates', *Proceedings of the National Academy of Sciences* **103**, 7978 (2006).
- [302] D. M. Jezek and H. M. Cataldo, 'Vortex velocity field in inhomogeneous media: A numerical study in Bose-Einstein condensates', *Physical Review A* **77**, 043602 (2008).
- [303] P. Mason, N. G. Berloff, and A. L. Fetter, 'Motion of a vortex line near the boundary of a semi-infinite uniform condensate', *Physical Review A* **74**, 043611 (2006).
- [304] P. Mason and N. G. Berloff, 'Motion of quantum vortices on inhomogeneous backgrounds', *Physical Review A* **77**, 032107 (2008).
- [305] H. M. Cataldo and D. M. Jezek, 'Influence of global features of a Bose-Einstein condensate on the vortex velocity', *The European Physical Journal D* **54**, 585 (2009).
- [306] P. G. Kevrekidis, W. Wang, R. Carretero-González, D. J. Frantzeskakis, and S. Xie, 'Vortex precession dynamics in general radially symmetric potential traps in two-dimensional atomic Bose-Einstein condensates', *Physical Review A* **96**, 043612 (2017).

- [307] S.-M. Chang, W.-W. Lin, and T.-C. Lin, 'Dynamics of vortices in two-dimensional Bose-Einstein condensates', *International Journal of Bifurcation and Chaos* **12**, 739 (2002).
- [308] F. E. A. dos Santos, 'Hydrodynamics of vortices in Bose-Einstein condensates: A defect-gauge field approach', *Physical Review A* **94**, 063633 (2016).
- [309] E. Šimánek, 'Adiabatic criterion for fermion bound states in the core of a moving vortex', *Physical Review B* **46**, 14054 (1992).
- [310] S. M. M. Virtanen, T. P. Simula, and M. M. Salomaa, 'Adiabaticity Criterion for Moving Vortices in Dilute Bose-Einstein Condensates', *Physical Review Letters* **87**, 230403 (2001).
- [311] S. J. Rooney, A. S. Bradley, and P. B. Blakie, 'Decay of a quantum vortex: Test of nonequilibrium theories for warm Bose-Einstein condensates', *Physical Review A* **81**, 023630 (2010).
- [312] H. H. Rose, *Geometrical Charged-Particle Optics*, Springer (2009).
- [313] R. J. Dodd, K. Burnett, M. Edwards, and C. W. Clark, 'Excitation spectroscopy of vortex states in dilute Bose-Einstein condensed gases', *Physical Review A* **56**, 587 (1997).
- [314] T. Isoshima and K. Machida, 'Bose-Einstein Condensation in a Confined Geometry with and without a Vortex', *Journal of the Physical Society of Japan* **66**, 3502 (1997).
- [315] S. M. M. Virtanen, T. P. Simula, and M. M. Salomaa, 'Structure and Stability of Vortices in Dilute Bose-Einstein Condensates at Ultralow Temperatures', *Physical Review Letters* **86**, 2704 (2001).
- [316] A. L. Fetter, 'Kelvin mode of a vortex in a nonuniform Bose-Einstein condensate', *Physical Review A* **69**, 043617 (2004).
- [317] T. P. Simula, T. Mizushima, and K. Machida, 'Kelvin Waves of Quantized Vortex Lines in Trapped Bose-Einstein Condensates', *Physical Review Letters* **101**, 020402 (2008).
- [318] S. J. Rooney, P. B. Blakie, B. P. Anderson, and A. S. Bradley, 'Suppression of Kelvin-induced decay of quantized vortices in oblate Bose-Einstein condensates', *Physical Review A* **84**, 023637 (2011).
- [319] A. Klein, I. L. Aleiner, and O. Agam, 'The internal structure of a vortex in a two-dimensional superfluid with long healing length and its implications', *Annals of Physics* **346**, 195 (2014).
- [320] L. A. Toikka and J. Brand, 'Asymptotically solvable model for a solitonic vortex in a compressible superfluid', *New Journal of Physics* **19**, 023029 (2017).
- [321] G. K. Batchelor, *An Introduction to Fluid Dynamics*, Cambridge University Press (1967).
- [322] V. Ambegaokar, B. I. Halperin, D. R. Nelson, and E. D. Siggia, 'Dynamics of superfluid films', *Physical Review B* **21**, 1806 (1980).
- [323] P. Ao and D. J. Thouless, 'Berry's phase and the Magnus force for a vortex line in a superconductor', *Physical Review Letters* **70**, 2158 (1993).
- [324] D. J. Thouless, P. Ao, and Q. Niu, 'Transverse Force on a Quantized Vortex in a Superfluid', *Physical Review Letters* **76**, 3758 (1996).
- [325] T. Simula, 'Vortex mass in a superfluid', *Physical Review A* **97**, 023609 (2018).

- [326] L. M. Pismen and J. Rubinstein, 'Motion of vortex lines in the Ginzburg–Landau model', *Physica D: Nonlinear Phenomena* **47**, 353 (1991).
- [327] B. Y. Rubinstein and L. M. Pismen, 'Vortex motion in the spatially inhomogeneous conservative Ginzburg–Landau model', *Physica D: Nonlinear Phenomena* **78**, 1 (1994).
- [328] K. Staliunas, 'Dynamics of optical vortices in a laser beam', *Optics Communications* **90**, 123 (1992).
- [329] D. Rozas, C. T. Law, and G. A. Swartzlander, 'Propagation dynamics of optical vortices', *Journal of the Optical Society of America B* **14**, 3054 (1997).
- [330] Y. S. Kivshar, J. Christou, V. Tikhonenko, B. Luther-Davies, and L. M. Pismen, 'Dynamics of optical vortex solitons', *Optics Communications* **152**, 198 (1998).
- [331] S. Middelkamp, P. G. Kevrekidis, D. J. Frantzeskakis, R. Carretero-González, and P. Schmelcher, 'Stability and dynamics of matter-wave vortices in the presence of collisional inhomogeneities and dissipative perturbations', *Journal of Physics B: Atomic, Molecular and Optical Physics* **43**, 155303 (2010).
- [332] P. Kuopanportti, J. A. M. Huhtamäki, and M. Möttönen, 'Size and dynamics of vortex dipoles in dilute Bose-Einstein condensates', *Physical Review A* **83**, 011603 (2011).
- [333] T. P. Simula, T. Mizushima, and K. Machida, 'Vortex waves in trapped Bose-Einstein condensates', *Physical Review A* **78**, 053604 (2008).
- [334] L. Koens, T. P. Simula, and A. M. Martin, 'Vibrations of a columnar vortex in a trapped Bose-Einstein condensate', *Physical Review A* **87**, 063614 (2013).
- [335] S. C. Crow, 'Stability theory for a pair of trailing vortices', *AIAA Journal* **8**, 2172 (1970).
- [336] N. G. Berloff and P. H. Roberts, 'Motion in a Bose condensate: IX. Crow instability of antiparallel vortex pairs', *Journal of Physics A: Mathematical and General* **34**, 10057 (2001).
- [337] T. P. Simula, 'Crow instability in trapped Bose-Einstein condensates', *Physical Review A* **84**, 021603 (2011).
- [338] E. B. Sonin, 'Vortex oscillations and hydrodynamics of rotating superfluids', *Reviews of Modern Physics* **59**, 87 (1987).
- [339] M. T. Reeves, T. P. Billam, B. P. Anderson, and A. S. Bradley, 'Signatures of coherent vortex structures in a disordered two-dimensional quantum fluid', *Physical Review A* **89**, 053631 (2014).
- [340] G. W. Stagg, A. J. Allen, N. G. Parker, and C. F. Barenghi, 'Generation and decay of two-dimensional quantum turbulence in a trapped Bose-Einstein condensate', *Physical Review A* **91**, 013612 (2015).
- [341] A. L. Fetter and A. A. Svidzinsky, 'Vortices in a trapped dilute Bose-Einstein condensate', *Journal of Physics: Condensed Matter* **13**, R135 (2001).
- [342] H. Aref, 'The development of chaotic advection', *Physics of Fluids* **14**, 1315 (2002).

- [343] T. Giamarchi, A. J. Millis, O. Parcollet, H. Saleur, and L. F. Cugliandolo, *Strongly Interacting Quantum Systems out of Equilibrium: Lecture Notes of the Les Houches Summer School: Volume 99, August 2012*, Oxford University Press (2012).
- [344] K. W. Schwarz, 'Three-dimensional vortex dynamics in superfluid He-4: Line-line and line-boundary interactions', *Physical Review B* **31**, 5782 (1985).
- [345] D. C. Samuels and C. F. Barenghi, 'Vortex Heating in Superfluid Helium at Low Temperatures', *Physical Review Letters* **81**, 4381 (1998).
- [346] H. E. Hall and W. F. Vinen, 'The Rotation of Liquid Helium II. II. The Theory of Mutual Friction in Uniformly Rotating Helium II', *Proceedings of the Royal Society of London A: Mathematical, Physical and Engineering Sciences* **238**, 215 (1956).
- [347] P. M. Chesler and A. Lucas, 'Vortex annihilation and inverse cascades in two dimensional superfluid turbulence', arXiv:1411.2610 (2014).
- [348] X. Yu, T. P. Billam, J. Nian, M. T. Reeves, and A. S. Bradley, 'Theory of the vortex-clustering transition in a confined two-dimensional quantum fluid', *Physical Review A* **94**, 023602 (2016).
- [349] H. Salman and D. Maestrini, 'Long-range ordering of topological excitations in a two-dimensional superfluid far from equilibrium', *Physical Review A* **94**, 043642 (2016).
- [350] M. Tsubota, K. Kasamatsu, and M. Ueda, 'Vortex lattice formation in a rotating Bose-Einstein condensate', *Physical Review A* **65**, 023603 (2002).
- [351] T. P. Simula and K. Machida, 'Kelvin-Tkachenko waves of few-vortex arrays in trapped Bose-Einstein condensates', *Physical Review A* **82**, 063627 (2010).
- [352] T. Simula, 'Collective dynamics of vortices in trapped Bose-Einstein condensates', *Physical Review A* **87**, 023630 (2013).
- [353] A. Lucas and P. Surówka, 'Sound-induced vortex interactions in a zero-temperature two-dimensional superfluid', *Physical Review A* **90**, 053617 (2014).
- [354] S. Nazarenko and M. Onorato, 'Freely decaying Turbulence and Bose-Einstein Condensation in Gross-Pitaevski Model', *Journal of Low Temperature Physics* **146**, 31 (2006).
- [355] L. A. Smirnov and A. I. Smirnov, 'Scattering of two-dimensional dark solitons by a single quantum vortex in a Bose-Einstein condensate', *Physical Review A* **92**, 013636 (2015).
- [356] S. Prabhakar, R. P. Singh, S. Gautam, and D. Angom, 'Annihilation of vortex dipoles in an oblate Bose-Einstein condensate', *Journal of Physics B: Atomic, Molecular and Optical Physics* **46**, 125302 (2013).
- [357] Y. Du, C. Niu, Y. Tian, and H. Zhang, 'Holographic thermal relaxation in superfluid turbulence', *Journal of High Energy Physics* **2015**, 1 (2015).
- [358] A. Cidrim, F. E. A. dos Santos, L. Galantucci, V. S. Bagnato, and C. F. Barenghi, 'Controlled polarization of two-dimensional quantum turbulence in atomic Bose-Einstein condensates', *Physical Review A* **93**, 033651 (2016).

- [359] C. W. Gardiner, J. R. Anglin, and T. I. A. Fudge, ‘*The stochastic Gross-Pitaevskii equation*’, arXiv:cond-mat/0112129 (2001).
- [360] H. J. Lewandowski, D. M. Harber, D. L. Whitaker, and E. A. Cornell, ‘*Simplified System for Creating a Bose–Einstein Condensate*’, *Journal of Low Temperature Physics* **132**, 309 (2003).
- [361] I. Coddington, P. C. Haljan, P. Engels, V. Schweikhard, S. Tung, and E. A. Cornell, ‘*Experimental studies of equilibrium vortex properties in a Bose-condensed gas*’, *Physical Review A* **70**, 063607 (2004).
- [362] T. P. Simula, P. Engels, I. Coddington, V. Schweikhard, E. A. Cornell, and R. J. Ballagh, ‘*Observations on Sound Propagation in Rapidly Rotating Bose-Einstein Condensates*’, *Physical Review Letters* **94** (2005).
- [363] Y. Yatsuyanagi, Y. Kiwamoto, H. Tomita, M. M. Sano, T. Yoshida, and T. Ebisuzaki, ‘*Dynamics of two-sign point vortices in positive and negative temperature states*’, *Physical Review Letters* **94**, 054502 (2005).
- [364] Y. Kagan, V. A. Kashurnikov, A. V. Krasavin, N. V. Prokof’ev, and B. V. Svistunov, ‘*Quasi-condensation in a two-dimensional interacting Bose gas*’, *Physical Review A* **61**, 043608 (2000).
- [365] C.-L. Hung, X. Zhang, N. Gemelke, and C. Chin, ‘*Observation of scale invariance and universality in two-dimensional Bose gases*’, *Nature* **470**, 236 (2011).
- [366] J. B. Keller, ‘*Corrected Bohr–Sommerfeld quantum conditions for nonseparable systems*’, *Annals of Physics* **4**, 180 (1958).
- [367] N. R. Cooper, ‘*Rapidly rotating atomic gases*’, *Advances in Physics* **57**, 539 (2008).
- [368] A. Powis, S. Sammut, and T. Simula, ‘*Vortex Gyroscope Imaging of Planar Superfluids*’, *Physical Review Letters* **113**, 165303 (2014).
- [369] The ACME Collaboration, J. Baron, W. C. Campbell, D. DeMille, J. M. Doyle, G. Gabrielse, Y. V. Gurevich, P. W. Hess, N. R. Hutzler, E. Kirilov, I. Kozyryev, B. R. O’Leary, C. D. Panda, M. F. Parsons, E. S. Petrik, B. Spaun, A. C. Vutha, and A. D. West, ‘*Order of Magnitude Smaller Limit on the Electric Dipole Moment of the Electron*’, *Science* **343**, 269 (2014).
- [370] N.-E. Guenther, P. Massignan, and A. L. Fetter, ‘*Quantized superfluid vortex dynamics on cylindrical surfaces and planar annuli*’, *Physical Review A* **96**, 063608 (2017).
- [371] P. B. Blakie, A. S. Bradley, M. J. Davis, R. J. Ballagh, and C. W. Gardiner, ‘*Dynamics and statistical mechanics of ultra-cold Bose gases using c-field techniques*’, *Advances in Physics* **57**, 363 (2008).
- [372] T. Mawson, G. Ruben, and T. Simula, ‘*Route to non-Abelian quantum turbulence in spinor Bose-Einstein condensates*’, *Physical Review A* **91**, 063630 (2015).
- [373] M. Kobayashi and M. Ueda, ‘*Topologically protected helicity cascade in non-Abelian quantum turbulence*’, arXiv:1606.07190 (2016).
- [374] A. M. Martin, N. G. Marchant, D. H. J. O’Dell, and N. G. Parker, ‘*Vortices and vortex lattices in quantum ferrofluids*’, *Journal of Physics: Condensed Matter* **29**, 103004 (2017).

-
- [375] A. Bulgac, M. M. Forbes, and G. Wlazłowski, '*Towards quantum turbulence in cold atomic fermionic superfluids*', *Journal of Physics B: Atomic, Molecular and Optical Physics* **50**, 014001 (2017).